

https://dspace.org/

Investigation of rhombohedral as an oxide conducting electrolyte for solid oxide fuel cell applications

Kerspuy, Tanner Royele Rowan

2023-09

University of the Witwatersrand, Johannesburg

https://hdl.handle.net/10539/41975

Kerspuy, Tanner Royele Rowan. (2023). Investigation of rhombohedral as an oxide conducting electrolyte for solid oxide fuel cell applications. [Master's dissertation, University of the Witwatersrand, Johannesburg]. https://hdl.handle.net/10539/41975

Downloaded from a DSpace repository. https://dspace.org/

UNIVERSITY OF THE WITWATERSRAND, JOHANNESBURG

School of CHEMISTRY

Investigation of rhombohedral Bi_2O_3 as an oxide conducting electrolyte for solid oxide fuel cell applications

Mr. Tanner R. R. Kerspuy

Student Number: 1655828

ORCID ID: 0000-0002-3710-8600

Supervisor: Prof. D. G. Billing

Co-supervisors: Prof. C. Billing & Prof. R. M. Erasmus

Abstract:

The synthesis of a bismuth system co-doped with neodymium (Nd^{3+}) and yttrium (Y^{3+}) was at the core of this project. The focus was placed on the synthesis of the rhombohedral phase of bismuth oxide, which has not been observed in pure bismuth oxide. Neodymium was selected as the main dopant (the one used in highest dopant concentration), due to its Shannon ionic radii. Upon doping with Nd^{3+} as a single dopant, it is observed that a mixture of the rhombohedral and monoclinic phases is obtained, thus noting that the single dopant system using Nd^{3+} does not stabilise the rhombohedral phase.

When using a co-doped system of 15 mol % Nd^{3+} and 5 mol % Y^{3+} (15Nd5YSB), it is observed that we are able to obtain a stable phase pure rhombohedral phase, with a total dopant concentration of 20 mol%. The total dopant concentration % ranges selected ranged between 8.5-10 mol %, 20 mol % and 22.5 mol %. The Rietveld refinement of the X-ray diffraction data obtained for both the laboratory and synchrotron-based techniques indicate sample phase purity and phase stability for the samples under investigation. The refinements obtained for the samples indicated that not only one structure model was used to fit the experimental data. The structural models which fit the Rietveld refinements of the experimental data resulted in the observation of pure phase and mixed phase rhombohedral samples being observed. The $Nd_{0.15}Y_{0.05}$-Bi_2O_3 (15Nd5YSB) sample resulted in a phase pure rhombohedral structural model. Hereafter all samples will be referred to with the shorthand notation.

The thermal analysis techniques are used to indicate the thermal dependence of the samples, this analysis also indicated phase stability across the temperature range of investigation as no phase transitions occurred throughout the heating and cooling cycles, and minimal weight loss is observed.

The samples of importance in this study were the 12.5Nd10YSB sample which obtained a conductivity of 2.4511×10^{-5} $S.cm^{-1}$ at 500 ℃, and the 15Nd5Y2.5TbSB sample which obtained a conductivity of 2.1725×10^{-5} $S.cm^{-1}$ at 500 ℃. The Arrhenius plots obtained indicated stability

of these samples across the 200-500 ℃ temperature range with no discontinuities, which suggests no phase transitions, or order-to-disorder transitions.

Variable temperature Raman spectroscopy indicated that the behaviour for all the samples analysed using Raman spectroscopy is consistent, however, a deviation was observed for the 15Nd5Y2.5ScSB sample which has a distinctive spot which exhibits different Raman shift behaviour as compared to all other samples. The VT-Raman spectroscopy spectra indicate a distinctive signature Raman peak at ~250 cm^{-1}, which can be concluded to be the Raman peak which is indicative of the rhombohedral Bi_2O_3, this peak also appears in the low cubic phase % sample after cooling back to room temperature. This assignment of the Raman spectral peak is confirmed through this peak being evident throughout all the spectra obtained and it being consistent throughout all the spectra observed.

Acknowledgements:

I would firstly like to thank GOD for providing me with the opportunity to further my academic career to this level. Secondly, I would like to thank my late mother, my foster mother and my late grandfather, Miss Marcia R. Kerspuy, Miss Miranda Z. Kerspuy and Mr John A. Kerspuy, for all the love, support, and sacrifices that they made to carry me to this point of my life. I would thirdly like to thank my supervisor, Professor Dave Billing, as well as my co-supervisors Professor Caren Billing, and Dr Rudolph M. Erasmus, for their continuous support, understanding, and guidance throughout the course of my Master of Science degree, as well as the constant stream of knowledge that they provided to me throughout the duration of my degree. I would also like to thank my friends and colleagues (namely those from the energy materials group) for their support, encouragement, and motivation that they provided me with through this journey. Lastly, I would like to thank the Gauteng City Region Academy (GCRA) for providing me with the funding for my MSc research project.

“I remember when my voice didn’t break, now it’s broken, and my voice make you shake.”- YoungstaCPT

Dedication:

I dedicate this thesis to Miss Marcia R. Kerspuy, Mr John A. Kerspuy, Miss Miranda Z. Kerspuy, Mr Tylo G. Dramat, and to all my family and friends who have been supportive beyond measure for me and have been there with me throughout the sleepless nights.

To Miss Marcia R. Kerspuy, and Mr John A. Kerspuy, although you are no longer of this world or in this world, your legacy lives on through the footprints that you have left for those of us to follow.

Miss Marcia R. Kerspuy

11/10/1963-31/01/2009

Mr John A. Kerspuy

29/08/1929-30/03/2018

To Miss Miranda Z. Kerspuy your continuous and unconditional support, love and sacrifices have moulded me into the man I am today, and for that I thank you.

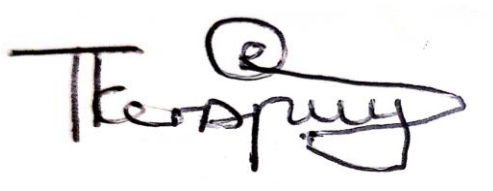
To Mr Tylo G. Dramat, I hope that the footprints I lay down before you will guide you and motivate you to achieve greatness.

“I want the world to recognize with me the open door of every consciousness”.

— Frantz Fanon, Black Skin, White Masks

Declaration:

I hereby declare that this dissertation submission is my own unaided work. This dissertation is submitted for the Master of Science degree at the University of the Witwatersrand, Johannesburg. This dissertation has not been submitted before for any degree at any other University.



_____

(Signature of candidate)

Submitted on:

____15_____day of ___September__2023___at_18 Virgo Street, Ext 1, Ennerdale 1830___

List of figures:

Figure 1.1.1: A schematic diagram of a solid oxide fuel cell and its components. 22
Figure 1.1.2: Unit cell diagram of neodymium yttrium stabilised bismuth (NdYSB) *R-3m*...28
Figure 4.1.3: Diagrammatic representation of a three-dimensional unit cell (Ameh, 2019)...61
Figure 4.1.4: Schematic diagram indicating the x-ray diffraction pattern, and the use of Pythagoras theorem.....66
Figure 4.1.5: Diagrammatical representation of the Ewald sphere indicating a set of planes as well as diffraction positions (Hammond, 2002) 68
Figure 4.1.6: Image of the D2 Phaser 73
Figure 4.1.7: Image showing the X-ray source and detector of the D2 Phaser 73
Figure 4.1.8: Image of the D9 Advance.....74
Figure 4.1.9: The various components that constitute the synchrotron radiation facility (Sedigh Rahimabadi et al., 2020).....76
Figure 4.1.10: Insertion devices and optics configuration which run through beamlines (Sedigh Rahimabadi et al., 2020).....76
Figure 4.1.11: Data detection mechanism employed by grazing-incidence X-ray diffraction 79
Figure 4.1.12: Small-angle X-ray scattering detection mechanism (Sedigh Rahimabadi et al., 2020) 82
Figure 4.1.13: A diagram indicating the WAXS and the SAXS detection mechanisms (Sedigh Rahimabadi et al., 2020) 83
Figure 4.1.14: The Jablonski diagram for all transitions involved during Rayleigh, infrared absorption, resonance Raman scattering, Raman Stokes, Raman anti-Stokes (Geraldes, 2020) 93
Figure 4.1.15: Diagrammatical representation of the SERS process (Jeon et al., 2016).....94
Figure 4.1.16: Image of the Raman Spectrometer used for room temperature and VT-Raman 99
Figure 4.1.17: Nyquist plot also indicating impedance as a vector, and the equivalent circuit used which has a single time constant (3*).....102
Figure 4.1.18: Symbolic representation of a perfect resistor (L. Zhu et al., 2014).....103
Figure 4.1.19: Symbolic representation of an ideal capacitor (8*-65) 104
Figure 4.1.20: Symbolic and Nyquist plots obtained for the CPE (8*-65) The semi-circle has its centre located at an angle which can be defined by (1-n) × 90° in relation to the origin, where n is the parameter of depression, thus if n = 1, ideal capacitance is observed. Non-ideal and non-uniform current distribution is an implication of the CPE, which could be as a result of variations in the thickness or composition of the electrode, highly distributed reaction rates, or electrode surface roughness (Holze, 2002b). 105
Figure 4.1.21: Symbolic representation of the Warburg element.....106
Figure 4.1.22: Diagrammatical representation of the Nyquist plots obtained for the FSW and FLW elements.....107
Figure 5.1.23: Rietveld refinement obtained for $15Nd5YSB$ sample. 109
Figure 5.1.24: Rietveld refinement obtained for $10YSB$ sample.....110
Figure 5.1.25: Rietveld refinement obtained for $10Nd12.5YSB$ sample. 111
Figure 5.1.26: Rietveld refinement obtained for $10NdSB$ sample. 112

Figure 5.1.27: Rietveld refinement obtained for $8.5NdSB$ sample. 112
Figure 5.1.28: Rietveld refinement obtained for $10Nd10YSB$ sample. 113
Figure 5.1.29: The Rietveld refinement of the 15Nd5YSB sample obtained from the BNL synchrotron beamline 28-ID-II 119
Figure 5.1.32: The Rietveld refinement of the 12.5Nd10YSB sample obtained from the BNL synchrotron beamline 28-ID-IIFigures 5.1.32, and 5.1.343is representative of the XRD pattern obtained for a double doped sample using the synchrotron X-ray diffractometer. The diffractogram obtained in 5.1.93for the 12.5Nd10YSB sample existed as pure rhombohedral phase sample, this is in agreement with the laboratory diffraction pattern measured on the D9 advance (see supplementary information), and thus indicates that the rhombohedral phase of $Bi2O3$ was stabilised at the ambient temperature conditions for the 22.5 mol % total dopant concentration. 121
Figure 5.1.35: The xPDF refinement of the 15Nd5YSB sample obtained from the BNL synchrotron beamline 28-ID-II 123
Figure 5.1.36: The xPDF refinement of the 12.5Nd10YSB sample obtained from the BNL synchrotron beamline 28-ID-II 124
Figure 6.1.37: The DTA scan obtained for 12.5Nd10YSB for the empty crucible and sample over the 30-800 ℃ temperature range. 126
Figure 6.1.38: The DTA scan obtained for 12.5Nd10YSB over the 30-800 ℃ temperature range showing the heating and cooling curves. 127
Figure 6.1.39: The DTA scan obtained for 15Nd5YSB for the empty crucible and sample over the 30-800 ℃ temperature range. 128
Figure 6.1.40: The DTA scan obtained for 15Nd5YSB over the 30-800 ℃ temperature range showing the heating and cooling curves. 129
Figure 6.1.41: The DTA scan obtained for 15Nd5Y2.5TbSB for the empty crucible and sample over the 30-800 ℃ temperature range. 130
Figure 6.1.42: The DTA scan obtained for 15Nd5Y2.5TbSB over the 30-800 ℃ temperature range showing the heating and cooling curves. 131
Figure 6.1.43: The DTA scan obtained for 15Nd5Y2.5SmSB for the empty crucible and sample over the 30-800 ℃ temperature range. 132
Figure 6.1.44: The DTA scan obtained for 15Nd5Y2.5SmSB over the 30-800 ℃ temperature range showing the heating and cooling curves. 133
Figure 6.1.45: The DTA scan obtained for 15Nd5Y2.5ScSB for the empty crucible and sample over the 30-800 ℃ temperature range. 134
Figure 6.1.46: The DTA scan obtained for 15Nd5Y2.5ScSB over the 30-800 ℃ temperature range showing the heating and cooling curves. 135
Figure 6.1.47: The TGA scan obtained for 12.5Nd10YSB over the 30-800 ℃ temperature range showing the heating and cooling curves. 136
Figure 6.1.48: The TGA scan obtained for 15Nd5YSB over the 30-800 ℃ temperature range showing the heating and cooling curves. 137
Figure 6.1.49: The TGA scan obtained for 15Nd5Y2.5TbSB over the 30-800 ℃ temperature range showing the heating and cooling curves. 138
Figure 6.1.50: The TGA scan obtained for 15Nd5Y2.5SmSB over the 30-800 ℃ temperature range showing the heating and cooling curves. 139
Figure 6.1.51: The TGA scan obtained for 15Nd5Y2.5ScSB over the 30-800 ℃ temperature range showing the heating and cooling curves. 140

Figure 7.1.52: The stacked VT-Raman spectra plot for 12.5Nd10YSB showing the heating cycle in the temperature range 22-800 ℃ as well as the spectra after cooling at 28 ℃.....141
Figure 7.1.53: The stacked VT-Raman spectra plot for 15Nd5YSB showing the heating cycle in the temperature range 22-800 ℃ as well as the spectra after cooling at 28 ℃ 142
Figure 7.1.54: The stacked VT-Raman spectra plot for 15Nd5Y2.5TbSB showing the heating cycle in the temperature range 22-800 ℃ as well as the spectra after cooling at 35 ℃.....143
Figure 7.1.55: The stacked VT-Raman spectra plot for 15Nd5Y2.5SmSB showing the heating cycle in the temperature range 27-800 ℃ as well as the spectra after cooling at 33 ℃.....144
Figure 8.1.56: The VT-EIS spectra for 12.5Nd10YSB between 200-250 ℃ 149
Figure 8.1.57: The VT-EIS spectra for 12.5Nd10YSB between 300-350 ℃. 150
Figure 8.1.58: The VT-EIS spectra for 12.5Nd10YSB between 400-500 ℃. 150
Figure 8.1.59: The VT-EIS spectra for 12.5Nd10YSB at 200 ℃ indicating the calculated spectra after fitting the data to a circuit model, where * indicates the calculated spectra. 151
Figure 8.1.60: The VT-EIS spectra for 12.5Nd10YSB at 250 ℃ indicating the calculated spectra after fitting the data to a circuit model, where * indicates the calculated spectra. 151
Figure 8.1.61: The circuit model used to fit the EIS data for 12.5Nd10YSB within the 200-250℃ temperature range. 152
Figure 8.1.62: The VT-EIS spectra for 12.5Nd10YSB at 300 ℃ indicating the calculated spectra after fitting the data to a circuit model, where * indicates the calculated spectra. 154
Figure 8.1.63: The circuit model used to fit the EIS data for 12.5Nd10YSB at 300 ℃ 155
Figure 8.1.64: The VT-EIS spectra for 12.5Nd10YSB at 350 ℃ indicating the calculated spectra after fitting the data to a circuit model, where * indicates the calculated spectra. 156
Figure 8.1.65: The VT-EIS spectra for 12.5Nd10YSB at 400 ℃ indicating the calculated spectra after fitting the data to a circuit model, where * indicates the calculated spectra. 157
Figure 8.1.66: The VT-EIS spectra for 12.5Nd10YSB at 450 ℃ indicating the calculated spectra after fitting the data to a circuit model, where * indicates the calculated spectra. 157
Figure 8.1.67: The circuit model used to fit the EIS data for 12.5Nd10YSB within the 350-450 ℃ temperature range. 158
Figure 8.1.68: The VT-EIS spectra for 12.5Nd10YSB at 500 ℃ indicating the calculated spectra after fitting the data to a circuit model, where * indicates the calculated spectra. 159
Figure 8.1.69: The circuit model used to fit the EIS data for 12.5Nd10YSB at 500 ℃ 159
Figure 8.1.70: The Arrhenius plot for 12.5Nd10YSB within the 200-500 ℃ temperature range.....163
Figure 8.1.71: The VT-EIS spectra for 15Nd5Y2.5TbSB between 200-250 ℃.....165
Figure 8.1.72: The VT-EIS spectra for 15Nd5Y2.5TbSB between 300-350 ℃.....165
Figure 8.1.73: The VT-EIS spectra for 15Nd5Y2.5TbSB between 400-500 ℃.....166
Figure 8.1.74: The VT-EIS spectra for 15Nd5Y2.5TbSB at 200 ℃ indicating the calculated spectra after fitting the data to a circuit model, where * indicates the calculated spectra. 166
Figure 8.1.75: The VT-EIS spectra for 15Nd5Y2.5TbSB at 250 ℃ indicating the calculated spectra after fitting the data to a circuit model, where * indicates the calculated spectra. 167
Figure 8.1.76: The circuit model used to fit the EIS data for 15Nd5Y2.5TbSB within the 200-250 ℃ temperature range. 167
Figure 8.1.77: The VT-EIS spectra for 15Nd5Y2.5TbSB at 300 ℃ indicating the calculated spectra after fitting the data to a circuit model, where * indicates the calculated spectra. 168
Figure 8.1.78: The VT-EIS spectra for 15Nd5Y2.5TbSB at 350 ℃ indicating the calculated spectra after fitting the data to a circuit model, where * indicates the calculated spectra. 169

Figure 8.1.79: The VT-EIS spectra for 15Nd5Y2.5TbSB at 400 ℃ indicating the calculated spectra after fitting the data to a circuit model, where * indicates the calculated spectra. 169
Figure 8.1.80: The circuit model used to fit the EIS data for 15Nd5Y2.5TbSB within the 300-400 ℃ temperature range. 170
Figure 8.1.81: The VT-EIS spectra for 15Nd5Y2.5TbSB at 450 ℃ indicating the calculated spectra after fitting the data to a circuit model, where * indicates the calculated spectra. 171
Figure 8.1.82: The VT-EIS spectra for 15Nd5Y2.5TbSB at 500 ℃ indicating the calculated spectra after fitting the data to a circuit model, where * indicates the calculated spectra. 172
Figure 8.1.83: The circuit model used to fit the EIS data for 15Nd5Y2.5TbSB within the 450-500 ℃ temperature range. 172
Figure 8.1.84: The Arrhenius plot for 12.5Nd10YSB within the 200-500 ℃ temperature range.....174
Figure 8.1.85: The Arrhenius plot for 15Nd5Y2.5TbSB within the 200-500 ℃ temperature range.....175
Figure 5.1.86:The XRD patterns obtained for all samples within the 8.5 – 10 mol % dopant concentration range using the D2 phaser. 213
Figure 5.1.87:The XRD patterns obtained for all samples within the 20 mol % dopant concentration range using the D2 phaser. 214
Figure 5.1.88: The XRD patterns obtained for all samples within the 17.5 mol % dopant concentration range for the double-doped samples using the D2 phaser.....214
Figure 5.1.89: The XRD patterns obtained for all samples within the 22.5 mol % dopant concentration range for the double-doped samples using the D2 phaser.....215
Figure 5.1.90: The XRD patterns obtained for all samples within the 22.5 mol % dopant concentration range for the triple-doped samples using the D2 phaser. 216
Figure 5.1.91: The XRD patterns obtained for aged samples within various dopant concentration ranges using the D2 phaser. 216
Figure 5.1.92: The XRD patterns obtained for all samples within the 20 mol % dopant concentration range using the D9 advance. 217
Figure 5.1.93: The XRD patterns obtained for all samples within the 22.5 mol % dopant concentration range using the D9 advance. 218

List of tables:

Table 3.1: Samples synthesised with actual masses and mol % indicated. 57

Table 2: Sample phase presence and percentage after Rietveld refinement.....113
Table 3: The input values which were used as a starting model for the Rietveld refinement analysis of all samples (where the fractional occupancy is dependent on the dopant mol % - using the 15Nd5YSB as an example) 116
Table 4: The refined structural parameters for all samples at room temperature using the rhombohedral structural model of space group *R-3m*. $Rexp$ is defined as the minimum achievable pattern residual, whereas Rwp is defined as the weighted pattern residual 117
Table 5: Values obtained when the EIS data is fitted using the circuit models described for each temperature range (T). Rb represents the bulk resistance, σb represents bulk conductivity, a represents the frequency constant, Cb representing the pseudo capacitance of the bulk, and Qbrepresents the constant phase element of the bulk. 161
Table 6: All the values used for the calculations of the Arrhenius plot parameters for 12.5Nd10YSB.....163
Table 7: The values obtained when the EIS data is fitted using the circuit models described for each temperature range (T). Rb represents the bulk resistance, σb represents bulk conductivity, a represents the frequency constant, Cb representing the pseudo capacitance of the bulk, and Qbrepresents the constant phase element of the bulk. 173
Table 8: All the values used for the calculations of the Arrhenius plot parameters for 15Nd5Y2.5TbSB 175
Table 9: Electrical parameters derived for the sample compositions under investigation within the 200-500℃ for both the heating and cooling cycles obtained from the Arrhenius plot by from plotting log (σb) against $1000T$:.....178

Table of Contents

Abstract: 2
Acknowledgements: 4
Dedication: 5
Declaration: 6
List of figures: 7
List of tables: 11
List of Abbreviations: 17
Chapter 1 18
Introduction: 18
Aims and Objectives: 26
Chapter 2 32
Literature Review 32
Solid Oxide Fuel Cells (SOFC's): 32
Solid Oxide Fuel Cell (SOFC) components: 34
2.1.1 Anode materials: 34
Nickel metal anode material: 36
Nickel/YSZ cermet: 36
Noble metal and copper cermet's: 37
Ceria and various other compounds: 38
Perovskite and double perovskites: 39
2.1.2 Cathode Materials: 39
Perovskite materials: 40
2.1.3 Electrolyte materials: 41
Fluorite structure oxide materials: 42
Pyrochlore electrolyte materials: 44
Perovskite-structure based electrolyte materials: 46

Perovskite-based electrolyte materials: 46

Perovskite-based electrolyte materials of the form $LnBO3$ (where B=Al, In, Sc, Y): 46

$La2Mo2O9$ (LAMOX) electrolyte materials: 47

Apatite structure-based electrolyte materials: 48

The brownmillerite-like electrolyte material phases: 49

The $\delta - Bi2O3$ and $Bi4V2O11$ structure based ceramic electrolyte materials: 50

Chapter 3: 54

Synthesis process & Sample Preparation 54

Introduction to sol-gel synthesis: 54

Sample Preparations: 55

3.1: Powder X-ray Diffraction (PXRD): 55

3.2: Simultaneous Thermal Analysis (STA) 56

3.3: Raman Spectroscopy (RS) 56

3.4: Electrochemical Impedance Spectroscopy (EIS) 56

Chapter 4 59

Characterisation 59

Powder X-ray diffraction: 59

Simultaneous Thermal Analysis (STA): 89

Raman Spectroscopy: 90

Electrochemical Impedance Spectroscopy: 99

Chapter 5 108

X-ray Diffraction (XRD) 108

Laboratory x-ray experimental data: 109

5.1.1 Purely rhombohedral sample Rietveld refinement: 109

5.1.2 Purely cubic sample Rietveld refinement: 110

5.1.3 Rhombohedral and cubic sample Rietveld refinement: 111

5.1.4 Rhombohedral and monoclinic sample Rietveld refinement: 111
5.1.5 Rhombohedral, tetragonal, and cubic sample Rietveld refinement: 112
5.1.6 Rhombohedral, monoclinic, and tetragonal sample Rietveld refinement: 113
Synchrotron x-ray experimental data (BNL): 118
X-ray diffraction: 119
5.3.1 15Nd5YSB: 119
5.3.2 12.5Nd10Y-Bi_2O_3: 121
xPDF: 122
5.4.1 15Nd5YSB: 123
5.4.2 12.5Nd10YSB 124
Chapter 6: 126
Simultaneous Thermal Analysis (STA) 126
Differential Thermal Analysis (DTA) & Thermogravimetric Analysis (TGA): 126
DTA: 126
6.1.1 12.5Nd10YSB: 126
6.1.2 15Nd5YSB: 128
6.1.3 15Nd5Y2.5TbSB: 130
6.1.4 15Nd5YSmSB: 132
6.1.5 15Nd5Y2.5ScSB: 134
TGA: 136
6.2.1 12.5Nd10YSB: 136
6.2.2 15Nd5YSB: 137
6.2.3 15Nd5Y2.5TbSB: 138
6.2.4 15Nd5Y2.5SmSB: 139
6.2.5 15Nd5Y2.5ScSB: 140
Chapter 7 141
Raman Spectroscopy 141

LabRam HR: 141
Variable temperature Raman Spectroscopy: 141
7.1.1 12Nd10YSB: 141
7.1.2 15Nd5YSB: 142
7.1.3 15Nd5Y2.5TbSB: 143
7.1.4 15Nd5Y2.5SmSB: 144
7.1.5 15Nd5Y2.5ScSB: 145
Chapter 8: 148
Electrochemical Impedance Spectroscopy (EIS) 148
Laboratory experimental data: 149
Variable temperature EIS: 149
8.1.1 12.5Nd10YSB: 149
8.1.2 15Nd5Y2.5TbSB: 165
Chapter 9: 180
Discussion and Conclusion 180
References: 184
Supplementary Information 213
X-ray diffraction 213
Laboratory experimental data analysis: 213
5.1.7 8.5 – 10 mol % dopant concentration: 213
5.1.8 20 mol % dopant concentration: 214
5.1.9 17.5 mol% dopant concentration: 214
5.1.10 22.5 mol % dopant concentration (double-doped): 215
5.1.11 22.5 mol % dopant concentration (triple-doped): 216
5.1.12 Aged samples (various dopant concentrations): 216
D9 Advance diffractometer data analysis: 217
5.2.1 20 mol % dopant concentration: 217

5.2.2 22.5 mol % dopant concentration: 218

List of Abbreviations:

1. SOFCs: Solid oxide fuel cells
2. LT-SOFCs: Low temperature solid oxide fuel cells
3. PEM: Polymer electrolyte membrane
4. DMFC: Direct methanol fuel cell
5. PAFCL Phosphoric acid fuel cell
6. AFC: Alkaline fuel cell
7. MCFC: Molten carbonate fuel cell
8. YSZ: Yttria stabilised zirconia
9. ScSZ: Scandium oxide stabilised zirconia
10. ASR: Area specific resistance
11. EJ: Exajoule
12. LSCM: Lanthanum strontium cerium manganese oxide
13. TEC; Thermal expansion coefficient
14. YSB: Yttria stablised bismuth oxide
15. NdSB: Neodymium stabalised bismuth oxide
16. NdYSB: Neodymium ytrria stablised bismuth oxide
17. PXRD: Powder X-ray diffraction
18. STA: Simultaneous thermal analysis
19. DTA: Differential thermal analysis
20. TGA: Thermogravimetric analysis
21. RS: Raman spectroscopy
22. EIS: Electrochemical impedance spectroscopy
23. VT-Raman spectroscopy: Variable temperature Raman spectroscopy
24. VT-EIS: Variable temperature electrochemical impedance spectroscopy

Chapter 1

Introduction:

The worldwide energy crisis emerges from a convergence of intricate factors affecting energy production, distribution, and consumption globally. These factors encompass escalating energy demand due to population growth and urbanization, finite fossil fuel reserves, environmental apprehensions, and geopolitical complexities. This complex situation underscores the need for innovative solutions to ensure sustainable and equitable energy provisions for the future. (International Energy Agency, 2022)

The expanding global population, urbanization, and industrialization collectively drive an ever-mounting need for energy. This demand is fuelled by modern lifestyles, technological progress, and the growth of various industries. Conventional fossil fuels such as coal, oil, and natural gas have long been the cornerstones of the global energy supply. However, their finite nature and the environmental repercussions associated with their extraction and consumption pose significant challenges. Dependence on a limited range of energy sources and the complexities of energy-rich regions can instigate concerns about energy security. Disruptions in energy supply due to conflicts or political instability can trigger substantial economic and social consequences. The combustion of fossil fuels releases greenhouse gases like carbon dioxide, which contribute to climate change. The energy sector's substantial greenhouse gas emissions necessitate a shift to cleaner energy alternatives. Effective energy infrastructure is vital for ensuring reliable energy production, transmission, and distribution. Aging infrastructure and insufficient investment can lead to energy inefficiencies and interruptions. A significant portion of the global population lacks access to reliable and affordable energy. This energy poverty obstructs socioeconomic progress, restricts educational opportunities, and diminishes overall living standards. (International Energy Agency, 2022)

Particularly in sub-Saharan Africa, the struggle with energy-related issues encompasses challenges such as constrained access to electricity, reliance on biomass-intensive cooking methods, and insufficient infrastructure. These hurdles impede fundamental services, hinder economic progress, limit educational opportunities, and adversely affect overall living

conditions. (Bougrea et al., 2008)

The transitioning to sustainable alternative energy sources becomes more apparent by the day. The global energy landscape is constantly evolving in order to combat the challenges addressed above, at the core of all the challenges is the transformation towards more sustainable energy sources and energy practices. These include but are not limited to the transition towards more renewable energy sources, focusing on energy efficiency, the employment of advanced technologies, energy decentralisation and electrification in sectors of key importance. (Bougrea et al., 2008)

The transition towards renewable energy sources, such as solar, wind, hydroelectric, geothermal, and ocean energy, to name but a few, are processes which harness natural processes to generate power without emitting greenhouse gasses as well as depleting resources. The process of enhancing energy efficiency in various industries, transportation as well as buildings results in the reduction of the overall energy demand, while economic activities are maintained. The integration of renewable energy sources into the existing energy infrastructure can be enhanced through employing research and development in energy storage, smart grids, as well as energy management systems, thus driving the use of advanced technologies to drive renewable energy generation. The decentralisation of the energy generation through distributed energy generation and microgrids is at the forefront in driving energy resilience through the enablement of local communities generating their own power and managing it as well. Electrification within sectors such as transportation and heat generation are also at the centre of reduction of fossil fuel reliance, and drives the use of clean energy.(International Energy Agency, 2022)(Bougrea et al., 2008)

The solid oxide fuel cells (SOFCs) are an area of the fuel cells which are currently attracting great interest in combating the global energy crisis which has become very evident mainly due to the imbalance observed in the current global energy demand versus global energy supply. It is projected that the global primary energy demand in 2050 will be within the range of 600-1000 EJ, when placed in comparison to that in 2008 which was about 500 EJ (Bauen et al., 2009). However, most of the global energy demands in the present day are still met by fossil fuels, which has its own limitations. The move to more renewable and environmentally friendly energy sources has been of key interest (Singh et al., 2017).

This need for more environmentally friendly and renewable energy sources has led to one of the focuses being placed on fuel cells. Fuel cells have a range of beneficial properties such as energy efficiency, fuel flexibility, and cleanliness, which leads them to be a suitable alternative to the conventional power sources still widely used today (Yamamoto, 2000). Fuel cells are thus key in their potential to act as power sources in stationary, portable and transport applications (Ormerod, 2003).

The conversion that occurs in a fuel cell is the conversion of the chemical energy in a fuel, such as H_2, hydrocarbons, directly into electricity. Fuel cell operations are comparable to that of batteries, however, fuel cells have gaseous electrodes, they also do not require recharging and run as long as the oxidant and fuel are being supplied to the electrodes (Kirubakaran et al., 2009)(Mahato et al., 2015). The efficiency of fuel cells unlike heat engines, are not limited to the Carrot cycle (Abdalla et al., 2018). The electrolyte characteristics are crucial in the determination of the category to which a fuel cell is grouped, there are six main groups. The six main groups are as follows: polymer electrolyte membrane (PEM), direct methanol (DMFC), phosphoric acid (PAFC), alkaline (AFC), solid oxide (SOFC), and molten carbonate (MCFC) (Zarabi Golkhatmi et al., 2022).

A Solid Oxide Fuel Cell (SOFC) is an electrochemical device that generates electricity through the electrochemical reaction of oxygen and a fuel source, typically hydrogen or hydrocarbons. SOFCs belong to the family of high-temperature fuel cells and operate at elevated temperatures. The solid oxide fuel cell (SOFC) is one of the most efficient fuel cells among all the different fuel cells. This is due to the SOFC having a great flexibility in the fuel choice used, it is noiseless, has a potential long lifetime of 40000-80000h, as well as shows low CO_2 emissions (Stambouli & Traversa, 2002).

In 1899 Nernst was the first to discover the solid oxide electrolytes, which eventually lead to the discovery of what is known today as the solid oxide fuel cell. Nernst noted that the conductivity for pure metal oxides increased relatively slowly with temperature and was

observed to remain only relatively low in comparison to mixed metal oxides which had higher conductivities (Nernst, 1899).

The solid oxide fuel cell (SOFC) is defined by it having a solid ceramic electrolyte which is a metal oxide. A SOFC can be broken down into its various components which all have a role in the overall functionality of the cell, namely, the anode where the fuel and oxide ions react, the electrolyte where the oxide ions pass through from the cathode to the anode, and the cathode which is key for the reduction of oxygen into oxide ions. These SOFC's, however, have a disadvantage, which is their relatively high operating temperatures. The required operating range falls within the range of 800-1000 ℃ (Ormerod, 2003). Figure 1.1 shows a schematic representation of a solid oxide fuel cell and its various components.

SOFCs have high working temperatures, these high working temperatures are required for adequate ionic conductivity to be obtained, these temperatures also provide excellent heat by-products which can be used for co-generation of energy or in combined cycle operations. The solid-state electrolyte is a merit of the SOFC, as it is manageable, has no handling issues, as well as does not result in the corrosion of the cell. SOFCs do not require expensive noble metals, and thus are considered as cost effective for mass production (Zakaria et al., 2020).

The harsh operating conditions of SOFCs also need to be taken into consideration, namely; the redox and thermal cycling, the poisonous atmosphere as well as high working temperatures (Price et al., 2021), several properties for components (sealant, interconnect, anode, cathode, electrolyte) of the SOFC need to be met. These properties, include but are not limited to the following (Fergus, 2006; Kendall & Kendall, 2015):

-Good chemical, thermal and mechanical compatibility with other components

-Adequate and appropriate conductivity (Electronic insulation and ability to provide good ionic conductivity are requirements for the electrolyte, and the electrodes are required to have promising ionic and electronic conductivity)

-High electrical conductivity, high resistivity against oxidation, sulfation and carbon deposition for interconnects, as well as perfect gas tightness

-Acceptable chemical, thermal, mechanical, and morphological stability

-Insulating and hermeticity sealant nature

All these requirements are to be achieved in an easy-to-fabricate as well as cost-effective manner (Zarabi Golkhatmi et al., 2022).

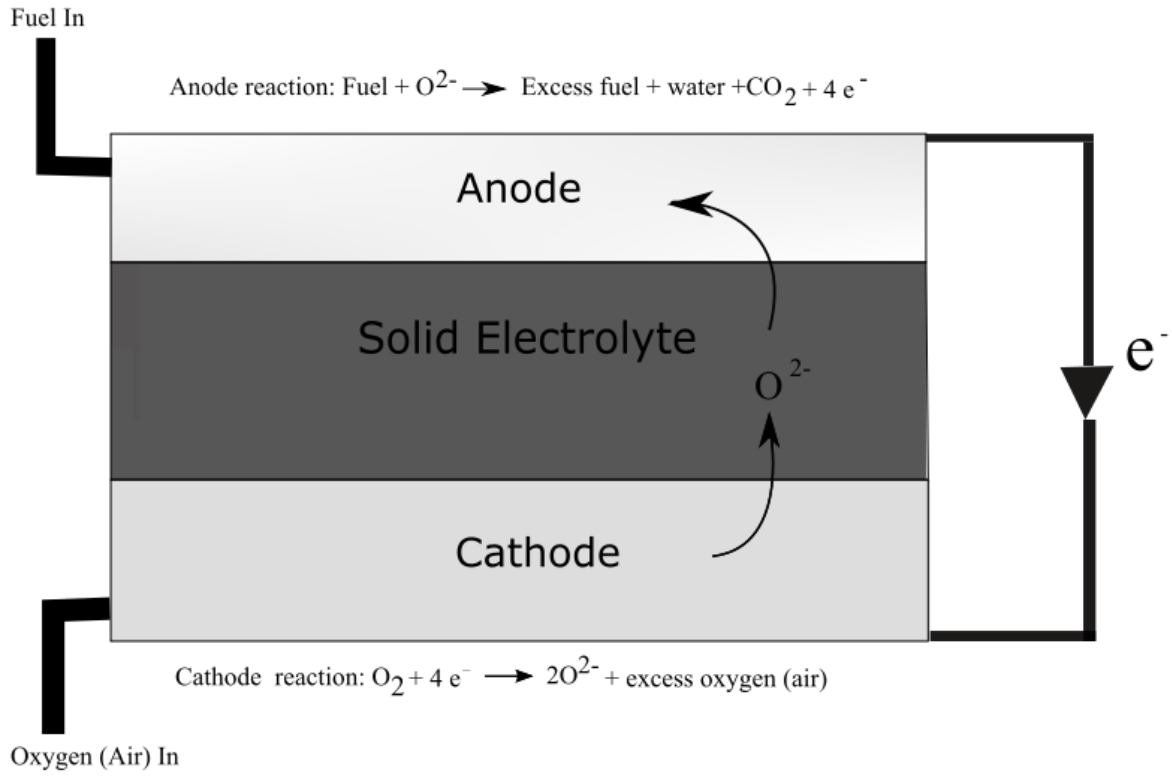


Figure 1.1.1: A schematic diagram of a solid oxide fuel cell and its components.

One of the greatest challenges which have been a crucial area of focus has been the attempt to reduce the operating temperature of the SOFCs, and thus the development of low temperature-solid oxide fuel cells (LT-SOFCs). The development of LT-SOFCs not only results in lower operation temperatures, but also provides various advantageous properties, namely, increasing the range of materials which can be used in SOFCs for each component, long term reliability with regards to robustness and strength of the materials used, a reduction in the required start up time, a reduction in system costs, higher overall cell reliability, as well as an increase in the

efficiency of these SOFCs when considered for commercial applications (Kilner & Burriel, 2014).

The core component of the SOFC is the electrolyte, which is defined as the component at which the oxide ions undergo conduction from the cathode to the anode. These ions then undergo a reaction with the hydrocarbon fuels to form H_2O, and CO_2, which is crucial in the completion of the overall electrochemical reaction which is occurring. The oxygen vacancy hopping mechanism is the model by which the conduction process of the oxide ions occurs, and this mechanism is considered to be a thermally activated process (Mahato et al., 2015).

Thus, one of the properties of great interest with regards to these electrolyte materials is conductivity. In the search to obtain greater ionic conductivity for these electrolyte materials (with the interest of this project being not only on obtaining high ionic conductivity but also on observing if these ionic conductivity capabilities are exhibited at lower operating temperatures), a key focus area has become the crystal structure of the materials under consideration. In order for these materials to obtain a sufficiently high ionic conductivity, the crystal structure needs to exhibit conduction pathways and oxide vacancies, resulting in the low migration enthalpy and a high level of point defect disorder being observed (Xia et al., 2017).

As a consequence of the severe working conditions of the SOFCs, a number of degradation processes that are diverse in nature can occur, these can arise from each component and their interactions, this thus hinders the long-term stability requirements. The commonly used characteristic that defines degradation is the loss of performance, with the rate of degradation being generally stated in voltage loss per 1000 h, which is especially crucial in stacks. The degradation of single cells can be measured by the change in area specific resistance (ASR) (Slodczyk et al., 2018). The degradation process in SOFCs is very complicated to study as this would require long-term studies, the operation factors, such as, current density, temperature, fuel impurities, etc., also affect the procedure (Batfalsky et al., 2016).

The SOFC electrolyte undergoes degradation due to various mechanisms, which are as follows (Skafte et al., 2016):
-Mechanical failures

-Dopant diffusion, phase transition, impurities

When the SOFC operates in harsh atmosphere as well as high temperatures, the electrolyte layer is susceptible to a phase change which can affect the performance of the SOFC, as a result of the reduction of ionic conductivity, and phase stability, which overall results in degradation (Zarabi Golkhatmi et al., 2022).

Yttria stabilised zirconia (YSZ) is one of the most commonly used electrolytes in SOFC's. YSZ has properties such as good stability under harsh operating conditions, competitive ionic conductivity across a vast range of partial oxygen pressures, as well as mechanical properties which are good under elevated temperature conditions. These properties however are hampered due to the degradation that occurs as a result of long exposure of the electrolyte to elevated temperature, namely at 1000℃, which result in microstructural changes, and thus impedes SOFC performance. The phase transition, which is the most notable phenomenon, is the phase change from cubic to tetragonal zirconia. This transition is strongly dependant on the Y_2O_3 concentration which is present in ZrO_2 (Butz et al., 2006)(Hattori et al., 2004). It us indicated that the optimised electrolyte dopant concentrations for the YSZ electrolyte is 9.5YSZ (Zakaria & Kamarudin, 2021). The defect mobility is lowered with an increase in the dopant concentration, as this causes the emergence of point defects (Fergus, 2006).

The scandium oxide stabilised zirconia (ScSZ) electrolyte also encounters the challenge of the phase transition, the ScSz electrolyte is a promising candidate for low-to-intermediate operating temperatures, the phase transition experienced is the cubic-rhombohedral-cubic phase transition that occurs at lower temperatures (Gao et al., 2017). The rhombohedral phase exhibits weaker ionic conductivity, and thus the cell faces an increase in the ASR, this then causes lower performance (Fergus, 2006). Consequently, the transition results in residual stress in the SOFC stack which is unwanted (Y. Sun et al., 2021).

An additional source of degradation is the chemical interactions that occur between the electrolyte and other components of the cell, the chemical interactions that occur between the electrolyte and the cathode has to especially be noted. This chemical reaction results in the formation of secondary insulating phases as well as an interface (Brandon et al., 2017)(Jang et al., 2019).

Degradation in both the electrolyte and the cathode performance is caused by extreme interdiffusion, as well as the formation of insulating layer. The chemical interaction between the electrolyte and anode, is less severe as compared to that which occurs between the electrolyte and cathode. The most common anode material is Ni-YSZ, and has no problem with the YSZ electrolyte. The formation of a resistive layer can however occur between Ni-based anodes and lanthanum strontium cerium manganese oxide (LSCM) which is an electrolyte material, and thus results in the degradation of the SOFC (Fergus, 2006).

The second mechanism which is responsible for SOFC electrolyte degradation is mechanical failure, which occurs due to chemical and thermal stresses. At high temperatures, SOFC's experience almost close to negligible stress at high working temperatures, however, as the cooling down from high temperatures to room temperature occurs, residual stresses build up as a result of the thermal expansion coefficients (TEC's) of the interactions of the electrolyte and cathode or the electrode and anode (Jang et al., 2019). Subsequently, the residual stress results in the introduction of delamination or crack initiation, which in turn leads to mechanical failure (Selçuk et al., 2001). Residual stresses are also introduced due to phase transformations, an example is the phase change which occurs in ScSZ, which experiences a phase transformation of a partial cubic to rhombohedral and back to cubic transformation within the 300℃-500℃ heating range (Y. Sun et al., 2021).

Chemical stress is also a source of the mechanical failure in the SOFC electrolyte, this chemical stress is influenced by the chemical environment shaped by the operational conditions of the SOFC. A crucial example is when Ni-based anode materials undergo an oxidation process which results in volume change. The irreversible expansion of the Ni-based anode occurs, due to either uncontrolled fuel utilization, or system leakage which causes the penetration of unwanted oxygen to the anode. Ni and NiO volumes exhibit differences which are very significant, this causes tension in the electrolyte, internal stress, and overall system failure. The other degradation mechanism is thus also sped up due to the gas permeation which occurs through the cracks formed (Wang et al., 2019).

Aims and Objectives:

The project focuses on the synthesis of the rhombohedral phase of Bi_2O_3 (space group R-3m) for the application as a solid oxide electrolyte material. This phase can only be achieved by doping of the Bi sites in the structure of Bi_2O_3, and elements such as neodymium (Nd), yttrium (Y), samarium (Sm), scandium (Sc), and terbium (Tb) as potential dopant will be considered. These dopant elements were chosen upon consideration on various factors, namely, the Shannon ionic radii and the stable oxidation state of these elements. The dopant elements under consideration all have Shannon ionic radii which are very close to that for lanthanum (La) (where lanthanum is the cation which has a sufficiently large cationic radius which is essential for the formation of the rhombohedral phase); they are all also have the same 3+ oxidation state as La and thus aliovalent doping is not considered.

The co-doping of these elements in the correct dopant concentration percentages (with possible considerations in the range of 7-10% total dopant concentration as per the article by Jolley, Jayathilake, and Wachsman (Jolley et al., 2019), however initially a higher total dopant concentration range of 10-20% was investigated as this dopant concentration range could possibly result in the product formed having a phase transition between the rhombohedral and cubic phases being observed) is expected to result in the synthesised material sitting within the cubic-rhombohedral phase transition window. The dopant range concentration range was then further extended to 22.5%.

The Bi_2O_3 based solid oxide electrolyte material systems are of interest due to the high oxide-ion conductivity which they exhibit, with the fluorite-like δ-Bi_2O_3 high temperature structure in particular exhibiting this attractive property (Harwig & Gerards, 1979). Bi_2O_3 has been reported to have six naturally occurring polymorphs, namely the stable phases; the monoclinicα-phase, and the cubic δ-phase, and the metastable phases; the tetragonal β-phase, the body centred cubic (bcc) γ-phase, the orthorhombic ε-phase, and the triclinic ω-phase (Michel Drache et al., 2007).

Other phases, such as the rhombohedral phase can only be formed when the crystal lattice is doped with a sufficiently large cation, or multiple sufficiently large cations (by means of co-doping) (Iwahara et al., 1981). The rhombohedral phase of Bi_2O_3 has, however, not been evaluated as an electrolyte material for SOFC's as extensively as the highly conductive cubic δ-phase of Bi_2O_3 (Jolley et al., 2019), and thus this project will focus on trying to further study the rhombohedral phase. Thus far lanthanum (La) and yttrium (Y) have been the commonly used dopants in the rhombohedral phase of Bi_2O_3 due to their similar ionic radii as compared to Bi (i.e., $La^{3+} = 1.16$ Å, $Bi^{3+} = 1.17$ Å, $Y^{3+} = 1.109$ Å) (Jolley et al., 2019).

Although the rhombohedral phase results in oxide-ion conductivity which is about ten times less when compared to that for the cubic δ-phase, the rhombohedral phase exhibits a greater phase stability at lower temperatures as compared to that obtained for the cubic δ -phase (thus also enabling the possibility of studying thermal expansion properties of this phase, although phase stability is not a prerequisite for these studies). When doping with Nd, it was noted that a secondary tetragonal phase is observed at dopant concentrations higher than 10% Nd and thus the ideal dopant range is 7-10%, as this results in the formation of a pure rhombohedral phase product exhibiting the property phase stability not only at low temperatures but also under aging conditions (where samples are left for a period of time under room temperature conditions or typical operating temperatures of the SOFCs, and characterised once again after a period of time) (Jolley et al., 2019). The co-doping of the material with the dopant elements considered, when doped in the right ratio is thus crucial in the stabilisation of the rhombohedral phase of Bi_2O_3 and this needs to be investigated. Figure 1.2 is a unit cell diagram of neodymium yttrium stabilised Bi_2O_3 (NdYSB) in the rhombohedral phase. Observing the diagram, it can be seen that the unit cell consists of multiple stacked segments, we also observe an inversion and rotation of each sub-segment of the unit cell, thus indicating multiple points through which oxygen diffusion, or oxygen hopping can occur. The rhombohedral Bi_2O_3 has its cations which occupy two sites, namely, the 3a (0, 0, 0), and 6c (0, 0, 0.2252) sites. The oxygen anions occupy three sites, namely, 6c (0, 0, 0.299), 6c (0, 0, 0.091), and 6c (0, 0, 446) sites.

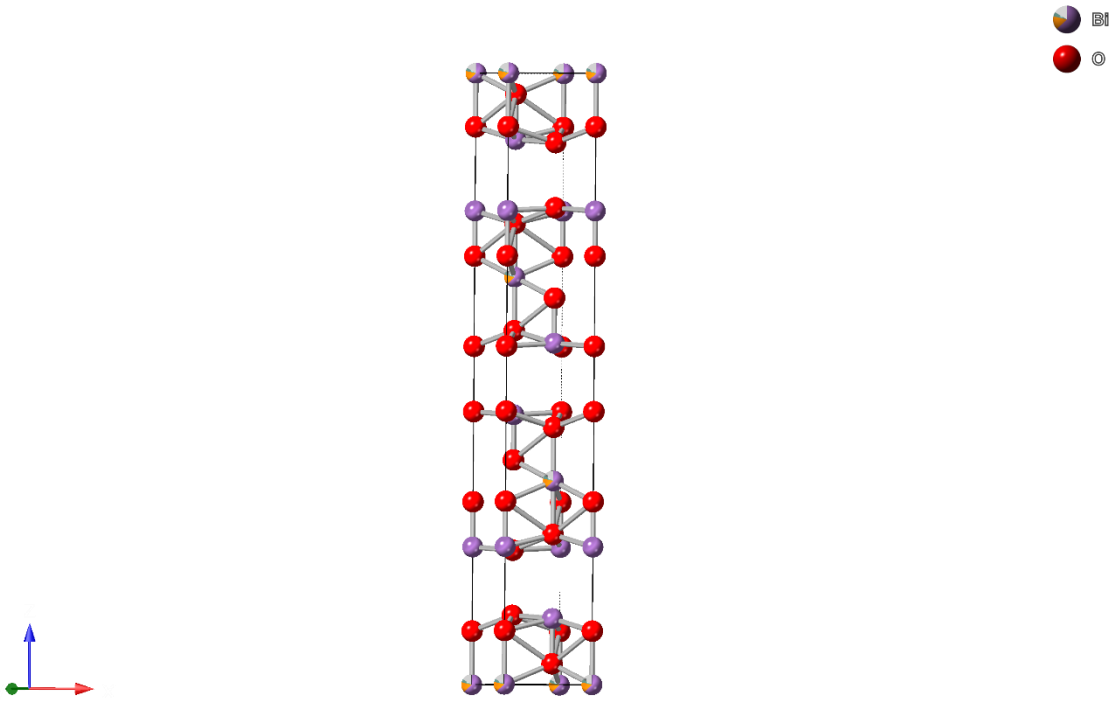


Figure 1.1.2: Unit cell diagram of neodymium yttrium stabilised bismuth (NdYSB) *R-3m*

The overall aims of the project are as follows:

To synthesise phase pure rhombohedral Bi_2O_3 with the use of Nd, Y, Sc, Sm and Tb as dopants (using the co-doping technique with a varying dopant concentration range), using the sol-gel synthesis method, single-doped, double-doped and triple-doped samples were synthesised. The total dopant mol concentration % samples synthesised, ranged between 8.5-10 mol%, 20 mol % and 22.5 mol %.

To characterise and determine the properties (i.e., physical, electrochemical, thermal etc.) of the pure rhombohedral phase Bi_2O_3 samples as prepared using various characterisation techniques. The use of simultaneous thermal analysis (STA) techniques which use a combination of differential scanning calorimetry (DSC) and thermogravimetric analysis (TGA) to study heat curves and weight loss observed in samples.

To investigate of the structure-property relationship of the synthesized rhombohedral Bi_2O_3. X-ray diffraction analysis, coupled with the STA as well as variable temperature Raman spectroscopy techniques are used to obtain structural information and relate this to various properties of the samples.

To investigating the electrochemical properties of the synthesized rhombohedral Bi_2O_3, in terms of oxide and electronic conduction. The variable temperature electrochemical impedance spectroscopy (EIS) technique is used to investigate the ionic conductivity of the synthesised samples within the low temperature range.

This dissertation is structured as follows:

Chapter 1 provides an introduction to the energy crisis, why the research into solid oxide fuel cells (SOFCs) is important as a source of environmentally friendly renewable energy, as well as provides an overview of the various types of materials and compositions used in SOFC electrolytes, and the benefits of the exploration into the rhombohedral phased bismuth oxide materials. Additionally, the aims and objectives of the work is also highlighted in this chapter.

Chapter 2 serves as a high-level comprehensive literature review which focuses on SOFCs, their use, the different components of the SOFCs, as well as a number of anode, cathode, and electrolyte materials used historically. Due to the limited literature that focuses on the rhombohedral phase of bismuth oxide, the literature review focuses a large part on the literature that is there based on all the relevant bismuth oxide materials recorded historically.

Chapter 3 provides information on the sample synthesis procedure, as well as indicates the steps taken for sample preparation prior to characterisation. A table of all the samples synthesised and all the required information is also provided in the chapter.

Chapter 4 of the work highlights the theoretical principles and background related to the various characterisation techniques used for sample analysis. This chapter includes detail descriptions on the techniques and the theory which inform the techniques, the laws which are important in these techniques, as well as highlight the fundamentals behind each technique and the importance of the information provided using each of the characterisation techniques, namely, X-ray diffraction, simultaneous thermal analysis, Raman spectroscopy, and electrochemical impedance spectroscopy. This chapter also provides the instrumental parameters for the instrumentation used to carry out these complementary characterisation techniques.

Chapter 5 in this study presents the experimental results obtained through sample characterisation using X-ray diffraction. This chapter provides detailed analysis and discussion of the results obtained from the laboratory and synchrotron experiments, to provide a comprehensive understanding of the technique and the information provided by the results and how these shapes understanding the properties and behaviour of the synthesised materials.

Chapter 6 of this study presents the experimental results obtained through the sample characterisation using simultaneous thermal analysis (STA) which compromises of the combination of differential thermal analysis (DTA) and thermogravimetric analysis (TGA), used to provide a comprehensive understanding of the thermal properties of the synthesised materials.

Chapter 7 of this study presents the experimental results obtained through sample characterisation using variable temperature Raman spectroscopy and provided insights on the sample properties and behaviour of the synthesised material.

Chapter 8 in presents the experimental results obtained through the sample characterisation using variable temperature electrochemical impedance spectroscopy and provided insights on the sample conductivity as a result of the variable temperature experiments and thus provides a comprehensive understanding of the sample properties and behaviour of the synthesised

materials.

Chapter 9 provides an overall discussion and conclusion for the study, as well as indicates the future work that needs to be done. This chapter draws all the insights provided in the previous chapters and summarises the key findings of the study, these insights are inclusive of the synthesis of the novel synthesised materials, the characterisation techniques and the information provided by all these techniques. This chapter then also highlights the complementary information that is provided through the characterisation techniques and how the information shapes the overall understanding of the properties and behaviour of the synthesised materials.

The supplementary materials section right at the end of this study provides additional information on data plots and other information that was not provided in the main text of this study. This is the inclusion of additional experimental results and futher detailed analysis information.

Chapter 2

Literature Review

Solid Oxide Fuel Cells (SOFCs):

Solid oxide fuel cells (SOFCs) have become an area of great interest, namely, due to the possibility of SOFC's to alleviate the global energy crisis. SOFCs are defined as electrochemical conversion devices which show great promise in the energy conversion device sector due to their high efficiency. However, as with any system these devices offer both pro's and con's, the pro's being that they are: considered to be low pollution technology, have high fuel flexibility, high efficiency, high reliability and great durability, with con's namely being: they require high operating temperatures in order to eliminate ohmic loss, and the reduction of the operating temperatures result in reduced ionic conductivity (Jolley et al., 2019).

The production of electricity in a SOFC occurs by mean of an electrochemical reaction in which the fuel is oxidized by oxide ions which diffuse through a solid-electrolyte which allows for the diffusion of oxide ions (Minh, 2004). SOFC's have the general structure of an electrolyte layer which is located in between a cathode and anode (electrodes) and contains a number of interconnects and sealants which are crucial to the functionality of the SOFC. SOFC's function mainly by two mechanisms of action namely the use of protons or the use of oxide ions for conduction (Mahato et al., 2015). The external circuit of a SOFC is completed when the electrons which are generated at the anode (as a result of the oxidation of the fuel) is accepted for reduction (oxygen reduction) at the cathode, and thus the electrochemical conversion occurs and produces electricity by means of the flow of the electrons which occurs in the external circuit (Lee et al., 2011). The high ionic conductivity of SOFC occurs as a result of the high operating temperatures of approximately 800-1000℃ which is imperative for the reduction or elimination of ohmic loss (Stambouli & Traversa, 2002).

The high operating temperature, however, imparts a large number of challenges on the SOFC system, such as, interfacial diffusion which is observed between electrode and electrolyte

materials, electrode sintering, poisoning of the catalyst material, mechanical as well as thermal stresses which occurs mainly caused by the difference in the coefficients of thermal expansion (CTE) of cell components in the SOFC, as well as the thermal instability of the materials used (Yamamoto, 2000). Due to these challenges, the main goal of current research with regards to SOFC's are based on the possible reduction of the high operating temperatures, to temperatures as low as 300-400℃, while maintaining the phase and thermal stability as well as high levels of ionic conductivity (Singhal, 2002).

In the search to reduce the operating temperatures of these SOFC's, it has been noted that for improvement of the overall performance of the SOFC's, the greatest challenge has been the choice of material, and thus the material properties of the material. These material properties are namely, low ionic resistance of the electrolytes, low electronic resistance of the electrodes, catalysts, interconnects, and sealants. It should also be noted that at lower operating temperatures, lower polarization loss is expected, due to the high electrochemical activity and thus rapid kinetics which occur at lower temperatures (Shao et al., 2012).

One of the key issues when it comes to the introduction of any new system into society, is the question of economic viability. Many solutions have been proposed for the improvement of the economic viability of SOFC's, as well as the reduction of system costs. One of the solutions proposed is the introduction of low-cost stainless steel into the stack designs, but this imparts an additional step, which is the coating of these steel parts in order to prevent high-temperature oxidation of air-facing steel surfaces. Minimization of the volatilization of chromium from the alloy is also necessary, in order to eliminate the degradation of the cell's overall performance due to the poisoning of the cathode material by chromium vapours (B. Zhu et al., 2018).

Another solution is the use of less expensive metallic interconnects, as well as low operating temperatures, which result in the reduction of maintenance costs, however this solution brings a challenge which is the increase of the ohmic losses observed at the electrolyte, thus reduced ionic conductivity, and a decrease in the catalytic activity observed at the electrodes, and thus result in an overall decrease in the cell performance observed. Thus, in order for the performance at low temperatures to be improved, these challenges need to be overcome. The

possible alternatives which allow for these challenges to be overcome, are namely; the use of thin electrolyte materials, and the introduction of nanoscale materials for both the electrolytes and the electrode materials (B. Zhu et al., 2018).

Many of the issues observed due to the high operating temperatures can be resolved when there is a reduction in the overall operating temperatures to a temperature around 500℃. One of the most beneficial properties which occur as a result of the decrease in operating temperature, is the elimination of the need for reforming fuel, as the lower operating temperatures result in the reduction of carbon deposition as a result of the direct and clean oxidation of the methane fuel. Although the reduction of the operating temperature has a large number of benefits for the SOFC, based on performance, economic viability and environmental friendliness, it still however exhibits a large number of constraints which need to be overcome. The key to understanding and potentially overcoming these constraints are based on not only understanding the reactions which occur in the components of the SOFC and the construction of the SOFC, but also understanding the complex electrochemistry and thermodynamics which are crucial to the various reactions which enable for the conversion of fuel into electrical energy (Baertsch et al., 2004).

Solid Oxide Fuel Cell (SOFC) components:

A SOFC is composed of various components which constitute what we know as a SOFC, each of these components are of crucial importance to the overall performance of the SOFC, as the reactions, oxide diffusion, electrical current conduction and separation of the fuel and oxidizer in the SOFC is dependent on each of these components (Mahato et al., 2015).

2.1.1 Anode materials:

The anode can be described as the component of a SOFC, where the fuel undergoes electrochemical oxidation. The electrochemical oxidation of the fuel occurs at specific surface sites, which are referred to as the triple-phase boundaries (TPB's). The TPB's are an interface between the electrode, electrolyte and the gas. The anodic polarization is largely impacted by a number of factors, such as; morphology of anode, anode microstructure, porosity content,

active anodic area, the distribution of porosity as well as the size of the pores which are crucial for the gas transportation efficiency which is obtained in the high temperature reducing environments, as well as the catalytic activities which occur on the surface of the materials (S. P. Jiang & Chan, 2004).

The most crucial requirements for any anode material used in a SOFC is; a) its ability to have high ionic conductivity and for the electrocatalytic activity which it possesses to be sufficient, these are mainly required in order to result in the minimization of the polarization losses which occur when the H_2 oxidation reaction occurs, and thus complete fuel oxidation is observed, b) its ability to have great thermal and chemical stability, paired with a minimization of the CTE mismatch which occurs between the anode and other cell components, and also mechanical strength which is sufficient enough to overcome mechanical stress and physical weight constraints, and c) the anode material needs to be compatible with the wide fuel flexibility of the fuel gases, such that the anode material should avoid reacting with the fuel supplied, as well as tolerate the carbon deposition, reoxidation and possible sulphur poisoning which can occur (Minh, 1993).

The development of the anode component (anode material) of a SOFC has had one great challenge to overcome, which is the understanding and ability to engineer anode materials which has result in charge-transfer as well as mass-transfer through the bulk of the material, surfaces of the materials, as well as at the interfaces of the materials, thus increasing the convenience, efficiency, economic processing methodology as well as fabrication technologies of these materials (Mahato et al., 2015).

Various materials are used as anodic materials, mainly as a result of their respective properties. Materials such as carbon were conventionally used as both anodic and cathodic materials, these materials include platinum, cobalt, iron, graphite, as well as nickel. They were mainly used due to their good chemical stability, low cost, and overall, the great catalytic activity that they exhibit when reactions such as the oxidation of hydrogen, as well as the hydrocarbon fuel reformation, and thus Ni, was used for a number of years as the key anode material. It is however observed that pure Ni results in a CTE mismatch being observed between the Ni anode

material and more commonly used electrolyte materials such as yttria-stabilised zirconia (YSZ), this then results in the weakening of the Ni interface with the electrolyte material. The introduction of cermets (ceramic-metallic composites, e.g. Ni-YSZ) as well as metal oxides occurred as a result of the optimization of electrode materials, it should however be noted that the metal oxides have a greater advantage as compared to the cermets, mainly due to the extended lengths of the TPB observed. The Ni-YSZ cermet has a number of benefits, namely, it has the capability to result in the overall increase in the efficiency of the SOFC due to its high electronic conductivity, ionic conductivity as well as good catalytic activity for the hydrogen oxidation process (Mahato et al., 2015).

Various materials have been considered as anode materials, these materials and a brief description of each material is listed below:

Nickel metal anode material:

Nickel (Ni) and platinum (Pt) electrodes are always placed in comparison, mainly due to the similarity in the behaviours of Ni and Pt electrodes. It is however noted that when electrochemical analysis is done on these materials as electrodes, it can be seen that the Ni electrodes are more electrochemically active as compared to the Pt electrodes. This is observed by comparison of the value of polarization resistance, it is observed that the value obtained for the Pt electrode is always noted to be higher than that of the Ni electrode. The controlled microstructure of the anode material is one of the most crucial factors in understanding the reactions and thus reaction mechanisms which occur at the electrode (anode) in the SOFC (T. Kawada et al., 1990). The greatest disadvantage experienced with the Ni anode materials is observed in the difficulty in the determination of the pathways of the reactions which take place, and hence determination of the rate-determining step for the Ni anode is difficult (T. Kawada *et al.*, 1990).

Nickel/YSZ cermet:

Upon the introduction of the cermet type anode materials, a number of advantages were observed, namely, the increase in stability, the improvement of the anchorage and adhesion between electrolyte and anode materials, as well as the increase in the area of the reaction sites in the form of TBP present on the electrode material (anode material). The establishment of the quantitative description of the microstructure of the cermet anodes (i.e., Ni/YSZ) (which has been defined as a complex microstructure), as well as obtaining an explanation for the complex impedance spectra obtained still remains a crucial challenge which needs to be understood and overcome (de Boer, 1998). Due to their less complex and complicated microstructure Ni metal electrodes have been employed in SOFC's as anode materials as compared to that of Ni/YSZ cermet electrodes, although the pure metal electrode materials allow for tailoring for fabrication purposes, as well as have the ability to avoid structural limitations and the ability for measurements to be done on purely chemical parameters which can be related to their microstructural properties, they still have more disadvantages as compared to the Ni/YSZ cermet electrode materials (Mahato et al., 2015). When considering the cermet anode materials, it is observed that they not only have the advantage of offering enough pores for the diffusion of the fuel gases, but also allow for the adequate transportation of O^{2-} ions through the electrochemically active region present on the anode material (H. Zhu et al., 2005). As a result of the introduction of the porous anode materials, the implementation of the direct utilization of hydrocarbons into SOFC's has become more convenient (Coutelieris et al., 2003). It is however important to note that upon the introduction of hydrocarbons into the SOFC, the amount of carbon atoms is important as with the Ni/YSZ cermet anodes, the amount of carbon atoms present in the fuel has the ability to result in the significant reduction of the output voltage and conversion efficiency of the SOFC. Due to this, numerous SOFC's have been developed with the preference of using hydrocarbons in conjunction with an external reformer, which can be accompanied with partial oxidation as well as steam reformation, and this preferential SOFC design is employed for long-term SOFC operations (Liese & Gemmen, 2005).

Noble metal and copper cermet's:

One of the metals which has been discovered to be inactive towards carbon deposition which occurs during the reformation of hydrocarbon fuels, is copper (Cu) (Costa-Nunes et al., 2005). A disadvantage however arises when considering Cu as an anode material, this disadvantage is that due to Cu having a lower melting point as compared to Ni, high temperature sintering becomes impractical. In order to combat this disadvantage, a new fabrication method called the wet impregnation method was introduced in order to fabricate Cu anode materials (Gorte et al., 2004). It was however also noted that no catalytic activity was rendered by Cu when considerations were done on the breaking of hydrocarbons. Thus, Cu can be considered as a poor catalyst for the bond-breaking of the C-C and C-H bonds of hydrocarbons, and this overall results in Cu being very stable in the hydrocarbon environment. This stability imparts an increase in the polarization activation of the cell. In order to combat the disadvantage which comes with the use of Cu as an anodic material, a combination of Cu with materials such as ceria which offers a higher catalytic activity, results in an increase in the catalytic activity and stability of the anodic material. When placed in combination with ceria, Cu provides the electronic conductivity, while ceria is an excellent oxidation catalyst (Lu et al., 2003).

Ceria and various other compounds:

When considerations on obtaining materials, which assist in the expansion of reaction zones beyond the triple phase boundary, a material of interest is cerium oxide (CeO_2) which is considered to be a mixed ionic-electronic conductor when placed in reducing atmospheres. One of the reasons this material is of great interest is due to it possessing an electronic conductivity which is significantly larger as compared to that of YSZ. This material also offers the ability to have its ionic conductivity controlled by the introduction of acceptor dopant oxides to the material, namely, Sm_2O_3, Y_2O_3, GdO_3, as well as CaO (Perry Murray et al., 1999).

Another advantage is that this material has the catalytic ability with regards to the direct oxidation reaction or process of hydrocarbons which contain various fuels, namely, methane, ethane, toluene, 1-butene, and n-butane. The material offers an additional benefit as it provides great compatibility with adjoining component materials of the cell (Mahato et al., 2015).

Perovskite and double perovskites:

Sulphur tolerance has been of key importance when considering electrode materials, and in the search for obtaining sulphur tolerant electrode materials, when considering anode materials which are Ni-free, nickel free conductive metal oxides were produced (Gong et al., 2007). Examples of these materials are as follows, $Sr_{1-x}La_xTiO_3$ (x=0.3-0.4), Y-doped $SrTiO_3$, $La_{1-x}Sr_xVO_3$ (x=0.5), $Ce_{0.9}Sr_{0.1}VO_x$ (x=3,4), its doped variants $La_{1-x}Sr_xCr_{1-y}Mn_yO_3$ (x=0.25, y=0.5), as well as the double perovskites, namely, $Sr_2Mg_{2-x}MoO_6$ (x=1), $Sr_2Fe_{4/3}Mo_{2/3}O_6$, and the pyrochlore type material $Gd_2Ti_{2-x}Mo_xO_7$ (x=0.6). Although these conductive oxide materials provided an increase in the sulphur tolerance which it exhibits, there are a few drawbacks, namely, although the materials show an increase in sulphur tolerance, they exhibit lower electronic conductivity as compared to the Ni-cermets thus resulting in decreased anode performance, they also show poor oxidation of fuels, a reduction in the catalytic activity, as well as a significant incompatibility with adjoining components of the cell especially at high temperatures (Mahato et al., 2015).

2.1.2 Cathode Materials:

The cathode can be defined as the SOFC component at which the reduction of molecular oxygen occurs. The mechanism of action by which this process occurs is as follows; when air flows through the SOFC, this air acts as an oxygen supply, this oxygen then undergoes adsorption onto the porous cathodic electrode, and this oxygen is then reduced to oxide ions as a result of the acceptance of electrons which are incoming from the current collector. The specific site of reaction is highly dependent on the nature of the cathodic material, such that the reduction reaction of the molecular oxygen can either occur at the electrode/electrolyte/gas interface or the electrode/gas interface. Upon either the partial or full reduction of the oxide ions or atomic species, these ions or species are then transported to the electrolyte/electrode/gas interface by means of transportation through the surface or bulk pathways where they are then subjected to complete reduction. Subsequent transportation of the oxide ions to the anode is observed and thus oxidation of the fuel occurs (Mahato et al., 2015).

The crucial requirements for a material which can be considered as a cathode material in the SOFC, are as follows; a) electronic conductivity which is relatively high, b) cost effectivity, c) relatively high oxide ion conductivity, d) excellent chemical compatibility of the cathode material with the electrolyte materials, as well as the interconnect materials, e) great catalytic activity mainly during the oxygen reduction reaction, f) great material stability when exposed to environments which promote oxidation (with the focus placed on both the operational and fabrication processes), g) the elimination, reduction, and minimalization of the mismatch of CTE values for the cathode materials as well as that of the other component materials in the SOFC, h) porosity which is sufficient, such that it allows for the fast rate of diffusion of oxygen gas from the cathode to the cathode-electrolyte interface (Corbel et al., 2005).

The starting point when it comes to understanding the kinetic and mechanism of action of the working cathode was first reported over 100 years ago, with the material of interest being a porous platinum electrode on YSZ which was used for the oxygen reduction process (Möbius, 1997). The oxygen reduction reaction is defined as the electrochemical reaction in which a charge transfer process is observed, and this process is believed to take place at the TPB's (Mahato et al., 2015). When consideration is placed on the oxygen reduction process it is noted that the process obeys Tafel kinetics in the range of moderate to high overpotential values.

Numerous materials have been considered as cathode materials, these materials and a brief description of each material is listed below:

Perovskite materials:

When considerations are done on the cathode materials of a SOFC, perovskite oxides have been of a great importance (Mahato et al., 2015). The first perovskite material reported for use as a cathode material in a SOFC was $La_{1-x}Sr_xCoO_{3-\delta}$ (LSC), and this material was introduced in 1966 by Button and Archer (Möbius, 1997), thereafter several perovskite materials were synthesised and their applicability and usage were tested subsequently. To date the most investigated cathode material for a SOFC cathode is $La_{1-x}Sr_xMnO_{3-\delta}$ (LSM), which was noted in 1973 and then exclusively used for cathode application (Mahato et al., 2015).

Perovskites are defined as oxide which have the general formula of ABO_3, where A and B are cations which have a combined net charge of +6. When consideration is done on the differentiation between the A and B sites, it is noted that the A site is the site which is occupied by the lower valance cations (rare earth and alkaline earth metals), they thus have the cations with the larger ionic radius as compared to the B site and thus are also coordinated to 12 oxide ions (12 coordinate). When considering the B site, it is noted that the B site is occupied by the higher valance reducible transition metal cations (they occupy the B site either in mixtures or alone), they thus have the cations with the smaller ionic radius as compared to the A site and are thus coordinated to 6 oxide ions (6 coordinate) (S. P. Jiang, 2008). Due to high temperature operation of these materials, it becomes evident that the octahedral symmetry of the material around the transitional metal cations result in the formation of a semi-conducting band structure and thus results in the observation of high electronic conductivity for these materials, and this then indicated that the B-site cations thus partake in a redox catalytic mechanism (Mahato et al., 2015).

When considering the perovskite materials, it is noted that the undoped perovskite materials have characteristically poor oxide ion conductivity in air, and thus when the material is doped and undergoes partial substitution of either the A-site cation, or B-site cation, with acceptor cations (i.e. Ca^{2+}, Ba^{2+}, and Sr^{2+}), or the reduction of Co^{3+}/Mn^{3+} to Co^{2+}/Mn^{2+}, which thus leads to the formation of oxygen deficient perovskite materials such as $La_{1-x}Sr_xCo_yCo_{1-y}O_{3-\delta}$. It is then noted that the oxygen vacancy defects which form as the basis of the oxide ion conduction in these perovskite materials result in conductivity values being observed for these materials which are as high as the conductivity values of solid electrolyte materials (C. Sun et al., 2010).

2.1.3 Electrolyte materials:

The electrolyte is considered as the core of the SOFC, as it is the component at which the oxide ions undergo conduction from the cathode to the anode where these ions then undergo a reaction with the hydrocarbon fuels to form H_2O, and CO_2, and thus this process is crucial in

the completion of the overall electrochemical reaction which is occurring. The conduction process of these oxide ions are as a result of the oxygen vacancy hopping mechanism, and this mechanism is considered to be a thermally activated process (Mahato et al., 2015).

When considerations are placed on obtaining high ionic conductivity for these electrolyte materials, the focus is placed on the materials crystal structure, such that in order for the high ionic conductivity property to be evident, the material crystal structure is required to have large interionic open spaces which thus allow for a high level of point defect disorder and low migration enthalpy. It is also noted that upon looking at the crystal lattice of these electrolyte materials (i.e., metal oxides), there is a size variation in the size of the oxide ions and the metal cations, namely, the oxide ions are larger when place in comparison with the metal cations (Xia et al., 2017). Due to the size variation observed, it is expected for the metal cations with small size to possess mobility in the lattice, however, it can also be noted that the metal cations although being smaller in size, also have large valance charges and this thus restricts the free mobility of the metal cations in the lattice. This, thus results in the formation of oxygen vacancy defects within the lattice which results in the diffusion of oxide ions inside the lattice with the application of a sufficient driving force which facilitates this diffusion (Mahato et al., 2015).

The crucial requirements for a material to be used as an electrolyte material, are as follows; a) the chemical inertness with relation to the electrode materials during the processing and service processes, b) the chemical and thermodynamic stability of the material over a vast range of temperatures at a variation of oxygen activities, c) sufficiently high oxide ion conductivity, d) volatilization which is negligible, e) reliable mechanical properties, f) electronic transference numbers which are low, g) possessing compatibility of the CTE with adjoining SOFC cell components (Basu et al., 2019).

A large variety of materials have been considered for electrolyte materials, these materials as well as a brief description of each of these materials are as follows:

<u>Fluorite structure oxide materials:</u>

The fluorite structure oxides are one of the materials considered as electrolyte materials, these oxides have face centred cubic arrangement of the cations with the anions taking occupancy of all the tetrahedral sites. A few examples of the materials of MO_2 oxides crystallizing with the fluorite structure are namely, UO_2, HfO_2, CeO_2, ThO_2, and ZrO_2, with only CeO_2, ZrO_2, and other oxides which exhibit the defect fluorite structure such as Bi_2O_3 (two unoccupied tetrahedral sites) are of great interest in the field of application as electrolyte materials in SOFC (Mahato et al., 2015).

The CeO_2 cubic fluorite structured material exhibits great stability from temperatures such as room temperature, up to temperatures as high as the materials melting point of ~2400 ℃ at 1 atm ambient pressure. When considering the structure of CeO_2, it is noted that this structure contains 4 large unoccupied octahedral sites which result in a path for the rapid oxide ion diffusion to be created and the ionic conduction in these oxides only occur via the mechanism of vacancy diffusion, it is also noted that within the structure, the Ce^{4+} and O^{2-} ions are located at the 4a (i.e. 0,0,0) and 8c (i.e. 1/4 , 1/4,1/4) Wyckoff positions, respectively. When observations are done on pure CeO_2, we observe that it does not have a sufficient amount of oxygen vacancies in order to have appreciable ionic conductivity, and thus in order to obtain a higher ionic conductivity, the introduction of oxygen vacancies occur via the substitution of the Ce^{4+} by acceptor cations, such as, Y^{3+}, Gd^{3+}, or Sm^{3+} (Etsell & Flengas, 1970).

Although the doped CeO_2 exhibits a sufficient amount of phase stability while operational at intermediate temperatures (~500-700 ℃), it is observed that the Ce^{4+} have the tendency to undergo reduction to formation of Ce^{3+} in the fuel environment. This however results in a number of disadvantages being observed, namely, high electronic conductivity, inferior mechanical properties, and chemical expansion (Mahato et al., 2015).

When considering pure ZrO_2, it is important to note that there are three polymorphs, namely, monoclinic (room temperature stable) which undergoes a transformation to the tetragonal form (above 1170℃), with the final transition to the cubic fluorite structure (at a temperature of 2370℃), and remains stable until it reaches the melting point temperature of 2680℃ (Taylor et al., 2005). However, a disadvantage arises when observing the cooling of these materials, this

disadvantage is that upon cooling of these structures, cracks are formed and this results in low thermal shock resistance, and is as a result of the martensitic nature of all the transformations which result in the reverse being true for the cooling process and thus during cooling a large volume change is also observed (Mahato et al., 2015).

In an attempt to combat this disadvantage, the high tetragonal or cubic phase of ZrO_2 has been noted to have the ability of being stabilized at room temperature by the substitution of Zr^{4+} with relatively low amounts of acceptor dopant cations, with the key focus being placed on Y (Y_2O_3) (Mahato et al., 2015). When the Y_2O_3 stabilised ZrO_2 (YSZ) is observed, it is noted that YSZ is a very crucial potential electrolyte material, mainly due to the high oxide ion conductivity that they exhibit, first recognised by Nernst in the 1890's. When considering the mechanism of action of ionic conductivity of YSZ, it is observed that it is similar to the mechanism of action for acceptor doped CeO_2. It is thus noted that the oxygen vacancies, which are generated by the addition of acceptor dopant cations, not only result in the stability of the cubic phase of the crystal lattice of ZrO_2, but it also results in the increase of the oxide ion conductivity (Minh, 1993).

When considering the other doped systems of ZrO_2, it is noted that another doped system has been of key research interest for its applications in the electrolyte of the SOFC's, and this is the Sc_2O_3 doped ZrO_2 (ScSZ) (Badwal & Ciacchi, 2000). Another system of interest is the high temperature fluorite structure of bismuth oxide (δ-Bi_2O_3) polymorph which displays intrinsic oxygen vacancies concentrations (25% of the oxygen sublattice sites) (Naixiong Jiang & Wachsman, 1999), and this thus results in the high ionic conductivity which is observed for δ-Bi_2O_3, with δ-Bi_2O_3 being the oxide ion conductor which has the highest ionic conductivity to date (Mahato et al., 2015).

Pyrochlore electrolyte materials:

When considering the pyrochlore structured materials, it is noted that these materials have a general formula of ${A_2}^{3+}{B_2}^{4+}O_7$, and this structure has been of key importance since 1960 due to its ionic conductivity (Mori et al., 2003). The pyrochlore structure is considered to be a

superstructure of the fluorite structure of general form AX_2, where the A-site and B-site cations have order and where an eighth of the anion sites are vacant (Lian et al., 2003). When considering the A-sites, it is noted that the large A^{3+} cations are situated at the 16d sites of the lattice and has a coordination number of 8, while the for the B-sites, it is noted that the B^{4+} cations are situated at the 16c sites, with the B-site cations having a coordination number of 6 and being located at the centre of a distorted octahedron. The oxide ions that are situated at the 48f sites are coordinated to two A^{3+} and two B^{4+} cations, as compared to the oxide ions situated at the 8b sites which have a tetrahedral coordination with only the A^{3+} cation, and the vacant 8a interstitial site is thus coordinated to four B^{4+} cations. Upon the reduction of the size of the A-site cations, it is reported that a transition from pyrochlore to fluorite structure is observed (Vladislav V. Kharton et al., 2010).

The reduction in the cation size results in a structure transformation from the ordered pyrochlore lattice of form $A_2B_2O_7$ to a fluorite structure that is completely disordered and exhibits anion deficiency defects and is of the structural form M_4O_7 (with M=A or B). An example of a pyrochlore structure material is $Gd_2Zr_2O_7$ which sits at the boundary which exists between the ordered pyrochlore structure and defective fluorite structure; however, it is important to note that this is only observed when the ionic radius ratio (r_A/r_B)=1.46 (Lian et al., 2003).

Placing the consideration on the oxide ion conductivity of $Gd_2Zr_2O_7$ (and other examples of pyrochlore based oxides), it is noted that the oxide ion conductivity observed for these materials are comparative to that of the YSZ (Mahato et al., 2015). It can also be noted that the ionic conductivity of these materials can be enhanced when either thermal treatment (Wuensch & Eberman, 2000) or chemical substitution (S. A. Kramer & Tuller, 1995) occurs. When the substitution of Zr^{4+} with Ti^{4+} from $Gd_2Zr_2O_7$ to $Gd_2(Zr_{0.3}Ti_{0.7})O_7$ and $Gd_2(Ti_{1-x}Zr_x)O_7$, it is observed that there is an enhancement that is observed in the conductivity (Subramanian et al., 1983). When further consideration is placed on the chemical substitution it is noted that when Gd^{3+} is substituted with Ca^{2+} in the $Gd_2Ti_2O_{7-\delta}$ materials, there is an increase observed in the p-type conductivity which results in an overall decrease in the n-type electronic conductivity of the material (S. Kramer et al., 1994).

Perovskite-structure based electrolyte materials:

Perovskite-based electrolyte materials:

Perovskite structure-type oxide materials of chemical formula ABO_3, has been of key focus with relation to ionic conductors (Ishihara et al., 1994) due to the high ionic conductivity which it exhibits (Mahato et al., 2015). An example of the perovskite structure oxide materials considered for electrolyte application in SOFC's is $LaGaO_3$ (Mahato et al., 2015). When considerations are placed on the mechanisms by which the oxide ion diffusion in the perovskite material occurs has resulted in investigations being done, and from these investigations, it was noted that the mechanism of oxide ion migration is based on a saddle point configuration, in which the migrating ion is expected to undergo migration through the centre of the triangle which forms due to two La^{3+} A-site cations and one Ga^{3+} B-site cation. This mechanism thus indicates that due to the high energy barrier of the perovskite lattice, the ionic diffusion in the perovskite material lattice thus has to take place with the migration of the oxide ions jumping into the adjacent vacant sites which are situated along the (110) edges of the octahedra formed by the BO_6 (Cherry et al., 1995). The ionic conductivity and catalytic activity of the $LaBO_3$ oxide materials have also been noted to increase with the addition of various acceptor donors, namely, Ba^{2+}, Sr^{2+}, Mg^{2+}, or Ca^{2+}, which undergo substitution at the La^{3+} A-sites (Ishihara et al., 1995).

Perovskite-based electrolyte materials of the form $LnBO_3$ (where B=Al, In, Sc, Y):

The perovskite materials of the form $LnBO_3$, namely, $LaAlO_3$ are termed the perovskite aluminates and have been of key interest in investigations since the 1970's. When placed in comparison with the other perovskite structure forms, such as, $LaGdO_{3-\delta}$ and $CeO_{2-\delta}$, the $LnBO_3$ perovskite structure oxide materials show a greater stability towards volatilization and reduction (Mahato et al., 2015).

These materials also exhibit a mechanical computability of good standard during the fabrication process, and this is as a result of the moderate CTE values which they have. A few disadvantages however arises, these materials show relatively low magnitudes of ionic conductivity with high levels of p-type electronic conductivity when considering oxidising atmospheres, these materials are also limited when it comes to their relatively high grain boundary resistance and poor sinterability (Mahato et al., 2015).

These perovskite aluminate materials have exhibited the ability to act as protective layers at the anode side of $LaGaO_3$ based materials, and they have also been considered as isomorphic additives of composite solid electrolyte materials (Yasuda et al., 2000).

$La_2Mo_2O_9$ (LAMOX) electrolyte materials:

The LAMOX family or better referred to as materials based one the $La_2Mo_2O_9$ compound have been of great interest due to their fast oxide ion conductivity (Lacorre, 2000). When considerations are placed on the LAMOX compounds, it is noted that when comparing the oxide ion conductivity of the LAMOX compounds, it is observed that the oxide ion conductivity of these materials are comparative to that of the stabilised ZrO_2 at a temperature of 800℃ (Mahato et al., 2015).

When considerations are placed on these materials and the phase transitions of these materials, it is noted that they undergo a phase transition from the α-form (monoclinic) at room temperature, to the β-form (cubic) at a temperature of approximately 580℃, and this transition results in an increase in the conductivity observed (Mahato et al., 2015).

The doping of the LAMOX family materials has been considered and has been a great field of research interest due to the predisposition with relation to not only the phase transition but also molybdenum reduction in a fuel environment, this research has been mainly focused on the doping of both the molybdenum and lanthanum sites. When the focus is placed on the doping at lanthanum sites, it is observed that the main dopant elements are Gd, Nd, and Y, which result

in the reduction of the susceptibility for the cubic to monoclinic phase transition when cooling occurs (Georges et al., 2003).

Apatite structure-based electrolyte materials:

The apatite structure-based electrolyte materials are defined as the materials with a general formula of $A_{10}(MO_4)_6X_{2\pm\delta}$, mainly where A is defined as an alkaline earth or rare earth cation element or Pb, where M is defined as an element from the p-block of the periodic table (i.e. P, V, Si, Ge), and where X is defined as halides, O^{2-}, OH^- (Kendrick et al., 2007).

When noting the most common chemical formula of the apatite-based oxide ion conductor family, it is noted that the typical formula is $Ln_{9.33+x}(Si/GeO_4)_6O_{2+3x/2}$, with the structure of these materials having an isolated MO_4 tetrahedra which are arranged in such a way that distinct anion and La channels are formed which are located parallel to the c-axis, and thus due to the oxide ion channels being centrally located they participate in ionic conductivity (Kendrick et al., 2007). The high ionic conductivity which are observed in this materials are exhibited as a result of these rare earth cations in the materials being situated in the 7- and 9-coordinated cavity sites, as well as there being additional oxide ions which are present in channels which run through the structure (Mahato et al., 2015).

When comparison is placed on the apatite family materials, it is seen that when observing that lanthanum silicate apatite materials offer greater ionic conductivity as compared to the lanthanum germinate apatite materials, with the ionic conductivity of the $La_{9.33}(SiO_4)_6O_2$ compound being higher as compared to the ionic conductivity of the $La_8Sr_2(SiO_4)_6O_2$ compound (V. V. Kharton et al., 2004). The differences observed in the ionic conductivity obtained for these two compounds is mainly due to the $La_{9.33}(SiO_4)_6O_2$ having La vacancies which result in the differences in the ionic conductivity between the compounds, although the content of the oxide ions is the same in both compounds (Sansom et al., 2001).

Investigations were also done to observe the effect that dopants would have on the conductivity obtained when dopants are used for the La-sites and the Si-sites. A large variety of dopants are used namely for the La-sites (Sr, Ba, Mn, Cu, Ca, Bi, Mg, Co, Ni) and for the Si-sites (P, Al, Mn, Mg, B, Co, Cu, Ti, Ge, Ni, Zn, Ga, Fe), some dopants have the ability to occupy both the La-sites and the Si-sites and are referred to as 'ambi-site' dopants (Mahato et al., 2015). When the dopant cation used for substitution at the La-site is small in size, the conductivity observed decreases (Kendrick et al., 2007). The isovalent dopant elements are however reported to result in higher conductivity being observed (Sansom & Slater, 2004).

The low ionic conductivity observed at low temperatures for the germanate based apatite compounds are as a result of the high activation energy which these compounds exhibit at low temperatures (Kendrick et al., 2007).

The brownmillerite-like electrolyte material phases:

The brownmillerite structure type oxide materials are defined by these materials having a general chemical formula of $A_2B_2O_5$, and these materials have alternating perovskite layers which exhibit corner sharing between the BO_4 tetrahedra and the BO_6 octahedra (Ferguson et al., 2011).

Materials of this structure type have been defined as perovskite materials which are oxygen deficient, and it is noted the oxygen vacancies are observed to order along the planes with (0 1 0) hkl, and this thus results in a contribution towards the ionic transport in the structure. This results in the formation of 1-D pathways, and thus allowing for migration of the oxide ions along the tetrahedral layers (Mancini et al., 2012).

Due to the large number of oxygen vacancies which are present in the structure, it is observed that these oxygen vacancies are in an ordered fashion. It is also noted that upon an increase in the temperature of the material, various phase transitions occur, namely, when increasing the

temperature from room temperature to a temperature within the range of 925℃-930℃, a phase transition is observed from the orthorhombic phase at room temperature, to the tetragonal phase in the abovementioned temperature range, when the temperature is further increased to approximately 1040℃ a phase transition from the tetragonal phase to a highly disordered cubic phase is observed (Berastegui et al., 2002).

The disordered cubic phase exhibits the ability to enable fast oxide ion conduction to occur, as a result of the amount of oxygen vacancies which are evident in the structure, however, a disadvantage becomes evident as the materials are humidity sensitive (Schober et al., 1997).

A compound with this structure type is $Ba_2In_2O_5$, this material is known to have properties of mixed conductivity, and it is also noted that the total conductivity in dry air obtained for this material is dominated by the oxide ion conductivity. As the temperature increases, it is observed that there is a phase transition which occurs at a temperature of approximately 930℃ to result in the formation of a disordered perovskite phased material with an increased ionic conductivity (J. B. Goodenough et al., 1990).

In an attempt to stabilise the disordered cubic perovskite phase, substitution at the In-sites in the crystal lattice with cation dopants of higher-valance is used, this also results in the enhancement of the ionic conductivity obtained at intermediate temperatures. The dopant cations of interest are namely, Hf^{4+}, Zr^{4+}, Sn^{4+}, and Ce^{4+} (Schober & Friedrich, 1998), other dopant cations such as Ga^{3+}, Y^{3+}, and Yb^{3+} are also of key interest (Yao et al., 2000)(Yamamura et al., 2002).

<u>The $\delta - Bi_2O_3$ and $Bi_4V_2O_{11}$ structure based ceramic electrolyte materials:</u>

The fluorite structure type-based oxide electrolyte material $\delta - Bi_2O_3$is defined as one of the best oxide ion conductors to date (Vladislav V. Kharton et al., 2001)(Mahato et al., 2015).

These materials not only offer an advantage of their high ionic conductivity, but exhibit a wide variety of additional advantages, such as, the increased electrocatalytic activity observed for the interconversion of O_2 and O^{2-} which occur at the low temperature range of approximately 300℃-350℃ (Mahato et al., 2015).

Bi_2O_3 is found in six naturally occurring polymorphs, namely, the stable phases; the monoclinic α-phase, and the cubic δ-phase, and the metastable phases; the tetragonal β-phase, the body centred cubic (bcc) γ-phase, the orthorhombic ε-phase, and the triclinic ω-phase (Michel Drache et al., 2007), and a rhombohedral phase which is not naturally occurring (Jolley et al., 2019).

It is noted that the cubic δ-phase has the highest conductivity recorded, as well as exhibits stability in the temperature range of 730℃-804℃, where 804℃ is defined as the melting point of this phase, it is also further observed that this phase exhibits oxide ion conductivity values which range about 1-2 magnitudes greater than that obtained for the stabilised ZrO_2 (Shuk et al., 1996). The stabilisation of this phase up to room temperature is possible when consideration is placed on the doping of this phase with dopant cations such as La^{3+}, Y^{3+}, Er^{3+}, and many more (Boyapati, Wachsman, & Chakoumakos, 2001).

When the cooling process of these materials are observed, it can be seen that when these materials are cooled below a temperature of 600℃, a transition takes place, this transition is describes as a first order vacancy order-disorder transition, and the overall result of this transition is the reduction of the obtained ionic conductivity by approximately 3 orders of magnitude (Boyapati, Wachsman, & Jiang, 2001).

When considerations are placed on the basic structure of the cubic δ-phase of Bi_2O_3, it is observed that the structure consist of two partially occupied O sites, namely the 8c site with hkl (1/4, 1/4, 1/4) and the 32f site with hkl (x, x, x) where x is approximately 0.3 (Battle et al., 1983). It is also noted that as aging of the materials occur, the 32f site occupancy increases and

thus results in an increase in the local vacancy ordering observed in these materials (N. Jiang et al., 1995). The room temperature stabilisation of this phase is achieved by the use of small cation sized elements which thus result in the contraction of the overall crystal structure of the material (Verkerk & Burggraaf, 1981).

The size mismatch of the cations play a crucial role in the stabilisation of this phase when the addition of dopant cations are considered, namely, when a large ionic radii mismatch is observed between the dopant cation and the Bi^{3+} cations is observed, lower dopant concentrations are required, and when there is a small ionic radii mismatch, a larger dopant concentration is required (Mahato et al., 2015). At low temperatures, the doping of the parent compound results in lower overall ionic conductivity being observed, however, at fixed dopant concentrations, it is noted that the oxide ion conduction increases as an increase is observed in the size of the dopant Ln^{3+} cation, which occurs as a result of the overall size of the Bi^{3+} cation (Vladislav V. Kharton et al., 2010).

Many disadvantages however arise when considering Bi_2O_3, namely, when trying to stabilise the Bi_2O_3 it should be noted that these materials are highly susceptible to the reduction of the Bi metal when placed under reducing conditions (Yaremchenko et al., 2000), corrosion, reduced mechanical strength, as well as the volatilization of Bi_2O_3 which occurs at moderate temperatures. These disadvantages result in the reduced applicability of these materials for practical applications, however, in an attempt to combat these challenges, the cathode side of the SOFC adopted a bilayer structure with Bi_2O_3, and a more stable electrolyte layer on the anode side (Park et al., 2005).

Another class or family of bismuth oxide-based electrolyte materials which has gained interest is the $\gamma - Bi_4V_2O_{11}$ materials, which stem from the BIMEVOX materials, and belong to the Aurivillius series. These BIMEVOX family materials (Bi-Bismuth, Me-additional metal additive, V-Vanadium, Ox-Oxygen) are defined as the new generation of the Bi_2O_3 based electrolyte materials (Mahato et al., 2015). These compounds exhibit relatively high ionic conductivity, it is also observed that at low temperatures, the stabilisation of the tetragonal $\gamma -$

$Bi_2VO_{5.5}$ structure can undergo partial substitution at the V-sites with metal cations such as, Mg, Cu, Zn, Co, Fe, and Ni (Pirovano et al., 2003).

Chapter 3:

Synthesis process & Sample Preparation

Introduction to sol-gel synthesis:

In order to synthesis the Bi_2O_3-Nd_2O_3-Y_2O_3 as well as the Bi_2O_3-Nd_2O_3-Y_2O_3-X_2O_3 (where X=Tb, Sm, Sc) systems, the starting compounds used in the sol-gel synthesis process were as follows: $Bi(NO_3)_3 \cdot 5H_2O$, $Nd(NO_3)_3 \cdot 6H_2O$, $Y(NO_3)_3 \cdot 6H_2O$, $Tb(NO_3)_3 \cdot 6H_2O$, $Sm(NO_3)_3 \cdot 6H_2O$, and $Sc(NO_3)_3 \cdot 6H_2O$, which were all high purity powders (≥99.99% Aldrich).

The sol-gel synthesis method is one of the two methods which will be considered for the synthesis of rhombohedral Bi_2O_3. In the sol-gel synthesis method, where X mol of $Bi(NO_3)_3 \cdot 5H_2O$, Y mol of $Ln(NO_3)_3 \cdot 6H_2O$, and Z mol of a different $Ln(NO_3)_3 \cdot 6H_2O$ (where Ln = Nd, Y, Sm, Sc and Tb), are dissolved in approximately 250ml of acetic acid (99.99%, Sigma-Aldrich) in a 600ml beaker under constant stirring (with the use of magnetic stirring) and heating conditions on a hot plate, and once dissolved approximately 5(X+Y+Z) mol % of citric acid for the doubled doped systems, and 5(X+Y+Z+B) mol % of citric acid for the triple doped systems (99.5%, Sigma-Aldrich), was added to the solution and allowed to stir under constant heating at 55℃ until a white/cream gel is formed (approximately 2.5-3 hours).

This gel was then calcined in a furnace at 500℃ for 12 hours in the beaker. Once the calcination is completed, the light orange/slightly yellow calcined powder was then transferred into a agate mortar where it was ground for 10 mins to obtain a homogenous powder mixture, after which it was transferred into a crucible and then further annealed in a furnace at 750℃ for 7 hours, after which the resulting light/pale yellow powder sample is then transferred into the mortar once more, ground until a homogenous powder mixture is obtained, and then it was transferred into a sample vial and stored for characterisation.

Initially, a total mol dopant concentration of 20 mol % was selected for the co-doped system, with the mol % of X mol of $Bi(NO_3)_3 \cdot 5H_2O$, kept at 80 mol %. Variations occurred between

the mol % of the dopants, namely, $Nd(NO_3)_3 \cdot 6H_2O$, $Y(NO_3)_3 \cdot 6H_2O$. The dopant mol % was then also varied comparatively to those presented by Jolley et al. in Optimizing rhombohedral Bi_2O_3 conductivity for low temperature SOFC electrolytes, thus optimizing the total mol dopant % to around 8.5-10% (Jolley et al., 2019). The mol dopant concentration % was also increased from 20 mol% to 22.5 mol % for stability studies, and triple dopant systems were also synthesised using the following dopants $Tb(NO_3)_3 \cdot 6H_2O$, $Sm(NO_3)_3 \cdot 6H_2O$, and $Sc(NO_3)_3 \cdot 6H_2O$. Table 1 below indicates the samples synthesis, their shorthand compositions, sample compositions (mol % atoms), as well as the actual mass and mol % of the various starting materials in grams and % respectively.

Post sample synthesis, each sample was characterised initially using x-ray diffraction (XRD) at room temperature, to identify the phases present in the samples. The samples were then characterised using simultaneous thermal analysis (STA) which uses differential thermal analysis (DTA) coupled with thermogravimetric analysis (TGA) as an attempt to understand the thermal characteristics of the samples. Variable-temperature (VT) Raman spectroscopy was employed due to its sensitivity to the local structure, and hence identify any other phases present in samples that are not identified by XRD. VT-electrochemical impedance spectroscopy (VT-EIS) was then also employed for the determination of the temperature at which the most optimal ionic conductivity in the samples is observed.

Sample Preparations:

3.1: Powder X-ray Diffraction (PXRD):

Post-synthesis sample preparation was done for characterisation using powder X-ray diffraction (PXRD). Using a spatula, ~0.1 g (a spatula tip) of sample was transferred to a zero-background sample holder and used for the laboratory experimental analysis. The zero-background sample holder uses a monocrystalline silicon wafer which is sliced on a plane that will not diffract through normal angular and energy ranges of laboratory XRD equipment. The sample was then pressed down using a glass slide, ensuring that the sample was packed tightly enough, but also ensuring that preferred orientation was avoided.

For the synchrotron samples sent to the Brookhaven National Laboratory (BLN) National Synchrotron Light Source II (NSLS-II), the samples were transferred into Kapton capillary containers, which were sealed on each side using an epoxy resin, ensuring that the samples

were packed without any disturbances in packing, and ensuring that the samples will not have their packing disturbed during transit.

3.2: Simultaneous Thermal Analysis (STA)

Approximately, 15 mg of sample was transferred into a small alumina crucible for simultaneous thermal analysis which comprises of differential thermal analysis (DTA) and thermogravimetric analysis (TGA)

3.3: Raman Spectroscopy (RS)

Approximately, 50 mg of sample was transferred to a glass slide for analysis. The sample was pressed down using a spatula tip to ensure that the sample was packed efficiently.

3.4: Electrochemical Impedance Spectroscopy (EIS)

In order for electrochemical impedance spectroscopy (EIS) measurements to be conducted, the samples needed to be pelletised. In order to form the pellets. ~2 g of each sample was ground in a mixture with two drops of 1% m/v aqueous polyvinyl alcohol (PVA) binding agent solution. (The solution was made using 1g of PVA powder dissolved in 100mL of distilled water, which was near boiling, and was under continuous stirring). This mixture was then left to air dry, once the drying was completed, the ground mixture was loaded into a 12 mm diameter die, then using a hydraulic press applying a load of 2.5 tonnes for 15 minutes. After the 15 minute period had passed, the pressure was slowly reduced, and then the pellets were gently released from the die.

The pellets were then sintered as follows, in order to result in an increased density and decreased porosity of the material. The pellets were loaded into alumina boats after being pressed, and then placed into the tube furnace. Based on knowledge gained from pripr work done within the research group, it was noted that PVA binding agent decomposition temperature was optimal at 450 ℃ at a heating rate of 10 ℃/min for an 8 hour duration. After this, the temperature was then ramped up further to 800 ℃ at the same heating rate for 12 hours. The pellets were then left to cool naturally to room temperature.

Once sintered and cooled to room temperature, the pellets were Sellotaped on the cylindrical sides, to ensure that short circuiting is prevented during the measurement process. The pellets were then coated with 10nm of pure gold on each of the flat sides using a turbo evaporate sputter coater. After coating, the Sellotape was removed, and once again the pellets were placed into the tube furnace and heated to 800 ℃ at a heating rate of 10 ℃/min and left for 8 hours to ensure that the gold coat and the pellet had efficient adhesion, once done, the pellets were then allowed to cool naturally to room temperature. Once this was done, the pellet dimensions were obtained using a vernier calliper.

Table 3.1: Samples synthesised with actual masses and mol % indicated.

Sample #	Shorthand sample composition	Sample	Actual mass						
			$Bi(NO_3)_3 \cdot 5H_2O$ (g) [mol %]	$Nd(NO_3)_3$ $6H_2O$ (g) [mol %]	$Y(NO_3)_3$ $6H_2O$ (g) [mol %]	$Tb(NO_3)_3$ $6H_2O$ (g) [mol %]	$Sm(NO_3)_3$ $6H_2O$ [mol %]	$Sc(NO_3)_3$ $6H_2O$ (g) [mol %]	Citric Acid (g)
1	Nd0.10Y0.10-Bi_2O_3	10Nd10YSB	4.0682 [80]	0.4578 [10]	0.4028 [10]	-	-	-	22.5000
2	Nd0.15Y0.05-Bi_2O_3	15Nd5YSB	4.0032 [80]	0.6779 [15]	0.1979 [5]	-	-	-	25.0071
3	Nd0.10-Bi_2O_3	10NdSB	4.0033 [90]	0.4016 [10]	-	-	-	-	25.0003
4	Y0.10-Bi_2O_3	10YSB	4.0056 [90]	-	0.3513 [10]	-	-	-	25.0039
5	Nd0.05Y0.15-Bi_2O_3	5Nd15YSB	4.006 [80]	0.2261 [5]	0.5928 [15]	-	-	-	25.0042
6	Nd0.05Y0.05-Bi_2O_3	5Nd5YSB	4.0002 [90]	0.2011 [5]	0.1761 [5]	-	-	-	25.0019
7	Nd0.085-Bi_2O_3	8.5NdSB	11.7074 [91.5]	0.9832 [8.5]	-	-	-	-	63.4485
8	Nd0.10Y0.10-Bi_2O_3	10Nd10YSB	10.8555 [80]	1.2265 [10]	1.0718 [10]	-	-	-	65.7617

9	Nd0.15Y0.05-Bi_2O_3	15Nd5YSB	10.7170 [80]	1.8161 [15]	0.5296 [5]	-	-	-	65.3067
10	Nd0.125Y0.10-Bi_2O_3	12.5Nd10YSB	10.5996 [77.5]	1.5486 [12.5]	1.0835 [10]	-	-	-	66.1081
11	Nd0.10Y0.125-Bi_2O_3	10Nd12.5YSB	10.6748 [77.5]	1.2508 [10]	1.3599 [12.5]	-	-	-	66.3368
12	Nd0.175Y0.05-Bi_2O_3	17.5Nd5YSB	10.4599 [77.5]	2.1348 [17.5]	0.5336 [5]	-	-	-	65.6368
13	Nd0.15Y0.075-Bi_2O_3	15Nd7.5YSB	10.5276 [77.5]	1.8423 [15]	0.8055 [7.5]	-	-	-	65.8659
14	Nd0.10Y0.075-Bi_2O_3	10Nd7.5YSB	11.0403 [82.5]	1.2102 [10]	0.7934 [7.5]	-	-	-	65.2064
15	Nd0.15Y0.05-Bi_2O_3	15Nd5YSB	10.7173 [80]	1.8167 [15]	0.5291 [5]	-	-	-	65.3098
16	Nd0.15Y0.05Tb0.025-Bi_2O_3	15Nd5Y2.5TbSB	10.4421 [77.5]	1.8266 [15]	0.5330 [5]	0.3021 [2.5]	-	-	65.5216
17	Nd0.15Y0.05Sm0.025-Bi_2O_3	15Nd5Y2.5SmSB	10.4532 [77.5]	1.8290 [15]	0.5333 [5]	-	0.3024 [2.5]	-	65.6138
18	Nd0.15Y0.05Sc0.025-Bi_2O_3	15Nd5Y2.5ScSB	10.5817 [77.5]	1.8514 [15]	0.5401 [5]	-	-	0.3068 [2.5]	66.3921
19	Nd0.15Y0.05-Bi_2O_3	15Nd5YSB	10.7170 [80]	1.8159 [15]	0.5292 [5]	-	-	-	65.4303

Chapter 4

Characterisation

Powder X-ray diffraction:

One of the most powerful non-destructive techniques for the characterisation of crystalline materials, is X-ray diffraction (XRD). XRD is used for studying the atomic spacing as well as crystal structures of materials. The XRD characterisation technique functions on the basis of constructive interference with regards to the monochromatic X-rays as well as the crystalline sample. X-ray generation occurs by the use of a cathode ray tube, they are then filtered to produce a monochromatic for of radiation, then collimated such that the X-rays are concentrated and directed towards the sample (Bunaciu et al., 2015).

When the incident X-rays interact with the sample, constructive interference (as well as a diffracted ray) are produced, namely when the conditions satisfy that of Bragg's Law, i.e., $n\lambda = 2dsin\vartheta$, where the variables are as follows, n is an integer, λ is defined as the wavelength of the X-ray radiation, d refers to the interplanar spacing which generates the diffraction, and where ϑ represents the diffraction angle (Wartak & Fong, 2019).

A key characteristic of powdered samples when considering x-ray diffraction, samples need to have random orientation. The random orientation of samples enables all the ranges of 2ϑ, as well as all the diffraction directions of the crystal lattice to be obtained. The diffraction peaks obtained for the sample are then converted to d-spacings to allow for the identification of compounds based on their unique d-spacing values (Bunaciu et al., 2015).

When considering PXRD, it is important to understand the fundamentals of basic crystallography, as this is the foundation of all structural analysis, especially when looking at materials using the x-ray diffraction technique.

Materials have their atoms arranged into either microstructures or crystal structures(Fultz & Howe, 2008). The arrangement of these atoms in a periodic manner are strongly dependent on a variety of external factors, including but not limited to, temperature, pressure, as well as the

heating and cooling rates which occur during the process of solidification (Scherer, 2017). These factors influence the various classes into which materials can be classified, namely as, amorphous, polycrystalline, as well as single crystals (single crystalline) materials (Razeghi, 2018).

The various material crystallinities can be described as follows (Ameh, 2019):

i. Amorphous solid materials are defined as materials which exhibit an isotropic nature. This is nature is as a result of the arrangement of the atoms in the material, the arrangement is not regular and has the same properties in all directions.
ii. Crystalline materials are materials which are defined as materials which are anisotropic as a result of the arrangement of their atoms in patterns which are regular and repeating in nature. It is important to note that their properties however vary as a result of direction.
iii. Polycrystalline materials are defined as materials which are characteristic of containing a combination of numerous crystals which differ in size and shape. The distribution of crystal shapes, sizes, as well as the orientations within the individual crystals are the characteristics on which the properties of polycrystalline materials are strongly dependent on.

The technique of x-ray diffraction is based on a number of crucial fundamentals, one of these fundamentals is the comparative wavelength of x-rays to atomic size. This comparative behaviour is the foundation on which x-ray diffraction is used as a technique for the characterisation and the probing of atomic arrangement in each unit cell, the position of atoms, as well as atomic spacing angles as a result of use of diffraction patterns and intensities (Pappas, 2006). Although x-ray diffraction is one of the most widely used techniques for industrial application, there is still a large gap in the understanding of the basic conceptualisation of crystal structures and x-ray crystallography(Ameh, 2019).

In order for one to fully understand and conceptualise crystal structures, and x-ray crystallography, theoretical understanding is required. In order to understand crystallography,

especially with our focus being on x-ray crystallography, it is crucial to first understand the theory being crystal structures.

Understanding crystal structures require the understanding of the fundamental building blocks of a crystal structure. Crystalline structures are defined as structures which have arrays of atoms which are arranged in a pattern that is regular and repeated. In this crystal structure, the smallest repeating element within this crystal is what we refer to as a unit cell. This unit cell is dependent on the lengths of three major axes (*a*,*b*,*c*), as well as the angles between these axes (R. Sharma et al., 2012). Figure below is a diagrammatic representation of a three-dimensional unit cell.

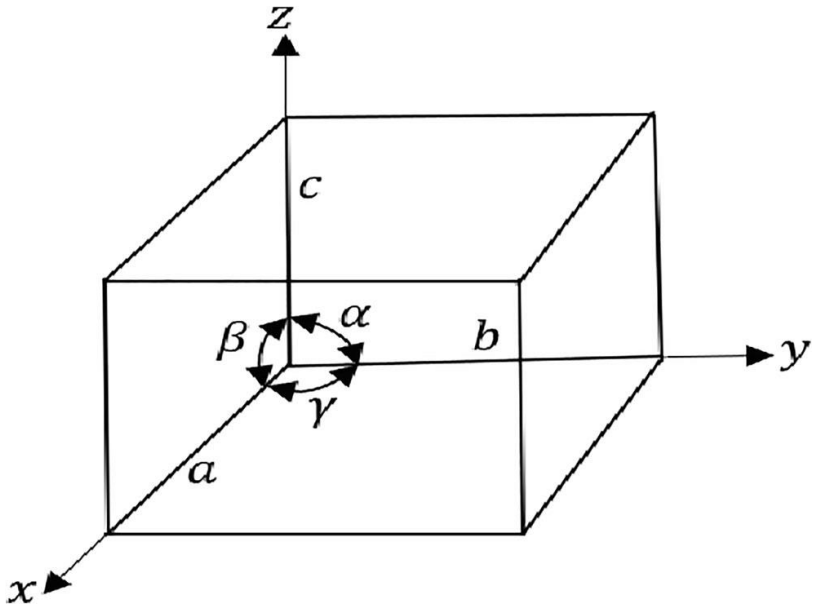


Figure 4.1.3: Diagrammatic representation of a three-dimensional unit cell (Ameh, 2019)

The arrangement of the arrays of atoms by pure translation (transformation), this excludes a change in rotation or orientation, but includes a change of the atoms position. There are three possibilities of the translation, namely, one-dimensional, two-dimensional, and three-dimensional (Putnam et al., 2007). Within a crystal there is also a periodic arrangement of points or a collection of points which is defined as a lattice. A lattice can either be represented in two-dimension or three-dimensions by a set of translational vectors (Ameh, 2019).

In 1848, a mathematical concept was introduced by Bravais, this concept called space lattice was used to describe the arrangement of crystal structures. This mathematical concept defines

that when considering an infinite number of points in space, such that the point arrangement around a point is identical around any other points. In the space lattice, the axes system used to designate point arrangements is the *x, y, z* system. 14 lattices define all the possible arrangements of points in lattice space, and these are classified as the 14 Bravais lattices. These lattices are classified into 7 crystal systems, and this classification is dependent on the length of the axes, angles between them, as well as symmetry properties (Ameh, 2019).

A certain shape or arrangement of an object is defined as the symmetry of that object. A symmetrical crystal structure is dependent on whether certain directions of geometry and physical property of crystals are reproduced by certain operations. Actual crystal structures can be formed through 230 different patterns of atomic elements (Pierret, 1987). All crystal structures have been classified into 7 crystal systems, when taking into account the symmetry operations, such as *n*-fold rotation, inversion centres, reflections, as well as rotation-inversion symmetry operations. The combination of the three symmetry operations furthermore result in 32 crystal symmetry class point groups (Ameh, 2019).

The Bravais lattice is defined as a lattice which is composed of a set of lattice points with relation to a position vector *R*, and a reciprocal lattice which is a set of vectors resulting in the Bravais lattice periodicity, vector *K*. Vector equations for these two lattice position vectors are defined as follows:

$R = n_1 a_1 + n_2 a_2 + n_3 a_3$

$K = hb_1 + kb_2 + lb_3$

When considering the equations above, it can be observed that there are a number of variables, namely, n_i (*i*= 1, 2, 3), which are integers; *h, k, l* which are the miller indices of the plane perpendicular to the reciprocal lattice vectors; a_x (*x*= 1, 2, 3) which represents the primitive lattice vectors for the position vector, and b_z (*z*= 1, 2, 3) which represents the primitive lattice vectors for the reciprocal vector (Hofmann, 2015).

The miller indices for planes, is referred to as a set of coordinates which are expressed as *h, k, l,* which are defined by a line originating from the origin, which cuts through the axes (*a, b, c)* or the axial vector (a_x (x= 1, 2, 3)) which are called miller indices for that specific set of lattice planes (Wood, 1964). The properties of miller indices allow them to be used to express lattice planes, as well as to specify orientation of the planes in space and not positionality. Letter *h, k, l,* are considered miller indices for planes, and are thus designated in curvilinear bracket, such as (*h, k, l)* (Ameh, 2019). When the atomic d-spacing along each plane are the same, the crystallographic planes are equivalent to each other by symmetry. The cubic crystal symmetry system has front and back faces which intercept the x-axis and is parallel to the y- and z-axes, and this yields miller indices (100), the top and bottom faces, intercepting the z-axis and parallel to the x- and y-axes (001). The left and right faces of this system intercept the y-axis and parallel to the x- and z-axes have the miller indices (010). A zero-miller index (000) thus implies that the plane (face) can be considered as parallel to the corresponding unit cell axis and at infinity (Dekker, 1957)(Hammond, 2002; Hargittai, 2009).

The miller indices for direction are based on the characteristic of single crystals or polycrystalline materials, in which the crystallographic direction is used to indicate the orientation. There are a number of properties that are in direct relation to these miller indices, namely, when considering the magnetic properties of magnetic materials such as iron, to name but one, these magnetic properties are strongly dependent on the crystallographic direction (Askeland & Wright, 2016; D. Askeland, P. Fulay, 2006). When considering crystallographic directions, it should be noted that three indices are used, namely, (*u, v, w),* which represent the *x, y, z* directions, and are usually represented through a square enclosed bracket as follows, [*u, v, w*]. For a cubic crystal symmetry system, it needs to be noted that because all parallel vectors have the same direction indices, thus the miller indices for the *x*-axis is [100], *y*-axis is [010], and for the *z*-axis is [001] (Dekker, 1957). It is also of importance to note that upon the condition that the atomic spacing along each direction are the same, then the direction is equivalent. This equivalence gives rise to what is defined as form or family indices (Ameh, 2019).

The x-ray diffraction principles are of crucial importance when considering materials analysis. The principles of x-ray diffraction focus on the use of x-rays, these x-rays are impinging upon

atoms in a solid sample, upon this impingement, the incident x-rays are scattered by the electrons in the atoms. Two types of interference can occur as a result of the incident x-rays, namely constructive or destructive wave interference which occur along a different direction as compared to the scattered (diffracted) waves, and these are emitted by atoms at different positions (Fultz & Howe, 2008). When a solid has a very orderly arrangement of its atomic structure, constructive interference is observed. There exists a very strong relationship between the periodic atomic structure of crystalline materials (the crystals in materials) and the diffraction patterns. The angles at which diffraction is evident depends on the atomic arrangement (periodicity), long repeated distances result in diffraction being observed at small angles, and short repeated distances result in diffraction being observed at high angles (Ameh, 2019).

The powder X-ray diffraction (PXRD) characterisation technique was used to determine the phase, phase purity and lattice parameters of the synthesised Bi_2O_3 materials formed. This information and data obtained was then used to understand the fundamentals of the crystallographic structures of the materials formed and the effects of the added dopants on the crystallographic parameters. Variable temperature PXRD was employed to study if phase transitions occur upon heating and to establish temperature dependent crystallographic parameters to determine thermal expansion coefficients. Characteristics of diffraction peaks also provide vital information, namely, peak position is used to determine the shape and size of the unit cell, while peak intensity determines atomic position within the unit cell, as well as indicates the atomic number (Zhang et al., 2002).

In order to fully comprehend the principles of the x-ray diffraction technique, the theories that govern this technique needs to be understood. Three key theories are Bragg's theory (Bragg's Law), Laue theory, and Ewald's theory (Ameh, 2019).

Bragg's law is based on the discovery that Bragg made after Laue discovered x-ray diffraction, this law is founded on the simple alternative explanation and measurement for the diffraction as a result of monochromatic x-rays from a single crystal (Authier, 2012). A number of

assumptions are made through the Bragg analysis process, firstly, the assumption is that crystals are in layers, or atomic planes (lattice plane-*hkl*) are in layers which have a spacing distance represented by *d*, and they produce a reflection when the impingement of the incident light/x-rays occur on the planes of atoms (Nelson, 2012; Sivia, 2011). The second assumption that is made is that the incident and diffracted beams have equal angles at the lattice plane. The consideration of constructive interference, as per Bragg requires specific conditions, namely, that the Bragg diffraction conditions are satisfied when the path difference lengths are equal to $n\lambda$, and follow Pythagorean theorem, the Bragg law equation was derived. Bragg's law states that for constructive interference to occur:

AB + BC = $n\lambda$

Thus, from x-ray diffraction patterns it is noted that, AB=BC, therefore:

$n\lambda$=2AB

In order to represent ΔABZ as per the figure shown, using the Pythagoras theorem derivation, the resulting equation is:

$$\sin\theta = \frac{AB}{d}$$

AB = $d \cdot \sin\theta$

$n\lambda = 2\ d \cdot \sin\theta$

Considering the variables, λ = wavelength of incident x-ray, n = reflection order, d = spacing distance, and θ = diffraction beam angle.

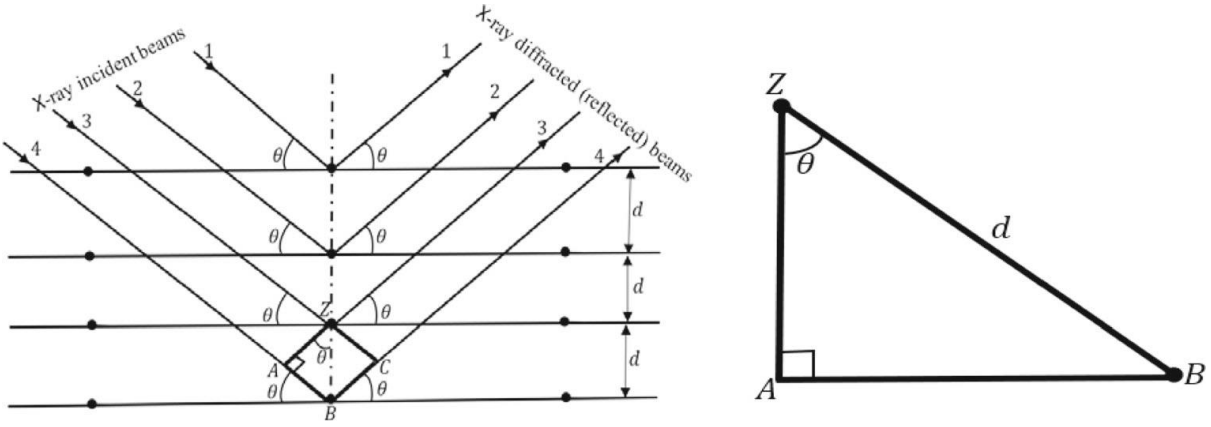


Figure 4.1.4: Schematic diagram indicating the x-ray diffraction pattern, and the use of Pythagoras theorem

When noting that *n* is defined as the order of diffraction (the reflections) from a set of lattice planes (*hkl*), we note that this has the interplanar spacing represented by d_{hkl}, this then leads to *d* being defined as:

$$d = \frac{d_{hkl}}{n}$$

So, when we consider this and rewrite the above equation of Bragg's law, we obtain the following equation:

$$\lambda = 2d_{hkl} \sin \theta_{hkl}$$

This allows us to obtain the two equations for Bragg's law(Ameh, 2019) (Nelson, 2012; Sivia, 2011).

Ewald theory set the foundation of the discovery of x-ray diffraction by Laue, however, was rarely employed in the study of crystal structure (Authier, 2012). The assumption made by Laue in the Laue analysis process, is that crystals are considered as a build-up of atomic rows which span along the *x*-axis, *y*-axis, and the *z*-axis in the three-dimensional space. In the figure below, presume that AB is defined as the incident beam wave crest, and CD is defined as the diffracted beam wave crest, which are related as they are the wave crests for the constructive interference for the waves from atoms along the *z*-axis (Dekker, 1957; Hammond, 2002; Hargittai, 2009). Putnam et al. (Putnam et al., 2007) stated in an article that if the diffracted path difference, and the integer (whole) number of incident beam wavelength corresponds, then the diffracted beam will undergo constructive (in-phase) interference. Conversely, when there is no correspondence between the incident beams and the wavelengths, then destructive (out-

of-phase) interference occurs. The figure below also indicates the vector notation that Laue's law employs for the incident and diffracted beam directions, as well as the path differences between the diffracted beams (Ameh, 2019). The first equation of Laue for the path difference can be described mathematically, for the path AB – CD, which corresponds to the integer number of wavelength for the constructive interference is as follows:

(AB – CD) = a ($\cos \alpha_n - \cos \alpha_0$) = $n_x \lambda$

Where the variables are defined as follows: a = atom spacing along *x*-axis (lattice parameter), α_n = diffracted beam to the *x*-axis angle, α_0 = incident angle to the *x*-axis, and n_x = order of diffraction integer (Hammond, 2002; Hargittai, 2009).

Now, when focusing on Ewald's theory, we note that Ewald postulated a theory which explains the relationship that exists between the distances of oscillators and the wavelength of light (Authier, 2012). There is no approximation to this postulated theory, and thus it is valid for any range and ratio of light wavelength to distancing oscillator. The Ewald sphere (also referred to as the Ewald construction) is based on a sphere of reflection and the reciprocal lattice, this is then used in the determination of whether the diffraction conditions for a reciprocal lattice point is met or not (Hammond, 2002). When placing a diffracting crystal in the centre of the Ewald sphere of $1/\lambda$ with the incident beam, where *I* passes through the diameter, which is represented as *IO*. Observing the incident beam, it is important to define *O* as the reciprocal lattice origin. Observing the figure illustrating the Ewald sphere below, it is noted that in order for Bragg's law for diffraction to occur and be obeyed based on the orientation of the crystal, the exit point of the incident beam *O*, and the exit point of the diffracted beam *B*, results in a vector *OB* (Hammond, 2002; Wood, 1964). Then, the vector length for the vector *OB* is equivalent to $1/d_{hkl}$ (Paul F. Fewster, 2018).

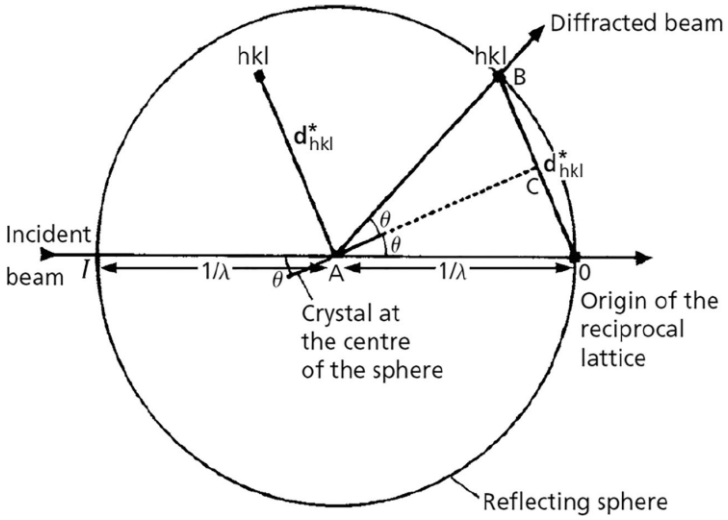


Figure 4.1.5: Diagrammatical representation of the Ewald sphere indicating a set of planes as well as diffraction positions (Hammond, 2002)

Bragg's law is fulfilled when there is correspondence between the reflecting planes (*hkl*) that intersect the Ewald sphere and the reciprocal lattice point which id defined by the reciprocal lattice vector d^*_{hkl} (P. F. Fewster, 1999). When considering the triangle *AOC*, the following is noted:

$$|OC| = \frac{1}{\lambda}\sin\theta = \frac{1}{2}|d^*_{hkl}| = \frac{1}{2d_{hkl}}$$

Thus, with the understanding of these three crucial theories, it is now possible to try and focus on the application of the x-ray diffraction technique. This analysis technique is widely employed in the study and structural determination of solid crystal structures, and thus is a very powerful technique. There are a vast range of applications for this analysis technique, which encompasses but is not limited to, phase identification, crystal size, crystal structure, lattice parameter determination, residual stress/strain, phase transformation, thermal expansion coefficient determination, as well as crystallographic orientation (Ameh, 2019) (Winter, 2000).

The phase quantification and phase identification of solid crystal samples is one of the applications of x-ray diffraction. Each crystalline solid has its own unique fingerprint, namely, the possess their own unique x-ray diffraction patterns, relative intensities, as well as set of interplanar spacing (R. Sharma et al., 2012). Bragg's law is used to calculate the interplanar spacings which correspond to the determined peak positions and peak intensities of the diffraction of a specimen (Ameh, 2019).

When considering phase identification of constituent phases present in an unknown sample, they can be identified using a computerised search and match function based on a powder diffraction standard database, that match interplanar spacing values that are recorded in the database, to the interplanar spacing values of the strongest peak intensity lines. When considering phase quantification of these unknown samples, determination can be done by employing the peak intensities of the strongest line, and using it as a function of the weight fractions of the phases which are present in a mixture (Gilmore et al., 2004).

The determination of crystalline size or grain size stems from the principle that as an increase in the width of diffraction, also referred to as peak broadening, is observed, this corresponds to a decrease in the crystallite size. This increase indicates the lack of sufficient planes in small crystallites to result in complete destructive interference (Barman & Sarma, 2012; Jacob et al., 2015). An equation for estimating particle size was formulated by Debye Scherrer, which is as follows (Dollase, 1985; A. West, 2014; A. R. West, 2014):

$$D = \frac{K\lambda}{B cos\theta}$$

Where the variables are defined as: D = particle size, θ = the diffraction angle, K = Scherrer constant (=0.9), λ= wavelength of the x-ray, B = full width at half maximum (FWHM) specifically measured in radians (Ameh, 2019). There are specific instrumental parameters that contribute to total peak broadening, namely, detector slit width as well as specimen properties, namely due to the reduction of crystallite strain and size. Specimen broadening FW(s) can thus be defined as (Jacob et al., 2015):

$$FW\ (s)cos\theta = \frac{K\lambda}{Size} + 4\varepsilon \sin\theta$$

The total peak broadening, B_t, as a result of instrument and specimens can be defined by (Jacob et al., 2015):

$$B_t{}^2 = \left[\frac{K\lambda}{D\cos\theta}\right] + [4\varepsilon \tan\theta]^2 + B_0{}^2$$

Where the variables are defined as: B_0 = broadening as a result of the instrument, and ε = strain. A method for the deconvolution of size and strain broadening into separate equations based on the assumption of peak width as a function of 2θ was proposed by Williamson and Hall (Williamson & Hall, 1953):

$$B_L = \frac{k\lambda}{D\cos\theta}$$

$$B_e = C\varepsilon\tan\theta$$

Where the variables are defined as: C = constant, B_L = size broadening, B_e = strain broadening.

The crystal structure determination is founded in the identification of the crystal structure being based on lattice parameters of the unit cell of the crystal structure, lattice points, packing factor of atoms in unit cell, number of atoms per unit cell, as well as the coordinate number of atoms in the unit cell (Askeland & Wright, 2016). An face centred cubic (FCC) crystal structure is defined by principle diffracting planes with miller indices (*hkl*) of either all odd or even numbers, whereas, when the principle diffracting places with the sum of miller indices (*h+k+l*) equalling an even number is defined as a body centred cubic (BCC) crystal structure (Tilley, 2004).

Placing focus on the residual stress and strain, it is noted that residual stress is defined as stress that is left in the crystal structure after the removal of external force. In order for stress to be analysed with x-ray diffraction techniques, the measurement of angular lattice strain distribution is required, and this is obtained by measuring the interplanar spacing with high diffraction peaks of a sample (R. Sharma et al., 2012). Hook's law is used to compute the average internal stress using values of strain obtained from the Williamson-Hall plot or equation (Ameh, 2019).

Dislocation density also needs to be considered, as an irregularity is formed within a crystal as a result of x-ray diffraction peaks getting equally broadened by the lattice defect that results from dislocation (Ungár, 1998). Dislocation density is defined as the length if dislocation lines per unit volume of a crystal. Weertman notes that dislocation density is inversely proportional to grain size, and directly proportional to strain (Weertman, 1993). An estimation of the dislocation density of a crystalline sample is done as follows (Subbaiah et al., 2006):

$$\delta = \frac{15B\cos\theta}{4aD}$$

Critical variables used in the establishment of chemical and physical properties that influence crystalline materials' states of stress and strain are the lattice parameters (P. F. Fewster, 1999). There are six parameters used to express the size, and shape of crystals, are called lattice

parameters or unit cell parameters are the length of the three axes, a, b, c, as well as the corresponding angles between them, α, β, γ (Jesche et al., 2016)(Toraya, 2016). Diffraction peak position is a function of the size and shape of the unit cell parameters, an diffraction peak intensities are as a function of atomic positions in the crystals. Thus, the determination of lattice parameters is obtained by the measurement of peak positions over a range of 2θ from an observed powder diffraction pattern which can be expressed mathematically with Bragg's law (Toraya, 2016).

The thermal expansion coefficient strongly influences electronic, optical and mechanical properties of materials at high temperatures (Hummer & Heaney, 2007)(Huang et al., 2006). The estimation of the thermal expansion coefficient of materials using Rietveld analysis of powder x-ray diffraction pattern obtained for a material, is best achieved through the use of the high temperature x-ray diffraction technique, as this is the most reliable technique (Naqash et al., 2018). Temperature and diffraction beam intensities are inversely proportional, and thus as the temperatures increase, the intensities of the diffraction beams decrease. This is because as the temperature increases, the atoms undergo an increase in the vibrations around their mean position (Naqash et al., 2018)(Pathak & Vasavada, 1970). As a result the values of the lattice parameters are dependent on temperature as they vary with temperature, thus the diffraction pattern of samples can be recorded during both the heating and cooling cycles at every given temperature. Polynomial models are thus used to express lattice parameters as a function of temperature to estimate the materials thermal coefficient (Jagtap et al., 2005).

Various analysis techniques can be used to observe phase transformation and outline the phase diagram, these are, transmission electron microscopy, nuclear magnetic resonance, scanning calorimetry, electrical resistivity as well as x-ray diffraction (Lekston & Zubko, 2016). The x-ray diffraction technique provides phase identity on both sides of the phase boundary. The compositional phase and the quantity present on the phase diagram is dependent on the timing, heat treatment temperature, and alloying content for alloyed materials (Pederson, 2002). X-ray diffraction is widely used in the study of phase transformation and use the mapping out of regions consisting of various crystal phases for the construction of temperature-compositional phase diagrams of compounds or alloying compositions (Caffrey & Hing, 1987). Identification of any shift of peak positions as a result of the change in lattice constant values which is a function and compositional phases is made possible through the continuous recording of the x-ray diffraction patterns obtained during the heating and cooling cycles of a samples

analysis(Caffrey & Hing, 1987)(Connolly, 2007). The changes in the peak positions or the diffraction pattern which corresponds to the phase boundary as well as the phases present at a given temperature are recorded accordingly (Pederson, 2002).

The spherical distribution of crystals in polycrystalline aggregates are defined as the crystallographic orientation, and this may be quantified by the calculation of the orientation distribution function, giving orientation density as a function of the rotation angle (Jia & Raabe, 2006). Series expansion or direct inversion is used to calculate the orientation distribution function (ODF) from pole figures (Cléton et al., 1999). The physical and mechanical properties of materials are affected by the crystallographic distribution as well as orientation. Various engineering materials have what is known as preferred crystallographic orientation due to the required or characteristic mechanical and physical properties of these materials (Connolly, 2007). Rotating x-ray diffraction is used to measure the crystallographic orientation of materials through the process of calculating pole figures or plotting pole figures as a stereographic projection (Guo et al., 2000). An integration approach is required for the measurement of the crystallographic orientation as this will result in the sum of total diffracted intensities over the entire pole sphere as well as in the three-dimensional diffraction pattern (Jia & Raabe, 2006). The random orientation of crystals within a crystalline material produces diffraction patterns which consist of concentric rings referred to as Debye-Scherrer rings if the crystals have a set of crystallographic planes (*h, k, l*) which are orientated in such a way that Bragg's diffraction conditions are adhered to. Preferential orientation of crystals prevent diffraction of some crystallographic planes due to the orientation of the crystals (Ameh, 2019).

The PXRD measurements for the samples were characterised both using laboratory instrumentation, as well as the use of the National Synchrotron Light Source II (NSLS-II) was used for high resolution powder diffraction patterns.

The laboratory instrumentation used for sample characterisation were namely:

As a starting point the Bruker D2 phaser was used to analyse and obtain the powder diffraction patter and thus powder lattice structure, or both the calcined and annealed sample powders. The D2 Phaser uses the Bragg-Brentano configuration, as well as is equipped with both primary and secondary soller slits, with a sealed Co K_α radiation tube, and a secondary beam Fe K_β

filter. The detector which is used in the D2 Phaser is the Bruker Lynxeye PSD detector, which is employed to obtain the scans used for phase identification at room temperature.

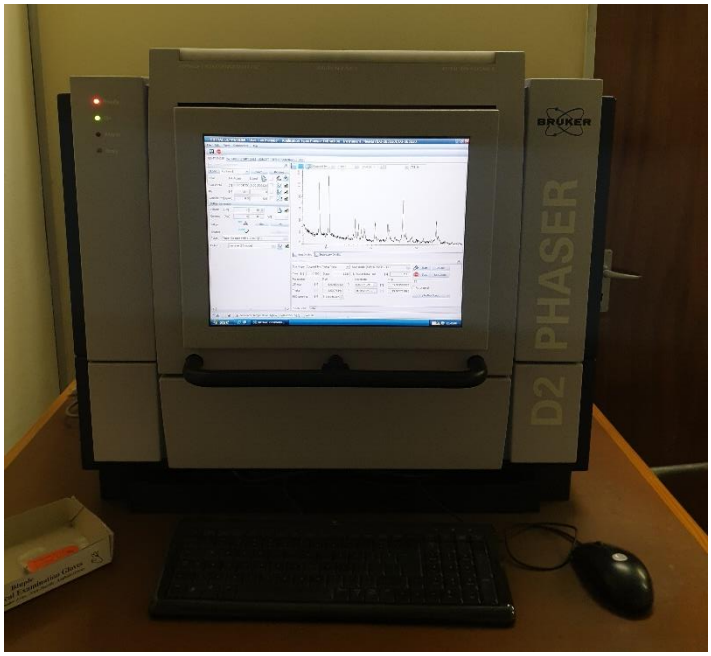


Figure 4.1.6: Image of the D2 Phaser

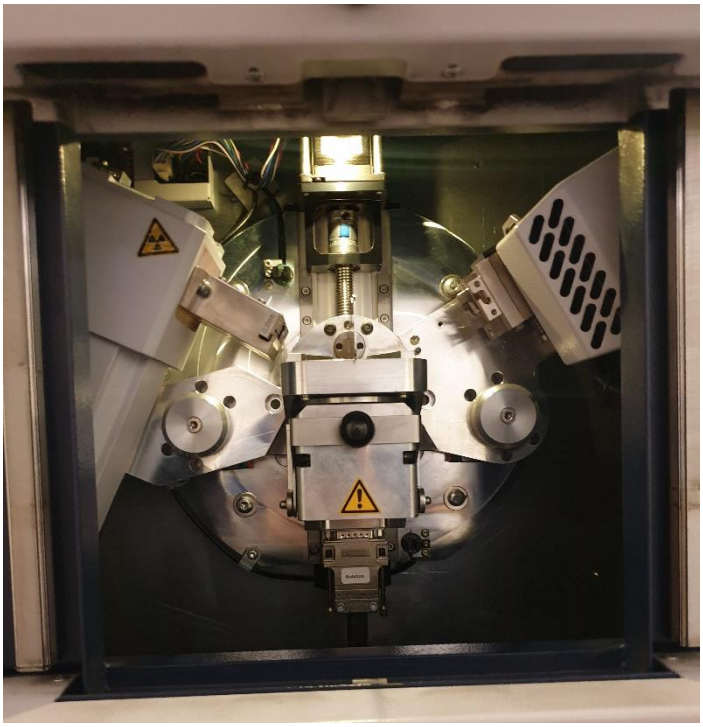


Figure 4.1.7: Image showing the X-ray source and detector of the D2 Phaser

In order to obtain better resolution data for the synthesised samples, the Bruker D9 Advance was used, and it uses a Molybdenum cathode ray tube.



Figure 4.1.8: Image of the D9 Advance

Material performance is improved through the study of their structure. Modification of the synthesis and manufacturing processes used in industry is dependent on obtaining information on the possible structural impurities and formation mechanisms involved in the synthesis process. Laboratory X-ray diffraction (XRD) and emission spectroscopy are used widely in this discovery process; however, these laboratory techniques have their limitations. The high-intensity, brilliance, collimated beams, and monochromatic nature of synchrotron radiation (SR), it has become one of the components of crucial importance in materials characterisation for materials within materials science, namely, energy materials, biomaterials, nanomaterials, to name but a few. SR is robust in the material types which it can be used to characterise, ranging from thin films, powders, to bulk forms which have complex amorphous or crystalline structures (Sedigh Rahimabadi et al., 2020).

SR and SR facilities can be used to overcome the limitations experience through laboratory instrumentation for the characterisation of materials. The production of high-flux, highly collimated, monochromatic X-ray beams characteristic with high brightness which is produced by SR is what makes it such a crucial role player and solution to challenges aced due to the laboratory instrumentation constraints. The tuning of the energy of the emitted beams from SR can contribute to signals with a high signal-to-noise ratio being obtained. These characteristics offered by SR X-ray techniques are advantageous and allow for the study of complex structures, crystalline structures, and amorphous structures elaborately. There are many applications of SR due to its benefits over laboratory instrumentation, namely it is used in materials characterisation for the investigation of the properties of ceramics, polymers, metals, biomaterials and nanomaterials (Sedigh Rahimabadi et al., 2020).

The electromagnetic radiation which is emitted by accelerated electrons close to the speed of light is defined as synchrotron radiation (SR). SR facilities are equipped with many sectors which are important for the production of SR X-rays, these are as follows, an electron accelerator (gun) which is used for the acceleration of electrons to the given energy (namely in the order of hundreds of MeV to multi-GeV); the injection source for these accelerated electrons which is a high vacuum storage ring, the electrons which are accelerated are injected into the ring in bunches, also referred to as pulses; as well as devices used to induce a magnetic field, such as wigglers, bending magnets, and undulators, these are used to result in the tuning of the emission light, and to conduct it to the beamlines. Slits, mirrors and monochromators are used in SR facilities to enable wavelength and sample spot selection (Khodaei & Petaccia, 2017).

A continuous spectrum of wavelengths is emitted as the electromagnetic radiation which occurs through bending magnets, and this spectrum ranges from infrared to hard X-rays. Insertion devices (IDs), namely wigglers and undulators result in the production of radiation, which is high in energy, with the distinguishing character being their wavelength difference. Undulators produce intense pseudomonochromatic light, and wigglers demonstrate spectra which have similar characteristics to that obtained by bending magnets (Awaji et al., 2010)(Balerna &

Mobilio, 2015). Wiggers have the flux distributed in a larger angle. Undulators have the flux distributed at a smaller distribution angle, which results in higher brilliance being observed, and thus enables beam suitability specifically for the probing of smaller sample areas (Sedigh Rahimabadi et al., 2020).

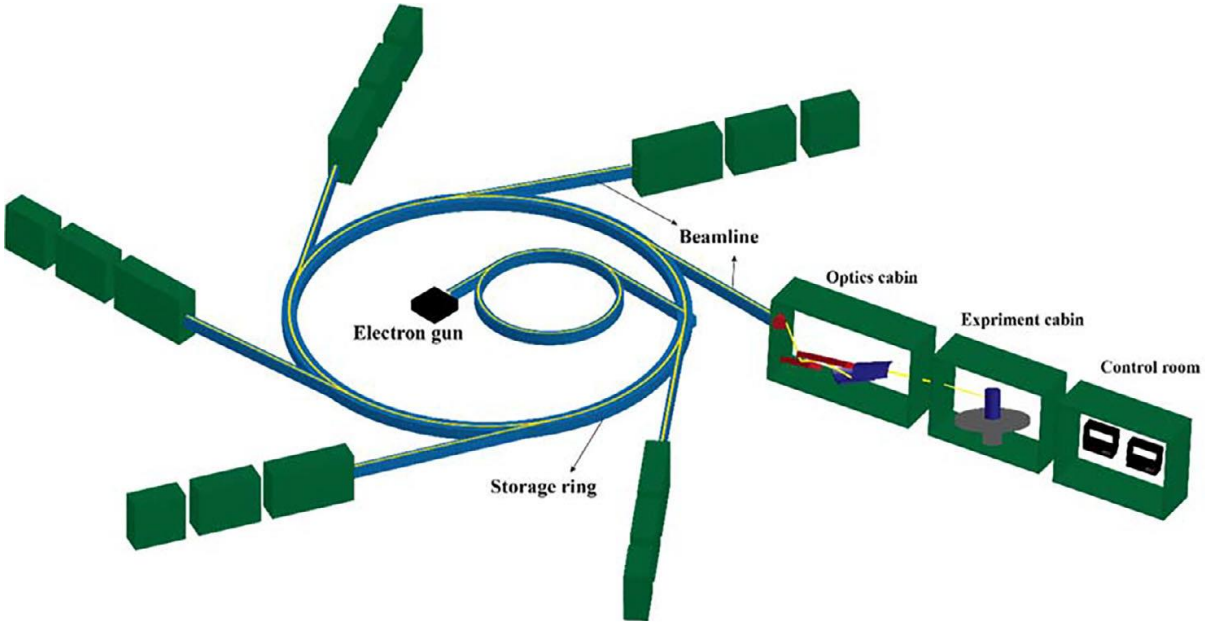


Figure 4.1.9: The various components that constitute the synchrotron radiation facility (Sedigh Rahimabadi et al., 2020)

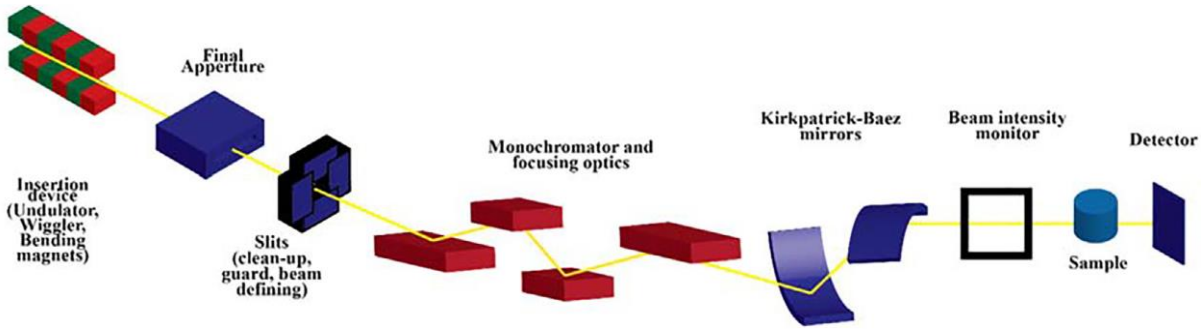


Figure 4.1.10: Insertion devices and optics configuration which run through beamlines (Sedigh Rahimabadi et al., 2020)

X-ray powder diffraction (XRPD also referred to as PXRD) is used to analyse the structure of polycrystalline materials and determine their properties. For higher resolution powder diffraction patterns, synchrotron radiation was used, namely the National Synchrotron Light Source II (NSLS-II) beamline 28-ID I (for pair distribution function (PDF) characterisation) and 28-ID II (for PXRD characterisation).

The brilliance and high flux which results from SR caused high signal-to-noise ratio diffraction patterns to be obtained, which also have distinct peaks. Studying complex structures can simultaneously be done with the use of Rietveld refinement. The Rietveld refinement method allows for the lattice parameters, phase composition, crystal structure, residual strain, and more information to be obtained. A combination of Rietveld refinement and the maximum entropy method (MEM) can also result in high-resolution electron density distribution data being obtained for the data obtained. The investigation of nanostructured materials makes use of this method (Sedigh Rahimabadi et al., 2020).

Using laboratory (conventional) PXRD analysis, Adachi et al. (Adachi et al., 1997)., studied the structural properties of a cuprate superconductor, and coupled this with Rietveld refinement. A key discussion are in this study was the relationship which existed between the structural layers and the superconductivity of the material investigated (Sedigh Rahimabadi et al., 2020) (Adachi et al., 1997).. The determination of oxygen occupancy is one of the most difficult properties to study in materials, as in noticeable in various literature studies conducted (Tatsuki et al., 1995). The use of laboratory XRD techniques to study the oxygen occupancy, however, not impossible, did prove very challenging (Dann & Weller, 1995). SR is thus a possible alternative to the conventional XRD technique to obtain valid O occupancy data which contains a high signal-to-noise ratio.

An XRD study by Takata et al. (Takata et al., 1996) to study fullerenes, which used SR as well as made use of the combination of the Rietveld refinement and MEM methods is another example. The use of this combined technique provided information which resulted in the determination that the C_{82} cage has a metal atom within it. The use of this combined technique enables the possibilities of studying the oxygen molecule arrangement within nanoporous

materials, with the use of the brilliant beams of SR to recognise the position of hydrogen atoms, and thus study metal atoms present within nanospaces (Takata et al., 1996).

The investigation of the structure of some oxide using SR-PXRD by Przenioslo et al. (Przenioslo et al., 1999), which also explains the function of full width at half maximum, provided the proof that XRD has greater sensitivity to grain size, distortions, grain shape and strain effects analysis as compared to that by neutron diffraction (Przenioslo et al., 1999).

The use of SR peculiarities, mainly its high brightness, results in the determination of more elaborative information related to the atomic occupancy, structure, and types of bonding which exist in powdered samples (Sedigh Rahimabadi et al., 2020).

Superficial phenomena, as well as the investigation of the surface structure and the crystalline region interface which has a different structure from the bulk of the material is studied using surface XRD techniques. One of the surface-sensitive techniques of great interest is grazing-incidence XRD (GIXRD), where the sample under investigation is positioned in such a way as to result in a small angle being present between the sample surface and the incident beam (the angle ranges between 1-3°). In-plane methods can be used to study material surface levels for materials with preferred orientation. A high-intensity diffraction within the reciprocal lattice and between two peaks are referred to as crystal truncation rods and can be used to reveal surface structure. This has dependency on arrangements like high-flux incident beams, a detector which has a high dynamic range, a controlled vacuum, as well as on the surface roughness (Sedigh Rahimabadi et al., 2020).

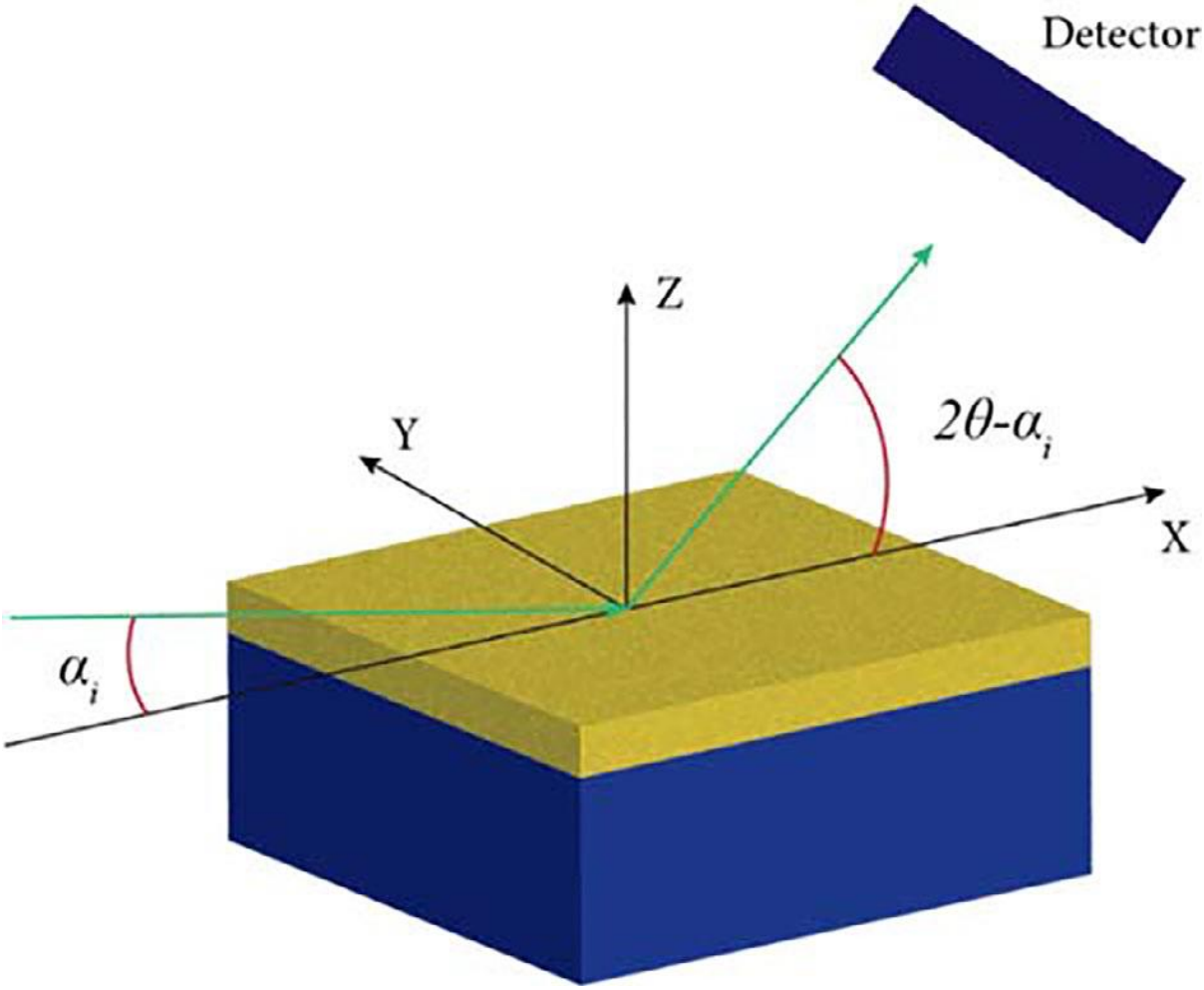


Figure 4.1.11: Data detection mechanism employed by grazing-incidence X-ray diffraction

Surface-sensitive analysing techniques are required for the study of complex systems, such as electrochemical cells. This is as a result of the charge transfer nature which occurs between and among ionic and electrical phases. The surface structure can be transformed or altered due to these charge transfers, and hence need to be studied at a surface level (Sedigh Rahimabadi et al., 2020).

A study was done by Etgens et al. (Etgens et al., 1999) which employed SR at the ID32 ESRF beamline, to investigate the growth of copper on an Au substrate in an electrochemical cell. The dense reconstruction of Au in top layers and the deposition mechanism were both indicated. The determination of the Cu structure on Au at various potentials and environmental conditions was carried out. A two-dimensional charge-coupled detector was employed in order

to investigate the electrodeposition of Cu, with its functioning comparative to reflection high-energy electron diffraction which occurs under ultrahigh vacuum (Etgens et al., 1999). The use of SR-based GIXRD, allowed for the in-situ study of the electrochemical reactions with the elimination of the limitations caused by the scattering of electrolyte elements and photon absorption (Brossard et al., 1997).

The surface hardened Ti-6Al-4V was studied by Berberich et al. (Berberich et al., 2000) using the ROBL station at ESRF. After the annealing of Ti-6Al-4V observed a decrease in hardness through the nitridation by ion implantation process, which is converse to what is expected, as an increase in hardness is expected and observed for Ti-6Al-4V prior to the annealing. The structural change mechanisms after the annealing heat treatment at 700℃ was investigated in this study. The GIXRD data obtained at a variety of angles revealed through the depth distribution of phases, the formation of nitride grains in the alloy was observed, and this is the main mechanism of hardening degradation. There was also a change in lattice parameters of phases observed and this was noted to be independent of thermal expansion (Berberich et al., 2000).

The above studies thus indicate how important the studying of material surfaces is, as this is defined as the area where the chemical reactions are triggered. The energy materials and surface engineering fields focus on the surface structure modification, and thus are a key area of study for advanced methods to provide detailed information about the material surface (Sedigh Rahimabadi et al., 2020).

One of the most critical areas of interest in the manufacturing and designing processes is residual stress, and hence stress analysis is crucial. Stresses at a microscopic and a macroscopic level are induced in materials through the manufacturing, coating, mechanical and thermal treatment, and all other processes. The residual stress of the macroscopic level is commonly studied, the microscopic residual stresses which exist between the single-phase alloy grains, and that existing in composites are often neglected. The residual stress analysis is often tackled by XRD techniques (Sedigh Rahimabadi et al., 2020). A study conducted by Fernández et al. (Fernández et al., 2018) was aimed at the investigation of residual stress that is present in

Al2014 which is cylindrical quenched and extruded, which at the macroscale and microscale have a texture with four different crystallographic orientations. The EDDI station at the BESSY SR facility which is specifically designed for stress analysis was used for this investigation. In the condition of the experiment, resulted in the conclusion that the macroscopic residual stress obeys a parabolic equation. The anisotropic nature of crystal plasticity result in the intergranular microscopic residual stress. The lattice spacing values obtained through the SR data were plotted as a function of distance from axes. The existence of microstresses becomes evident through the different fits for different reflections (Fernández et al., 2018).

Another field of interest for researchers is thin films, with the focus mainly on perovskite oxides due to their vast application potential. Coating and deposition processes are processes which could result in an amount of stress being induced within the thin film and substrate, and hence the studying of these structures and the determination of already existing residual stress within them are crucial (Sedigh Rahimabadi et al., 2020).

Shiman et al. (Shiman et al., 2012) studied the strain state of a hybridised zirconium alloy during the process of temperature fluctuation. The mechanical behaviour of this material is profoundly impacted by the existence of brittle hybrids. Hence, the thermal induction to these strains within the bulk and the grains of the material are of key importance. SR-based XRD was used to overcome the limitations of XRD from laboratory-based instrumentation. This method has stress evaluation planes which are two-dimensional, these are, axial-hoop, hoop-radial, and axial radial, which enable this technique to be used practically for the investigation of materials which have grains of differing orientations (Shiman et al., 2012).

Small-angle X-ray scattering (SAXS) is a technique which is employed for the characterisation of the constituents present within systems which are governed by the microscale and nanoscale dimensions and lack long-range order. Electron density is what is used to achieve SAXS curves. SAXS data provides information with relation to surface, dimensions, and interfaces. SAXS is also crucial for the study of biological systems, as it can be used to investigate samples in liquid environments. Two laws, namely, Porod's law and Guiner's law can be used to determine surface details (interface between two materials, and particle size), as well as the gyration radius (macromolecular size measurements). SR of the third generation overcome the

constrains of this technique in conventional X-ray analysis due to their monochromatic properties and the low-divergence beams (Willmott, 2011).

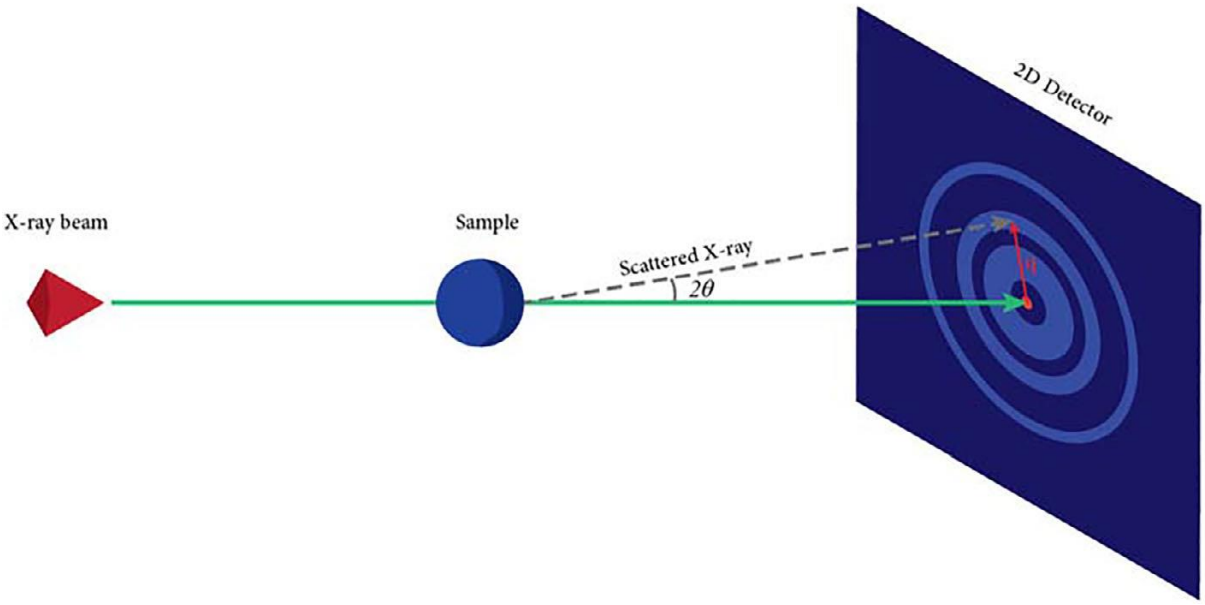


Figure 4.1.12: Small-angle X-ray scattering detection mechanism (Sedigh Rahimabadi et al., 2020)

Nanostructured superficial regions can be investigated through the combination of SAXS and grazing-incidence X-ray diffraction, namely referred to as grazing-incidence SAXS (GISAXS), which is non-destructive and intrinsic. Catalysts, quantum dots (QDs), and biological systems as the systems most often studied using GISAXS. This technique is achieved in reflection geometry rather than transition geometry and the incident angle thus results in normal scattering as well as a reflection being observed (Müller-Buschbaum, 2009).

The high surface area to volume ratio of QDs, impact the adjacent area around them, and result in a difference in their behaviour being observed. The properties of QDs, namely, their electrical, optical and vibrational properties allow them to be considered as key in the production of silicon film solar cells. In a study by Juraić et al. (Juraić et al., 2010), the properties of QDs were studied as well as the properties of its surrounding, using the GISAXS technique as well as grazing-incidence wide-angle X-ray scattering (GIWAXS). The experiment was conducted at the ELETTRA beamline in Australia. Various QD fractions of nanocrystalline Si were deposited on a class substrate using the plasma-enhanced chemical

vapour deposition technique. A domain size ranging from 2-6nm were observed for the nanostructures, demonstrating that the use of GISAXS of high energy SR allows for QDs to be observed in an amorphous matrix. Investigating the structure of nanostructure materials and optimizing them through the use of various treatments are essential as their properties are dependent in the particle distribution, particle shape, and particle size (Juraić et al., 2010).

The wide-angle X-ray scattering (WAXS) technique is similar to that of the SAXS, however, the detector distance used is much greater than that that for the SAXS. The investigation of the polymer structures which have nano-sized membranes can be done using the WAXS technique. The SAXS and WAXS are used in combination to extract as much information about the phase composition, structure and other characteristics of the materials under investigation (Sedigh Rahimabadi et al., 2020).

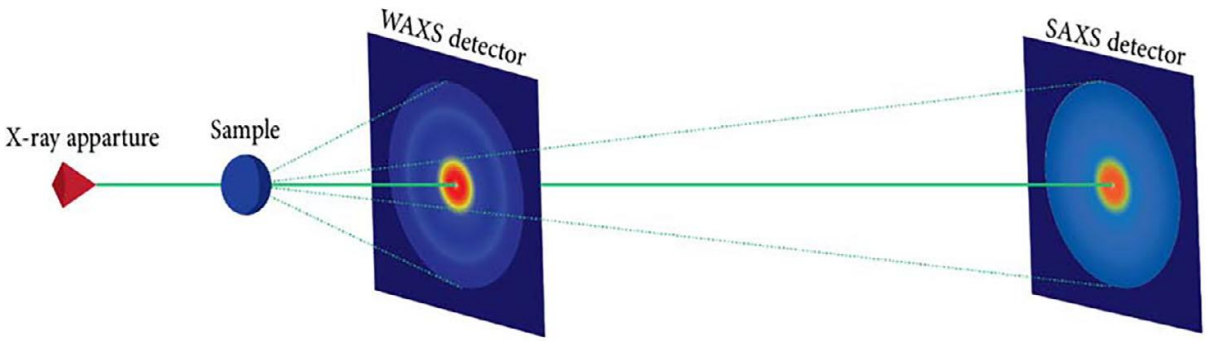


Figure 4.1.13: A diagram indicating the WAXS and the SAXS detection mechanisms (Sedigh Rahimabadi et al., 2020)

Titanium oxide nanoparticles have three differing morphologies, and thus result in it having wide range of applications in hydrogen fuel production, as catalysts in solar cells. As well in geochemical processes. It is crucial to study the crystallisation processes of titanium oxide as the crystallisation pathways impact its phase composition, size and material morphology. The investigation of TiO_2 evolution from aqueous $TiCl_4$ solution at 100℃ using WAXS was done by Hummer et al. (Hummer & Heaney, 2007). The study revealed that initially the formation of an anatase metastable phase occurred which had an average particle size of 7 nm, this phase then underwent a transformation to the rutile phase which experience a growth from less than

3 to 10 nm. The energy of the system increases due to the critical size of the anatase nanoparticles being 7nm, however, due to the transformation to the rutile phase, a decrease in the system total energy is observed, and thus the system becomes more stable (Hummer & Heaney, 2007).

The emergence of diffraction peaks within the scattering profile are determined through the crystalline structure. Statistical fluctuations that result in the microstructural and structural properties of a sample has an impact on the areas, shape and positions of peaks, and any underlying diffuse scattering (Peter Debye & Scherrer, 1916)(Patterson, 1939).

The microstructural properties of materials are very crucial and are thus a key area of investigation. Two different line-profile analysis techniques are used for the interpretation of two reciprocal representations which can be observed for powder-scattering data, namely, traditional diffraction profiles, which as the scattered intensity as a function of the scattering angel, and the pair distribution function (PDF) which is the Fourier transform of the scattering data. The Fourier transform and the diffraction profile provide the same information, the PDF analysis is more sensitive to short-range information, whereas diffraction profile analysis is more sensitive to long-range information. The current range of study which is crucial with regards to the length scale in the crystal structure is a few nanometres and this achieved through PDF which resolves the crystal to a length scale of a few nanometres (Usher et al., 2018).

The limitation placed on the experimental resolution for the PDF analysis technique, results in longer range distance structural distortions are not easily extracted as PDF is more sensitive to the short-range information, and thus lack the required information for these longer ranges. PDF due to it's focus on short-range information, has the ability to resolve the local features which are challenging to determine with the use of powder-scattering intensity profiles. The PDF peaks easily reveal the signal of a secondary phase which is possibly hidden in the diffuse scattering, this includes but is not limited to the adsorption of molecules to the surface of the particles under investigation. The distinct source of the disorder is responsible for the dependence of the profile broadening on the scattering angle or pair distances (Brandstetter et al., 2005)(Ungár et al., 1998).

Bragg theory no longer becomes strictly applicable when complex disorder scenarios need to be dealt with, this also includes situations where the variation of the structure factor is significant across peaks, due to the scattering profile changes not conforming to a peak-by-peak treatment (Rebuffi et al., 2016)(Leonardi & Bish, 2017).

In 1915 the scattering of an ideally disordered amorphous phase was tackled by Debye, resulting in the emergence of PDF through the solutions obtained for the Debye scattering equation (DSE) (P. Debye, 1915). The crystal structure of complex molecules or the local distortions present in crystalline materials can determined through the Debye theory (Billinge & Egami, 1993)(David A. Keen, 2001)(McGreevy, 1995). Debye theory results in the ability to estimate explicitly the atomistic model of a crystal, which also takes into account the presence of defects as well as structure discontinuities which are symmetry-dependent or chemical inhomogeneities.

The computational time required for a PDF solution in the powdered sample, is minimised through the use of a single or a limited number of atomistic models being used. Although this minimising technique is employed, the PDF computation, for a single model is much slower as compared to that of the modelling done using Bragg's law through the modelling of the reciprocal scattering profile. Resulting model reliability is dependent on the uniformity of the crystals in the sample. The structural and microstructural property dispersions are present within the limited set of atomistic models analysed. The PDF technique does not accurately resolve long-range information, and is thus limited when it comes to the analysis of the property dispersions across the entire powder sampled, with the short-range pair distances being most affected through crystals which are large in size (Leonardi, 2021).

The whole pair distribution function modelling (WPDFM) technique is a technique which can be used to target the intermediate regime between the short-range and long-range regions. The model is based on Bragg's law and is used to simplify the computation of an entire PDF, and overall has the modelling of the scattering data done via the DSE. Bragg's law-based models result in solutions of the dispersion of crystal properties in powdered samples which have

statistical significance and are also efficient. The PDF mean results in the exploitation of Debye theory's flexibility. Thus, it can be observed that Bragg's law approaches do not provide information which is suitable for the local structure, whereas PDF does not provide accurate and good statistical properties. This technique uses the combination of every independent crystallographic direction contribution which is calculated through directional PDF's (D-PDF's) and the solutions obtained from the DSE and uses this to obtain the intensity profile. The need for an atomistic model of the materials under investigation is thus voided (Leonardi, 2021).

The Fourier transformation of the data from the scattering profile to result in the PDF being obtained, it needs to be noted that the diffraction pattern has to have a large Q_{max} value, as well as good statistical values (Bordet, 2018), where Q_{max} is the maximum measured value. Q can be defined as follows:

$$Q = 4\pi \sin\frac{\theta}{\lambda}$$

The G (r) function used for PDF is defined by the following equation:

$$G\,(r) = \frac{1}{r}\sum_i \sum_j \left[\frac{b_i b_j}{\langle b\rangle^2}\delta(r - r_{ij})\right] - 4\pi r\rho_0$$

The variables can be defined as indicated, r_{ij} = distance, b_i = atom *i* scattering power which is either the electron scattering factor or the X-ray scattering factor, ρ_0 = numerical density (number of atoms per unit volume), $\langle b\rangle$ = average sample scattering power, as well as the sum which is distributed through the structural model atoms. Peaks that occur are as a result of peaks at *r* values which correspond to the interatomic distances of the model, with the peak intensity being related to the product of the atoms which result due to the scattering factors of the pairs (Olaj & Pelinka, 1976).

For a given coordination number or atom, the $G\,(r)$ function gives details relating to how many atoms occupy the spherical distance (r). This enables information to be obtained with regards to the local disorders which are prevalent in the systems under investigation, also allowing for the quantification of the atom pair distances. The PDF can also be used to extract atom-to-atom

distances as well as coordination numbers, in cases where the structure of a sample is undistinguishable (Davis et al., 2013).

The distance distribution within a material is thus indicated through PDF peak position, thus when the PDF observed is a flat plot, $G\ (r)$ = 0 at any given r and there is a total random distribution of atoms. The normalisation term $4\pi r\rho_0$ is used to compensate the increase in ρ_0 due to the increase in the number of atomic pairs. Nearest atomic neighbours are indicated through short distances, and isolated peaks can be obtained. Statistical distribution and thermal vibrations have an influence on the peak with observed as this is dependent on the distance distribution around their average value, and thus is related to structural disorder (Dykhne et al., 2011).

The periodicity of the unit cell, atom coordinates, and atomic displacement parameters are crucial for the interatomic distribution in crystalline solids, with a peak being produced at each distance, and peak width of this peak is related to the relative atomic displacement parameters of the atomic pairs (Kaban et al., 2007).

PDF is required to provide an estimate of particle size which is precise and is representative of the interatomic distance distribution within the particles. Amorphous compounds, obtain similar PDF effects as that observed when investigating nanoparticles, where upon normalisation, the PDF peaks disappear due to the fact that the scattering atoms in nanoparticles are governed by the volume of each individual particle as no peak in the PDF will be obtained above the maximum interatomic difference which is described within the particles. In the amorphous compounds the PDF peaks vanish as a result of the loss of structural coherence which is caused due to disorder (Kaban et al., 2007).

The $G\ (r)$ function now becomes:

$$G\ (r) = 4\pi r[\rho(r) - \ \rho_0] = \frac{2}{\pi}\int_0^\infty Q[S(Q) - 1]\sin(Qr)dQ$$

Where the variables are as follows: $\rho(r)$ = microscopic pair density, $S(Q)$ = total structure function (normalised coherent scattered intensity). $G\ (r)$ obtains the entire diffraction pattern. Using $S(Q)$ to generate $G\ (r)$, with the use of a sinus Fourier transform, taking into account the normalised scattering intensity = $I\ (Q)$, the total scattering factor $S(Q)$ can be calculated through the following equation:

$$S(Q) = \frac{I(Q) - \sum c_i |f_i(Q)|^2}{|\sum c_i f_i(Q)|} + 1$$

The variable can be defined as follows: c_i = atomic concentration, $f_i(Q)$ = atomic shape factor (type i atoms which are based on Q) (Kaban et al., 2007).

A background measurement is done using an empty sample container identical to that used for the sample, and this measurement is used to do a background subtraction. A background subtraction is crucial in PDF data where the sample scattering is weakly distributed as compared to that of the background, and the subtraction results in the diffuse scattering pattern resulting being only due to the sample under investigation (D. A. Keen et al., 2005).

SR can also be used for processes such as absorption (X-ray absorption spectroscopy such as X-ray near edge structure (XANES), and extended X-ray absorption fine structure (EXAFS)), imaging (X-ray imaging through SR-induced X-ray emission (SRIXE)), X-ray photoelectron spectroscopy (XPS), as well as X-ray microbeam/nanobeam analysis. However, our only area of interest in this study is the diffraction applications, and hence this was described in detail.

In order to characterise the synthesised samples, after calcination and annealing, the powdered samples were ground into further such that we could obtain a homogenous mixture, this also allows for the random orientation within the powdered sample. Approximately, one and a half spatula tips of the powdered sample were then placed in the centre of a silicon waver disk, referred to as a zero-background sample holder. A glass slide was then used to press down the sample, such that a flat and uniform surface was obtained, in order to preserve the random orientation of the lattice (this is for the laboratory-based sample analysis).

Simultaneous Thermal Analysis (STA):

Simultaneous thermal analysis will also be used to study thermal properties of the materials. The simultaneous thermal analysis technique employs the combination of differential scanning calorimetry (DSC) and thermogravimetric analysis (TGA) to study the thermal properties of materials.

Differential scanning calorimetry (DSC) is defined as a thermal analysis technique, which is used to measure the thermal effects in a temperature programmed process. Thermogravimetric analysis (TGA) is used to determine mass loss either as a result of gas loss or any other process which occurs in the material under investigation. DSC is a crucial component in the study of thermal stabilities and chemical compatibilities of energetic materials through the process of quantifying the thermal effects in materials. This technique is often employed in materials where the thermal effects are based on the decomposition of the material, where there is either no or negligible amounts of gas or sample mass released through the decomposition process. The sample size requirements are a key reason why these thermal analysis techniques are crucial, as due to the small sample size required, the analysis can be done efficiently (Liu, 2021).

DSC is a very effective technique which can be used for the investigation of phase transitions as a result of the thermal effects which occur. DSC and TGA can both be used for the investigation of the interactions which occur between different components within a system which consists of a mixed energetic system, where there are different thermal properties for each component within the system, and this can only be differentiated through the thermal decomposition processes characteristic of each individual component of the system (Liu, 2021).

TGA is a thermal analysis technique which makes use of the relationship which exists between a samples weight and that between the temperature of the system or the time (Nikolic et al., 2000). The process of heating or cooling the sample under investigation through a controlled process results in a weight change, and this weight change is recorded in relation to the temperature change. The weight change which is induced as a function of time is referred to as

the isothermal mode, whereas the weight change induced as a function of temperature is referred to as the scanning mode (Schmidt et al., 1994).

The properties of the TGA technique thus result in its applicability in a number of fields, such as the investigation of chemical reaction kinetics through a variety of experimental parameters, as well as the thermal stability studies of the samples under investigation. A mass shift is observed through the TGA process, and this is one of the crucial areas of focus when optimising sample synthesis procedures. Many factors impact the mass shift observed, these are namely, but are not limited to, the environmental conditions of the analysis process, the weight and volume of the material under investigation, material physical properties, sample holder parameters, atmospheric conditions of the investigation, as well as the rate of heating or cooling employed (Apostolescu, 1995).

The Perkin Elmer STA 6000 was used for the thermal analysis procedures in this study. This instrument simultaneously makes use of the DSC and TGA techniques when a sample is under investigation. The DSC technique is used to obtain heat flow curves and give data on the heat flow of the sample, and TGA is used to measure the weight loss within the sample. The investigation on the materials was carried out using this instrument for the thermal analysis of samples within the temperature range of 30-800 ℃.

Raman Spectroscopy:

One of the very powerful tools for material analysis used to explore a variety of material properties for a vast range of materials is Raman spectroscopy (Orlando et al., 2021). Process monitoring of any kind require non-destructive spectroscopic techniques as a top-choice (Bicchieri et al., 2006).

Raman spectroscopy can be considered as one of the most versatile and solid tools used for the analysis of a vast number of materials, in both laboratory and in the field conditions (Orlando et al., 2021). The first independent development of Raman spectroscopy was made by the Nobel laureate Chandrasekhara Venkata Raman and Grigorij Samuiloviˇc Landsberg in the first half of the 20th century (Raman, 1941) (Orlando et al., 2021). Raman spectroscopy was however only fully established post implementation of laser light equipped spectrometers which occurred in the second half of the 20th century (P.J. Hendra & Stratton, 1968).

As Rama spectroscopy was established, the possibility for more detailed material analysis became prominent, with particular emphasis being on carbonaceous materials (Tuinstra & Koenig, 1970). The advancement of Raman spectroscopy has also resulted in it being applied in various industrial sectors such as the textile and food industries (Poornima Parvathi et al., 2019)(Yang & Ying, 2011).

Raman spectroscopy exhibits a number of features which are advantageous as compared to other analysis techniques, such as infrared spectroscopy. In Raman spectroscopy, the signal quality of the collected signal is almost negligibly affected by water presence, thus allowing for its application for samples where infrared analysis is unreliable (Auer & Skinner, 2008).

Although Raman spectroscopy offers several advantageous, it is also susceptible to a number of challenges, namely, the development of methods of data analysis which are trustworthy and quantitatively robust (Rohleder et al., 2005). Another disadvantage is the presence of highly active Raman species masking the presence of other species within a sample (Jung et al., 2010). There are a number of principles which govern Raman spectroscopy. A quantum mechanical approach is used to understand these principles. The interaction between matter and electromagnetic radiation can occur through a number of phenomena, such as, transmittance, absorption, as well as scattering. For the absorption process there needs to be a matching between the energy gap between the two electronic energy levels and the energy of the incident photon (Born & Wolf, 1999). On the contrary, when considering the scattering process, the requirement for the presence of adequate energy levels is null, this being due to the fact that the occurrence of the mechanism being dependent on the interaction of a photon with a crystal lattice or a molecule, which induces a distortion of the electron cloud, resulting in the polarization of the species being altered with the involvement of virtual states (Kudelski, 2008).

The virtual state is however a short-lived state, and as it decays, the electron in left in the real ionic level of the system and the photon departs from the system. Elastic scattering (Rayleigh) is determined by the matching of the energy of the incoming and scattered photon, with the electron involved returning to a state with the same energy as the initial one, when this does not occur, the scattering is inelastic. In inelastic scattering conditions, the photon energy loss or gain is equal to the energy difference that results between the final and initial electronic levels. When the outgoing photon energy is lower as compared to the incoming one, the

scattering is a Stokes one, and conversely, the scattering is an anti-Stokes one when this is not the case. The Raman shift is defined as the energy difference between the outgoing and incoming photon energies (Orlando et al., 2021).

When taking a quantum mechanical approach, it is noted that the energy which corresponds to each vibrational level for a diatomic molecule can be defined as follows:

$$E_v = hv(n + \frac{1}{2})$$

The variables are as follows, v = the vibrational frequency, h = Plank's constant, n = vibrational quantum number (integer values). To simplify this, the harmonic approximation expression is used, however, it is limited. Only the fundamental transitions are allowed ($\Delta v = \pm 1$), with the separation between adjacent levels being constant, however this is not true for real diatomic molecules (Ferraro et al., 2003). It can also be observed from the above equation, when n = 0, the energy expression becomes $E = \frac{hv}{2}$, which is a direct consequence of the Heisenberg principle. Stokes and anti-Stokes processes have the same matrix elements which define the probability of a transition for a single Raman event between two electronic states. The differences in electron population at thermal equilibrium of the two electronic levels in a Raman process result in a difference being observed in the number of scattered photons (Orlando et al., 2021).

The majority of molecules populate the ground state under room temperature conditions, resulting in anti-Stokes components being less intense as compared to the Stokes components. The Boltzmann equation is used to describe the different energy level populations.

$$\frac{N_{ex}}{N_g} = \frac{g_{ex}}{g_g} e^{\frac{-(E_{ex} - E_g)}{kT}}$$

The variables are as follows, N_{ex} = number of molecules in the excited state, N_g = number of molecules in the ground state, g_{ex} and g_g is the degeneracy of the energy levels, E_{ex} = energy of the excited state, E_g = energy of the ground state (Orlando et al., 2021).

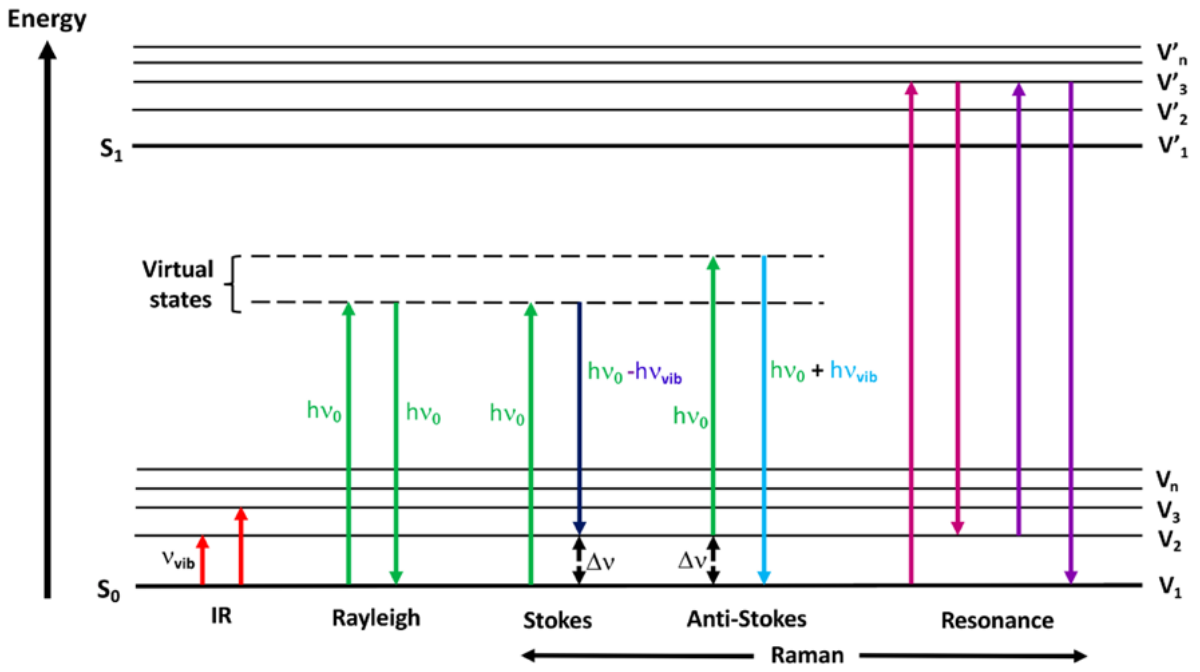


Figure 4.1.14: The Jablonski diagram for all transitions involved during Rayleigh, infrared absorption, resonance Raman scattering, Raman Stokes, Raman anti-Stokes (Geraldes, 2020)

Resonant Raman scattering occurs when the incoming photon energy is such that a real electronic state of the molecule is reached by the electron, resulting in signal intensity enhancements of up to 10^6 (Smith & Dent, 2019). Placing a comparison between Rayleigh and Raman scattering, it is important to note that Raman scattering is a weak phenomenon as compared to Rayleigh, with only one in 10^8 scattering photons actually undergoing Raman scattering. This is crucial as all Raman spectrometers have a notch filter (or other device) which filters out the Rayleigh component. Raman scattered radiation intensity is defined by the following expression (Colthup, 2012):

$$I_R \propto I_0 v^4 N (\frac{\partial \alpha}{\partial Q})^2$$

With the variables being defined as, I_0 = incident light intensity, v = incident light frequency, N = number of scattering molecules in a given state, α = polarizability, and Q = vibrational coordinate amplitude. Only when a change in polarizability occurs due to the interaction with the incoming photon, can Raman scattering occur.

A misleading conclusion can be reached when misinterpreting the above expression, namely, that the best Raman spectroscopy signal-to-noise ratio is obtainable through the maximisation of the incident light frequency. Unfortunately, there is a substantial increase in material photodegradation and/or photon absorption as a result of the beam of light in the sample becoming more energetic. This leads to visible light lasers commonly being used. Fluorescent phenomena can however be very intense, significantly leading to an increase in the background noise (Colthup, 2012) (Orlando et al., 2021).

The presence of metal nanoparticles enhances the Raman signal through exploiting the plasmonic effects, this technique is known as surface-enhanced Raman spectroscopy (SERS). SERS, is representative highly specific, powerful, and sensitive technique used for the investigation of the single-molecular level molecular structure based on Raman scattering (Orlando et al., 2021).

The interaction between the surface of plasmonic nanostructures and the molecules are the mechanism through which SERS is exploited. Copper nanoparticles and noble metals are frequently used as a consequence of their interaction with the electromagnetic waves, this leads to the induction of the localized surface plasmons which almost cover all the near infrared and visible wavelength range (Naik et al., 2013)(Naik et al., 2011).

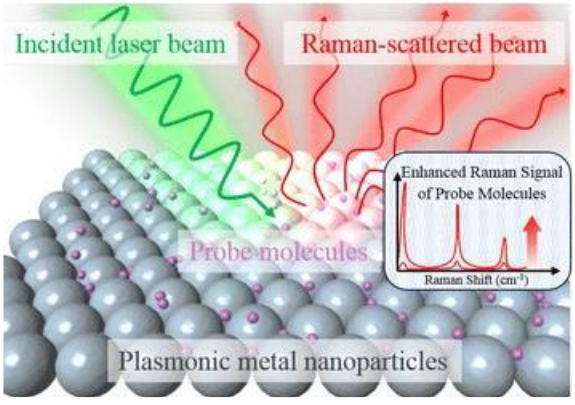


Figure 4.1.15: Diagrammatical representation of the SERS process (Jeon et al., 2016)

The noble metal nanoparticle optical properties have extinction spectra which are dominating. The local electromagnetic field can be significantly modified by the intensity of the localised

surface plasmons (Kooij et al., 2011). Two theories can be used to describe this phenomenon, the chemical theory and the electromagnetic theory, however the greatest experimental support is provided for the electromagnetic theory (Tsuneda et al., 2019).

Mie's theory is used to explain the dynamics of the SERS, by employing the analysis of the optical response to metal nanoparticles (Duque et al., 2017)(Horvath, 2009). Drude theory is used to calculate the complex dielectric function of the nanoparticles, which is a crucial parameter in Mie's theory (Drude, 1900). Intraband ($\varepsilon_{intra}(\omega)$) and interbrand ($\varepsilon_{inter}(\omega)$) electron transitions are major contributors to the dielectric function, and is defined through the equation that follows (Orlando et al., 2021):

$$\varepsilon_{EXP}(\omega) = \varepsilon_{intra}(\omega) + \varepsilon_{inter}(\omega)$$

The electronic transitions at the Fermi level in the bands that are not completely filled are definitive of the intraband. The electronic transitions which occur from the transition to empty states sitting in bands separated by an energy cap by occupied states are definitive of the interband contributions. The Drude model describes the contribution to $\varepsilon(\omega)$, an additional term, the damping term τ is included in this model. Considering nanoparticles, the effect of the nanoparticle surface is what the damping term is related to. The nanoparticle surface alters the electron motion, as a result of the electron mean free path λ, which is related to the lifetime τ, being larger in size or comparable to the particle size. The shape of the particles also influences the nanoparticle surface effect (Coronado & Schatz, 2003). Accounting for the inclusion of the surface dispersion in the Drude model, the damping term is added to the intraband contribution. The dielectric function which is dependent on the nanoparticle structure, as well as includes the free electron contribution, surface damping, as well as interband transition, has the following equation (Kreibig, 1974):

$$\varepsilon(\omega, a) = \varepsilon_{inter}(\omega) + \varepsilon_{intra}^{NP}(\omega, \alpha) = \left(\varepsilon_{exp}(\omega) - \varepsilon_{intra}(\omega)\right) + \left(\frac{\omega_p^2}{\omega\left(\omega + \frac{1}{\tau} + \frac{1}{\tau(a)}\right.}\right)$$

The variables are defined as follows, $\frac{1}{\tau}$ = damping constant (as a result of electron dispersion), ω_p = plasma frequency. The smaller the particles, the more important the surface dispersion effect.

When incident light is in resonance with the surface plasmon modes of the nanoparticles or of a metallic thin film, electromagnetic enhancement occurs. Fine tuning of the spectral positions of these surface plasmons are essential in ensuring that the resonance condition is achieved. Strong enhancement of the Raman modes of the absorbed particle on the metal surface under analysis occurs when there is an induction of the electromagnetic field onto the metal surface. The equation that follows indicates the average field of the Raman scattered light (Kneipp et al., 2002):

$$E_R \propto \alpha_R A(v_L) E_0$$

Where the variables can be described as follows, $A(v_L)$ = field enhancement (averaged over metal particle surface), α_R = Raman scattering component, and E_0 = incident field magnitude.

SERS has many applications, including but not limited to, sensing and imaging applications, namely, spectro-electrochemistry, analytical and biological applications, and single molecule SERS (Abalde-Cela et al., 2010)(Langer et al., 2020). SERS is very powerful as it can be employed in the identification of chemical species, as well as attain accurate structural information with regards to materials science, polymer science, biochemistry, catalysis, biosensing, as well as electrochemistry (B. Sharma et al., 2012)(F. Zhao et al., 2021).

Tip enhanced Raman spectroscopy (TERS) is another technique which is based on the enhancement of the Raman signal (Stöckle et al., 2000). It is a near-field method which is used to spectroscopically analyse a variety of biological and chemical samples to a spatial resolution which is of high quality of a few nanometres and is limited by the shape and apex size of the tip. Fiederling et al. describe that the tip can be considered to be an individual plasmonic nanostructure which utilises scanning probe microscopy techniques to scan over the sample (Fiederling et al., 2020). When coming into a few nanometres from the sample, a localised region of SERS enhancement is provided (Stöckle et al., 2000). This technique can possibly overcome SERS enhancement limitations, as the SERS enhancement is dependent on substrate penetration. TERS has the ability of Raman signal enhancement and topographical information attainment simultaneously (Bailo & Deckert, 2008).

Initially Raman spectroscopy utilised non-coherent light sources (Raman, 1941), however, as

time progressed, all Raman spectrometers now make use of laser sources, which are either pulsed lasers, or continuous wave lasers. Continuous wave lasers were initially, Kr, Ar, or Kr-Ar lasers, but lately diode-pumped solid-state lasers are used (Hoehse et al., 2011). Nd:YAG (1064 nm) are used for pulse lasers or excimer lasers are used for pulse lasers, and these lasers are characterised by a higher power output (10-100 mW) (Ferraro et al., 2003). The pulse lasers have a limitation based on the pulse duration, and thus need to be locked in. Gated detectors and ultrafast lasers can be utilised to exploit the fluorescence and Raman scattering emission time differences, and thus be employed for the removal of the fluorescence from the spectrum recorded (Ariese et al., 2009)(Burgess & Shepherd, 1977).

There are differing systems which can be used for the collection of signal spectral intensity in Raman spectrometers. One of the methods used is the dispersive method, this method has the requirement of a diffraction grating, which is formed by a series of grooves introduced on a reflective support. The change in angle of incidence of the polychromatic radiation, which is scattered, results in frequency selection, enabling for the measurement of intensity in relation to wavenumber or frequency. The whole spectrum can also be obtained by the use of interferometric spectral analysers. Once the spectrum is obtained, computational methods can be used to Fourier transform (FT) the data obtained, which results in the change in domain from the time domain to the frequency domain, and this is classified as FT-Raman spectroscopy (Orlando et al., 2021).

Low spatial resolution of approximately 1 nm^2 is characteristic of Raman spectroscopy, and thus micro-Raman spectroscopy is the preferred technique for the sample characterisation of samples which are nanostructured, both inorganic and organic samples. A Raman spectrometer is combined with a optical microscope to achieve micro-Raman spectroscopy. The use of a high magnification objective lens allows for the laser beam to be focused on approximately a 1 μm area, this thus only introduces limitations caused by the light diffraction limit, and a scanning sample depth raging from a few hundred nm up to 1 μm being reached (Yoo et al., 2014)(Sekar et al., 2017). Due to the benefits of micro-Raman spectroscopy, it has a wide variety of applications such as the evaluation of the stresses which occur internally within various nanocomposite materials (Dietrich & Dombrowski, 1999)(Wermelinger et al.,

2009)(Q. Zhao & Wagner, 2004), graphene and carbon nanotube structural and electronical property probing (Ferrari et al., 2006)(Anderson et al., 2007), polymer combination composition and phase mapping (Hashida et al., 2005)(Van Overbeke et al., 2003), as well as the determination of crystal orientation in nanometric structures (Fan et al., 2008)(Livneh et al., 2006).

The Raman spectroscopy characterisation technique was used to provide information on the sample composition or sample phase and will act as a complementary technique to the XRD characterisation. Raman spectroscopy is also able to detect small concentrations of impurity phases in some instances. The characterisation will also be carried out under variable temperature conditions to obtain information of any changes which occur in the sample composition as a result of temperature change.

The Raman spectroscopy characterisation technique was done using a Horiba LabRam HR Raman spectrograph, which is coupled with a Lexel Argon ion laser tuned to 514.5 nm, with a Linkham TS1500 sample stage. In-situ variable temperature Raman spectroscopy analysis was done on the samples in the temperature range 22-800 ℃, with a temperature interval of 50 ℃ being used for data analysis from 100-800 ℃, where the dwell time was 10 minutes, and a heating rate of 10℃. min^{-1} being used.



Figure 4.1.16: Image of the Raman Spectrometer used for room temperature and VT-Raman

Electrochemical Impedance Spectroscopy:

Many applications are based on the field of electrochemistry as this is the foundation thereof (Bard & Faulkner, 2001). These applications are included but not limited to, energy production and storage (Placke et al., 2017)(C. Choi et al., 2020)(Chao et al., 2020)(Kwak et al., 2020), electrocatalysis (Stamenkovic et al., 2016)(Goyal et al., 2020), corrosion (Tallman et al., 2002)(MacDonald, 2011)(Esmaily et al., 2017)(Ogle, 2019), sensors (Rowley-Neale et al., 2018)(Manikandan et al., 2018), as well as fundamental electrochemistry (Koper, 2011)(Costentin et al., 2012)(Oleinick et al., 2019)(Doblhoff-Dier & Koper, 2021).

Surface analysis and analytical sciences use electrochemistry through the measurement if current or potential as a method of analysis of the working electrode reactivity, or through the process of driving the potential or current for the tuning of interfacial properties, from macroscopic films to atomic or molecular levels. Electrochemical impedance spectroscopy (EIS) is one of the electrochemical techniques which is used for the analysis of the samples based on the application of a stimulus to the interface which has small amplitude and uses the advantageous characteristic of the frequency-resolved measurements which are performed

under steady-state conditions of the electrochemical system (Watson & Orazem, 2020)(Lasia, 2014)(Barsoukov & Macdonald, 2005).

The variation of the applied perturbation frequency to the millihertz from megahertz domain, allows for the isolation of the different time constraints which are specific to each elementary step related to a global mechanism, which include adsorption, mass transport, double-layer charging, and electrochemical charge transfer (Vivier & Orazem, 2022).

EIS measurements can be done in different atmospheric environments or in a vacuum at a variety of temperatures, and temperature ranges. Two identical electrodes are used and placed on the parallel sides of the sample under investigation, these act as two probes. The samples investigated in EIS measurements are either a rectangular block when solid specimens and cylindrical pellets for powdered samples, and these measurements are used for the characterisation of the conductivity of the materials under investigation (Hollins, 1988).

This technique can be used to investigate the degradation mechanisms, failure modes, and reaction pathways of complex fuel cell samples, using it's linear electrochemical alternating current (A.C.) perturbation method (Holze, 2002a)(John B. Goodenough, 2003). The use of this technique in fuel cell research enables the ability for activation polarization, ohmic, and concentration contributions (Holze, 2002a). In this study, the EIS technique was used to investigate the electrolyte material to determine its electrochemical properties.

The data obtained through the ESI analysis technique is plotted in the form of a Nyquist plot and is studied in detail using the process of equivalent circuit modelling (ECM), where the equivalent circuit is built up from circuit elements, these elements could be resistors, capacitors, to name but a few. These circuit models can have these circuit elements in series or in parallel configurations, and these configurations are selected such that the equivalent circuit models the behaviour of the material under investigation when the equivalent circuit is fitted to the experimental data obtained. The fitting procedure makes use of complex non-linear squares (CNLS), which are coupled to a stochastic error structure assessment, namely, to result in a simulation process which is valid (Holze, 2002a).

The alternating voltage as a result of impedance (also linked to a complex resistance) is used in the A.C. impedance spectroscopy measurement, as the response to this alternating voltage

is measured. This process takes into account the frequency domain of a variation of single-frequency voltages and their related impedance measurements. The wide range used for the frequency ranges from 1Hz to 1MHz. The application of an A.C. potential in a sine wave formation to an electrochemical cell is representative of the electrochemical impedance process, the current through the cell is then also measured, which is characteristic for high resistance systems, the response to the applied potential is an A.C. signal, where the sum of the sinusoidal functions (in a Fourier series) is representative of this current signal. A pseudo-linear approach is used to represent the cell's response, and this is characteristic of the use of a small excitation signal for the electrochemical impedance process. In a linear (or pseudo-linear) system the response to the sinusoidal potential as a current signal, is a sinusoid which has the same characteristic frequency but is shifted in phase. The equation used to represent this excitation signal with regards to time, is indicated below (John B. Goodenough, 2003):

$E_t = E_0 \sin(\omega t)$

The variables are as follows: E_0 = signal amplitude, E_t = potential at time *t*, ω = radial frequency. There exists a relationship between ω, the radial frequency which has units of radians.s^{-1} and the frequency f, with units of hertz is defined as follows:

$\omega = 2\pi f$

I_t, which is represented as the response signal, has a different amplitude as compared to I_0, as there is a shift in phase represented in a linear system by $(\omega t + \phi)$:

$I_t = I_0 \sin(\omega t + \phi)$

The system impedance is measured by the equation below, which is similar to Ohm's law (4*):

$$Z = \frac{E_t}{I_t} = \frac{E_0\, sin(\omega t)}{I_0 \sin(\omega t + \phi)} = Z_0 \frac{sin(\omega t)}{\sin(\omega t + \phi)}$$

Using Eulers expression (indicated below) (3*):

$\exp(j\phi) = \cos\phi + j\, sin\phi$

The complex function for impedance can be represented, where the potential is:

$E_t = E_0 exp(j\omega t)$

The current response is as follows:

$I_t = I_0 exp(j\omega t + \phi)$

Expressing the impedance as a complex number now becomes:

$$Z(\omega) = \frac{E}{I} = Z_0 \exp(j\phi) = Z_0(\cos\phi + j\, sin\phi)$$

$Z(\omega)$ has a real and an imaginary component. A "Nyquist plot" is formed when the real component is plotted on the x-axis and when the imaginary component is plotted on the y-axis. The y-axis is plotted as a negative imaginary impedance, with each point representing the impedance obtained at a given frequency. The Nyquist lot has low frequencies on the right side of the plot, and the higher frequencies on the left side of the plot (W. Choi et al., 2020).

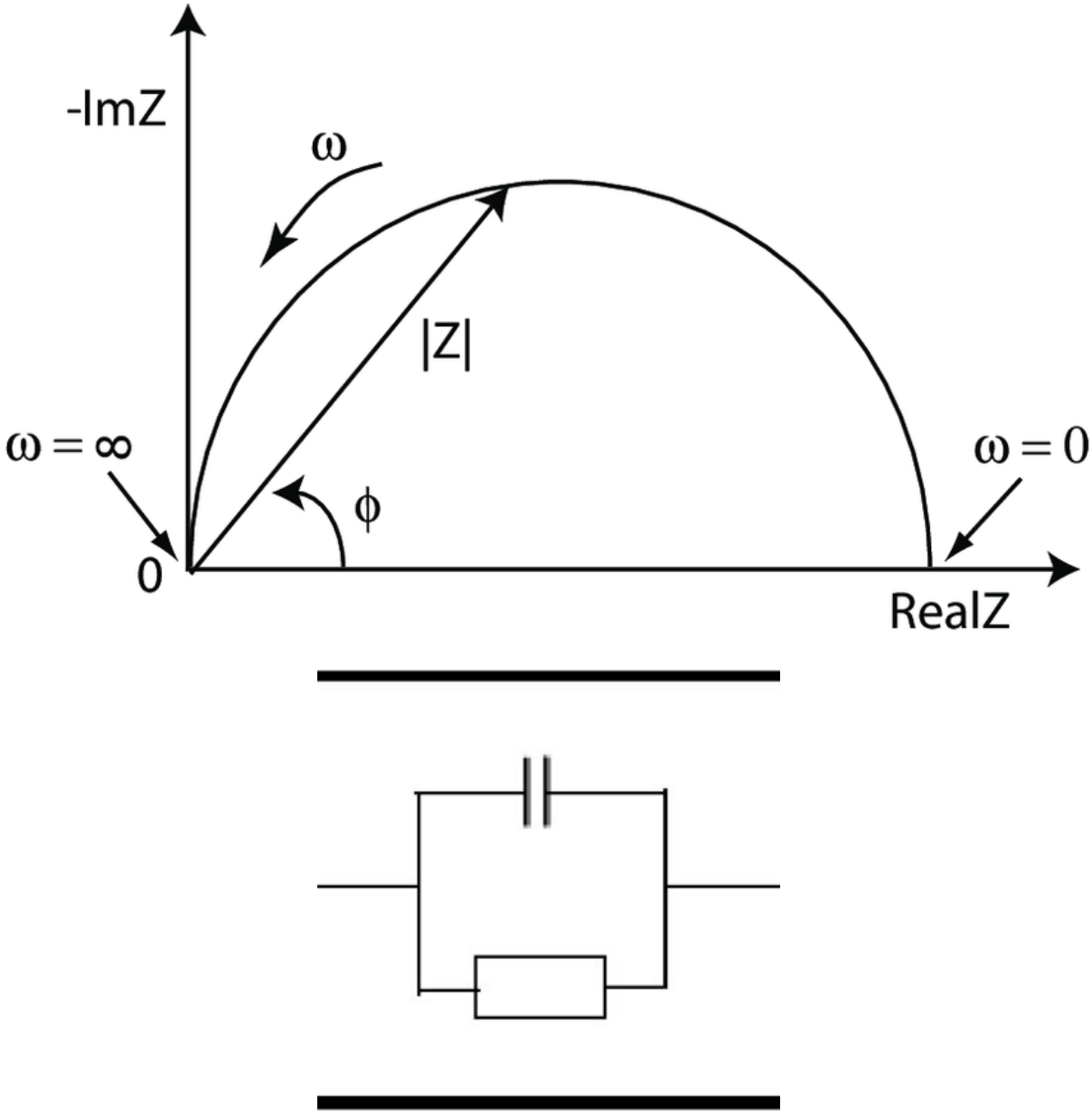


Figure 4.1.17: Nyquist plot also indicating impedance as a vector, and the equivalent circuit used which has a single time constant (3*)

There are three crucial factors which need to be focused on when measuring EIS data, these are namely, stability – current response contains minimal to no drift or background noise,

linearity – a small input amplitude to achieve a linear output, causality – the potential disturbance is the only factor triggering the current response (L. Zhu et al., 2014). The use of the Kramer Kronig (K-K) transformation is used to check the validity and quality of the data obtained, to ensure that the three conditions are met before the circuit model is used for fitting (Hollins, 1988)(Holze, 2002a).

Understanding the ECM, the circuit elements need to be understood. Ideal behaviour makes use of three elements which are considered as primary, namely capacitors (C), inductors (L), as well as idea resistors (R), and when considering non-ideal behaviour, these primary elements may no longer apply, and thus special circuit elements are utilised, a few examples are, the Warburg element (W), the constant phase element (CPE), etc (L. Zhu et al., 2014).

The perfect resistor element (R) represents a circuit element which has characteristics of being independent of frequency as well as independent of an imaginary part. Through a resistor with voltage across it, the current remains in phase, $\phi = 0$ (6*). Thus, the Nyquist plot obtained will just consist of a single x-axis point, showing that this value will be the same across a range of frequencies, and thus only a real impedance value is characteristic (L. Zhu et al., 2014).



Figure 4.1.18: Symbolic representation of a perfect resistor (L. Zhu et al., 2014)

Perfect capacitors have purely reactive impedance and is characteristic of zero resistance. The has angle obtained is -90° on the application of an A.C. voltage and is defined as the current leading the voltage. A capacitor indicates an inverse relationship between its impedance and frequency, thus there is an increase in impedance as there is a frequency decrease. Only an imaginary constituent of impedance is observed for real capacitors, where the charge (q) is represented as follows (7*-64):

$$q = CE$$

The impedance of the capacitor is defined as:

$$Z_c = \frac{1}{j\omega C}$$

Where j = imaginary unit, ω = radial frequency, C = capacitance. Thus, the Nyquist plot obtained for a capacitor is a vertical line where the Z' = 0 through the frequency range (7*-64).

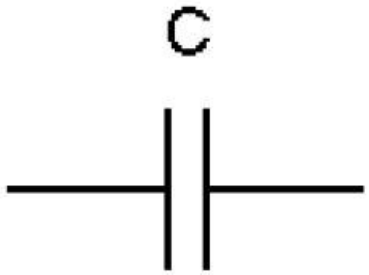


Figure 4.1.19: Symbolic representation of an ideal capacitor (8*-65)

A constant phase element (CPE) has the symbol Q and is representative of non-ideal capacitance or a non-ideal capacitor and is used to model solid state systems which deviate from ideal behaviour. Q in a Nyquist plot indicates a sloped linear plot. A QR circuit in a Nyquist plot having the circuit placed in parallel indicates a depressed semi-circle (which deviates from the series CR circuit semi-circle) and has its centre below the actual x-axis. The impedance can be defined as follows (Kalinin & Bonnell, 2002):

$$Z_Q = \frac{1}{Q(j\omega)^n}$$

The phase is independent of frequency and thus is constant, it is also equal to $(-90\times n)^{\circ}$ with n being a number between 0 and 1.

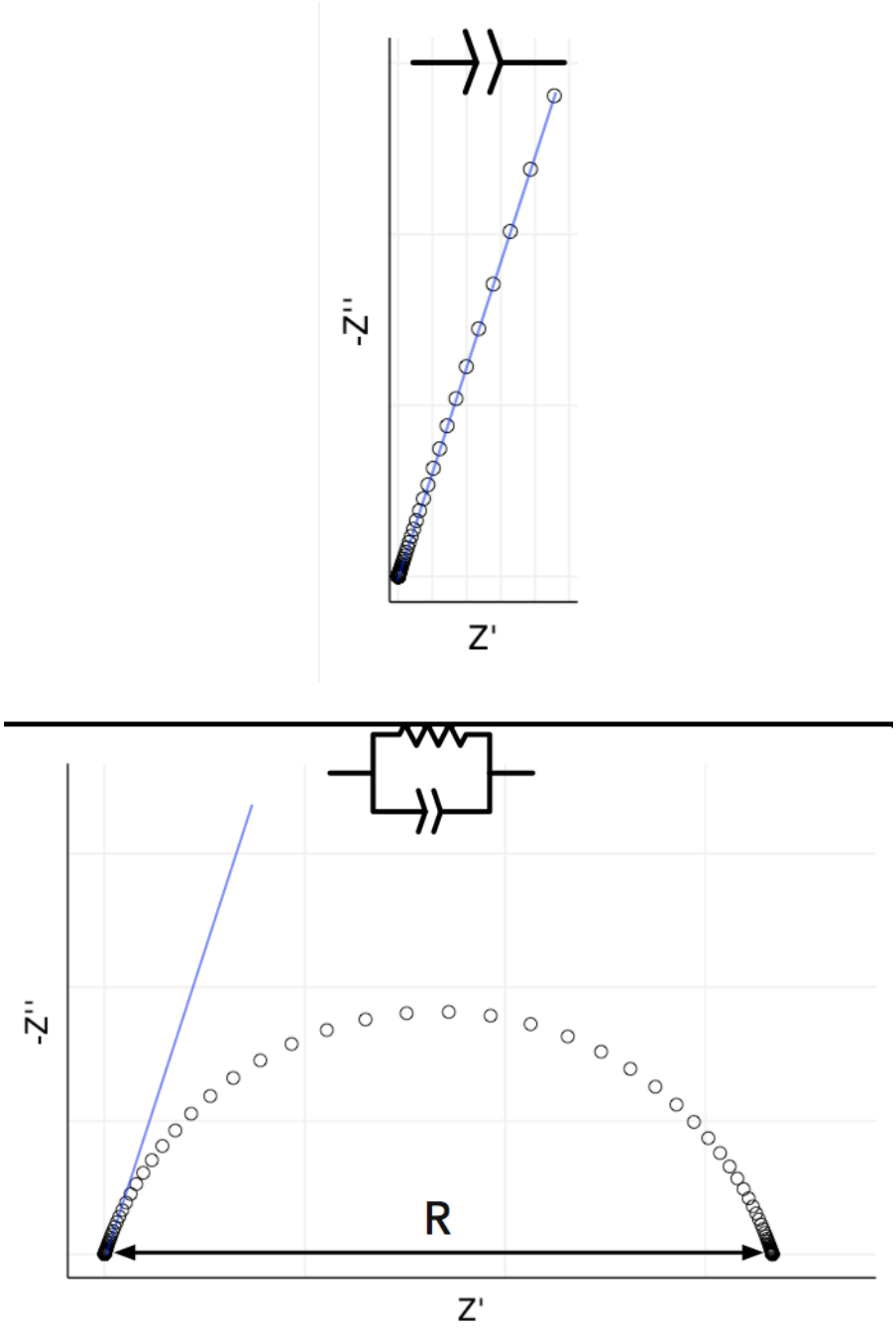


Figure 4.1.20: Symbolic and Nyquist plots obtained for the CPE (8*-65)

The semi-circle has its centre located at an angle which can be defined by (1-n) × 90° in relation to the origin, where n is the parameter of depression, thus if n = 1, ideal capacitance is observed. Non-ideal and non-uniform current distribution is an implication of the CPE, which could be as a result of variations in the thickness or composition of the electrode, highly distributed reaction rates, or electrode surface roughness (Holze, 2002b).

The Warburg impedance which has the symbol W, is used to model semi-infinite diffusion, which is defined by the one-dimensional diffusion which is solely bounded relative to a large planar electrode on one side (Rodrigues et al., 1999).The equation which is definitive of this element is indicated below:

$$Z_w = \sigma\omega^{-0.5} + j\sigma\omega^{-0.5}$$

With the following variables being defined, σ = Warburg coefficient ($\Omega.s^{-0.5}$), with the Warburg impedance being employed to model the low frequency regions, with the slow process of diffusion dominating (Rodrigues et al., 1999). The Nyquist plot representation of the Warburg element is a straight line with a slope at a 45° angle to the x-axis, or a slope of 0.5.



Figure 4.1.21: Symbolic representation of the Warburg element

Finite diffusion behaviour is observed when the diffusion of the system is further limited by the experimental constraints, or system constraints, when the system tends away from the semi-infinite conditions. This type of diffusion contains two main equivalent circuits, defined as the finite space Warburg (FSW), also referred to as the open Warburg elements, and the finite length Warburg (FLW) also referred to as the short Warburg element.

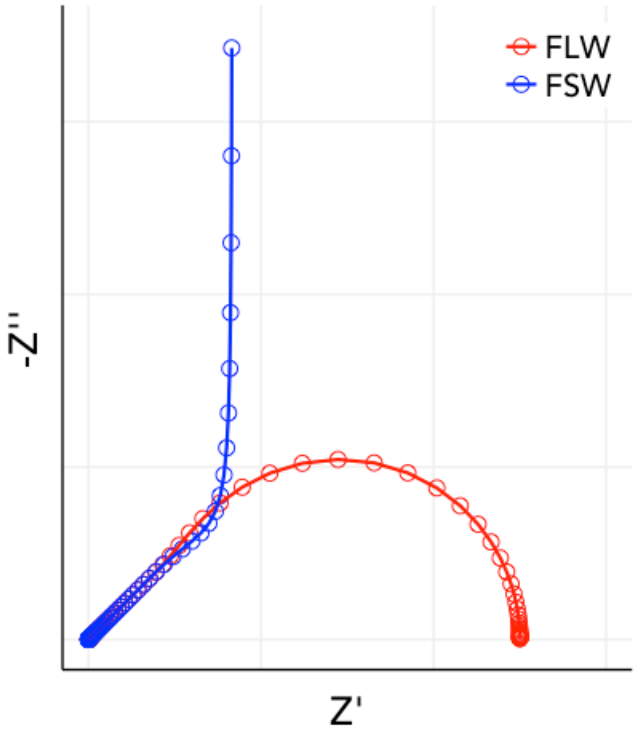


Figure 4.1.22: Diagrammatical representation of the Nyquist plots obtained for the FSW and FLW elements

Electrochemical impedance spectroscopy was used to determine the ionic conductivity of the Bi_2O_3 materials formed (as a function of temperature) and check that electronic conductivity is minimal. These measurements on sintered pellets occurred by using a BioLogic MTZ-35 frequency response analyser which is interfaced with a computer running the MT-Lab software version 1.21. This was coupled with a BioLogic HTF-1100 furnace as well a HTSH-1100 sample holder. The impedances as a result of the instrumentation were compensated for before any measurements were done on the sample. The frequency range used was that of 0.1Hz to 1MHz with an amplitude of 10mV. The variable temperature analysis took place in the temperature range of 150-500 ℃ with increments of 50 ℃ being used for measurements, the 150℃ data was excluded from the set as it was very noisy. Two platinum discs are present in the sample holder, and they are of similar diameter to the sample, the pellet is spring-loaded in between these platinum discs and tightened. A 10nm coating of pure gold was used on the pellets investigated. The Nyquist plots obtained were modelled using the ECM technique and employed the EC-Lab version 11.21 software.

Chapter 5

X-ray Diffraction (XRD)

Initially the total dopant concentration that was of key interest was the 20 mol % dopant concentration. A total of three different dopant concentration ranges were focused on for synthesis and PXRD analysis, namely, in the range of 8.5-10 mol%, 20 mol %, as well as 22.5 mol%. The low dopant concentration mol % range was chosen in correlation to a study done by Jolley et al. (Jolley et al., 2019) who stated that the optimised dopant concentration range for a purely rhombohedral sample using only Nd as a dopant is achieved at a 7-10 mol% dopant concentration range using the solid-state synthesis method. The higher dopant concentration range of 20 mol% was used in correlation to studies done for the cubic phase. The highest dopant concentration range of 22.5% was used to ensure sample phase stability this also allowed the introduction of a third dopant to the system.

For the study done by Jolley et al. various dopants were used, however the Nd dopant system was of importance to us in this study. They determined that phase pure rhombohedral Bi_2O_3 (space group R-3m) for the Nd dopant was achieved within the 7-10 mol % dopant concentration range using the solid-state synthesis method (Jolley et al., 2019).

Lower total dopant concentration samples were synthesised to be comparative to that of the study by Jolley et al., although the synthesis methods varied, the results are thought to be comparitive. The ionic conductivity which was exhibited as the highest conductivity was that of the lanthinum (La) and yttrium (Y) double-doped Bi_2O_3 system, which exhibited a conductivity of 3×10^{-2} S/cm at 500℃ (Jolley et al., 2019).

The 20 mol % total dopant concentration samples were synthesised in comparison to previous studies of the cubic δ-phase Bi_2O_3 samples, as well as following the disproval of the conclusion reached by Jolley et al. (Jolley et al., 2019), these samples were used to determine the minimum total dopant concentration mol % required for co-dopant systems which result in a phase pure and phase stable rhombohedral Bi_2O_3 (space group R-3m) samples. The optimal co-dopant variation of interest which yielded phase stable and phase pure rhombohedral Bi_2O_3 (space

group R-3m) was the sample with 15% Nd and 5% Y (15Nd5YSB), with this sample being used as the template sample for all other samples synthesised.

Using the 15% Nd and 5% Y (15Nd5YSB) sample composition as a template sample composition for the co-dopant mol %, for the 22.5% double doped samples synthesised, this was used, while trying to optimize the total dopant concentration mol % to determine whether the sample composition can be varied to get the major dopant mol % concentration lower and the other higher, while still maintaining phase purity and stability. For the triple doped samples synthesised with a total dopant concentration mol % of 22.5%, the 15% Nd and 5% Y (15Nd5YSB) sample composition as a template sample composition due to this being the ideal sample, and thus phase stability and phase purity were investigated using 2.5 mol % for three dopants resulting in a triple dopant system. The nomenclature for the samples indicate ann, where ann indicates annealed, as the annealed samples were investigated.

Laboratory x-ray experimental data:

5.1.1 Purely rhombohedral sample Rietveld refinement:

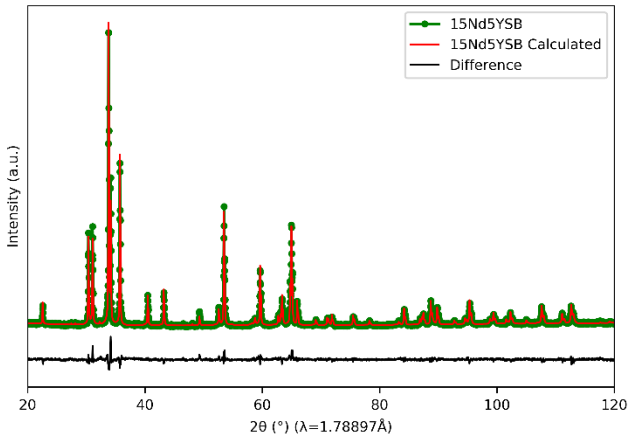


Figure 5.1.23: Rietveld refinement obtained for $15Nd5YSB$ sample.

The above figure, figure 5.1.23 shows the XRD Rietveld refinement pattern obtained for the 15Nd5YSBsample, using the laboratory X-ray diffractometer. The Rietveld refinement plot as shown above is applicable to all phase pure rhombohedral samples. When observing the Rietveld refinement results, it is important to firstly understand that the Rietveld method uses

an iterative approach to minimize the residual by making various but controlled adjustments to the refinable parameters. Table 2 and table 4, is used to indicate the observed phase composition percentages, and the Rietveld refinement statistics respectively. Table 3 indicates the input parameters used for the structure file used in the refinement. The R-factors, for the 15Nd5YSB sample are as follows, R_{exp} = 3.48%, R_{wp} = 5.57%, where the R-factors are indicative of the best fit being modelled between the experimental data and the calculated data for the XRD diffractograms. The goodness-of-fit (GOF) is used to define the refinement quality, for the 15Nd5YSB sample, the GOF = 1.598. Slight peak intensity mismatches are observed between the experimental and calculated diffraction patterns, indicated through the difference pattern. This mismatch in the peak intensities could be attributed several factors, however, a more accurate reason being preferred orientation of the sample as a result of sample packing, as well as the solution being an increase in the count time used for a x-ray diffraction scan.

5.1.2 Purely cubic sample Rietveld refinement:

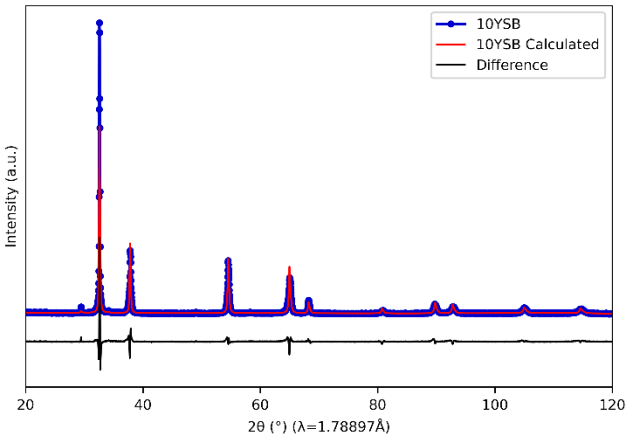


Figure 5.1.24: Rietveld refinement obtained for $10YSB$ sample.

The above figure, figure 5.1.24 shows the XRD Rietveld refinement pattern obtained for the 10YSB sample, using the laboratory X-ray diffractometer, which indicates a phase pure cubic sample. The R-factors, for the 10YSB sample are as follows, R_{exp} = 7.02%, R_{wp} = 13.9%, where the R-factors are indicative of the best fit being modelled between the experimental data and the calculated data for the XRD diffractograms. The goodness-of-fit (GOF) is used to define the refinement quality, for the 10YSB sample, the GOF = 4.371.

5.1.3 Rhombohedral and cubic sample Rietveld refinement:

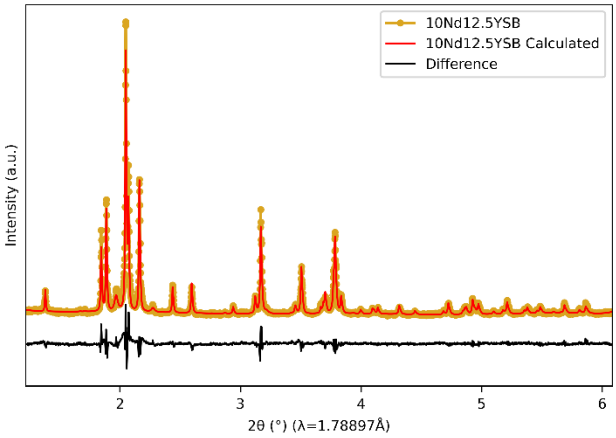


Figure 5.1.25: Rietveld refinement obtained for $10Nd12.5YSB$ sample.

The above figure, figure 5.1.25 shows the XRD Rietveld refinement pattern obtained for the 10Nd12.5YSB sample, using the laboratory X-ray diffractometer. The Rietveld refinement plot as shown above is applicable to all mixed phase rhombohedral and cubic samples, where the rhombohedral phase is the major phase. The R-factors, for the 10Nd12.5YSB sample are as follows, R_{exp} = 2.94%, R_{wp} = 7.95%. For the 10Nd12.5YSB sample, the GOF = 2.706. There is a peak intensity mismatch observed in the difference diffractogram, we also notice that there is slight peak asymmetry, which is as a result of the mixture of phases being observed, the secondary cubic phase results in peak asymmetry.

5.1.4 Rhombohedral and monoclinic sample Rietveld refinement:

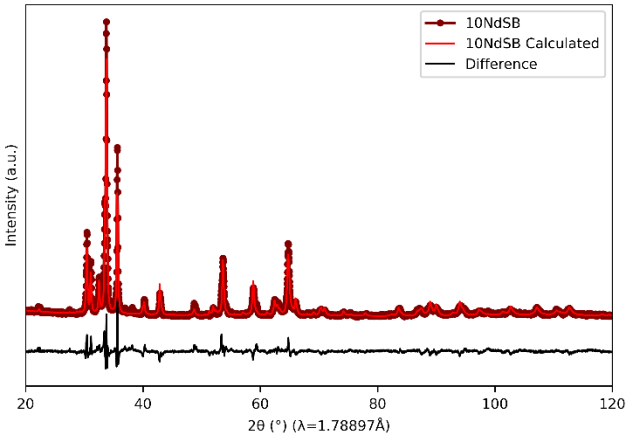


Figure 5.1.26: Rietveld refinement obtained for $10NdSB$ sample.

Figure 5.1.26 shows the XRD Rietveld refinement pattern obtained for the 10NdSB sample, using the laboratory X-ray diffractometer. The Rietveld refinement plot as shown above is applicable to all mixed phase rhombohedral and monoclinic samples, where the rhombohedral phase is the major phase. The R-factors, for the 10NdSB sample are as follows, R_{exp} = 3.50%, R_{wp} = 9.79%. For the 10NdSB sample, the GOF = 2.800. The sample difference diffractogram indicates peak intensity mismatches, as well as some peak asymmetry. This is as a result of the secondary monoclinic phase being present.

5.1.5 Rhombohedral, tetragonal, and cubic sample Rietveld refinement:

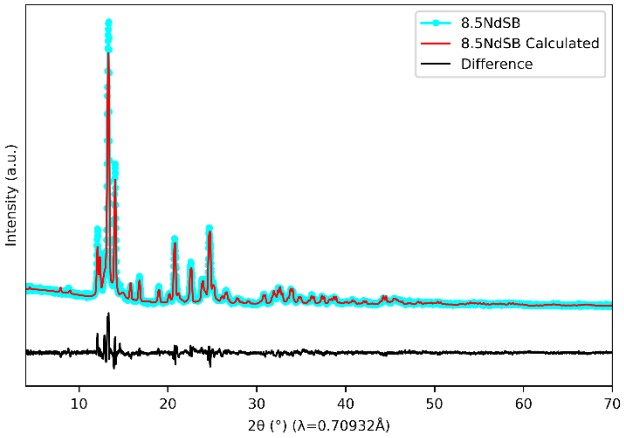


Figure 5.1.27: Rietveld refinement obtained for $8.5NdSB$ sample.

The above figure, figure 5.1.27 shows the XRD Rietveld refinement pattern obtained for the 8.5NdSB sample, using the laboratory X-ray diffractometer. The Rietveld refinement plot as shown above is applicable to all mixed phase rhombohedral, tetragonal and cubic samples, where the rhombohedral phase is the major phase. The R-factors, for the 8.5NdSB sample are as follows, R_{exp} = 5.28%, R_{wp} = 10.7%. For the 8.5NdSB sample, the GOF = 2.024. The difference diffractogram shows peak intensity mismatches, as well as peak asymmetry and some peak broadening as a result of some overlapping peaks due to the multiple phases present in the sample. The peak broadening effects observed are as a result of microstructural changes which result due to the imperfections in crystal structure caused as a consequence of the multiple phases observed.

5.1.6 Rhombohedral, monoclinic, and tetragonal sample Rietveld refinement:

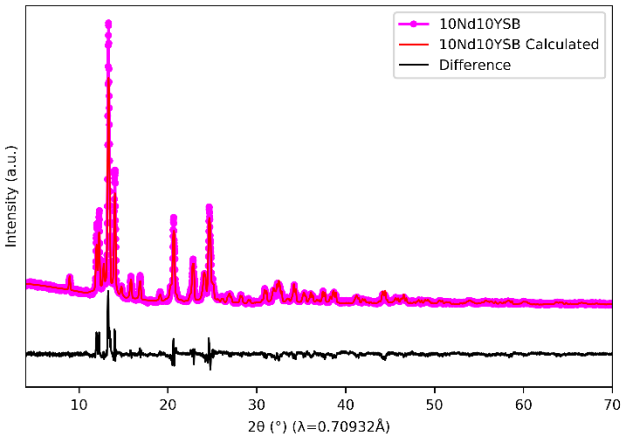


Figure 5.1.28: Rietveld refinement obtained for $10Nd10YSB$ sample.

Figure 5.1.28 shows the XRD Rietveld refinement pattern obtained for the 10Nd10YSBsample, using the laboratory X-ray diffractometer. The Rietveld refinement plot as shown above is applicable to all mixed phase rhombohedral and monoclinic, and tetragonal samples, where the rhombohedral phase is the major phase. The R-factors, for the 10Nd10YSB sample are as follows, R_{exp} = 5.77%, R_{wp} = 8.18%. For the 10Nd10YSB sample, the GOF = 1.416. The difference diffractogram shows peak intensity mismatches, as well as peak asymmetry caused due to the multiple phases present in the sample.

Table 2: Sample phase presence and percentage after Rietveld refinement

Sample #	**Shorthand sample composition**	**Shorthand sample composition**	**Sample**	**Sample composition (mol % atoms)**	**Phases Present**		
					Major phase (%)	Minor phase1 (%)	Minor phase 2 (%)
1	Nd0.10Y0.10-Bi_2O_3	Nd0.10Y0.10-Bi2O3	10Nd10YSB_Ann_(1)	Bi:32.0,Nd:4.0,Y:4.0,O:60.0	Rhombohedral (100%)	-	-

2	Nd0.15Y0.05-Bi_2O_3	Nd0.15Y0.05-Bi2O3	15Nd5YSB_Ann_(3)	Bi:32.0,Nd:6.0,Y:2.0,O:60.0	Rhombohedral (100%)	-	-
3	Nd0.10-Bi_2O_3	Nd0.10-Bi2O3	10NdSB_Ann_(4)	Bi:36.0,Nd:4.0.0,O:60.0	Rhombohedral (71.36%)	Monoclinic (28.64 %)	-
4	Y0.10-Bi_2O_3	Y0.10-Bi2O3	10YSB_Ann_(5)	Bi:36.0,Y:4.0,O:60.0	Cubic (100%)	-	-
5	Nd0.05Y0.15-Bi_2O_3	Nd0.05Y0.15-Bi2O3	5Nd15YSB_Ann_(6)	Bi:32.0,Nd:2.0,Y:6.0,O:60.0	Rhombohedral (75.69%)	Monoclinic (16.76 %)	Cubic (7.54%)
6	Nd0.05Y0.05-Bi_2O_3	Nd0.05Y0.05-Bi2O3	5Nd5YSB_Ann_(7)	Bi:36.0,Nd:2.0,Y:2.0,O:60.0	Rhombohedral (80.57%)	Monoclinic (19.43 %)	-
7	Nd0.085-Bi_2O_3	Nd0.085-Bi2O3	8.5NdSB_Ann_(8)	Bi:36.6,Nd:3.4,O:60.0	Rhombohedral (69.68%)	Tetragonal (15.81 %)	Cubic (14.51%)
8	Nd0.10Y0.10-Bi_2O_3	Nd0.10Y0.10-Bi2O3	10Nd10YSB_Ann_(9)	Bi:32.0,Nd:4.0,Y:4.0,O:60.0	Rhombohedral (54.40%)	Monoclinic (40.97 %)	Tetragonal (4.62%)
9	Nd0.15Y0.05-Bi_2O_3	Nd0.15Y0.05-Bi2O3	15Nd5YSB_Ann_(10)	Bi:32.0,Nd:6.0,Y:4.0,O:60.0	Rhombohedral (100%)	-	-
10	Nd0.125Y0.10-Bi_2O_3	Nd0.125Y0.10-Bi2O3	12.5Nd10YSB_Ann_(11)	Bi:31.0,Nd:5.0,Y:4.0,O:60.0	Rhombohedral (100%)	-	-

11	Nd0.10Y0.125-Bi_2O_3	Nd0.10Y0.125-Bi2O3	10Nd12.5YSB_Ann_(12)	Bi:31.0,Nd:4.0,Y:5.0,O:60.0	Rhombohedral (91.43%)	Cubic (8.57%)	-
12	Nd0.175Y0.05-Bi_2O_3	Nd0.175Y0.05-Bi2O3	17.5Nd5YSB_Ann_(16)	Bi:31.0,Nd:7.0,Y:2.0,O:60	Rhombohedral (100%)	-	-
13	Nd0.15Y0.075-Bi_2O_3	Nd0.15Y0.075-Bi2O3	15Nd7.5YSB_Ann_(17)	Bi:31.0,Nd:6.0,Y:3.0,O:60.0	Rhombohedral (100%)	-	-
14	Nd0.10Y0.075-Bi_2O_3	Nd0.10Y0.075-Bi2O3	10Nd7.5YSB_Ann_(18)	Bi:33.0,Nd:4.0,Y:3.0,O:60.0	Rhombohedral (100%)	-	-
15	Nd0.15Y0.05-Bi_2O_3	Nd0.15Y0.05-Bi2O3	15Nd5YSB_Ann_(19)	Bi:32.0,Nd:6.0,Y:4.0,O:60.0	Rhombohedral (100%)	-	-
16	Nd0.15Y0.05Tb0.025-Bi_2O_3	Nd0.15Y0.05Tb0.025-Bi2O3	15Nd5Y2.5TbSB_Ann_(20)	Bi:31.0,Nd:6.0,Y:2.0,Tb:1.0,O:60.0	Rhombohedral (100%)	-	-
17	Nd0.15Y0.05Sm0.025-Bi_2O_3	Nd0.15Y0.05Sm0.025-Bi2O3	15Nd5Y2.5SmSB_Ann_(21)	Bi:31.0,Nd:6.0,Y:2.0,Sm:1.0,O:60.0	Rhombohedral (100%)	-	-
18	Nd0.15Y0.05Sc0.025-Bi_2O_3	Nd0.15Y0.05Sc0.025-Bi2O3	15Nd5Y2.5Sc_Ann_(22)	Bi:31.0,Nd:6.0,Y:2.0,Sc:1.0,O:60.0	Rhombohedral (97.37%)	Cubic (2.63%)	-
19	Nd0.15Y0.05-Bi_2O_3	Nd0.15Y0.05-Bi2O3	15Nd5YSB_Ann_(23)	Bi:32.0,Nd:6.0,Y:4.0,O60.0	Rhombohedral (100%)	-	-

For each Rietveld refinement, a rhombohedral phase structure file is used, namely, the starting model for Bismuth lanthanum oxide (0.78/0.23/1.5) (ICSD 50637)(M. Drache et al., 1999).

This structure file is based on the space group *R-3m*. The cation sites which are occupied are the 3a (0, 0, 0) and 6c (0, 0, z) sites, followed by the three oxygen sites which all occupy the 6c (0, 0, z) site. The site occupancy, position, scale factor and temperature factors were all refined for both the cation and anion sites, to result in the measured and calculated profiles having a good statistical fit.

Table 3: The input values which were used as a starting model for the Rietveld refinement analysis of all samples (where the fractional occupancy is dependent on the dopant mol % - using the 15Nd5YSB as an example)

Atom	Site symmetry	x	y	z	Fractional occupancy	Thermal parameter
Bi1	3a	0	0	0	0.80	1
Nd1	3a	0	0	0	0.15	1
Y1	3a	0	0	0	0.05	1
Bi2	6c	0	0	0.2252	0.80	1
Nd2	6c	0	0	0.2252	0.15	1
Y2	6c	0	0	0.2252	0.05	1
O1	6c	0	0	0.299	1	3.3
O2	6c	0	0	0.091	0.78	1.8
O3	6c	0	0	0.446	0.47	1.8

Prior to any sample refinements, the determination of the instrument resolution function (IRF) (Dinnebier et al., 2018) was done using the NIST 660a (LaB_6) standard, and the calibration for all instrumentation was done using the IRF as defined by the Thompson Cox Hastings (TCHZ) Psuedo-Voight function (Thompson et al., 1987).

The Rietveld refinement analysis process for all samples was done by using a whole profile fitting, through the use of DIFFRAC.TOPAS suite. The background matching for each XRD profile was done by using a polynomial function of degree eight, crystallite size and strain broadening for each experimental profile were carried out using the Pseudo-Voight (pV) (TCHZ) function and allowed for them to be carried out individually. The statistical parameters

employed to observe the minimization are namely the expected error (R_{exp}) as well as the weighted residual error (R_{wp}).

Table 4: The refined structural parameters for all samples at room temperature using the rhombohedral structural model of space group *R-3m*. R_{exp} is defined as the minimum achievable pattern residual, whereas R_{wp} is defined as the weighted pattern residual

Sample	Laboratory data refinements					Synchrotron data refinements				
	a (Å)	c (Å)	R_{exp} (%)	R_{wp} (%)	GoF	a (Å)	c (Å)	R_{exp} (%)	R_{wp} (%)	GoF
Nd0.10Y0.10-Bi_2O_3	3.9707	27.3623	3.33	5.62	1.686	-	-	-	-	-
Nd0.15Y0.05-Bi_2O_3	3.9645	27.3415	3.48	5.57	1.598	-	-	-	-	-
Nd0.10-Bi_2O_3	3.9690	27.9611	3.50	9.79	2.800	-	-	-	-	-
Y0.10-Bi_2O_3	5.524	-	7.02	13.9	4.371	-	-	-	-	-
Nd0.05Y0.15-Bi_2O_3	3.9647	27.3882	2.86	7.37	2.581	-	-	-	-	-
Nd0.05Y0.05-Bi_2O_3	3.9610	27.8492	3.12	7.80	2.499	-	-	-	-	-
Nd0.085-Bi_2O_3	3.9617	27.9436	5.28	10.7	2.024	-	-	-	-	-
Nd0.10Y0.10-Bi_2O_3	3.9619	27.3119	5.77	8.18	1.416	-	-	-	-	-
Nd0.15Y0.05-Bi_2O_3	3.9792	27.4383	5.17	8.54	1.651	3.9589	27.2948	4.54	11.8	2.606
Nd0.125Y0.10-Bi_2O_3	3.9680	27.3351	4.88	7.97	1.633	3.9501	27.2070	4.65	11.1	2.385
Nd0.10Y0.125-Bi_2O_3	3.9662	27.3228	2.94	7.95	2.706	-	-	-	-	-

Nd0.175Y0.05-Bi_2O_3	3.9823	27.4120	2.75	9.05	3.286	-	-	-	-	-
Nd0.15Y0.075-Bi_2O_3	-	-	-	-	-	-	-	-	-	-
Nd0.10Y0.075-Bi_2O_3	-	-	-	-	-	-	-	-	-	-
Nd0.15Y0.05-Bi_2O_3	3.9837	27.4609	2.86	7.82	2.735	-	-	-	-	-
Nd0.15Y0.05Tb0.025-Bi_2O_3	3.9772	27.3861	2.86	8.93	3.126	-	-	-	-	-
Nd0.15Y0.05Sm0.025-Bi_2O_3	3.9839	27.4220	2.75	11.3	4.088	-	-	-	-	-
Nd0.15Y0.05Sc0.025-Bi_2O_3	3.9841	27.4489	2.84	6.90	2.431	-	-	-	-	-
Nd0.15Y0.05-Bi_2O_3	3.9870	27.3910	2.91	8.20	2.235	-	-	-	-	-

Synchrotron x-ray experimental data (BNL):

A total of 10 samples were sent for X-ray diffraction (XRD) characterisation at the National Synchrotron Light Source II (NSLS-II) beamline 28-ID at Brookhaven National Laboratory (BNL). The powder XRD characterisation was done at beamline 28-ID-II (far-field), and the X-ray pair distribution function (xPDF) characterisation was done at beamline 28-ID-II (near-field). Due to a limited number of samples allowed to be analysed for techniques such as Raman spectroscopy as electrochemical impedance spectroscopy (EIS) as a result of instrumentation availability and access, only two samples were fully characterised and interpreted from all the data obtained from the synchrotron, the samples are namely, 15Nd5YSB and 12.5Nd10YSB.

X-ray diffraction:

5.3.1 15Nd5YSB:

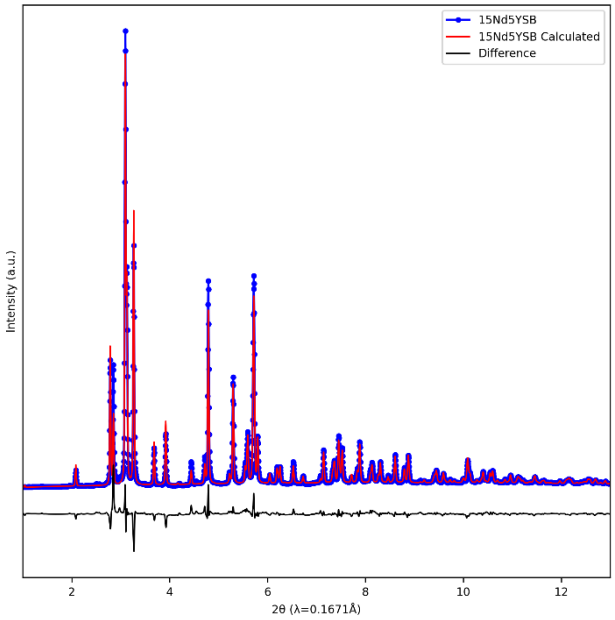


Figure 5.1.29: The Rietveld refinement of the 15Nd5YSB sample obtained from the BNL synchrotron beamline 28-ID-II

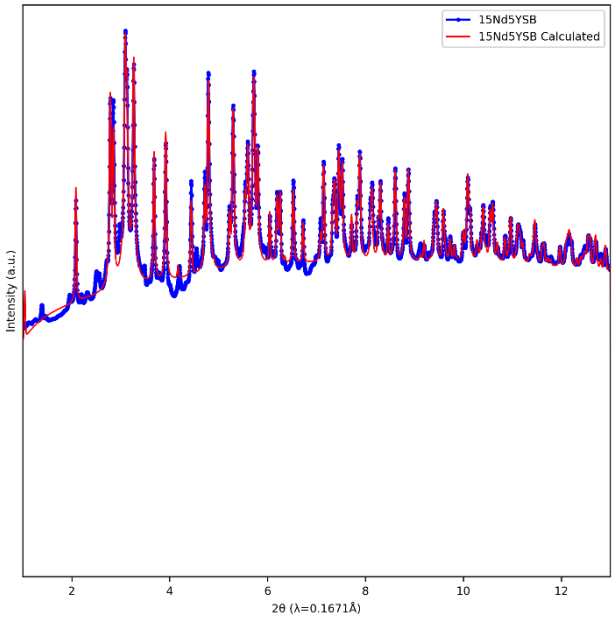


Figure 5.1.30: The Rietveld refinement of the 15Nd5YSB sample obtained from the BNL synchrotron beamline 28-ID-I with the y axis in lny

The above figures, figures 5.1.29,and 5.1.30 shows the XRD pattern obtained for a double doped sample using the synchrotron X-ray diffractometer. The diffractogram obtained in 5.1.92 for the 15Nd5YSB sample existed as pure rhombohedral phase sample, this is in agreement with the laboratory diffraction pattern measured on the D9 advance (see supplementary information), and thus indicates that the rhombohedral phase of Bi_2O_3 was stabilised at the ambient temperature conditions for the 20 mol % total dopant concentration.

The Rietveld refinement data indicates slight peak intensity mismatches being observed, this could be as a result of the calculated diffraction pattern underestimating as well as possibly overestimating peak intensities. No peak asymmetry is observed in any of the peaks, this is confirmed when looking at the lny diffractogram, thus no secondary phase is present, and no microstructural defects are observed. The lny offset on the y-axis (intensity axis) shows a clearer view of the peaks in the diffractogram, as the ln y plot highlights peaks which are not usually visible under normal y (intensity), and thus reveals peaks which are not identified for.

5.3.2 12.5Nd10Y-Bi_2O_3:

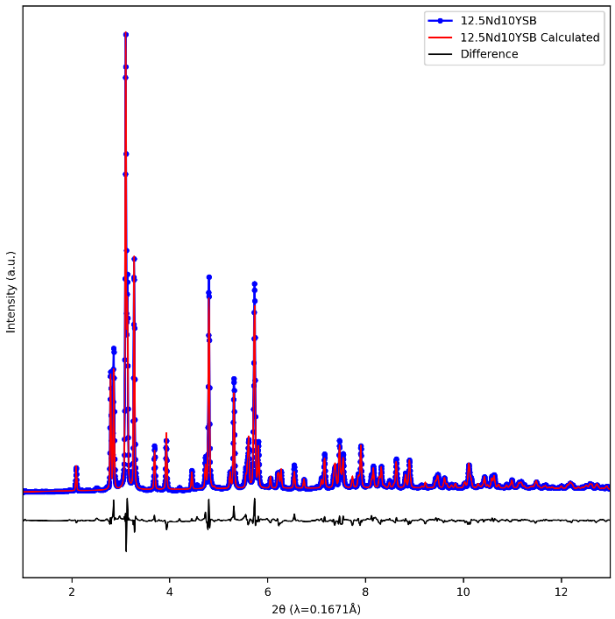


Figure 5.1.30: The Rietveld refinement of the 12.5Nd10YSB sample obtained from the BNL synchrotron beamline 28-ID-IIFigures 5.1.32, and 5.1.343is representative of the XRD pattern obtained for a double doped sample using the synchrotron X-ray diffractometer. The diffractogram obtained in 5.1.93for the 12.5Nd10YSB sample existed as pure rhombohedral phase sample, this is in agreement with the laboratory diffraction pattern measured on the D9 advance (see supplementary information), and thus indicates that the rhombohedral phase of Bi_2O_3 was stabilised at the ambient temperature conditions for the 22.5 mol % total dopant concentration.

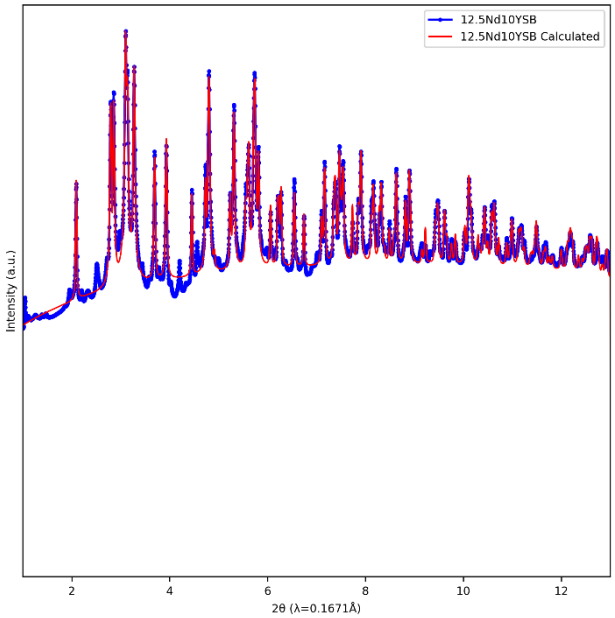


Figure 5.1.33: The Rietveld refinement of the 12.5Nd10YSB sample obtained from the BNL synchrotron beamline 28-ID-II with the y axis in lny

Slight peak intensity mismatches are also observed in the Rietveld refinement and could be as a result of the calculated diffraction pattern underestimating as well as possibly overestimating peak intensities. Peak asymmetry is not observed in any of the peaks, this is confirmed when looking at the lny diffractogram, thus no secondary phase is present, and no microstructural defects are observed. The lny offset on the y-axis (intensity axis) shows a clearer view of the peaks in the diffractogram, as the ln y plot highlights peaks which are not usually visible under normal y (intensity), and thus reveals peaks which are not identified for.

xPDF:

The xPDF done on the two samples used the same Rietveld refinement rhombohedral phase structure file as the starting structure model. The refinement was done using the Philip Chater method, as compared to the John Evans method of xPDF refinements. The difference being that the Philip Chater method uses dQ convergence and thus allows the refinement to continue after convergence to obtain the best fit even after stop criteria is met.

5.4.1 15Nd5YSB:

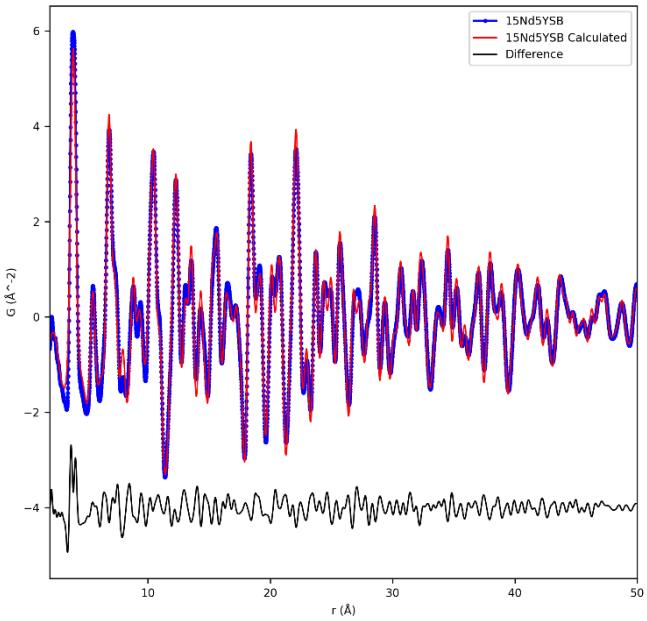


Figure 5.1.31: The xPDF refinement of the 15Nd5YSB sample obtained from the BNL synchrotron beamline 28-ID-II

5.4.2 12.5Nd10YSB

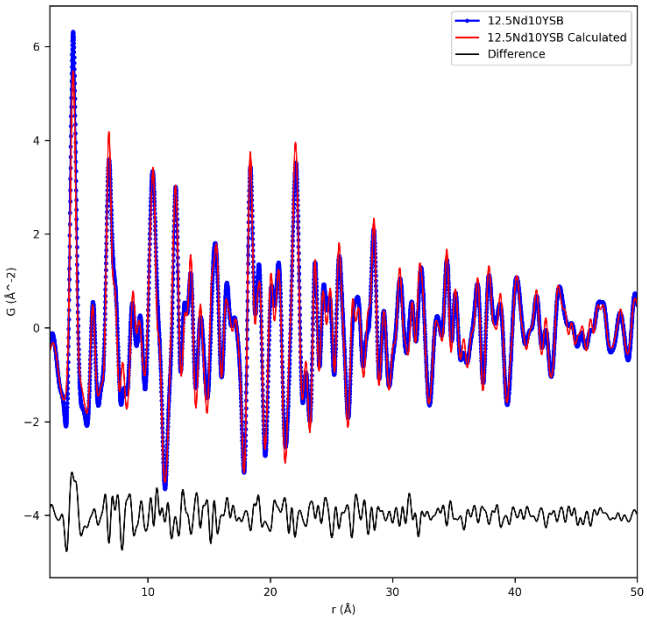


Figure 5.1.32: The xPDF refinement of the 12.5Nd10YSB sample obtained from the BNL synchrotron beamline 28-ID-II

Figures 5.1.35, and 5.1.36 correspond to the xPDF patterns obtained for a double doped sample using the synchrotron X-ray diffractometer. The data used for the PDF refinement was obtained at room temperature. When fitting the experimental G(r) data across the G(r) range of 0-50 Å, it can be observed that the average structure model fits very well with no substantive difference between the average and local structure models. This observation indicated that the average and the local structure are the same. This is seen when looking at the refinement in two segments, namely, the segment in the $8 \leq r \leq 50$ Å range (the range which corresponds to the average structure), and the $0 \leq r \leq 8$ Å range (the range which corresponds to the local structure). The average structure model best interprets the peak intensity, peak shape, and peak position of the experimental data G(r) peaks within the $8 \leq r \leq 50$ Å range, where the fit quality is much better as compared to the fit quality observed in the $0 \leq r \leq 8$ Å range. A possible explanation for this decrease in the fit quality, and hence mismatch of peak intensity, peak shape, and peak position, is due to a distortion being observed in the local structure, hence a local disorder within the $0 \leq r \leq 8$ Å range.

The 15Nd5YSB sample refined for in figure 5.1.35, obtained a R_{wp} of 17.039 across the entire r range. The 12.5Nd10YSB sample refined for in figure 5.1.36, obtained a R_{wp} of 18.218 across the entire r range. Both refinements show a deviation when it comes to the fit quality observed within the $0 \leq r \leq 8$ Å range

Chapter 6:

Simultaneous Thermal Analysis (STA)

Differential Thermal Analysis (DTA) & Thermogravimetric Analysis (TGA):

The samples were analysed using a PerkinElmer STA 6000, all the samples investigated were analysed at a heating and cooling rate of 10 ℃/min over the temperature range of 30 ℃ to 800 ℃. The results obtained for the simultaneous thermal analysis (STA) of the samples using differential thermal analysis (DTA) and thermogravimetric analysis (TGA) are presented in the figures below.

DTA:

6.1.1 12.5Nd10YSB:

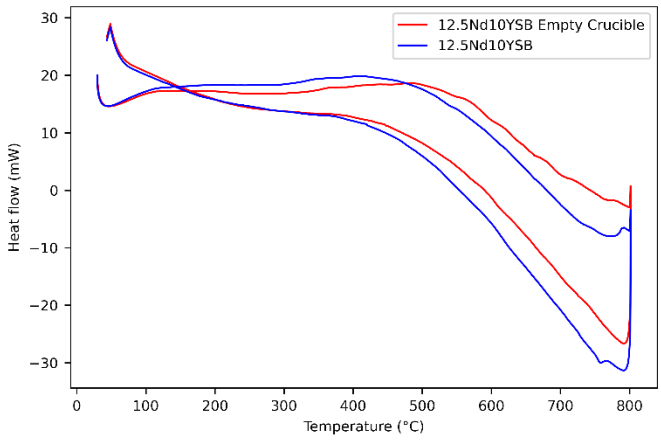


Figure 6.1.33: The DTA scan obtained for 12.5Nd10YSB for the empty crucible and sample over the 30-800 ℃ temperature range.

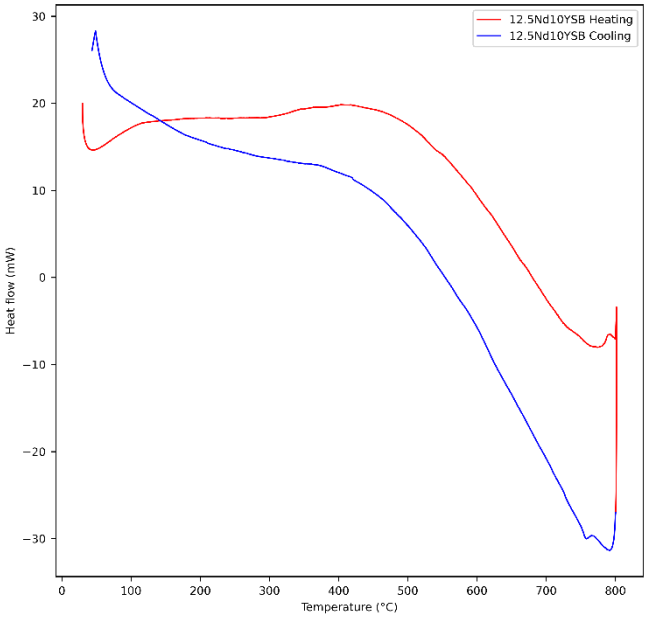


Figure 6.1.34: The DTA scan obtained for 12.5Nd10YSB over the 30-800 ℃ temperature range showing the heating and cooling curves.

6.1.2 15Nd5YSB:

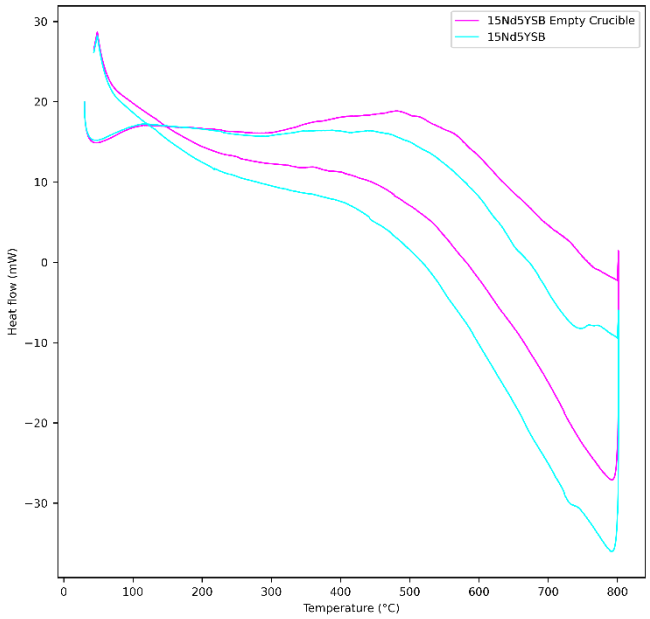


Figure 6.1.35: The DTA scan obtained for 15Nd5YSB for the empty crucible and sample over the 30-800 ℃ temperature range.

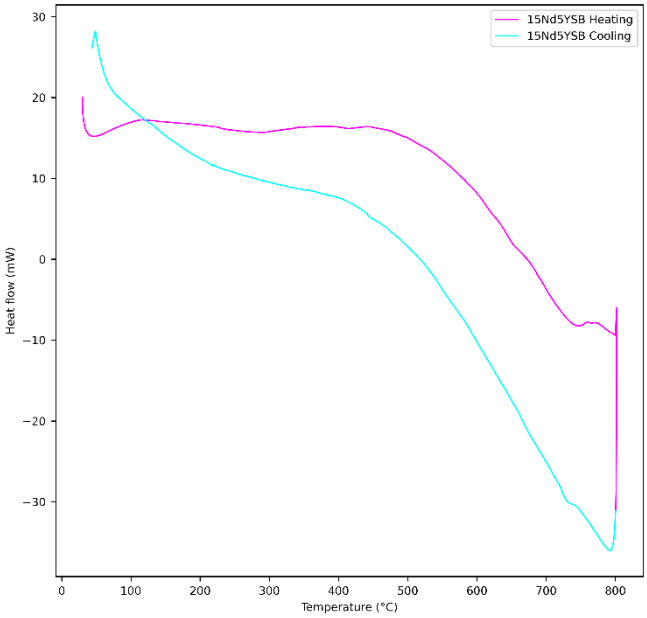


Figure 6.1.36: The DTA scan obtained for 15Nd5YSB over the 30-800 ℃ temperature range showing the heating and cooling curves.

6.1.3 15Nd5Y2.5TbSB:

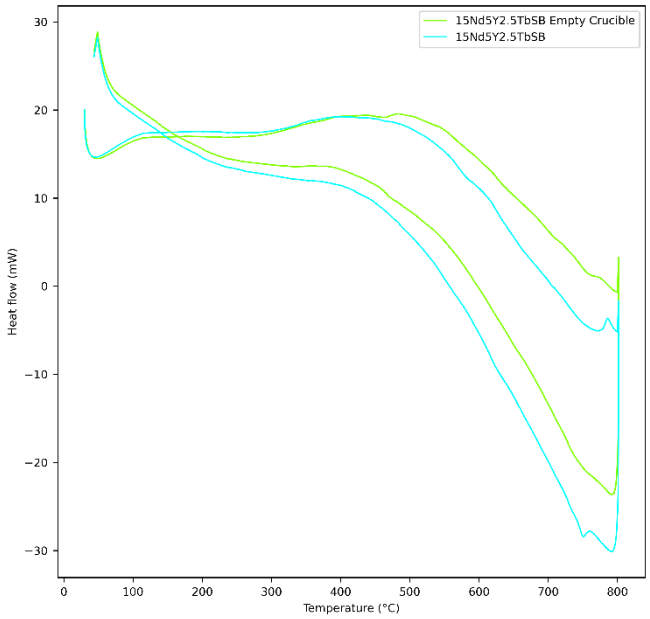


Figure 6.1.37: The DTA scan obtained for 15Nd5Y2.5TbSB for the empty crucible and sample over the 30-800 ℃ temperature range.

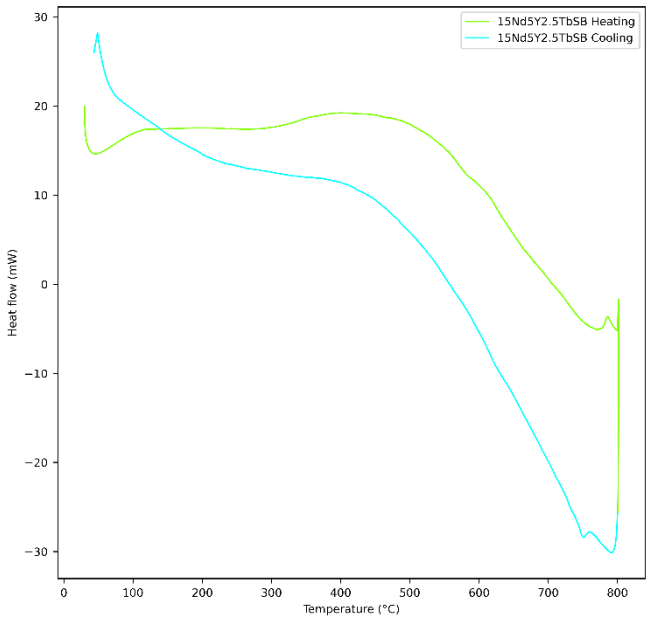


Figure 6.1.38: The DTA scan obtained for 15Nd5Y2.5TbSB over the 30-800 ℃ temperature range showing the heating and cooling curves.

6.1.4 15Nd5YSmSB:

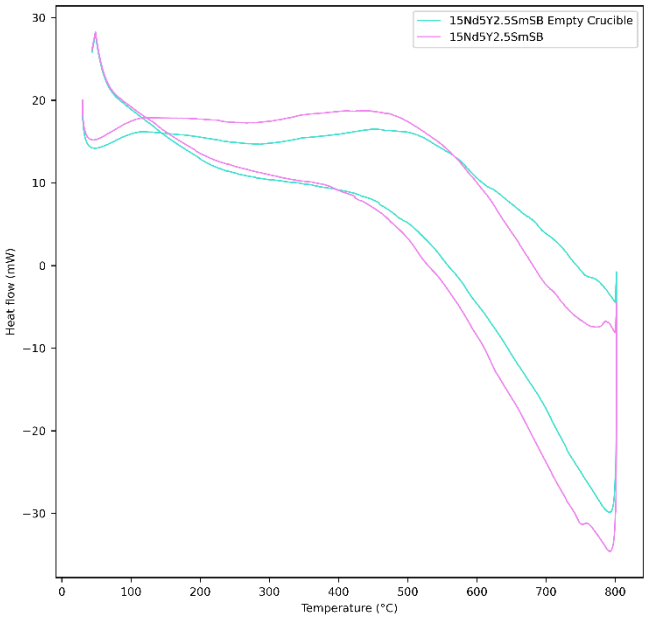


Figure 6.1.39: The DTA scan obtained for 15Nd5Y2.5SmSB for the empty crucible and sample over the 30-800 ℃ temperature range.

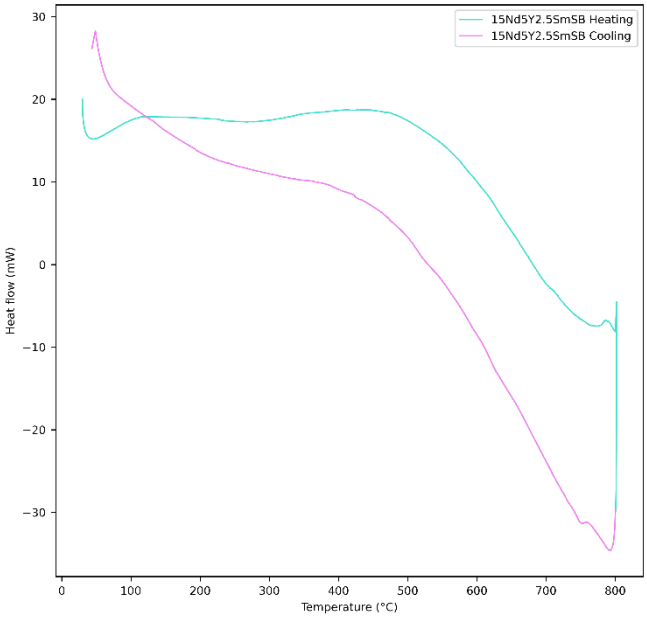


Figure 6.1.40: The DTA scan obtained for 15Nd5Y2.5SmSB over the 30-800 ℃ temperature range showing the heating and cooling curves.

6.1.5 15Nd5Y2.5ScSB:

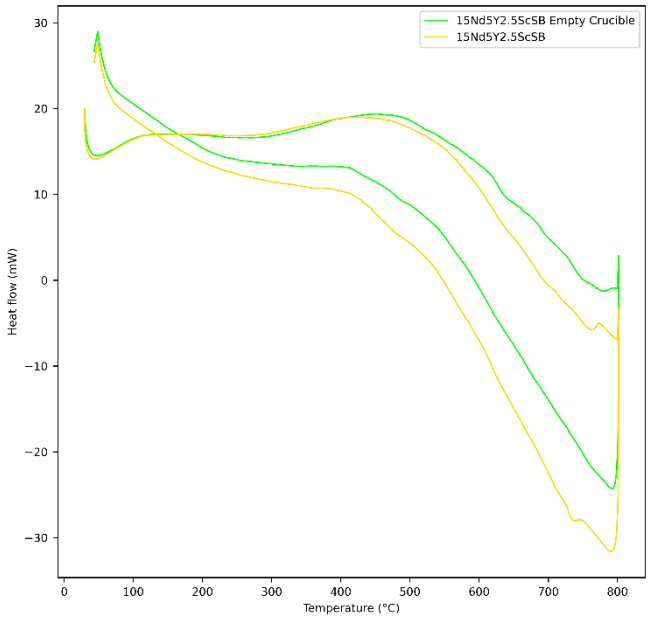


Figure 6.1.41: The DTA scan obtained for 15Nd5Y2.5ScSB for the empty crucible and sample over the 30-800 ℃ temperature range.

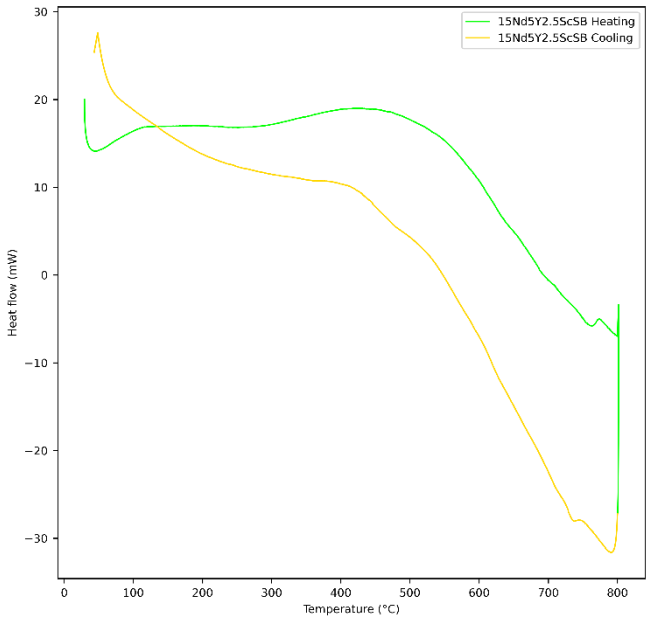


Figure 6.1.42: The DTA scan obtained for 15Nd5Y2.5ScSB over the 30-800 ℃ temperature range showing the heating and cooling curves.

The differential thermal analysis (DTA) scans obtained for 12.5Nd10YSB, 15Nd5YSB$_3$, 15Nd5Y2.5TbSB, 15Nd5Y2.5SmSB, as well as 15Nd5Y2.5ScSB, all indicate thermal stability through the temperature range of 30-800 ℃ for both the hearing and cooling curves. However, with the temperature range of 720-750 ℃ for all the samples, we notice that there is an endothermic maximum that is reached in both the heating and cooling curves, this peak could correspond to a possible phase transition which occurs.

However, this event is short lived as in the cooling curves, it can be observed that the endothermic maximum, becomes an exothermic minimum. This could either be due to an order-disorder transition occurring, or the possible short lived phase transition from the rhombohedral to cubic δ-phase, and back to the rhombohedral phase.

TGA:

6.2.1 12.5Nd10YSB:

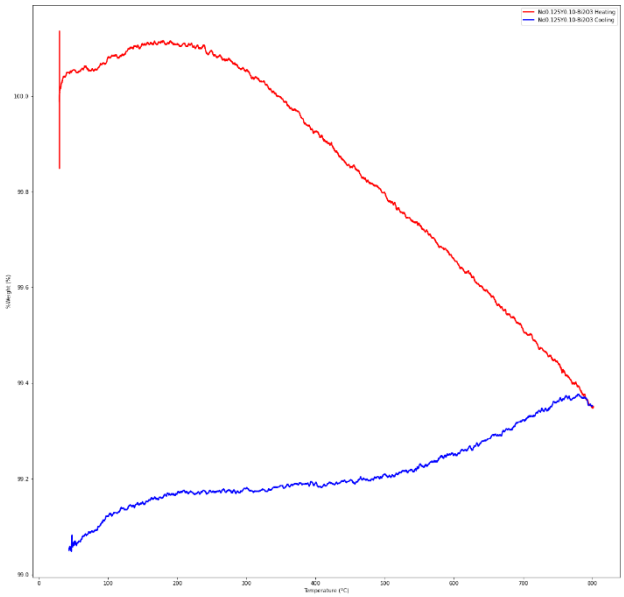


Figure 6.1.43: The TGA scan obtained for 12.5Nd10YSB over the 30-800 ℃ temperature range showing the heating and cooling curves.

6.2.2 15Nd5YSB:

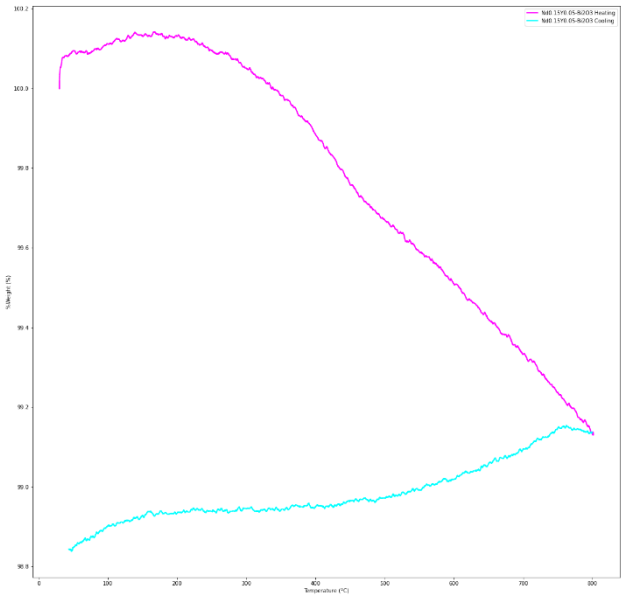


Figure 6.1.44: The TGA scan obtained for 15Nd5YSB over the 30-800 ℃ temperature range showing the heating and cooling curves.

6.2.3 15Nd5Y2.5TbSB:

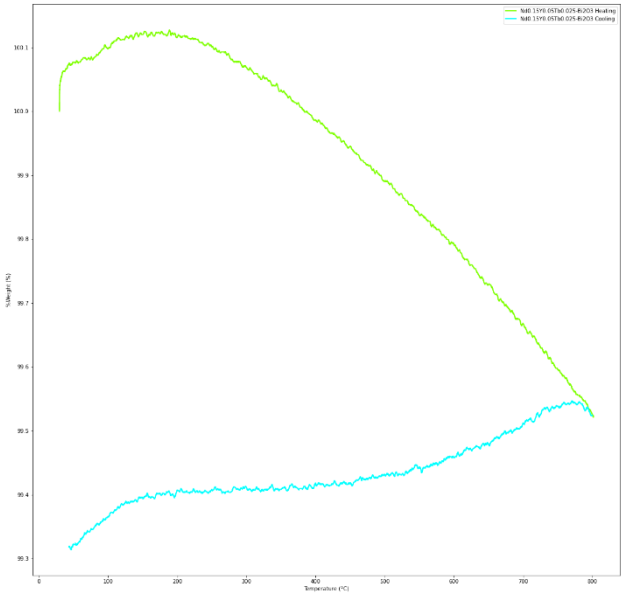


Figure 6.1.45: The TGA scan obtained for 15Nd5Y2.5TbSB over the 30-800 ℃ temperature range showing the heating and cooling curves.

6.2.4 15Nd5Y2.5SmSB:

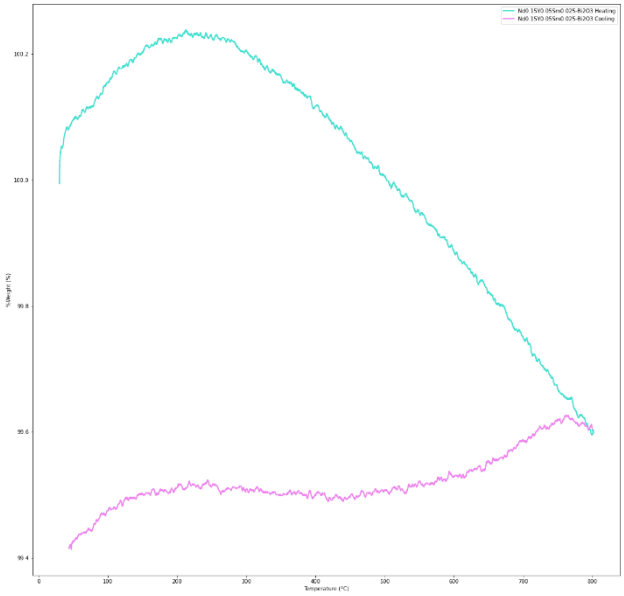


Figure 6.1.46: The TGA scan obtained for 15Nd5Y2.5SmSB over the 30-800 ℃ temperature range showing the heating and cooling curves.

6.2.5 15Nd5Y2.5ScSB:

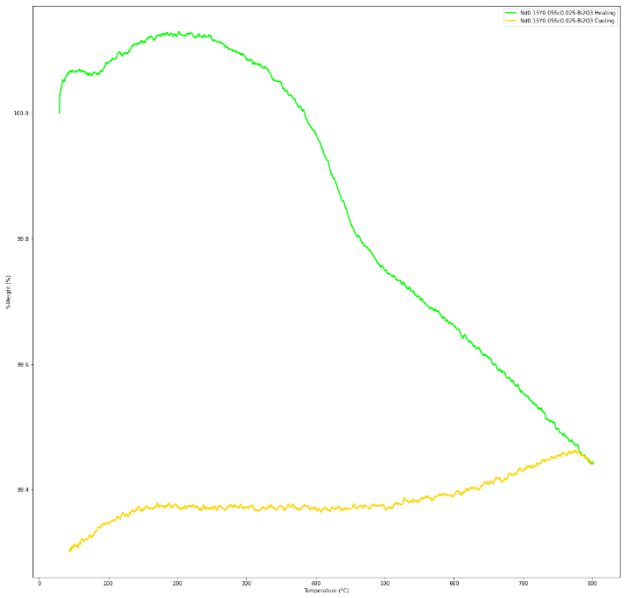


Figure 6.1.47: The TGA scan obtained for 15Nd5Y2.5ScSB over the 30-800 ℃ temperature range showing the heating and cooling curves.

The thermogravimetric analysis (TGA) scans obtained for 12.5Nd10YSB, 15Nd5YSB, 15Nd5Y2.5TbSB, 15Nd5Y2.5SmSB, as well as 15Nd5Y2.5ScSB, all indicate exceptional thermal stability through the temperature range of 30-800 ℃, with approximately less than 1.0% weight loss being observed upon heating of samples. Four samples observe weight loss throughout the temperature range, without any specific weight loss temperature intervals, however, when observations are done on the 15Nd5Y2.5ScSB sample TGA scan, it is seen that at ~250 ℃ weight loss at a specific temperature interval is observed, this weight loss occurs up to ~480 ℃, and continues up to 800 ℃. Upon the cooling of all samples, it can be observed that the total weight loss obtained is less than 0.4%.

Chapter 7

Raman Spectroscopy

LabRam HR:

Variable temperature Raman Spectroscopy:

Variable temperature Raman spectroscopy was used to analyse small sample sizes of approximately 50 mg which was placed on a glass slide. The results of thesample characterisation are presented below

7.1.1 12Nd10YSB:

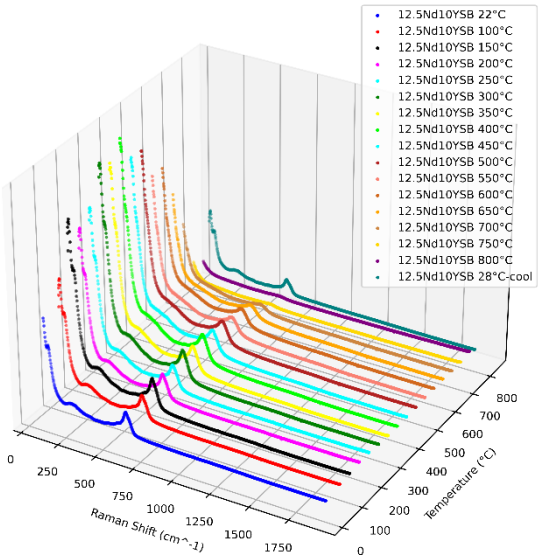


Figure 7.1.48: The stacked VT-Raman spectra plot for 12.5Nd10YSB showing the heating cycle in the temperature range 22-800 ℃ as well as the spectra after cooling at 28 ℃

7.1.2 15Nd5YSB:

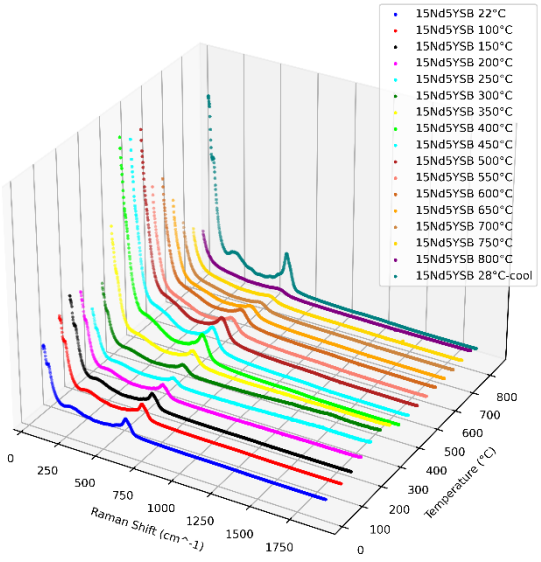


Figure 7.1.49: The stacked VT-Raman spectra plot for 15Nd5YSB showing the heating cycle in the temperature range 22-800 ℃ as well as the spectra after cooling at 28 ℃

7.1.3 15Nd5Y2.5TbSB:

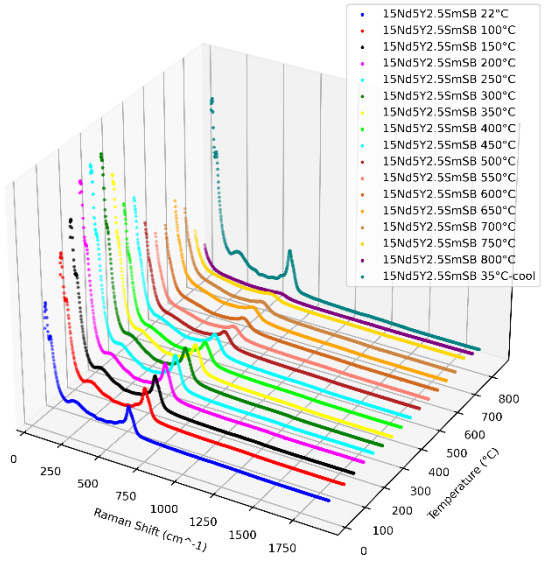


Figure 7.1.50: The stacked VT-Raman spectra plot for 15Nd5Y2.5TbSB showing the heating cycle in the temperature range 22-800 ℃ as well as the spectra after cooling at 35 ℃

7.1.4 15Nd5Y2.5SmSB:

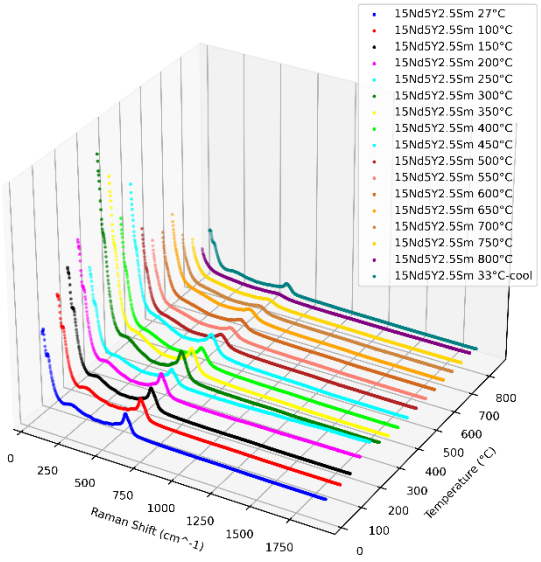


Figure 7.1.51: The stacked VT-Raman spectra plot for 15Nd5Y2.5SmSB showing the heating cycle in the temperature range 27-800 ℃ as well as the spectra after cooling at 33 ℃

7.1.5 15Nd5Y2.5ScSB:

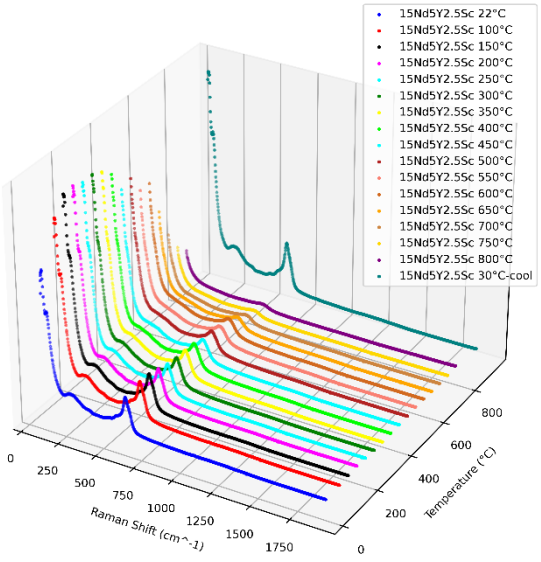


Figure 7.1.56: The stacked VT-Raman spectra plot for 15Nd5Y2.5ScSB showing the heating cycle in the temperature range 22-800 ℃ as well as the spectra after cooling at 30 ℃ (Spot 2)

The variable temperature Raman spectra obtained for 12.5Nd10YSB, 15Nd5YSB, 15Nd5Y2.5TbSB 15Nd5Y2.5SmSB, as well as 15Nd5Y2.5ScSB (spot 2) samples within the temperature range of 22-800 ℃ indicates two significant peaks and slight peaks of negligible intensity at the shoulder. A weak intensity peak is observed at ~250 cm^{-1}, as well as an intense peak at 620 cm^{-1}. There is also the presence of a very weak shoulder peak at ~110 cm^{-1}. Upon the increase in temperature, a decrease in peak intensity is observed, with the weak shoulder peak completely disappearing, with the weak peak at ~250 cm^{-1} and the major peak at 620 cm^{-1} also almost completely disappearing at 800 ℃. There is also peak broadening for all peaks, as well as a left shift. When the sample is cooled back to approximately room temperature, it is observed that the spectrum returns back to the initial spectra observed before heating occurred, with all the identified peaks present. The broad peak observed at 620 cm^{-1} is observed because of the number of oxygen vacancies within the sample, and thus corresponds to the oxygen vibrational modes (as a result of the oxygen vacancies). When further investigation was done on literature to identify the peak at ~250 cm^{-1}, no literature indicates a peak at that Raman shift, and thus the presence of this peak serves as confirmation

that the 12.5Nd10YSB sample is purely rhombohedral and the peak at ~250 cm^{-1} can be classified as the identifying peak for the rhombohedral phase Bi_2O_3.

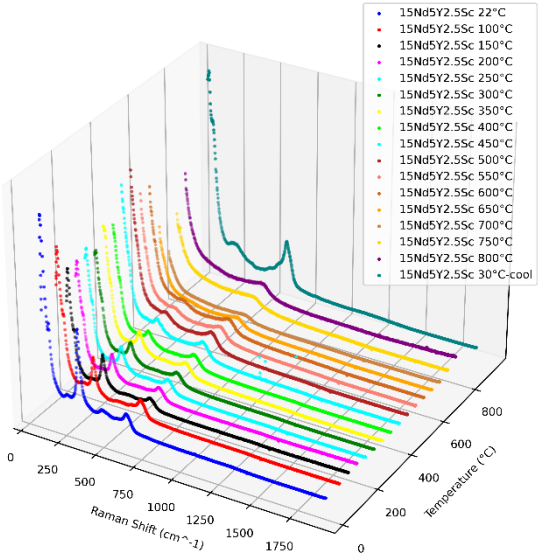


Figure 7.1.57: The stacked VT-Raman spectra plot for 15Nd5Y2.5ScSB showing the heating cycle in the temperature range 22-800 ℃ as well as the spectra after cooling at 30 ℃ (Spot 1)

The variable temperature Raman spectrum obtained for the 15Nd5Y2.5ScSB (spot 1) within the temperature range of 22-800 ℃ indicates two significant peaks and slight peaks of negligible intensity at the shoulder. As compared to the other samples, it can be observed that there is an intense peak at 620 cm^{-1}, a very weak shoulder peak at ~110 cm^{-1}, and there arises a new peak at ~310 cm^{-1}. Noting that from the XRD pattern obtained for this sample, there is approximately 2.63% of the cubic phase present in the sample. Upon the increase in temperature, we observe a decrease in the intensity of the new apparent peak at ~310 cm^{-1}, with the greatest peak intensity decreases being observe at the 100 ℃ temperature increase increments. This peak completely disappears from the spectrum at 700 ℃. Upon the cooling process, the peak does not reform, and we now observe the formation weak intensity peak observed at ~250 cm^{-1}, which corresponds to the spectral behaviour we observed in previous samples. The peak at ~310 cm^{-1} is characteristic of the metastable tetragonal β-phase of

Bi_2O_3. After the cooling back to room temperature, the Raman peak at $\sim$250 cm^{-1}, which can be concluded to be the Raman peak which is indicative of the rhombohedral Bi_2O_3 appears.

The DTA analysis indicates a slight endothermic peak in the temperature range of 720-750 ℃, which could possibly be due to a phase transition occurring, or an order-disorder transition. From the results obtained from the analysis of our Raman spectroscopy data, it is clear that no phase transition occurs in all sample, with the exception of the phenomena observed in the 15Nd5Y2.5ScSB and thus we can conclude that the changes observed in the spectra are as a result of an order-disorder transition occurring.

Chapter 8:

Electrochemical Impedance Spectroscopy (EIS)

The electrochemical impedance spectroscopy (EIS) characterisation was conducted at open circuit voltage, within the 200-500℃ temperature range in air atmosphere. As the temperature changed, slight changes were observed in the impedance spectra obtain, and hence variations in methodology were used to account for these changes.

Three samples were chosen for characterisation using EIS, however due to experimental instrumentation faults only two samples could be analysed, namely, the 12.5Nd10YSB, and 15Nd5Y2.5TbSB samples. The samples were chosen based on the information they could provide, namely the 15Nd5YSB sample was chosen as this was the sample which provided the phase pure rhombohedral bismuth oxide composition, however this sample was not analysed due the instrumentation error. The 12.5Nd10YSB and 15Nd5Y2.5Tb samples were selected as these provide information which builds up from the 15Nd5YSB parent sample and have comparable total dopant mol % compositions and provide information on how the triple doped system behaves as compared to the double doped system.

The EIS characterisation technique was used to investigate whether the rhombohedral phase Bi_2O_3 obtained from all the XRD analysis is stable over a temperature range. The temperature range for this variable temperature study was chosen due to the requirement for operation at intermediate temperature ranges, as well as the stability of rhombohedral phase Bi_2O_3 in the temperature range chosen, as reported by *Jolley, et al* (Jolley et al., 2019). The temperature intervals chosen was 50 ℃. The samples were pressed into pellets, sintered at 800 ℃ and subsequently coated with a 10 nm coat of pure gold on each side of the pellet, this coating was used for better contact between the pellet and the two solid platinum disk electrodes.

Laboratory experimental data:

Variable temperature EIS:

8.1.1 12.5Nd10YSB:

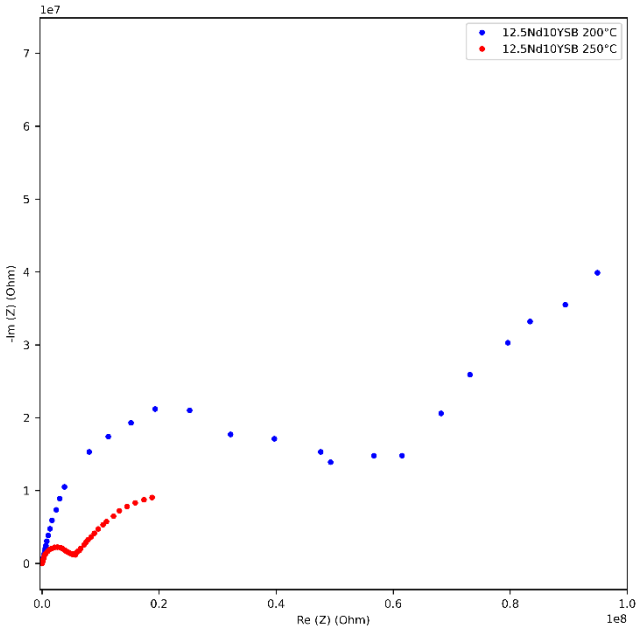


Figure 8.1.52: The VT-EIS spectra for 12.5Nd10YSB between 200-250 ℃

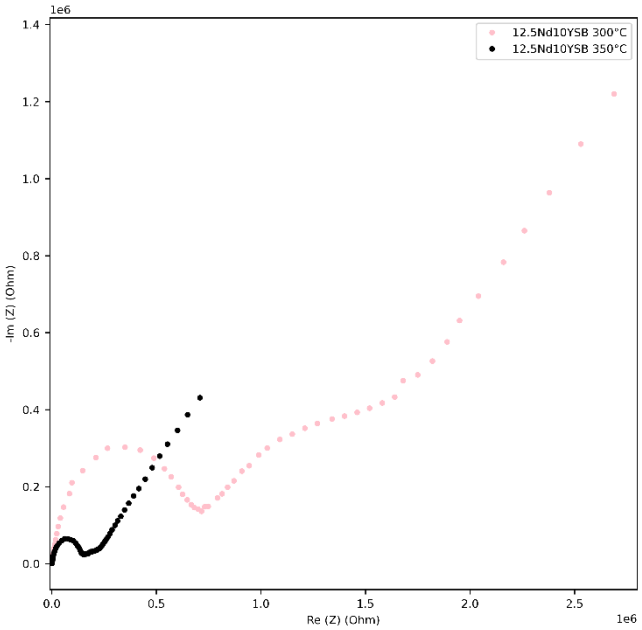


Figure 8.1.53: The VT-EIS spectra for 12.5Nd10YSB between 300-350 ℃.

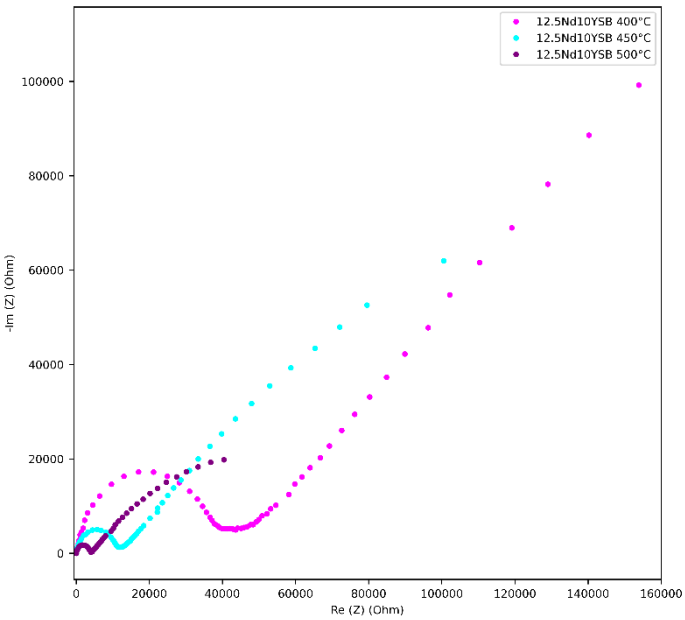


Figure 8.1.54: The VT-EIS spectra for 12.5Nd10YSB between 400-500 ℃.

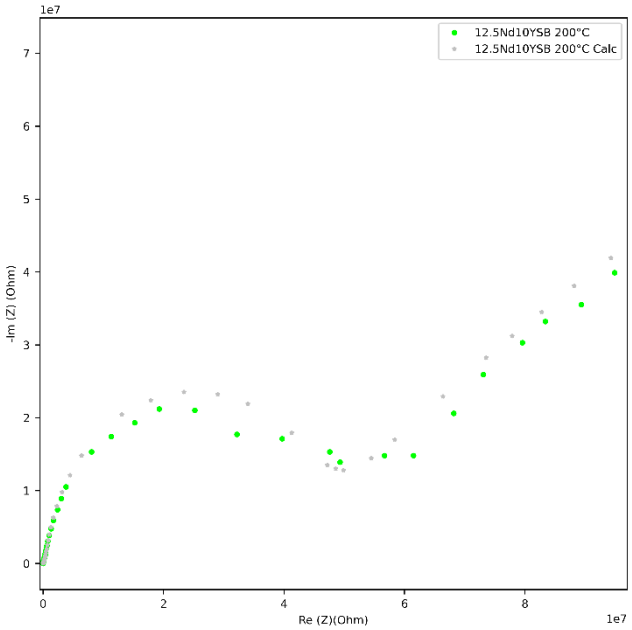


Figure 8.1.55: The VT-EIS spectra for 12.5Nd10YSB at 200 ℃ indicating the calculated spectra after fitting the data to a circuit model, where * indicates the calculated spectra.

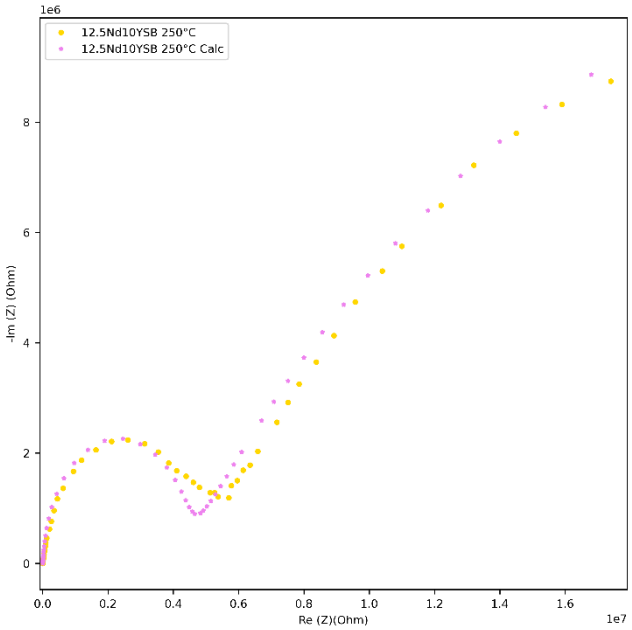


Figure 8.1.56: The VT-EIS spectra for 12.5Nd10YSB at 250 ℃ indicating the calculated spectra after fitting the data to a circuit model, where * indicates the calculated spectra.

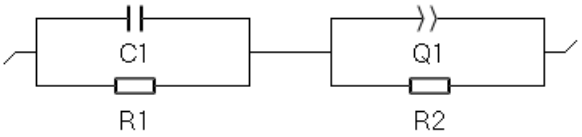


Figure 8.1.57: The circuit model used to fit the EIS data for 12.5Nd10YSB within the 200-250℃ temperature range.

The temperature range of 200-25 0℃ yields complex impedance spectra which consist of a semi-circle and a small ray arc, which is represented in figures 8.1.59 and 8.1.60. The equivalence circuit model used to describe the various phenomena such as polarisation and charge migration which occurs within the various frequency ranges is illustrated in figure 8.1.61. The circuit model uses "/" to describe circuit elements which are in parallel, and "+" to describe circuit elements which are in series. The equivalence circuit model can then be described as C1/R1+Q1/R2. The processes which occur in the bulk of the grains is modelled by the C1/R2 portion, followed by the conduction through the grain boundaries or the electrolyte/electrode interface polarization resistance (R_{el}) is modelled by the Q1/R2 portion.

The bulk resistance of the grain's (R_b) is represented by the lower frequency intercept of the semicircle which represents the grain(C1/R2) with the real axis (Z'). The electrolyte/electrode interfacial polarization resistance (R_{el}) or the grain boundaries resistance (R_{gb}), the total resistance then becomes the sum of the individual resistances, $R_t = R_b + R_{el}$ (or R_{gb}). All individual resistances, R_b, R_{el} and R_{gb} are inversely proportional to temperature, thus as the temperature increases, the resistances decrease, which indicates a negative temperature coefficient of resistance. The charge carriers thus observe a decrease in average potential barrier energies, and/or charge carrier mobility increases are observed.

Observing the Nyquist plot obtained, we observe a semi-circle which has the properties which are characteristically observed for electrolyte samples as a result of their polycrystallinity. When an ideal "perfect" semi-circle is obtained as a result, the Cx/Rx circuit (where x indicates the number of the component) is used to fit the semi-circle. When a non-ideal "depressed" semi-circle is obtained, a Q = constant phase element (CPE) is introduced to account for the

non-ideal behaviour of the semi-circle, and thus the Qx/Rx circuit is used to fit the non-ideal semi-circle.

The use of Q results in the calculation of what is defined as pseudo-capacitance (also referred to as equivalent capacitance) as compared to capacitance. The circuit fitting of Q/R follows an equation, which will be defined below, and is used to calculate the C (capacitance) value of the maximum imaginary component of the Nyquist plot, where C is at an angular frequency ($\omega_c = 2\pi f_c$). The equation is as follows:

$$\frac{1}{2\pi(RQ)^{1/a}} = \frac{1}{2\pi RC} \Longrightarrow C = Q^{1/a}R^{\left(\frac{1}{a}\right)-1}$$

Where the variables are as follows, Q = constant phase element, R = resistance, C = capacitance, *a* = frequency constant (being between 0-1, preferably > 0.5).

The EClab software by BioLogic was used to analyse the impedance plots obtained. The analysis tool in the software, which was used, is the ZFit tool. ZFit uses the Levenberg-Marquardt algorithm to fit the function representative of the equivalence circuit model to the data obtained by the exploitation of a nonlinear least squares regression. When fitting the experimental data to the function which represents the equivalent circuit model, based on the equivalence circuit model used, parameters are refined (changed) until the mathematical function of the circuit model matches that of the experimental data. The χ^2 (chi-squared) value is a statistical value used to indicate the goodness of fit observed between the experimental data and the mathematical function represented by the equivalent circuit model used for fitting. As the χ^2 value is a statistical value, the closer to 0 the value, the better the fit. The equation below is used to calculate the χ^2:

$$\chi^2 = \sum_{i=1}^{N} \left| \frac{Z_i(f_i) - Z(f_i)}{E} \right|^2$$

Where the variables are as follows, $Z_i(f_i)$ = measured impedance at f_i, $Z(f_i)$ = calculated impedance at f_i, in relation to a given set of parameter values, N = number of points. The χ^2 values can also be normalised to result in the value being independent of N, and this normalisation process is expressed as $\chi/\sqrt{N}$.

When observing the equivalence circuit model which is used to fit the EIS spectra (Nyquist plot) obtained for the analysis in the temperature range of 200-250 ℃, it can be observed that we have C1/R1 + Q1/R1.

For the Nyquist plot (EIS spectral data) observed for 200 ℃, when fitting the data to the equivalence circuit model, we obtain C1 = 23.23× 10^{-12} F, R1 = 41.23× 10^{6} Ω, Q1 = 7.579× 10^{-9} F.s^{a-1} , a1 = 0.5000, and R2 = 0.4029 × 10^{9} Ω. We also obtain χ^2 = 0.8093× 10^{15} and $\chi/\sqrt{N}$ = 3.642× 10^{6}. We observe a semi-circle followed by a tail.

The Nyquist plot (EIS spectral data) observed for 250 ℃ also has a semi-circle followed by a tail, when fitting the data to the equivalence circuit model, we obtain C1 = 20.35× 10^{-12} F, R1 = 4.245× 10^{6} Ω, Q1 = 31.27× 10^{-9} F.s^{a-1} , a1 = 0.5518, and R2 = 46.79× 10^{6} Ω. We also obtain χ^2 = 11.76× 10^{12} and $\chi/\sqrt{N}$ = 418911. When going from 200 ℃ to 250 ℃, we observe a drastic decrease in the χ^2 value.

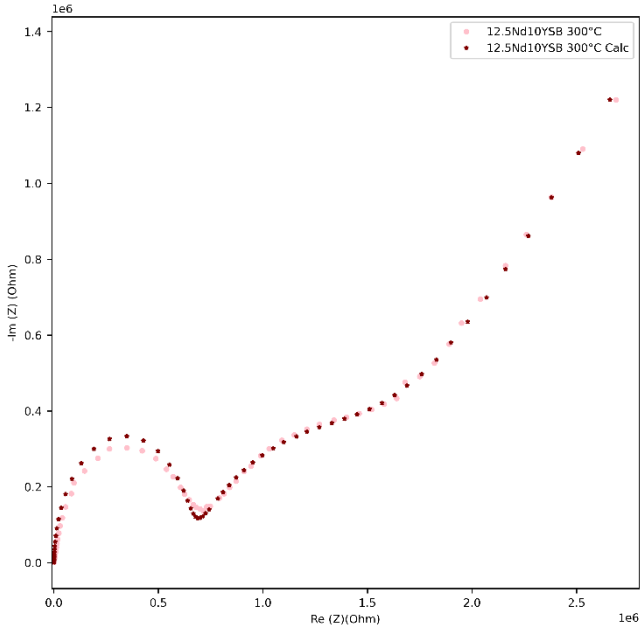


Figure 8.1.58: The VT-EIS spectra for 12.5Nd10YSB at 300 ℃ indicating the calculated spectra after fitting the data to a circuit model, where * indicates the calculated spectra.

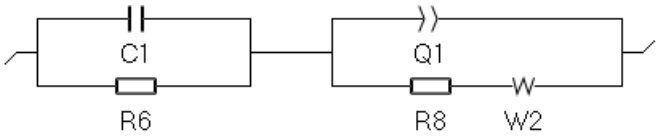


Figure 8.1.59: The circuit model used to fit the EIS data for 12.5Nd10YSB at 300 ℃

To fit semi-infinite diffusion of species through the diffusion layer, the Warburg element (W) is utilised. The perturbation frequency is a factor on which the oxide diffusion in the electrolyte is dependant, and this corresponds to the low-frequency region in the EIS spectra, which has a sloping line. The bulk of the electrolyte to electrode interface represents the area at which the diffusion occurs, and this is represented by W. The circuit model used to fit the above spectra is a modification of the Randles circuit model, which involves a Warburg diffusion element (W) in series with a resistor to describe the charge transfer.

When observing the equivalence circuit model which is used to fit the EIS spectra (Nyquist plot) obtained for the analysis at 300 ℃, we observe a semi-circle, followed by a very depressed semi-circle and then a tail. The equivalence circuit model used to fit the spectra is as follows, have C1/R6 + Q1/(R8+W2), where W2 is defined as the Warburg impedance element which is related to the oxide species mass transfer as a result of diffusion. Q1 is representative of the depressed capacitance, R8 represents the electrolyte/electrode interfacial polarisation resistance or the grain boundaries resistance. C1 represents the bulk capacitance, and R6 represents the bulk resistance which is defined as the electrolyte resistance.

For the Nyquist plot (EIS spectral data) observed for 300 ℃, when fitting the data to the equivalence circuit model, we obtain C1 = 23.49× 10^{-12} F, R6 = 636702 Ω, Q1 = 52.28× 10^{-9} F.s^{a-1} , a1 = 0.6251, and R8 = 1.078 × 10^{6} Ω, s2 = 1.107× 10^{6} Ω.$s^{-\frac{1}{2}}$. We also obtain χ^2 = 66.65× 10^{9} and $\chi/\sqrt{N}$ = 30425.

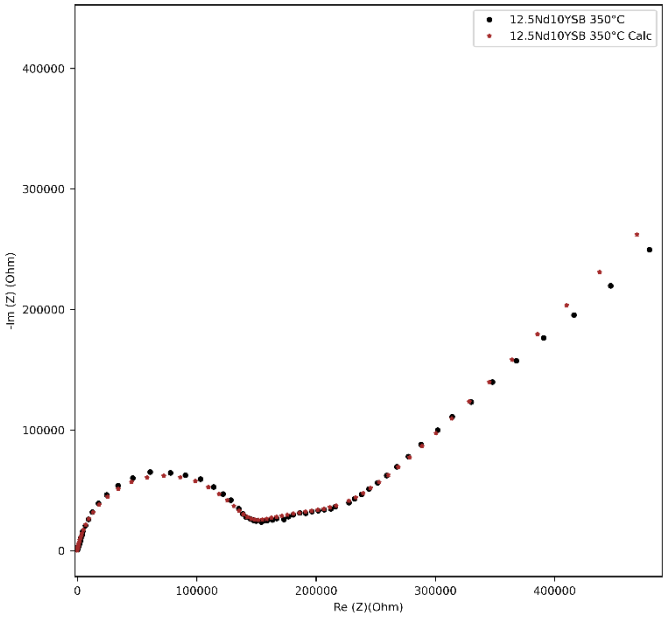


Figure 8.1.60: The VT-EIS spectra for 12.5Nd10YSB at 350 ℃ indicating the calculated spectra after fitting the data to a circuit model, where * indicates the calculated spectra.

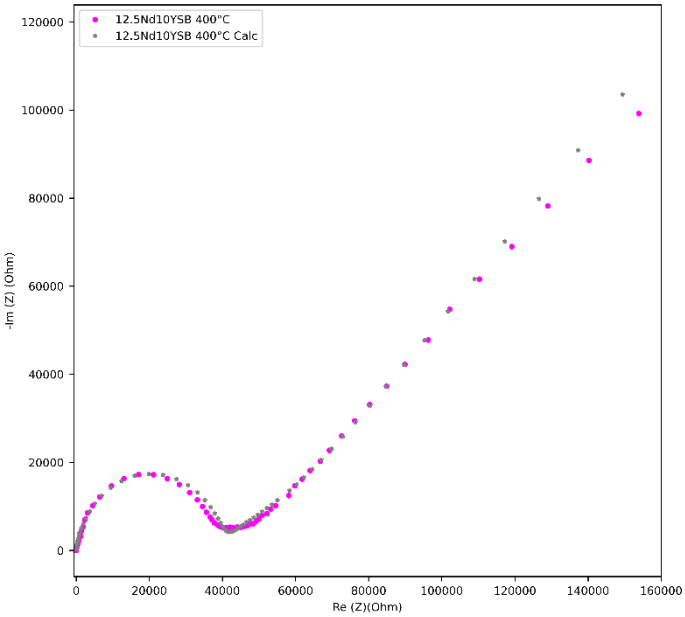


Figure 8.1.61: The VT-EIS spectra for 12.5Nd10YSB at 400 ℃ indicating the calculated spectra after fitting the data to a circuit model, where * indicates the calculated spectra.

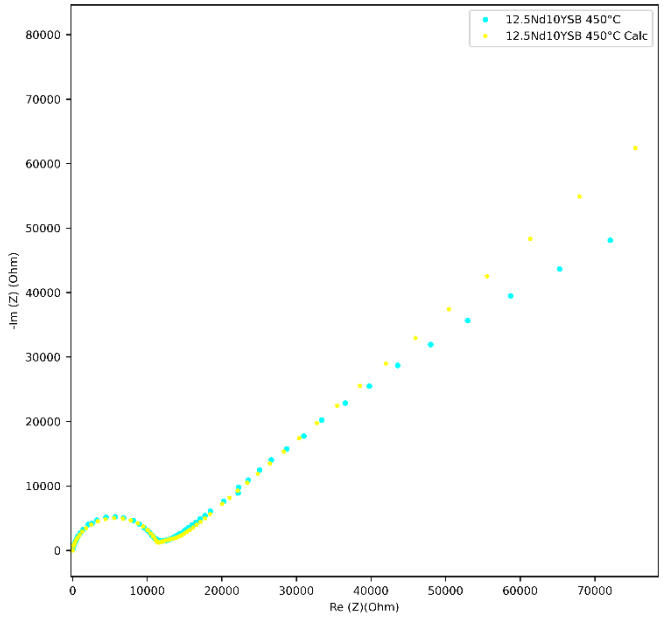


Figure 8.1.62: The VT-EIS spectra for 12.5Nd10YSB at 450 ℃ indicating the calculated spectra after fitting the data to a circuit model, where * indicates the calculated spectra.

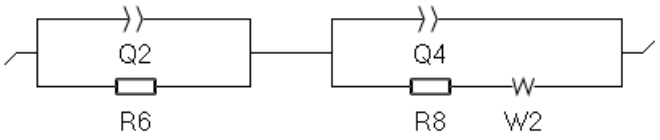


Figure 8.1.63: The circuit model used to fit the EIS data for 12.5Nd10YSB within the 350-450 ℃ temperature range.

When observing the equivalence circuit model which is used to fit the EIS spectra (Nyquist plot) obtained for the analysis at 350-450 ℃, the equivalence circuit model used to fit the spectra is as follows, Q2/R6 + Q4/(R8+W2), where W2 is defined as the Warburg impedance element which is related to the oxide species mass transfer as a result of diffusion. Q4 is representative of the depressed capacitance, R8 represents the electrolyte/electrode interfacial polarisation resistance or the grain boundaries resistance. Q2 represents the bulk pseudo-capacitance, and R6 represents the bulk resistance which is defined as the electrolyte resistance.

For the Nyquist plot (EIS spectral data) observed for 350 ℃, we observe a semi-circle, followed by a very weakly defined depressed semi-circle which combines with the tail. When fitting the data to the equivalence circuit model, we obtain C2 = 31.36× 10^{-12} F (derived from Q2 = 98.95× 10^{-12} F.s^{a-1}), a2 = 0.9071 , R6 = 135561 Ω, Q4 = 93.90× 10^{-9} F.s^{a-1} , a1 = 0.6337, and R8 = 907791 Ω, s2 = 407500 Ω.$s^{-\frac{1}{2}}$. We also obtain χ^2 = 0.9184× 10^9 and $\chi/\sqrt{N}$ = 3759.

The Nyquist plot (EIS spectral data) observed for 400 ℃, we observe a semi-circle, followed a tail. The fitting of the data to the equivalence circuit model, results in the following, C2 = 31.46× 10^{-12} F (derived from Q2 = 0.1377× 10^{-9} F.s^{a-1}), a2 = 0.8913 , R6 = 40118 Ω, Q4 = 0.6063× 10^{-6} F.s^{a-1} , a1 = 0.6193, and R8 = 22280 Ω, s2 = 235982 Ω.$s^{-\frac{1}{2}}$. We also obtain χ^2 = 0.2124× 10^9 and $\chi/\sqrt{N}$ = 1794.

For 450 ℃, the Nyquist plot observed shows a semi-circle followed by a tail. Using the equivalence circuit model to fit the data, results in the following being obtained, C2 = 31.00× 10^{-12} F (derived from Q2 = 0.1178× 10^{-9} F.s^{a-1}), a2 = 0.9101 , R6 = 11464 Ω, Q4

= 13.42× 10^{-9} F.s^{a-1} , $a1$ = 0.9962, and R8 = 1989 Ω, s2 = 121100 Ω.$s^{-\frac{1}{2}}$. We also obtain χ^2 = 0.658× 10^9 and $\chi/\sqrt{N}$ = 3158.

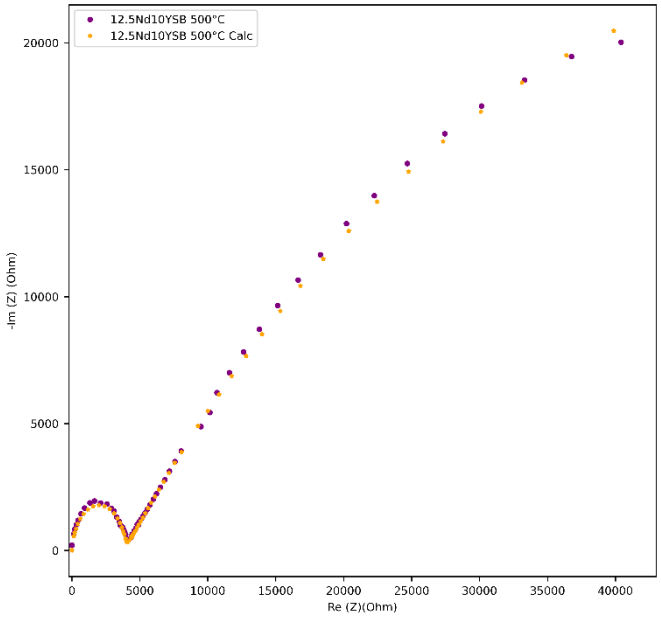


Figure 8.1.64: The VT-EIS spectra for 12.5Nd10YSB at 500 ℃ indicating the calculated spectra after fitting the data to a circuit model, where * indicates the calculated spectra.

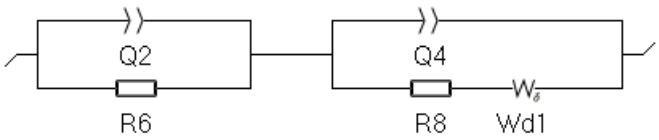


Figure 8.1.65: The circuit model used to fit the EIS data for 12.5Nd10YSB at 500 ℃

As the temperature increases to a higher temperature, it is important to note that at this high temperature, the mobility of the oxide ions is drastically increased. This drastic increase in oxide ion mobility result in charge carriers at low frequencies being able to move across the entire sample, reaching the end of the diffusion path prior to that directional switch of the alternating signal, mainly due to there now being sufficient time for this migration (Bard & Faulkner, 2001).

The Warburg semi-infinite diffusion model is no longer applicable due to this increase in mobility, and thus the Warburg diffusion element of finite length type (W_δ) is employed. The impedance where W_δ is employed is only applicable when the diffusion layer has an infinite thickness, however, this is very often not true, and thus when there is a parameter which results in the diffusion layer being bound, lower frequency impedances move from obeying the one formula below, to obeying the next, resulting in the equation which is more general and is defined as the porous bounded Warburg (Gerischer, 1951).

$$Z_w = \sigma\omega^{-0.5} - j\sigma\omega^{-0.5} \Longrightarrow Z_{FLW} = Z_0(j\omega\tau)^{-0.5}\tanh(j\omega\tau)^{-0.5}$$

Where the variables are as follows, σ = Warburg coefficient ($\Omega.s^{-0.5}$), Z_w = Warburg impedance, ω = angular (radial) frequency, j = imaginary unit, Z_0 = impedance approached at lower frequencies, τ = time factor.

For the Nyquist plot (EIS spectral data) observed for 500 ℃, we observe a semi-circle, followed by a tail which curves in such a way that it forms a second semi-circle. This is characteristic of the bounded diffusion layer and thus we use the finite length Warburg (FLW) element, which also bases the equation of calculation on the Nernst model approximation which notes that the variation in concentration of the species present as a result of the electrochemical reactions which occur, only occur in the diffusion layer and thus not in the bulk (outside the diffusion layer), with the concentrations within the bulk being constant(Michel & Montella, 2015).

The equivalence circuit model used to fit the spectra is as follows, have Q2/R6 + Q4/(R8+W_δ(Wd1)), where W_δ(Wd1) is defined as the finite length Warburg (FLW) impedance element which is related to the oxide species mass transfer as a result of diffusion (as well as convection, which is not applicable for our sample as it is solid). Q4 is representative of the depressed capacitance, R8 represents the electrolyte/electrode interfacial polarisation resistance or the grain boundaries resistance. Q2 represents the bulk pseudo-capacitance, and R6 represents the bulk resistance which is defined as the electrolyte resistance.

When fitting the data to the equivalence circuit model, we obtain C2 = 31.37× 10^{-12} F (derived from Q2 = 94.37× 10^{-12} F.s^{a-1}), a2 = 0.9308 , R6 = 3906 Ω, Q4 = 7.657× 10^{-6} F.s^{a-1} , a1

= 0.5000, and R8 = 108958 Ω, Rd1 = 1492 Ω, td1 = 0.05099 s. We also obtain χ^2 = 2.366× 10^6 and $\chi/\sqrt{N}$ = 203.7.

Table 5: Values obtained when the EIS data is fitted using the circuit models described for each temperature range (T). R_b represents the bulk resistance, σ_b represents bulk conductivity, a represents the frequency constant, C_b representing the pseudo capacitance of the bulk, and $Q_b$represents the constant phase element of the bulk.

Sample	T (℃)	R_b (Ω)	σ_b ($\Omega^{-1}.cm^{-}$ $S.cm^{-1}$)	a	C_b (F)	Q_b(F. s^{a-1})	χ^2	$\chi/\sqrt{N}$
$Nd_{0.125}Y_{0.1}$ -Bi_2O_3 (12.5Nd10 YSB)	200	41.23 e^6	2.3200 e^{-9}	0.5000	23.23 e^{-12}	7.579 e^{-9}	0.8093 e^{15}	3.642 e^6
	250	4.245 e^6	2.2553 e^{-8}	0.5518	20.35 e^{-12}	31.27 e^{-9}	11.76 e^{12}	41891 1
	300	636702	1.5037 e^{-7}	0.6251	23.49 e^{-12}	52.28 e^{-9}	66.65e^9	30425
	350	135561	7.0625 e^{-7}	0.6337	31.36 e^{-12}	93.9 e^{-9}	0.9184 e^9	3759
	400	40118	2.3865 e^{-6}	0.6193	31.46 e^{-12}	0.6063 e^{-6}	0.2124 e^9	1794
	450	11464	8.3513 e^{-6}	0.9962	31.00 e^{-12}	13.42 e^{-9}	0.6584 e^9	3158
	500	3906	2.4511 e^{-5}	0.5000	31.37 e^{-12}	7.657 e^{-6}	2.366e^6	203.7

The bulk electrical conductivity (σ_b) first needs to be calculated before the activation energy (in units of eV) of the conduction process can be determined. The calculation of σ_b makes use of the following equation:

$$\sigma_b = \frac{4e}{\pi d^2 R_b}$$

Where the variables are defined as follows, R_b = bulk resistance, $\frac{\pi d^2}{4}$ = area of the sample, e = sample thickness, d = diameter (but seeing that we have a pellet which is round, d = 2r, where r = radius), the sample area can thus be calculated by πr^2 (using mathematical manipulation). When measuring the data at a maximum frequency of 1 MHz, we still observe the initial semi-circle which is representative of the bulk impedance at the highest temperature measured. The conductivity of the electrolyte for both compositions were calculated using the sample dimensions measured for the pellets, and the bulk resistance determined through the fitting of the experimental data to the equivalence circuit model.

The activation energy can be calculated using the Arrhenius equation. The equation is defined as:

$$\sigma = \sigma_o \exp\left(-\frac{E_a}{K_b T}\right)$$

The variables can be described as follows, σ_o = pre-exponential factor, σ = conductivity, K_b = Boltzmann's constant, T = absolute temperature, and E_a = activation energy. The activation energy, E_a, is determined by observing the slope of the plot of ln σ (as we are observing the bulk, σ_b = bulk conductivity) versus $\frac{1}{T}$. Ionic conducting ceramics have inherent thermally activated conductivity mechanisms which give specific behaviour in the Arrhenius plots for bulk conductivities (Ormerod, 2003). The conductivities of ionic conducting ceramics are directly proportional to temperature, thus as temperature increases, the conductivities increase, and as the temperature decreases the conductivities decrease.

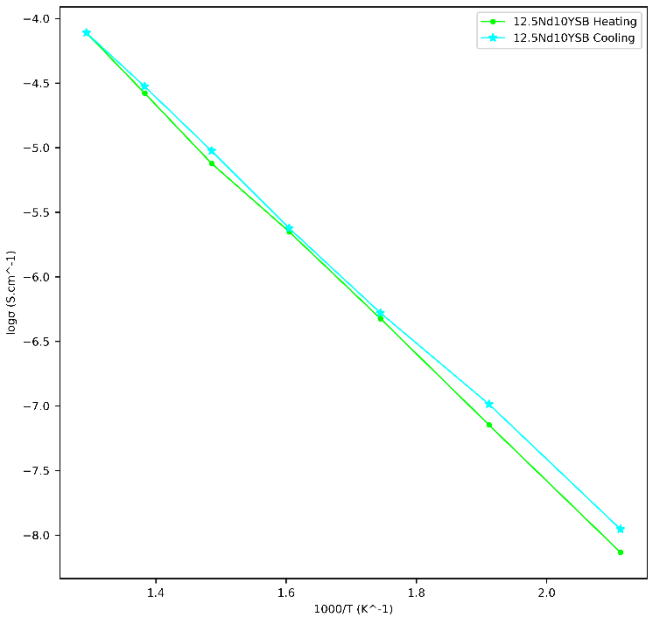


Figure 8.1.66: The Arrhenius plot for 12.5Nd10YSB within the 200-500 ℃ temperature range.

Table 6: All the values used for the calculations of the Arrhenius plot parameters for 12.5Nd10YSB

Cycle	T (℃)	T (K)	1/T (K^{-1})	1000/T (K^{-1})	Logσ (S.cm^{-1})
Heating	200	437.15	0.002113	2.113	-8.634
	250	523.15	0.001911	1.911	-7.647
	300	573.15	0.001744	1.744	-6.823
	350	623.15	0.001604	1.604	-6.151
	400	673.15	0.001485	1.485	-5.622
	450	723.15	0.001382	1.382	-5.078

	500	773.15	0.001293	1.293	-4.611
Cooling	200	437.15	0.002113	2.113	-8.455
	250	523.15	0.001911	1.911	-7.487
	300	573.15	0.001744	1.744	-6.780
	350	623.15	0.001604	1.604	-6.124
	400	673.15	0.001485	1.485	-5.525
	450	723.15	0.001382	1.382	-5.026
	500	773.15	0.001293	1.293	-4.611

Considering the Arrhenius plots obtained from both the heating and cooling cycles for the 12.5Nd10YSB within the 200-500 ℃ temperature range, it is observed that a linear plot is obtained for both cycles. This indicates that the sample does not undergo any phase changes or order to disorder transitions within the temperature range under investigation. The conductivity measurements and sample behaviour of the 12.5Nd10YSB sample is in agreement with the conclusions reached through variable temperature Raman spectroscopy. The conductivities obtained for the 12.5Nd10YSB sample at 200, 300, 400 and 500 ℃, were as follows, 200 ℃ = 2.3200×10^{-9}, 300℃ = 1.5037×10^{-7}, 400℃ = 2.3865×10^{-6}, and 500℃ = 2.4511×10^{-5} $S.cm^{-1}$.

8.1.2 15Nd5Y2.5TbSB:

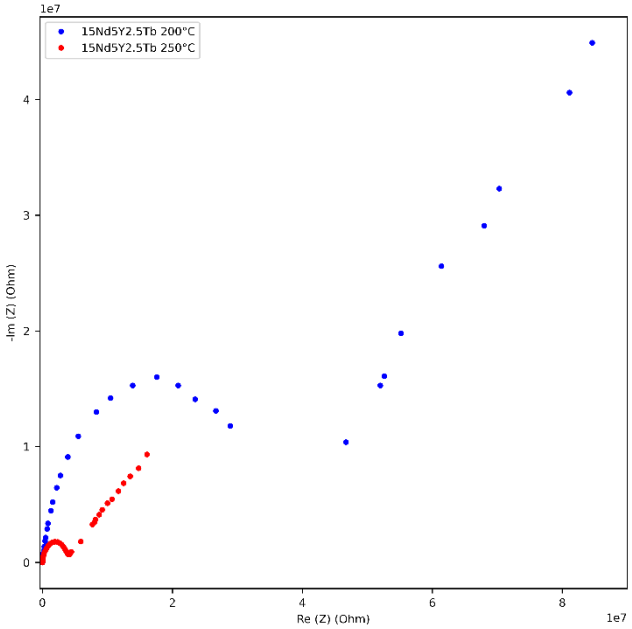


Figure 8.1.67: The VT-EIS spectra for 15Nd5Y2.5TbSB between 200-250 ℃.

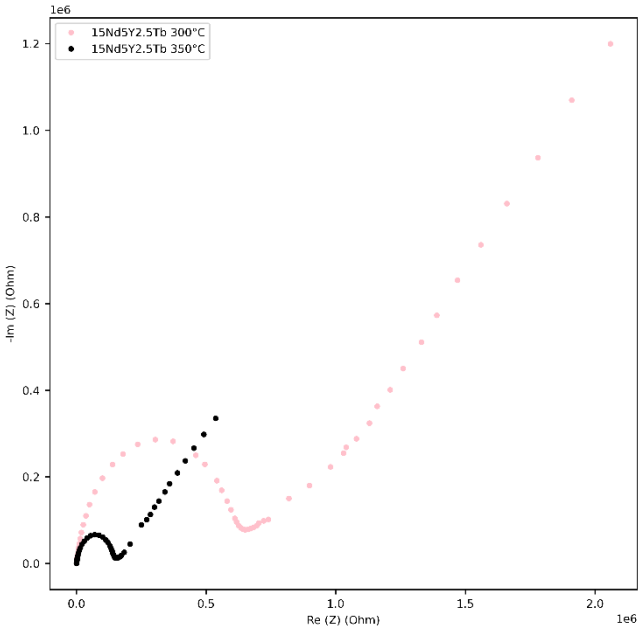


Figure 8.1.68: The VT-EIS spectra for 15Nd5Y2.5TbSB between 300-350 ℃.

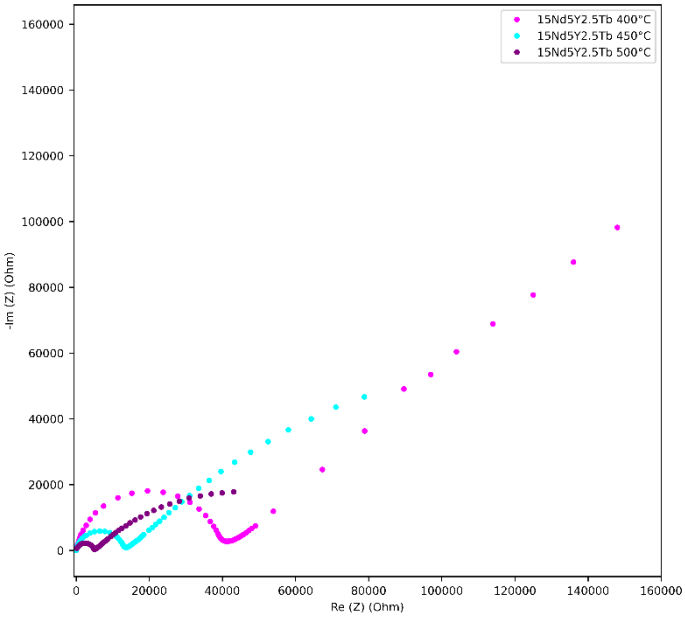


Figure 8.1.69: The VT-EIS spectra for 15Nd5Y2.5TbSB between 400-500 ℃.

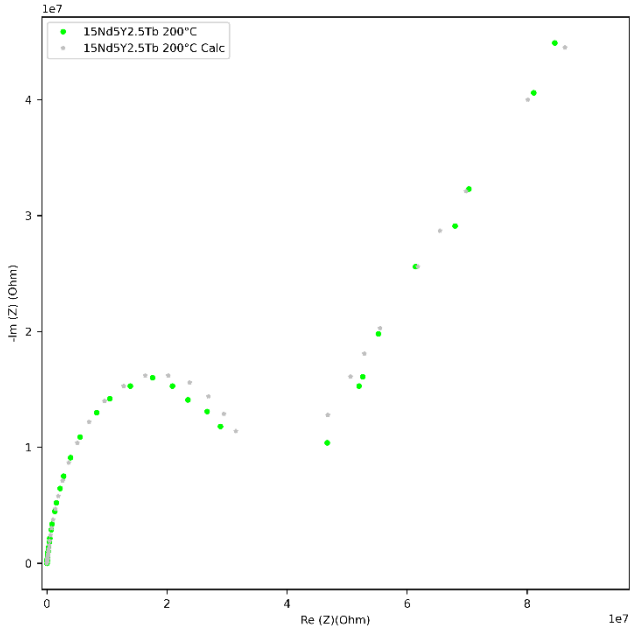


Figure 8.1.70: The VT-EIS spectra for 15Nd5Y2.5TbSB at 200 ℃ indicating the calculated spectra after fitting the data to a circuit model, where * indicates the calculated spectra.

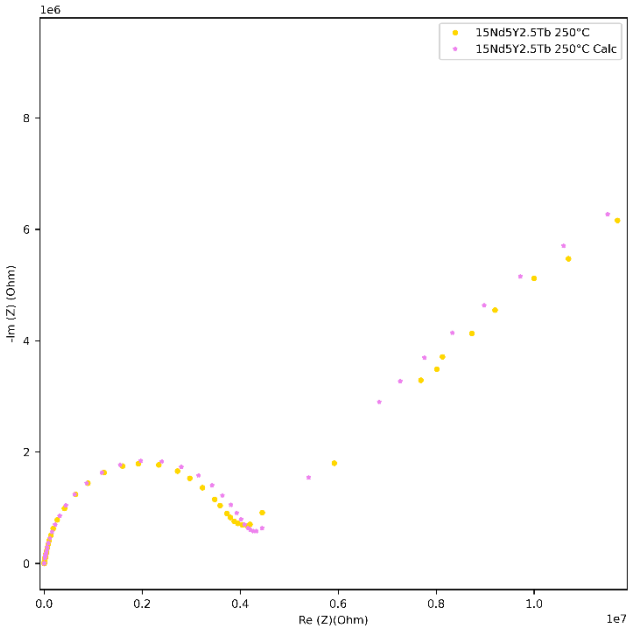


Figure 8.1.71: The VT-EIS spectra for 15Nd5Y2.5TbSB at 250 ℃ indicating the calculated spectra after fitting the data to a circuit model, where * indicates the calculated spectra.

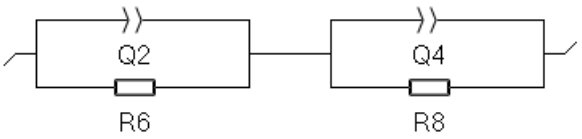


Figure 8.1.72: The circuit model used to fit the EIS data for 15Nd5Y2.5TbSB within the 200-250 ℃ temperature range.

The equivalence circuit model which is used to fit the EIS spectra (Nyquist plot) obtained for the analysis in the temperature range of 200-250 ℃, it can be observed that we have Q2/R6 + Q4/R8.

For the Nyquist plot (EIS spectral data) observed for 200 ℃, when fitting the data to the equivalence circuit model, we obtain C2 = 18.80× 10^{-12} F (derived from Q2 = 30.90× 10^{-12} F.s^{a-1}), $a2$ = 0.9325 , R6 = 33.84× 10^{6} Ω, Q4 = 16.78× 10^{-9} F.s^{a-1} , $a4$ = 0.5000, and R8 =

0.5896× 10^9 Ω. We also obtain χ^2 = 92.60× 10^{12} and $\chi/\sqrt{N}$ = 1.286× 10^6. We observe a semi-circle followed by a tail.

The Nyquist plot (EIS spectral data) observed for 250 ℃ also has a semi-circle followed by a tail, when fitting the data to the equivalence circuit model, we C2 = 19.42× 10^{-12} F (derived from Q2 = 40.41× 10^{-12} F.s^{a-1}), a2 = 0.9225 , R6 = 4.027× 10^6 Ω, Q4 = 63.17× 10^{-9} F.s^{a-1} , a4 = 0.5543, and R8 = 43.44× 10^6 Ω. We also obtain χ^2 = 3.383× 10^{12} and $\chi/\sqrt{N}$ = 290808. We also obtain χ^2 = 0.9184× 10^9 and $\chi/\sqrt{N}$ = 3759.

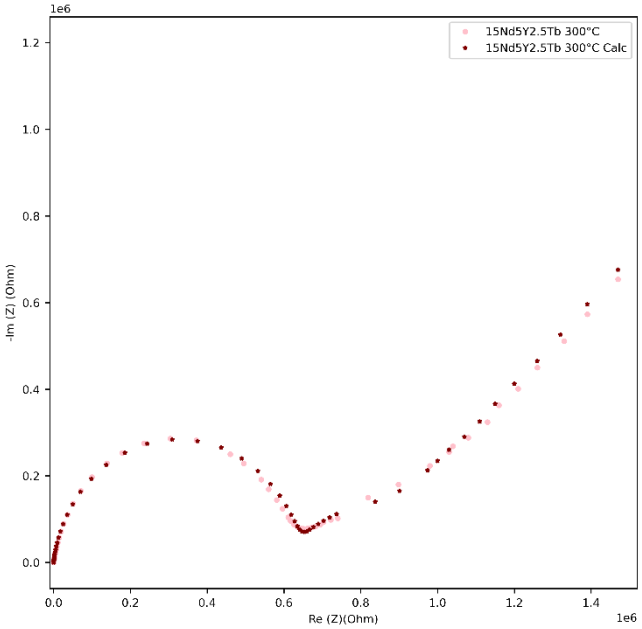


Figure 8.1.73: The VT-EIS spectra for 15Nd5Y2.5TbSB at 300 ℃ indicating the calculated spectra after fitting the data to a circuit model, where * indicates the calculated spectra.

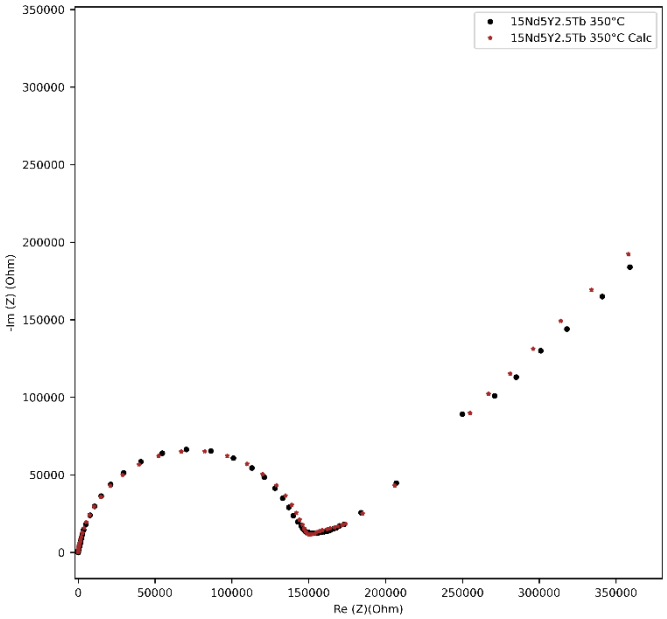


Figure 8.1.74: The VT-EIS spectra for 15Nd5Y2.5TbSB at 350 ℃ indicating the calculated spectra after fitting the data to a circuit model, where * indicates the calculated spectra.

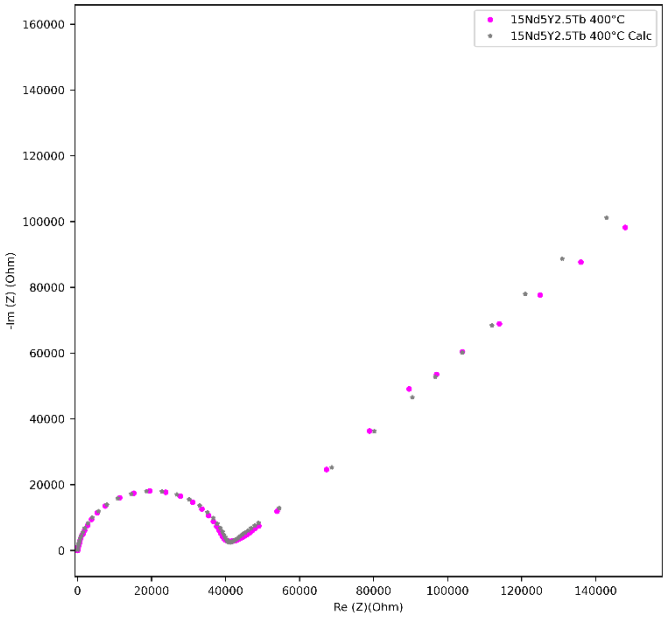


Figure 8.1.75: The VT-EIS spectra for 15Nd5Y2.5TbSB at 400 ℃ indicating the calculated spectra after fitting the data to a circuit model, where * indicates the calculated spectra.

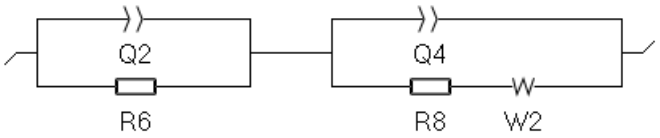


Figure 8.1.76: The circuit model used to fit the EIS data for 15Nd5Y2.5TbSB within the 300-400 ℃ temperature range.

When observing the equivalence circuit model which is used to fit the EIS spectra (Nyquist plot) obtained for the analysis at 300-400 ℃, we observe a semi-circle, followed by a very depressed semi-circle and then a tail. The equivalence circuit model used to fit the spectra is as follows, have Q2/R6 + Q4/(R8+W2), where W2 is defined as the Warburg impedance element which is related to the oxide species mass transfer as a result of diffusion. Q4 is representative of the depressed capacitance, R8 represents the electrolyte/electrode interfacial polarisation resistance or the grain boundaries resistance. Q2 represents the bulk pseudo-capacitance, and R6 represents the bulk resistance which is defined as the electrolyte resistance.

For the Nyquist plot (EIS spectral data) observed for 300 ℃, we observe a semi-circle, followed by a tail. When fitting the data to the equivalence circuit model, we obtain C2 = 20.16× 10^{-12} F (derived from Q2 = 52.52× 10^{-12} F.s^{a-1}), a2 = 0.9149 , R6 = 643960 Ω, Q4 = 20.02× 10^{-9} F.s^{a-1} , a1 = 0.8809, and R8 = 205242 Ω, s2 = 1.012× 10^{6} Ω.$s^{-\frac{1}{2}}$. We also obtain χ^2 = 7.131× 10^{9} and $\chi/\sqrt{N}$ = 10994.

The Nyquist plot (EIS spectral data) observed for 350 ℃, we observe a semi-circle, followed a tail. The fitting of the data to the equivalence circuit model, results in the following, C2 = 20.19× 10^{-12} F (derived from Q2 = 61.17× 10^{-12} F.s^{a-1}), a2 = 0.9128 , R6 = 149348 Ω, Q4 = 28.31× 10^{-9} F.s^{a-1} , a1 = 0.9385, and R8 = 21043 Ω, s2 = 288626 Ω.$s^{-\frac{1}{2}}$. We also obtain χ^2 = 0.3775× 10^{9} and $\chi/\sqrt{N}$ = 2596.

For 400 ℃, the Nyquist plot observed shows a semi-circle followed by a tail. Using the equivalence circuit model to fit the data, results in the following being obtained, C2 =

20.31× 10^{-12} F (derived from Q2 = 59.70× 10^{-12} F.s^{a-1}), $a2$ = 0.9231 , R6 = 40033 Ω, Q4 = 2.146× 10^{-6} F.s^{a-1} , $a1$ = 0.5572, and R8 = 40959 Ω, s2 = 263859 Ω.$s^{-\frac{1}{2}}$. We also obtain χ^2 = 0.1094× 10^{9} and $\chi/\sqrt{N}$ = 1385.

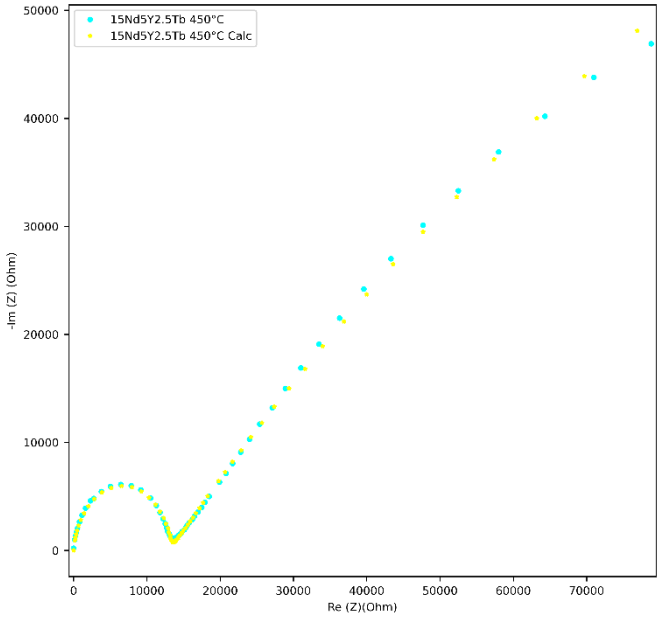


Figure 8.1.77: The VT-EIS spectra for 15Nd5Y2.5TbSB at 450 ℃ indicating the calculated spectra after fitting the data to a circuit model, where * indicates the calculated spectra.

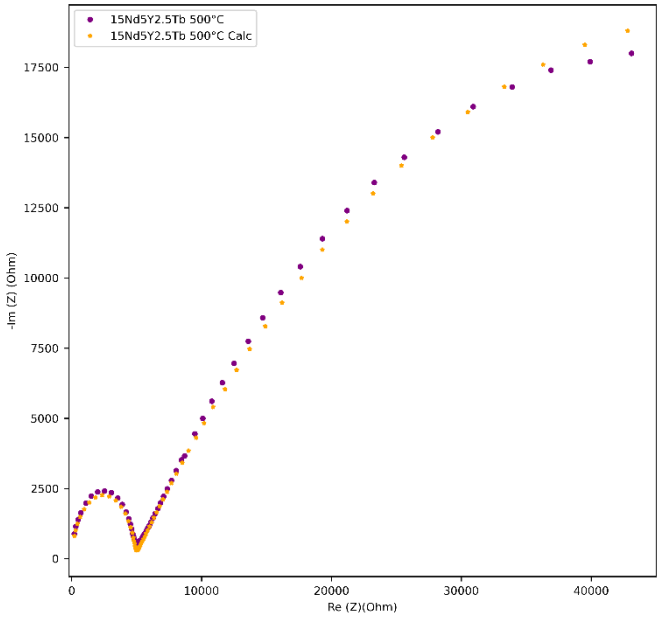


Figure 8.1.78: The VT-EIS spectra for 15Nd5Y2.5TbSB at 500 ℃ indicating the calculated spectra after fitting the data to a circuit model, where * indicates the calculated spectra.

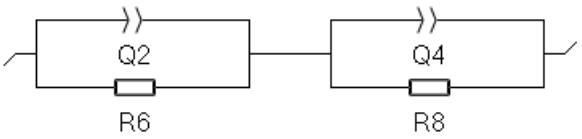


Figure 8.1.79: The circuit model used to fit the EIS data for 15Nd5Y2.5TbSB within the 450-500 ℃ temperature range.

The equivalence circuit model which is used to fit the EIS spectra (Nyquist plot) obtained for the analysis in the temperature range of 400-500 ℃, it can be observed that we have Q2/R6 + Q4/R8. The observed spectra indicate a semi-circle followed by a tail that largely starts forming a second semi-circle. The Warburg element does not fit the experimental data for the diffusion of the oxide ions at this high temperature.

For the Nyquist plot (EIS spectral data) observed for 200 ℃, when fitting the data to the equivalence circuit model, we obtain C2 = 20.46× 10^{-12} F (derived from Q2 = 57.76× 10^{-12} F.s^{a-1}), a2 = 0.9314 , R6 = 13182 Ω, C4 = 7.059× 10^{-6} F (derived from Q4 = 6.249× 10^{-6} F.s^{a-1}), a4 = 0.5000, and R8 = 407163 Ω. We also obtain χ^2 = 14.70× 10^6 and $\chi/\sqrt{N}$ = 471.9.

The Nyquist plot (EIS spectral data) observed for 500 ℃ , using the equivalence circuit model to fit the data, results in the following being obtained, C2 = 20.51× 10^{-12} F (derived from Q2 = 45.72× 10^{-12} F.s^{a-1}), a2 = 0.9503 , R6 = 4833 Ω, C4 = 7.059× 10^{-6} F (derived from Q4 = 8.677× 10^{-6} F.s^{a-1}), a4 = 0.5002, and R8 = 93743 Ω. We also obtain χ^2 = 3.383× 10^{12} and $\chi/\sqrt{N}$ = 290808. We also obtain χ^2 = 4.457× 10^6 and $\chi/\sqrt{N}$ = 257.9.

Table 7: The values obtained when the EIS data is fitted using the circuit models described for each temperature range (T). R_b represents the bulk resistance, σ_b represents bulk conductivity, a represents the frequency constant, C_b representing the pseudo capacitance of the bulk, and $Q_b$represents the constant phase element of the bulk.

Sample	**T (℃)**	**R_b (Ω)**	**σ_b ($\Omega^{-1}.cm^{-1}$ $S.cm^{-1}$)**	**a**	**C_b (nF)**	**Q_b(F.s^{a-1})**	**χ^2**	**χ^2 ($\sqrt{N}$)**
$Nd_{0.15}Y_{0.05}Tb$-Bi_2O_3 (15Nd5Y2.5TbSB)	200	33.84 e^6	3.1000e^{-9}	0.9325	18.80e^{-12}	16.78e^{-9}	92.60 e^{12}	1.286 e^6
	250	4.027 e^6	2.6074e^{-8}	0.9225	19.42 e^{-12}	63.17e^{-9}	3.383 e^{12}	290808
	300	643960	1.6305e^{-7}	0.9149	20.16 e^{-12}	20.02e^{-9}	7.131 e^9	10994
	350	149348	7.0304e^{-7}	0.9385	20.19 e^{-12}	28.31e^{-9}	0.3775 e^9	2596
	400	40033	2.6228e^{-6}	0.9231	20.31 e^{-12}	2.146e^{-6}	0.1094 e^9	1385
	450	13182	7.9562e^{-6}	0.9314	20.46 e^{-12}	15.90e^{-6}	14.70 e^6	471.9

	500	4833	$2.1725e^{-6}$	0.9503	20.51 e^{-12}	$7.059e^{-6}$	4.457 e^{6}	257.9

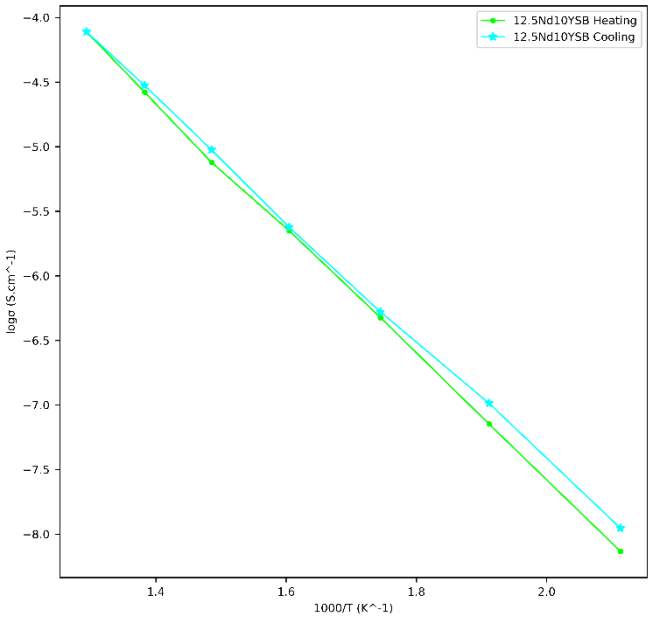


Figure 8.1.80: The Arrhenius plot for 12.5Nd10YSB within the 200-500 ℃ temperature range.

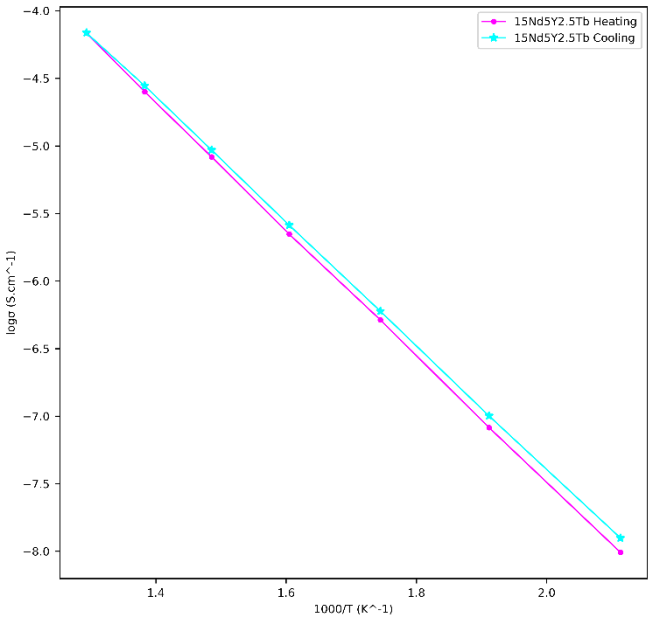


Figure 8.1.81: The Arrhenius plot for 15Nd5Y2.5TbSB within the 200-500 ℃ temperature range.

Table 8: All the values used for the calculations of the Arrhenius plot parameters for 15Nd5Y2.5TbSB

Cycle	T (℃)	T (K)	1/T (K^{-1})	1000/T (K^{-1})	Logσ (S.cm^{-1})
Heating	200	437.15	0.002113	2.113	-8.508
	250	523.15	0.001911	1.911	-7.584
	300	573.15	0.001744	1.744	-6.788
	350	623.15	0.001604	1.604	-6.153
	400	673.15	0.001485	1.485	-5.581

	450	723.15	0.001382	1.382	-5.100
	500	773.15	0.001293	1.293	-4.663
Cooling	200	437.15	0.002113	2.113	-8.402
	250	523.15	0.001911	1.911	-7.500
	300	573.15	0.001744	1.744	-6.723
	350	623.15	0.001604	1.604	-6.087
	400	673.15	0.001485	1.485	-5.530
	450	723.15	0.001382	1.382	-5.055
	500	773.15	0.001293	1.293	-4.663

The Arrhenius plots obtained from both the heating and cooling cycles for the 15Nd5Y2.5TbSB within the 200-500 ℃ temperature range, indicates a linear plot being obtained for both cycles. This indicates that the sample does not undergo and phase changes or order to disorder transitions within the temperature range under investigation. The conductivity measurements and sample behaviour of the 15Nd5Y2.5TbSB sample is in agreement with the conclusions reached through variable temperature Raman spectroscopy. The conductivities obtained for the 15Nd5Y2.5TbSB sample at 200, 300, 400 and 500 ℃, were as follows, 200 ℃ = 3.1000×10^{-9}, 300 ℃ = 1.6305×10^{-7}, 400 ℃ = 2.6228×10^{-6}, and 500 ℃ = 2.1725×10^{-5} S.cm^{-1}.

In the study done by Jolley et al. in Optimizing rhombohedral Bi_2O_3 conductivity for low temperature SOFC electrolytes, the composition La5.1Y1.4 exhibited the highest conductivity, 3×10^{-2} S.cm^{-1} at 500 ℃ (Jolley et al., 2019). However, upon the observation of the XRD

diffractogram obtained, we observe slight peaks which indicate phase impurities. We also observe parasitic inductance when observing the Nyquist plots obtained for the samples tested using the EIS technique, and hence the conductivity value obtained is inaccurate as the relevant compensation for open circuit and short circuit impedance first needs to be done in order to eliminate the impact of the parasitic inductance on the experimental data. For the compositions investigated, for the 12.5Nd10YSB sample at 500℃, the conductivity obtained is 2.4511×10^{-5} S.cm^{-1}, and for the 15Nd5Y2.5TbSB sample at 500 ℃, the conductivity obtained is 2.1725×10^{-5} S.cm^{-1}. Although the two conductivity values obtained are much lower as compared to that obtained in the study by Jolley et al. (Jolley et al., 2019), the Nyquist plots obtained are absent of any parasitic inductance, and also indicate the presence of the bulk semi-circle present throughout the investigated temperature range and thus are a better representation of the ionic conductivity of the pure phase rhombohedral Bi_2O_3.

The increase in temperature results in an increase in the O^{2-} ions mobility (these O^{2-} ions can either be interstitial or any other defect type, depending on the crystallographic arrangement of the ions in the lattice). The thermal vibration energy ions are directly proportional to the temperature, and thus as the temperature increases, the thermal vibrational energy increases, and this results in the oxygen ionic mobility increasing. Theoretically, the oxide anionic conductivity is defined as indicated below (Gil et al., 2006) :

$$\sigma_b = 2ne\mu$$

The variables are as defined, e = elementary electric charge, n = carrier density, and μ = oxide ion mobility. The number of charge carriers and the mobility impacts the bulk conductivity, in such a way as to improve it. The O^{2-} anions thermal energy at low temperatures is not sufficient enough for the oxygen to hop to the nearest neighbouring vacancy in the structure by means of the oxygen hopping model, even though there are interstitial O^{2-} vacancies present within the crystal structure. At lower temperatures the total random O^{2-} vacancy distribution is very low, due to the ordered structure of the O^{2-} vacancy sublattice (Ozlu Torun et al., 2015).

In the rhombohedral Bi_2O_3 structure, we observe an inverse stacking of the cells, and thus ordered but also random oxygen vacancies, and oxygen hopping pathways. At elevated temperature conditions, the thermal vibrations for charge carriers have the ability to briefly aid

the oxygen hopping model process, through two mechanisms, namely, the extension of the hopping conduction pathways which occur throughout the crystal lattice, or through the process of shortening the distances through which the oxygen ions need to hop to the nearest neighbour vacancy point.

The dopant concentration mol % is inversely proportional to conductivity and polarizability. The conductivity decreases as a result of the increased dopant concentration mol %, this is due to the stronger dopant ion and O^{2-} ion associations which result in stronger bonding, reducing the O^{2-} ion mobility. The dopant ion Shannon ionic radius also has an impact on the conductivity (Takahashi et al., 1975).

Most oxide ion conductors' ionic conductivity, thus in principle is directly proportional to the concentration of oxygen vacancies. The ionic conductivity is influenced by various other factors, namely, properties related to microstructure and the crystallography of the samples, namely, grain sizes and porosities (Takahashi et al., 1975).

The Arrhenius plot obtained from plotting log (σ_b) against $\frac{1}{T}$ is used to calculate E_a (eV), is calculated as follows (Whittingham, 1989):

$$E_a = \frac{-slope \times \ln 10 \times R}{(1.602177 \times 10^{-19}\, J.eV^{-1}).N_A}$$

Table 9: Electrical parameters derived for the sample compositions under investigation within the 200-500℃ for both the heating and cooling cycles obtained from the Arrhenius plot by from plotting log (σ_b) against $\frac{1000}{T}$:

Samples	Cycles	$E_a\ (eV)$
$Nd_{0.125}Y_{0.10}$-Bi_2O_3 (12.5Nd10YSB)	Heating	1.7400
	Cooling	1.8111
$Nd_{0.15}Y_{0.05}Tb_{0.025}$-$Bi_2O_3$ (15Nd5Y2.5TbSB)	Heating	1.8439
	Cooling	1.8529

The activation energies for the samples are presented in the table above. It is observed that there are differences in the heating and cooling cycle values, the differences are however not that great. This indicates that the relaxation which occurs at the cooling cycle due to relaxation is non-Debye in nature. The 12.5Nd10YSB sample indicates the greatest change in activation energies, and this is also expected as this sample is the one with the greatest conductivity value.

Total activation energy for the ionic conductivity can theoretically be represented as follows (Walker, 1967):

$$E_a = E_m + E_d$$

The variables can be defined as follows, E_d = metal-oxygen ionic bond breaking energy, E_m = interstitial O^{2-} migration activation energy (oxygen hopping responsible for hopping of O^{2-} to appropriate O^{2-} lattice vacancies). The oxygen-binding energy, as well as the O^{2-} anion migration pathways are crucial in the determination of the activation energy. The activation energy determination is thus defined by two major factors, namely, it being a representation of the energy which results due to the mobility of O^{2-} ions between empty O^{2-} lattice points and the filled interstitial points, as well as being defined as the energy which is required to break a cation-oxygen bond within a lattice (Walker, 1967).

Chapter 9:

Discussion and Conclusion

Understanding the potential that the rhombohedral phase unlocks as an electrolyte for low and intermediate temperature SOFC operations, revolves around understanding the rhombohedral phase bismuthates. Throughout this study, a variety of bismuthate samples were synthesised using the sol-gel synthesis method. These samples were then investigated using a number of complementary sample analysis techniques, namely, powder X-ray diffraction, variable temperature Raman spectroscopy, simultaneous thermal analysis, as well as variable temperature electrochemical impedance spectroscopy. The use of these analysis techniques results in the understanding of the properties of the mixed phase and pure phase rhombohedral bismuthate samples synthesised. A total of 19 samples were synthesised, each yielding a variety of sample compositions, revealed through the characterisation using the abovementioned techniques. The number of publications which study the rhombohedral phase bismuthates are low, and this study finds the investigations and conclusions by these publications inconsistent, where these inconsistencies are shown by the characterisation of the samples synthesised.

The Rietveld refinement techniques was used to interpret the XRD experimental data obtained. The refinement of the various experimental diffraction patterns obtained indicated several pure phase and mixed phase samples, each with their own defining characteristics in the difference diffractogram patterns.

The refinement of the XRD structure model for the 15Nd5YSB sample resulted in a phase pure rhombohedral structural model fitting the refinement. The difference diffractogram indicated peak intensity mismatches which could be as a result of the low count-time of the experimental data. The overfitting and underfitting of peaks within the diffractograms resulting in the observed mismatch can also be attributed to preferred orientation of the sample as a result of sample packing, as well as sample preparation. The zero-background holder used also attributed to this.

The 10YSB sample yields a refinement of a structure model which indicates a phase pure cubic sample. From previous experimental studies done in the laboratory, it should be noted that this composition is not fully cubic, and in order for this to be correlated with the previous sample analysis data, higher resolution XRD would need to be done on the sample. The laboratory XRD data, however, does reveal peak asymmetry and slight peak intensity mismatches, which can be attributed to the presence of a secondary phase in low quantity that cannot be accounted for within the refinement.

10Nd12.5YSB yields a refinement which contains a mixed phase structural model with a major rhombohedral phase, and a minor cubic phase. The cubic phase presence is accounted for by the observation of slight peak asymmetry in the diffractograms. The 10NdSB sample also indicates slight peak asymmetry in its refinement, and this is as a result of the sample having a mixture of phases, with a major rhombohedral phase, and a minor monoclinic phase. The cubic and monoclinic phases are stable phases, and thus have a great impact on the samples.

A triple phase structural model Rietveld refinement is obtained for the 8.5NdSB sample, which has a major rhombohedral phase composition, with the two minor phases being the metastable tetragonal phase, and the stable cubic phase. The refined structural model indicates slight peak asymmetry as well as slight peak broadening, which is as a result of slight peak overlap between some of the peaks in the major phase and that in the minor tetragonal phase. The 10Nd10YSBsample also yields a triple phase refinement, with a major rhombohedral phase composition, and the two minor phases being the metastable tetragonal phase, and the stable monoclinic phase. As with the 8.5NdSB sample, the refinement shows slight peak broadening and peak asymmetry, as a result of the overlap between some of the peaks of the major rhombohedral phase and that in the minor tetragonal phase.

This study focused on the use of co-doping to synthesis the rhombohedral phase of Bi_2O_3. Both double-doping and triple-doping was used to stabilize bismuth oxides. These double-doped and triple-doped Bi_2O_3 samples were synthesised and investigated through the use of various comparative materials characterisation techniques. Three different total dopant mol % concentration ranges were investigated, with the low dopant mol % range, 8.5-10 mol % indicating that the rhombohedral phase was in fact not stabilised as reported by (Jolley et al.,

2019). The higher dopant mol % ranges (20-22.5 mol %) samples, indicates that the rhombohedral phase of Bi_2O_3 is stabilised at these high dopant mol % ranges, for both the double-doped and triple-doped samples as per conclusion of the XRD analysis technique using the Rietveld refinement technique. The triple-doped samples however indicated the introduction of a very low cubic phase % as a secondary phase for the 15Nd5Y2.5ScSB sample, with the secondary cubic phase being observed in the Rietveld refinement of the sample XRD diffractogram, as well as the deviation observed in the VT-Raman spectroscopy studies.

The STA analysis indicated the same behaviour for all samples in both the DTA and the TGA. The DTA scans obtained all indicate an endothermic maximum being observed within the 720-750℃ temperature range for all the samples, which could either be due to an order-disorder transition occurring, or the possible short lived phase transition from the rhombohedral to cubic δ-phase, and back to the rhombohedral phase. The TGA scans obtained all indicate less the 1.0% weight loss observed across the 30-800℃ temperature range, with the 15Nd5Y2.5ScSB sample having defined weight loss intervals.

Variable temperature (VT)- Raman spectroscopy indicates the same behaviour across all samples, besides the 15Nd5Y2.5ScSB sample as described above which contains a very low (almost negligible) cubic phase %, which has a distinctive spot which exhibits different Raman shift behaviour as compared to all other samples. The VT-Raman spectroscopy spectra indicate a distinctive signature Raman peak at $\sim 250 cm^{-1}$, which can be concluded to be the Raman peak which is indicative of the rhombohedral Bi_2O_3, this peak also appears in the low cubic phase % sample after the cooling back to room temperature.

The Arrhenius plot obtained for both the samples investigated using VT-EIS indicated no phase changes, as well as no order to disorder transitions, as only one linear region is observed. Between the two samples, the 12.5Nd10YSB sample at showed the greatest conductivity at 500℃. No VT-XRD was done, and hence no coefficient of thermal expansion (CTE) could be determined, and thus no indication could be made on whether there is a change in oxygen sublattice through the use of VT-XRD. However, with EIS being more sensitive as compared to VT-XRD, and no phase changes were observed in the samples analysed.

The xPDF results also indicated that for the samples investigated, there was no substantive difference in the average and local structural models, indicating that they behave the same.

The combination of all the information obtained from the various comparative and complementary analysis techniques indicates that the samples analysed and characterised subsequently using XRD (both laboratory and synchrotron), STA analysis, VT-Raman spectroscopy, as well as VT-EIS indicates the phase purity and phase stability of the rhombohedral phase Bi_2O_3, which is not only maintained at room temperature but across the temperature ranges investigated.

There is future work required to further investigate the properties of the phase pure rhombohedral samples, these include but are not limited to:

- Variable temperature powder diffraction measurement, both laboratory and high-resolution synchrotron experiments, to result in the better understanding and resolution of the phase content present in the samples. This will enable better evidence for understanding of phase pure material. This will also provide us with better resolutioned data to try and resolve peak intensity mismatches and overestimating and underestimating of the calculated and raw data in the refinements.
- Big box modelling of xPDF experimental data, as well as gathering some EXAFS data can be used to enable a more conclusive understanding of the sample behaviours at both the average and local structures.
- Variable temperature EIS can be done on more phase pure rhombohedral and mixed phase samples, to answer the question as to whether the phase pure samples are more conductive as compared to the mixed phase samples.

References:

Abalde-Cela, S., Aldeanueva-Potel, P., Mateo-Mateo, C., Rodríguez-Lorenzo, L., Alvarez-Puebla, R. A., & Liz-Marzán, L. M. (2010). Surface-enhanced Raman scattering biomedical applications of plasmonic colloidal particles. In *Journal of the Royal Society Interface* (Vol. 7, Issue SUPPL. 4). https://doi.org/10.1098/rsif.2010.0125.focus

Abdalla, A. M., Hossain, S., Azad, A. T., Petra, P. M. I., Begum, F., Eriksson, S. G., & Azad, A. K. (2018). Nanomaterials for solid oxide fuel cells: A review. In *Renewable and Sustainable Energy Reviews* (Vol. 82). https://doi.org/10.1016/j.rser.2017.09.046

Adachi, S., Wu, X. J., Tamura, T., Tatsuki, T., Tokiwa-Yamamoto, A., & Tanabe, K. (1997). Synthesis and superconducting properties of fluorinated La2CuO4 using NH4F. *Physica C: Superconductivity and Its Applications*, *291*(1–2). https://doi.org/10.1016/S0921-4534(97)01707-3

Ameh, E. S. (2019). A review of basic crystallography and x-ray diffraction applications. *International Journal of Advanced Manufacturing Technology*, *105*(7–8), 3289–3302. https://doi.org/10.1007/s00170-019-04508-1

Anderson, N., Hartschuh, A., & Novotny, L. (2007). Chirality changes in carbon nanotubes studied with near-field Raman spectroscopy. *Nano Letters*, *7*(3). https://doi.org/10.1021/nl0622496

Apostolescu, D. (1995). Thermal methods of analysis, principles, applications and problems. *Journal of Thermal Analysis*, *45*(1–2). https://doi.org/10.1007/bf02548698

Ariese, F., Meuzelaar, H., Kerssens, M. M., Buijs, J. B., & Gooijer, C. (2009). Picosecond Raman spectroscopy with a fast intensified CCD camera for depth analysis of diffusely scattering media. *Analyst*, *134*(6). https://doi.org/10.1039/b821437a

Askeland, D. R., & Wright, W. J. (2016). The Science and Engineering of Materials 7th Edition. In *Cengage Learning 20 Channel Center Street Boston, MA 02210 USA, ISBN: 978-1-305-07676-1*.

Auer, B. M., & Skinner, J. L. (2008). IR and Raman spectra of liquid water: Theory and interpretation. *Journal of Chemical Physics*, *128*(22). https://doi.org/10.1063/1.2925258

Authier, A. (2012). Optical properties of X-rays - Dynamical diffraction. *Zeitschrift Fur Kristallographie*, *227*(1). https://doi.org/10.1524/zkri.2012.1449

Awaji, N., Nomura, K., & Doi, S. (2010). Materials analysis using synchrotron radiation and neutron beams. *Fujitsu Scientific and Technical Journal*, *46*(3), 263–268.

Badwal, S. P. S., & Ciacchi, F. T. (2000). Oxygen-ion conducting electrolyte materials for solid oxide fuel cells. *Ionics*, *6*(1–2). https://doi.org/10.1007/BF02375543

Baertsch, C. D., Jensen, K. F., Hertz, J. L., Tuller, H. L., Vengallatore, S. T., Spearing, S. M., & Schmidt, M. A. (2004). Fabrication and structural characterization of self-supporting electrolyte membranes for a micro solid-oxide fuel cell. *Journal of Materials Research*, *19*(9). https://doi.org/10.1557/JMR.2004.0350

Bailo, E., & Deckert, V. (2008). Tip-enhanced Raman spectroscopy of single RNA strands: Towards a novel direct-sequencing method. *Angewandte Chemie - International Edition*, *47*(9). https://doi.org/10.1002/anie.200704054

Balerna, A., & Mobilio, S. (2015). Introduction to synchrotron radiation. In *Synchrotron Radiation: Basics, Methods and Applications*. https://doi.org/10.1007/978-3-642-55315-8_1

Bard, A. J., & Faulkner, L. R. (2001). Electrochemical Methods: Fundamentals and Applications, 2nd Edition. In *Electrochemical Methods - Fundamentals and Applications*.

Barman, B., & Sarma, K. C. (2012). Structural characterization of PVA capped ZnS nanostructured thin films. *Indian Journal of Physics*, *86*(8), 703–707. https://doi.org/10.1007/s12648-012-0116-0

Barsoukov, E., & Macdonald, J. R. (2005). Impedance Spectroscopy: Theory, Experiment, and Applications. In *Impedance Spectroscopy: Theory, Experiment, and Applications*. https://doi.org/10.1002/0471716243

Basu, R. N., Mukhopadhyay, J., Ghosh, S., & Das Sharma, A. (2019). Solid-State Electrolytes and Electrode Materials for Fuel Cell Application. *Transactions of the Indian Institute of Metals*, *72*(8). https://doi.org/10.1007/s12666-019-01719-8

Batfalsky, P., Malzbender, J., & Menzler, N. H. (2016). Post-operational characterization of

solid oxide fuel cell stacks. *International Journal of Hydrogen Energy*, *41*(26). https://doi.org/10.1016/j.ijhydene.2016.05.065

Battle, P. D., Catlow, C. R. A., Drennan, J., & Murray, A. D. (1983). The structural properties of the oxygen conducting δ phase of Bi 2O3. *Journal of Physics C: Solid State Physics*, *16*(17). https://doi.org/10.1088/0022-3719/16/17/003

Bauen, A., Berndes, G., Junginger, M., Vuille, F., & Londo, M. (2009). Bioenergy-A Sustainable and Reliable Energy Source. A Review of Status and Prospects. In *Structure*.

Berastegui, P., Hull, S., García-García, F. J., & Eriksson, S. G. (2002). The crystal structures, microstructure and ionic conductivity of Ba2In2O5 and Ba(Inx Zr1-x)O3-x/2. *Journal of Solid State Chemistry*, *164*(1). https://doi.org/10.1006/jssc.2001.9455

Berberich, F., Matz, W., Richter, E., Schell, N., Kreißig, U., & Möller, W. (2000). Structural mechanisms of the mechanical degradation of Ti-Al-V alloys: In situ study during annealing. *Surface and Coatings Technology*, *128–129*. https://doi.org/10.1016/S0257-8972(00)00595-8

Bicchieri, M., Sodo, A., Piantanida, G., & Coluzza, C. (2006). Analysis of degraded papers by non-destructive spectroscopic techniques. *Journal of Raman Spectroscopy*, *37*(10). https://doi.org/10.1002/jrs.1603

Billinge, S. J. L., & Egami, T. (1993). Short-range atomic structure of <math display="inline"> <mrow> <msub> <mrow> <mi mathvariant="normal">Nd</mi> </mrow> <mrow> <mn>2</mn> <mi mathvariant="normal">−</mi> <mi mathvariant="italic">x</mi> </mrow> </msub> </mrow> </math> <math display="inline">. *Physical Review B*, *47*(21).

Bordet, P. (2018). Application of the pair distribution function analysis for the study of cultural heritage materials. *Comptes Rendus Physique*, *19*(7). https://doi.org/10.1016/j.crhy.2018.06.001

Born, M., & Wolf, E. (1999). Principles of optics: electromagnetic theory of propagation, interference ... In *Principles of Optics Electromagnetic Theory of Propagation INterference and Diffraction of Light 2nd edition by Max Born Emil Wolf New York NY Pergamon Press 1964* (Vol. 1).

Bougrea, A., Van Coppenolle, H., Taghon, S., & Haesebrouck, T. (2008). Tackling the Global Energy Crisis. *IAEA Bulletin, September*, 50–51.

Boyapati, S., Wachsman, E. D., & Chakoumakos, B. C. (2001). Neutron diffraction study of occupancy and positional order of oxygen ions in phase stabilized cubic bismuth oxides. *Solid State Ionics*, *138*(3–4), 293–304. https://doi.org/10.1016/S0167-2738(00)00792-X

Boyapati, S., Wachsman, E. D., & Jiang, N. (2001). Effect of oxygen sublattice ordering on interstitial transport mechanism and conductivity activation energies in phase-stabilized cubic bismuth oxides. *Solid State Ionics*, *140*(1–2). https://doi.org/10.1016/S0167-2738(01)00698-1

Brandon, N. P., Ruiz-Trejo, E., & Boldrin, P. (2017). Solid Oxide Fuel Cell Lifetime and Reliability: Critical Challenges in Fuel Cells. In *Solid Oxide Fuel Cell Lifetime and Reliability: Critical Challenges in Fuel Cells*.

Brandstetter, S., Budrović, Ž., Van Petegem, S., Schmitt, B., Stergar, E., Derlet, P. M., & Van Swygenhoven, H. (2005). Temperature-dependent residual broadening of x-ray diffraction spectra in nanocrystalline plasticity. *Applied Physics Letters*, *87*(23). https://doi.org/10.1063/1.2138359

Brossard, F., Etgens, V. H., & Tadjeddine, A. (1997). In situ surface X-ray diffraction using a new electrochemical cell optimised for third generation synchrotron light sources. *Nuclear Instruments and Methods in Physics Research, Section B: Beam Interactions with Materials and Atoms*, *129*(3). https://doi.org/10.1016/S0168-583X(97)00285-1

Bunaciu, A. A., Udriştioiu, E. gabriela, & Aboul-Enein, H. Y. (2015). X-Ray Diffraction: Instrumentation and Applications. *Critical Reviews in Analytical Chemistry*, *45*(4), 289–299. https://doi.org/10.1080/10408347.2014.949616

Burgess, S., & Shepherd, I. W. (1977). Fluorescence suppression in time-resolved Raman spectra. *Journal of Physics E: Scientific Instruments*, *10*(6). https://doi.org/10.1088/0022-3735/10/6/015

Butz, B., Kruse, P., Störmer, H., Gerthsen, D., Müller, A., Weber, A., & Ivers-Tiffée, E. (2006). Correlation between microstructure and degradation in conductivity for cubic Y2O3-doped ZrO2. *Solid State Ionics*, *177*(37–38). https://doi.org/10.1016/j.ssi.2006.09.003

Caffrey, M., & Hing, F. S. (1987). A temperature gradient method for lipid phase diagram construction using time-resolved x-ray diffraction. *Biophysical Journal*, *51*(1), 37–46. https://doi.org/10.1016/S0006-3495(87)83309-X

Chao, D., Zhou, W., Xie, F., Ye, C., Li, H., Jaroniec, M., & Qiao, S. Z. (2020). Roadmap for advanced aqueous batteries: From design of materials to applications. *Science Advances*, *6*(21). https://doi.org/10.1126/sciadv.aba4098

Cherry, M., Islam, M. S., & Catlow, C. R. A. (1995). Oxygen ion migration in perovskite-type oxides. *Journal of Solid State Chemistry*, *118*(1). https://doi.org/10.1006/jssc.1995.1320

Choi, C., Ashby, D. S., Butts, D. M., DeBlock, R. H., Wei, Q., Lau, J., & Dunn, B. (2020). Achieving high energy density and high power density with pseudocapacitive materials. In *Nature Reviews Materials* (Vol. 5, Issue 1). https://doi.org/10.1038/s41578-019-0142-z

Choi, W., Shin, H. C., Kim, J. M., Choi, J. Y., & Yoon, W. S. (2020). Modeling and applications of electrochemical impedance spectroscopy (Eis) for lithium-ion batteries. In *Journal of Electrochemical Science and Technology* (Vol. 11, Issue 1). https://doi.org/10.33961/jecst.2019.00528

Cléton, F., Jouneau, P. H., Henry, S., Gäumann, M., & Buffat, P. A. (1999). Crystallographic orientation assessment by electron backscattered diffraction. *Scanning*, *21*(4). https://doi.org/10.1002/sca.4950210402

Colthup, N. (2012). Introduction to Infrared and Raman Spectroscopy - Norman Colthup - Google Books. In *The Delivery of Nanoparticles*.

Connolly, J. R. (2007). Introduction to X-ray Powder Diffraction. *Eps400-002*.

Corbel, G., Mestiri, S., & Lacorre, P. (2005). Physicochemical compatibility of CGO fluorite, LSM and LSCF perovskite electrode materials with La2Mo2O9 fast oxide-ion conductor. *Solid State Sciences*, *7*(10). https://doi.org/10.1016/j.solidstatesciences.2005.05.007

Coronado, E. A., & Schatz, G. C. (2003). Surface plasmon broadening for arbitrary shape nanoparticles: A geometrical probability approach. *Journal of Chemical Physics*, *119*(7). https://doi.org/10.1063/1.1587686

Costa-Nunes, O., Gorte, R. J., & Vohs, J. M. (2005). Comparison of the performance of Cu-CeO2-YSZ and Ni-YSZ composite SOFC anodes with H2, CO, and syngas. *Journal of Power Sources*, *141*(2). https://doi.org/10.1016/j.jpowsour.2004.09.022

Costentin, C., Drouet, S., Robert, M., & Savéant, J. M. (2012). Turnover numbers, turnover frequencies, and overpotential in molecular catalysis of electrochemical reactions. Cyclic voltammetry and preparative-scale electrolysis. *Journal of the American Chemical Society*, *134*(27). https://doi.org/10.1021/ja303560c

Coutelieris, F. A., Douvartzides, S., & Tsiakaras, P. (2003). The importance of the fuel choice on the efficiency of a solid oxide fuel cell system. *Journal of Power Sources*, *123*(2). https://doi.org/10.1016/S0378-7753(03)00559-7

D. Askeland, P. Fulay, and W. W. (2006). The Science and Engineering of Materials, Sixth Edition, CT. *Cengage Learning.Stamford*.

Dann, S. E., & Weller, M. T. (1995). Structure and oxygen stoichiometry in Sr3Co2O7-y (0.94 ≤ y ≤ 1.22). *Journal of Solid State Chemistry*, *115*(2). https://doi.org/10.1006/jssc.1995.1165

Davis, T., Johnson, M., & Billinge, S. J. L. (2013). Toward phase quantification at the nanoscale using the total scattering pair distribution function (TSPDF) method: Recrystallization of cryomilled sulfamerazine. *Crystal Growth and Design*, *13*(10). https://doi.org/10.1021/cg400179p

de Boer, B. (1998). SOFC Anode : Hydrogen Oxidation at Porous Nickel and Nickel/Yttria-Stabilised Zirconia Cermet Electrodes. In *Fuel Cells Bulletin* (Vol. 4, Issue 31).

Debye, P. (1915). Zerstreuung von Röntgenstrahlen. *Annalen Der Physik*, *351*(6). https://doi.org/10.1002/andp.19153510606

Debye, Peter, & Scherrer, P. (1916). Interferenz an regellos orientierten Teilchen im Röntgenlicht I. *Physikalische Zeitschrift*, *17*.

Dekker, A. J. (1957). Solid state physics. *Physics Today*, *10*(11), 38–40. https://doi.org/10.1063/1.3060172

Dietrich, B., & Dombrowski, K. F. (1999). Experimental challenges of stress measurements

with resonant micro-Raman spectroscopy. *Journal of Raman Spectroscopy*, *30*(10). https://doi.org/10.1002/(SICI)1097-4555(199910)30:10<893::AID-JRS468>3.0.CO;2-3

Dinnebier, R. E., Leineweber, A., & Evans, J. S. O. (2018). Rietveld refinement: Practical powder diffraction pattern analysis using TOPAS. In *Rietveld Refinement: Practical Powder Diffraction Pattern Analysis using TOPAS*. https://doi.org/10.1515/9783110461381

Doblhoff-Dier, K., & Koper, M. T. M. (2021). Modeling the Gouy-Chapman Diffuse Capacitance with Attractive Ion-Surface Interaction. *Journal of Physical Chemistry C*, *125*(30). https://doi.org/10.1021/acs.jpcc.1c02381

Dollase, W. A. (1985). Solid state chemistry and its applications by A. R. West . *Acta Crystallographica Section B Structural Science*, *41*(6). https://doi.org/10.1107/s0108768185002476

Drache, M., Obbade, S., Wignacourt, J. P., & Conflant, P. (1999). Structural and Conductivity Properties of Bi0.775Ln0.225O1.5Oxide Conductors (Ln=La, Pr, Nd, Sm, Eu, Gd, Tb, Dy) with Rhombohedral Bi-Sr-O Type. *Journal of Solid State Chemistry*, *142*(2), 349–359. https://doi.org/10.1006/jssc.1998.8043

Drache, Michel, Roussel, P., & Wignacourt, J. P. (2007). Structures and oxide mobility in Bi-Ln-O materials: Heritage of Bi2O3. *Chemical Reviews*, *107*(1), 80–96. https://doi.org/10.1021/cr050977s

Drude, P. (1900). Zur Elektronentheorie der Metalle. *Annalen Der Physik*, *306*(3). https://doi.org/10.1002/andp.19003060312

Duque, J. S., Blandón, J. S., & Riascos, H. (2017). Localized Plasmon resonance in metal nanoparticles using Mie theory. *Journal of Physics: Conference Series*, *850*(1). https://doi.org/10.1088/1742-6596/850/1/012017

Dykhne, T., Taylor, R., Florence, A., & Billinge, S. J. L. (2011). Data requirements for the reliable use of atomic pair distribution functions in amorphous pharmaceutical fingerprinting. *Pharmaceutical Research*, *28*(5). https://doi.org/10.1007/s11095-010-0350-0

Esmaily, M., Svensson, J. E., Fajardo, S., Birbilis, N., Frankel, G. S., Virtanen, S., Arrabal, R., Thomas, S., & Johansson, L. G. (2017). Fundamentals and advances in magnesium alloy corrosion. In *Progress in Materials Science* (Vol. 89). https://doi.org/10.1016/j.pmatsci.2017.04.011

Etgens, V. H., Martins Alves, M. C., & Tadjeddine, A. (1999). In situ surface X-ray diffraction studies of electrochemical interfaces at a high-energy third-generation synchrotron facility. *Electrochimica Acta*, *45*(4–5). https://doi.org/10.1016/S0013-4686(99)00237-6

Etsell, T. H., & Flengas, S. N. (1970). The electrical properties of solid oxide electrolytes. *Chemical Reviews*, *70*(3). https://doi.org/10.1021/cr60265a003

Fan, H. M., Fan, X. F., Ni, Z. H., Shen, Z. X., Feng, Y. P., & Zou, B. S. (2008). Orientation-dependent Raman spectroscopy of single wurtzite CdS nanowires. *Journal of Physical Chemistry C*, *112*(6). https://doi.org/10.1021/jp7096839

Fergus, J. W. (2006). Electrolytes for solid oxide fuel cells. *Journal of Power Sources*, *162*(1), 30–40. https://doi.org/10.1016/j.jpowsour.2006.06.062

Ferguson, J. D., Kim, Y., Kourkoutis, L. F., Vodnick, A., Woll, A. R., Muller, D. A., & Brock, J. D. (2011). Epitaxial oxygen getter for a brownmillerite phase transformation in manganite films. *Advanced Materials*, *23*(10). https://doi.org/10.1002/adma.201003581

Fernández, R., Ferreira-Barragáns, S., Ibáñez, J., & González-Doncel, G. (2018). A multi-scale analysis of the residual stresses developed in a single-phase alloy cylinder after quenching. *Materials and Design*, *137*. https://doi.org/10.1016/j.matdes.2017.10.013

Ferrari, A. C., Meyer, J. C., Scardaci, V., Casiraghi, C., Lazzeri, M., Mauri, F., Piscanec, S., Jiang, D., Novoselov, K. S., Roth, S., & Geim, A. K. (2006). Raman spectrum of graphene and graphene layers. *Physical Review Letters*, *97*(18). https://doi.org/10.1103/PhysRevLett.97.187401

Ferraro, J. R., Nakamoto, K., & Brown, C. W. (2003). Introductory Raman Spectroscopy: Second Edition. In *Introductory Raman Spectroscopy: Second Edition*. https://doi.org/10.1016/B978-0-12-254105-6.X5000-8

Fewster, P. F. (1999). Absolute lattice parameter measurement. *Journal of Materials Science:*

Materials in Electronics, *10*(3). https://doi.org/10.1023/A:1008935709977

Fewster, Paul F. (2018). Response to fraser & wark's comments on a new theory for X-ray diffraction. *Acta Crystallographica Section A: Foundations and Advances*, *74*(5). https://doi.org/10.1107/S2053273318007489

Fiederling, K., Abasifard, M., Richter, M., Deckert, V., Gräfe, S., & Kupfer, S. (2020). The chemical effect goes resonant-a full quantum mechanical approach on TERS. *Nanoscale*, *12*(11). https://doi.org/10.1039/c9nr09814c

Fultz, B., & Howe, J. M. (2008). Transmission electron microscopy and diffractometry of materials. In *Transmission Electron Microscopy and Diffractometry of Materials*. https://doi.org/10.1007/978-3-540-73886-2

Gao, P., Bolon, A., Taneja, M., Xie, Z., Orlovskaya, N., & Radovic, M. (2017). Thermal expansion and elastic moduli of electrolyte materials for high and intermediate temperature solid oxide fuel cell. *Solid State Ionics*, *300*. https://doi.org/10.1016/j.ssi.2016.11.015

Georges, S., Goutenoire, F., Altorfer, F., Sheptyakov, D., Fauth, F., Suard, E., & Lacorre, P. (2003). Thermal, structural and transport properties of the fast oxide-ion conductors La2-xRxMo2O9 (R=Nd, Gd, Y). *Solid State Ionics*, *161*(3–4). https://doi.org/10.1016/S0167-2738(03)00279-0

Geraldes, C. F. G. C. (2020). Introduction to infrared and raman-based biomedical molecular imaging and comparison with other modalities. In *Molecules* (Vol. 25, Issue 23). https://doi.org/10.3390/molecules25235547

Gerischer, H. (1951). Wechselstrompolarisation von Elektroden mit einem potentialbestimmenden Schritt beim Gleichgewichtspotential I. *Zeitschrift Für Physikalische Chemie*, *198*(1). https://doi.org/10.1515/zpch-1951-19824

Gil, V., Tartaj, J., Moure, C., & Durán, P. (2006). Sintering, microstructural development, and electrical properties of gadolinia-doped ceria electrolyte with bismuth oxide as a sintering aid. *Journal of the European Ceramic Society*, *26*(15). https://doi.org/10.1016/j.jeurceramsoc.2005.09.068

Gilmore, C. J., Barr, G., & Paisley, J. (2004). High-throughput powder diffraction. I. A new approach to qualitative and quantitative powder diffraction pattern analysis using full pattern profiles. *Journal of Applied Crystallography*, *37*(2). https://doi.org/10.1107/S002188980400038X

Gong, M., Liu, X., Trembly, J., & Johnson, C. (2007). Sulfur-tolerant anode materials for solid oxide fuel cell application. In *Journal of Power Sources* (Vol. 168, Issue 2). https://doi.org/10.1016/j.jpowsour.2007.03.026

Goodenough, J. B., Ruiz-Diaz, J. E., & Zhen, Y. S. (1990). Oxide-ion conduction in Ba2In2O5 and Ba3In2MO8 (M=Ce, Hf, or Zr). *Solid State Ionics*, *44*(1–2). https://doi.org/10.1016/0167-2738(90)90039-T

Goodenough, John B. (2003). Oxide-ion electrolytes. *Annual Review of Materials Research*, *33*, 91–128. https://doi.org/10.1146/annurev.matsci.33.022802.091651

Gorte, R. J., Vohs, J. M., & McIntosh, S. (2004). Recent developments on anodes for direct fuel utilization in SOFC. *Solid State Ionics*, *175*(1–4). https://doi.org/10.1016/j.ssi.2004.09.036

Goyal, A., Marcandalli, G., Mints, V. A., & Koper, M. T. M. (2020). Competition between CO2Reduction and Hydrogen Evolution on a Gold Electrode under Well-Defined Mass Transport Conditions. *Journal of the American Chemical Society*, *142*(9). https://doi.org/10.1021/jacs.9b10061

Guo, Z., Fu, T., & Fu, H. (2000). Crystal orientation measured by XRD and annotation of the butterfly diagram. *Materials Characterization*, *44*(4). https://doi.org/10.1016/S1044-5803(00)00084-X

Hammond, C. (2002). The Basics of Crystallography and Diffraction (2nd edn). *Measurement Science and Technology*, *13*(2). https://doi.org/10.1088/0957-0233/13/2/708

Hargittai, I. (2009). Christopher Hammond: The basics of crystallography and diffraction. Third edition. *Structural Chemistry*, *20*(4). https://doi.org/10.1007/s11224-009-9480-6

Harwig, H. A., & Gerards, A. G. (1979). The polymorphism of bismuth sesquioxide. *Thermochimica Acta*, *28*(1). https://doi.org/10.1016/0040-6031(79)87011-2

Hashida, T., Jeong, Y. G., Hua, Y., Hsu, S. L., & Paul, C. W. (2005). Spectroscopic study on morphology evolution in polymer blends. *Macromolecules*, *38*(7). https://doi.org/10.1021/ma047492a

Hattori, M., Takeda, Y., Sakaki, Y., Nakanishi, A., Ohara, S., Mukai, K., Lee, J. H., & Fukui, T. (2004). Effect of aging on conductivity of yttria stabilized zirconia. *Journal of Power Sources*, *126*(1–2). https://doi.org/10.1016/j.jpowsour.2003.08.018

Hoehse, M., Gornushkin, I., Merk, S., & Panne, U. (2011). Assessment of suitability of diode pumped solid state lasers for laser induced breakdown and Raman spectroscopy. *Journal of Analytical Atomic Spectrometry*, *26*(2). https://doi.org/10.1039/c0ja00038h

Hofmann, P. (2015). Solid State Physics: An Introduction. In *Wiley-VCH* (Vol. 53, Issue 9).

Hollins, P. (1988). Impedance spectroscopy: Emphasizing solid materials and systems. *Spectrochimica Acta Part A: Molecular Spectroscopy*, *44*(8). https://doi.org/10.1016/0584-8539(88)80155-7

Holze, R. (2002a). Book Review: Electrochemical Methods. Fundamentals and Applications (2nd Edition). By Allen J. Bard and Larry R. Faulkner. *Angewandte Chemie International Edition*, *41*(4). https://doi.org/10.1002/1521-3773(20020215)41:4<655::aid-anie655>3.0.co;2-i

Holze, R. (2002b). Book Review: Instrumental Methods in Electrochemistry. Edited by Southampton Electrochemistry Group. *Angewandte Chemie International Edition*, *41*(4). https://doi.org/10.1002/1521-3773(20020215)41:4<655::aid-anie1111655>3.0.co;2-a

Horvath, H. (2009). Gustav Mie and the scattering and absorption of light by particles: Historic developments and basics. *Journal of Quantitative Spectroscopy and Radiative Transfer*, *110*(11). https://doi.org/10.1016/j.jqsrt.2009.02.022

Huang, C. Y., Hsu, Y. C., Chen, J. G., Suryanarayanan, V., Lee, K. M., & Ho, K. C. (2006). The effects of hydrothermal temperature and thickness of TiO2 film on the performance of a dye-sensitized solar cell. *Solar Energy Materials and Solar Cells*, *90*(15). https://doi.org/10.1016/j.solmat.2006.03.012

Hummer, D. R., & Heaney, P. J. (2007). *Thermal expansion of anatase and rutile between 300*

and 575 K using synchrotron powder X-ray diffraction. 352–357. https://doi.org/10.1154/1.2790965

International Energy Agency. (2022). International Energy Agency (IEA) World Energy Outlook 2022. *Https://Www.Iea.Org/Reports/World-Energy-Outlook-2022/Executive-Summary*, 524. https://www.iea.org/reports/world-energy-outlook-2022

Ishihara, T., Kudo, T., Matsuda, H., & Takita, Y. (1995). Doped PrMnO3 Perovskite Oxide as a New Cathode of Solid Oxide Fuel Cells for Low Temperature Operation. *Journal of The Electrochemical Society*, *142*(5). https://doi.org/10.1149/1.2048606

Ishihara, T., Matsuda, H., & Takita, Y. (1994). Doped LaGaO3 Perovskite Type Oxide as a New Oxide Ionic Conductor. *Journal of the American Chemical Society*, *116*(9). https://doi.org/10.1021/ja00088a016

Iwahara, H., Esaka, T., Sato, T., & Takahashi, T. (1981). Formation of high oxide ion conductive phases in the sintered oxides of the system Bi2O3Ln2O3 (Ln = LaYb). *Journal of Solid State Chemistry*, *39*(2). https://doi.org/10.1016/0022-4596(81)90328-5

Jacob, R., Nair, H. G., & Isac, J. (2015). Structural and Morphological Studies of Nano-Crystalline Ceramic $BaSr_{0.9}Fe_{0.1}TiO_4$. *International Letters of Chemistry, Physics and Astronomy*, *44*. https://doi.org/10.18052/www.scipress.com/ilcpa.44.95

Jagtap, N., Bhagwat, M., Awati, P., & Ramaswamy, V. (2005). Characterization of nanocrystalline anatase titania: An in situ HTXRD study. *Thermochimica Acta*, *427*(1–2). https://doi.org/10.1016/j.tca.2004.08.011

Jang, I., Kim, S., Kim, C., Lee, H., Yoon, H., Song, T., & Paik, U. (2019). Interface engineering of yttrium stabilized zirconia/gadolinium doped ceria bi-layer electrolyte solid oxide fuel cell for boosting electrochemical performance. *Journal of Power Sources*, *435*. https://doi.org/10.1016/j.jpowsour.2019.226776

Jeon, T. Y., Kim, D. J., Park, S. G., Kim, S. H., & Kim, D. H. (2016). Nanostructured plasmonic substrates for use as SERS sensors. In *Nano Convergence* (Vol. 3, Issue 1). https://doi.org/10.1186/s40580-016-0078-6

Jesche, A., Fix, M., Kreyssig, A., Meier, W. R., & Canfield, P. C. (2016). X-Ray diffraction

on large single crystals using a powder diffractometer. *Philosophical Magazine*, *96*(20). https://doi.org/10.1080/14786435.2016.1192725

Jia, J., & Raabe, D. (2006). Evolution of crystallinity and of crystallographic orientation in isotactic polypropylene during rolling and heat treatment. *European Polymer Journal*, *42*(8). https://doi.org/10.1016/j.eurpolymj.2006.02.013

Jiang, N., Buchanan, R. M., Stevenson, D. A., Nix, W. D., Li, J. Z., & Yang, J. L. (1995). Anion ordering in aged stabilized bismuth oxide. *Materials Letters*, *22*(5–6). https://doi.org/10.1016/0167-577X(95)00271-5

Jiang, Naixiong, & Wachsman, E. D. (1999). Structural stability and conductivity of phase-stabilized cubic bismuth oxides. *Journal of the American Ceramic Society*, *82*(11). https://doi.org/10.1111/j.1151-2916.1999.tb02202.x

Jiang, S. P. (2008). Development of lanthanum strontium manganite perovskite cathode materials of solid oxide fuel cells: A review. *Journal of Materials Science*, *43*(21). https://doi.org/10.1007/s10853-008-2966-6

Jiang, S. P., & Chan, S. H. (2004). A review of anode materials development in solid oxide fuel cells. *Journal of Materials Science*, *39*(14). https://doi.org/10.1023/b:jmsc.0000034135.52164.6b

Jolley, A. G., Jayathilake, R., & Wachsman, E. D. (2019). Optimizing rhombohedral Bi2O3 conductivity for low temperature SOFC electrolytes. *Ionics*, *25*(8), 3531–3536. https://doi.org/10.1007/s11581-019-02920-x

Jung, N., Crowther, A. C., Kim, N., Kim, P., & Brus, L. (2010). Raman enhancement on graphene: Adsorbed and intercalated molecular species. *ACS Nano*, *4*(11). https://doi.org/10.1021/nn102227u

Juraić, K., Gracin, D., Šantić, B., Meljanac, D., Zorić, N., Gajović, A., Dubček, P., Bernstorff, S., & Čeh, M. (2010). GISAXS and GIWAXS analysis of amorphous-nanocrystalline silicon thin films. *Nuclear Instruments and Methods in Physics Research, Section B: Beam Interactions with Materials and Atoms*, *268*(3–4). https://doi.org/10.1016/j.nimb.2009.09.046

Kaban, I., Jóvári, P., Hoyer, W., & Welter, E. (2007). Determination of partial pair distribution functions in amorphous Ge15Te85 by simultaneous RMC simulation of diffraction and EXAFS data. *Journal of Non-Crystalline Solids*, *353*(24–25). https://doi.org/10.1016/j.jnoncrysol.2006.09.072

Kalinin, S. V., & Bonnell, D. A. (2002). Scanning impedance microscopy: From impedance spectra to impedance images. *Materials Research Society Symposium - Proceedings*, *699*. https://doi.org/10.1017/s1551929500050471

Kawada, T., Sakai, N., Yokokawa, H., Dokiya, M., Mori, M., & Iwata, T. (1990). Structure and polarization characteristics of solid oxide fuel cell anodes. *Solid State Ionics*, *40–41*(PART 1). https://doi.org/10.1016/0167-2738(90)90367-Z

Kawada, Tatsuya, Sakai, N., Yokokawa, H., Dokiya, M., Mori, M., & Iwata, T. (1990). Characteristics of Slurry-Coated Nickel Zirconia Cermet Anodes for Solid Oxide Fuel Cells. *Journal of The Electrochemical Society*, *137*(10). https://doi.org/10.1149/1.2086156

Keen, D. A., Tucker, M. G., & Dove, M. T. (2005). Reverse Monte Carlo modelling of crystalline disorder. *Journal of Physics Condensed Matter*, *17*(5 SPEC. ISS.). https://doi.org/10.1088/0953-8984/17/5/002

Keen, David A. (2001). A comparison of various commonly used correlation functions for describing total scattering. *Journal of Applied Crystallography*, *34*(2). https://doi.org/10.1107/S0021889800019993

Kendall, K., & Kendall, M. (2015). High-Temperature Solid Oxide Fuel Cells for the 21st Century: Fundamentals, Design and Applications: Second Edition. In *High-Temperature Solid Oxide Fuel Cells for the 21st Century: Fundamentals, Design and Applications: Second Edition*. https://doi.org/10.1016/C2011-0-09278-5

Kendrick, E., Islam, M. S., & Slater, P. R. (2007). Developing apatites for solid oxide fuel cells: Insight into structural, transport and doping properties. *Journal of Materials Chemistry*, *17*(30). https://doi.org/10.1039/b704426g

Kharton, V. V., Shaula, A. L., Patrakeev, M. V., Waerenborgh, J. C., Rojas, D. P., Vyshatko, N. P., Tsipis, E. V., Yaremchenko, A. A., & Marques, F. M. B. (2004). Oxygen Ionic and

Electronic Transport in Apatite-Type Solid Electrolytes. *Journal of The Electrochemical Society*, *151*(8). https://doi.org/10.1149/1.1768948

Kharton, Vladislav V., Marques, F. M. B., Kilner, J. A., & Atkinson, A. (2010). ChemInform Abstract: Oxygen Ion Conducting Materials. *ChemInform*, *41*(50). https://doi.org/10.1002/chin.201050212

Kharton, Vladislav V., Naumovich, E. N., Yaremchenko, A. A., & Marques, F. M. B. (2001). Research on the electrochemistry of oxygen ion conductors in the former Soviet Union - IV. Bismuth oxide-based ceramics. *Journal of Solid State Electrochemistry*, *5*(3). https://doi.org/10.1007/s100080000141

Khodaei, M., & Petaccia, L. (2017). X-ray Characterization of Nanostructured Energy Materials by Synchrotron Radiation. In *X-ray Characterization of Nanostructured Energy Materials by Synchrotron Radiation*. https://doi.org/10.5772/62715

Kilner, J. A., & Burriel, M. (2014). Materials for intermediate-temperature solid-oxide fuel cells. *Annual Review of Materials Research*, *44*, 365–393. https://doi.org/10.1146/annurev-matsci-070813-113426

Kirubakaran, A., Jain, S., & Nema, R. K. (2009). A review on fuel cell technologies and power electronic interface. In *Renewable and Sustainable Energy Reviews* (Vol. 13, Issue 9). https://doi.org/10.1016/j.rser.2009.04.004

Kneipp, K., Kneipp, H., Itzkan, I., Dasari, R. R., & Feld, M. S. (2002). Surface-enhanced Raman scattering and biophysics. In *Journal of Physics Condensed Matter* (Vol. 14, Issue 18). https://doi.org/10.1088/0953-8984/14/18/202

Kooij, E. S., Ahmed, W., Zandvliet, H. J. W., & Poelsema, B. (2011). Localized plasmons in noble metal nanospheroids. *Journal of Physical Chemistry C*, *115*(21). https://doi.org/10.1021/jp112085s

Koper, M. T. M. (2011). Thermodynamic theory of multi-electron transfer reactions: Implications for electrocatalysis. *Journal of Electroanalytical Chemistry*, *660*(2). https://doi.org/10.1016/j.jelechem.2010.10.004

Kramer, S. A., & Tuller, H. L. (1995). A novel titanate-based oxygen ion conductor:

Gd2Ti2O7. *Solid State Ionics*, *82*(1–2). https://doi.org/10.1016/0167-2738(95)00156-Z

Kramer, S., Spears, M., & Tuller, H. L. (1994). Conduction in titanate pyrochlores: role of dopants. *Solid State Ionics*, *72*(PART 2). https://doi.org/10.1016/0167-2738(94)90125-2

Kreibig, U. (1974). Electronic properties of small silver particles: The optical constants and their temperature dependence. *Journal of Physics F: Metal Physics*, *4*(7). https://doi.org/10.1088/0305-4608/4/7/007

Kudelski, A. (2008). Analytical applications of Raman spectroscopy. In *Talanta* (Vol. 76, Issue 1). https://doi.org/10.1016/j.talanta.2008.02.042

Kwak, W. J., Rosy, Sharon, D., Xia, C., Kim, H., Johnson, L. R., Bruce, P. G., Nazar, L. F., Sun, Y. K., Frimer, A. A., Noked, M., Freunberger, S. A., & Aurbach, D. (2020). Lithium-Oxygen Batteries and Related Systems: Potential, Status, and Future. In *ACS Applied Materials and Interfaces*. https://doi.org/10.1021/acs.chemrev.9b00609

Lacorre, P. (2000). The LPS concept, a new way to look at anionic conductors. *Solid State Sciences*, *2*(8). https://doi.org/10.1016/S1293-2558(00)01106-7

Langer, J., de Aberasturi, D. J., Aizpurua, J., Alvarez-Puebla, R. A., Auguié, B., Baumberg, J. J., Bazan, G. C., Bell, S. E. J., Boisen, A., Brolo, A. G., Choo, J., Cialla-May, D., Deckert, V., Fabris, L., Faulds, K., Javier García de Abajo, F., Goodacre, R., Graham, D., Haes, A. J., … Liz-Marzán, L. M. (2020). Present and future of surface-enhanced Raman scattering. In *ACS Nano* (Vol. 14, Issue 1). https://doi.org/10.1021/acsnano.9b04224

Lasia, A. (2014). Electrochemical impedance spectroscopy and its applications. In *Electrochemical Impedance Spectroscopy and its Applications* (Vol. 9781461489337). https://doi.org/10.1007/978-1-4614-8933-7

Lee, T. S., Chung, J. N., & Chen, Y. C. (2011). Design and optimization of a combined fuel reforming and solid oxide fuel cell system with anode off-gas recycling. *Energy Conversion and Management*, *52*(10). https://doi.org/10.1016/j.enconman.2011.05.009

Lekston, Z., & Zubko, M. (2016). X-ray diffraction studies of the reversible phase transformation in NiTi shape memory alloy. *Acta Physica Polonica A*, *130*(4). https://doi.org/10.12693/APhysPolA.130.1059

Leonardi, A. (2021). Whole pair distribution function modeling: The bridging of Bragg and Debye scattering theories. *IUCrJ*, *8*, 257–269. https://doi.org/10.1107/S2052252521000324

Leonardi, A., & Bish, D. L. (2017). Interactions of lattice distortion fields in nano polycrystalline materials revealed by molecular dynamics and X-ray powder diffraction. *Acta Materialia*, *133*. https://doi.org/10.1016/j.actamat.2017.04.072

Lian, J., Wang, L., Chen, J., Sun, K., Ewing, R. C., Farmer, J. M., & Boatner, L. A. (2003). The order-disorder transition in ion-irradiated pyrochlore. *Acta Materialia*, *51*(5). https://doi.org/10.1016/S1359-6454(02)00544-X

Liese, E. A., & Gemmen, R. S. (2005). Performance comparison of internal reforming against external reforming in a Solid Oxide Fuel Cell, gas turbine hybrid system. *Journal of Engineering for Gas Turbines and Power*, *127*(1). https://doi.org/10.1115/1.1788689

Liu, Z. (2021). FirePhysChem Review and prospect of thermal analysis technology applied to study thermal properties of energetic materials. *FirePhysChem*, *1*(3), 129–138. https://doi.org/10.1016/j.fpc.2021.05.002

Livneh, T., Zhang, J., Cheng, G., & Moskovits, M. (2006). Polarized Raman scattering from single GaN nanowires. *Physical Review B - Condensed Matter and Materials Physics*, *74*(3). https://doi.org/10.1103/PhysRevB.74.035320

Lu, C., Worrell, W. L., Vohs, J. M., & Gorte, R. J. (2003). A Comparison of Cu-Ceria-SDC and Au-Ceria-SDC Composites for SOFC Anodes. *Journal of The Electrochemical Society*, *150*(10). https://doi.org/10.1149/1.1608003

MacDonald, D. D. (2011). The history of the Point Defect Model for the passive state: A brief review of film growth aspects. *Electrochimica Acta*, *56*(4). https://doi.org/10.1016/j.electacta.2010.11.005

Mahato, N., Banerjee, A., Gupta, A., Omar, S., & Balani, K. (2015). Progress in material selection for solid oxide fuel cell technology: A review. *Progress in Materials Science*, *72*, 141–337. https://doi.org/10.1016/j.pmatsci.2015.01.001

Mancini, A., Shin, J. F., Orera, A., Slater, P. R., Tealdi, C., Ren, Y., Page, K. L., & Malavasi,

L. (2012). Insight into the local structure of barium indate oxide-ion conductors: An X-ray total scattering study. *Dalton Transactions*, *41*(1). https://doi.org/10.1039/c1dt11660f

Manikandan, V. S., Adhikari, B. R., & Chen, A. (2018). Nanomaterial based electrochemical sensors for the safety and quality control of food and beverages. In *Analyst* (Vol. 143, Issue 19). https://doi.org/10.1039/c8an00497h

McGreevy, R. L. (1995). RMC: progress, problems and prospects. *Nuclear Inst. and Methods in Physics Research, A*, *354*(1). https://doi.org/10.1016/0168-9002(94)00926-0

Michel, R., & Montella, C. (2015). Diffusion-convection impedance using an efficient analytical approximation of the mass transfer function for a rotating disk. *Journal of Electroanalytical Chemistry*, *736*. https://doi.org/10.1016/j.jelechem.2014.11.009

Minh, N. Q. (1993). Ceramic Fuel Cells. *Journal of the American Ceramic Society*, *76*(3). https://doi.org/10.1111/j.1151-2916.1993.tb03645.x

Minh, N. Q. (2004). Solid oxide fuel cell technology - Features and applications. In *Solid State Ionics* (Vol. 174, Issues 1–4). https://doi.org/10.1016/j.ssi.2004.07.042

Möbius, H. H. (1997). On the history of solid electrolyte fuel cells. *Journal of Solid State Electrochemistry*, *1*(1). https://doi.org/10.1007/s100080050018

Mori, M., Tompsett, G. M., Sammes, N. M., Suda, E., & Takeda, Y. (2003). Compatibility of GdxTi2O7 pyrochlores (1.72≤x≤2.0) as electrolytes in high-temperature solid oxide fuel cells. *Solid State Ionics*, *158*(1–2). https://doi.org/10.1016/S0167-2738(02)00761-0

Müller-Buschbaum, P. (2009). Applications of Synchrotron Light to Scattering and Diffraction in Materials and Life Sciences: A Basic Introduction to Grazing Incidence Small-Angle X-Ray Scattering. *Lect. Notes in Phys.*, *776*.

Naik, G. V., Kim, J., & Boltasseva, A. (2011). Oxides and nitrides as alternative plasmonic materials in the optical range [Invited]. *Optical Materials Express*, *1*(6). https://doi.org/10.1364/ome.1.001090

Naik, G. V., Shalaev, V. M., & Boltasseva, A. (2013). Alternative plasmonic materials: Beyond gold and silver. In *Advanced Materials* (Vol. 25, Issue 24). https://doi.org/10.1002/adma.201205076

Naqash, S., Gerhards, M. T., Tietz, F., & Guillon, O. (2018). Coefficients of thermal expansion of al-and y-substituted nasicon solid solution na3+2x alx yx zr2−2x si2 po12. *Batteries*, *4*(3). https://doi.org/10.3390/batteries4030033

Nelson, A. (2012). Elementary Scattering Theory for X-ray and Neutron Users. *Neutron News*, *23*(1). https://doi.org/10.1080/10448632.2012.645434

Nernst, W. (1899). About the electrolytic conduction of solid body at very high temperatures. *Z. Elektrochem.*, *6*(2).

Nikolic, J., Expósito, E., Iniesta, J., González-García, J., & Montiel, V. (2000). Theoretical Concepts and Applications of a Rotating Disk Electrode. *Journal of Chemical Education*, *77*(9). https://doi.org/10.1021/ed077p1191

Ogle, K. (2019). Atomic emission spectroelectrochemistry: Real-time rate measurements of dissolution, corrosion, and passivation. In *Corrosion* (Vol. 75, Issue 12). https://doi.org/10.5006/3336

Olaj, O. F., & Pelinka, K. H. (1976). Pair distribution function and pair potential of lattice model chains under theta conditions, 1. Numerical evaluation. *Die Makromolekulare Chemie*, *177*(11). https://doi.org/10.1002/macp.1976.021771123

Oleinick, A., Svir, I., & Amatore, C. (2019). A few key theoretical issues of importance in modern molecular electrochemistry. In *Current Opinion in Electrochemistry* (Vol. 13). https://doi.org/10.1016/j.coelec.2018.10.008

Orlando, A., Franceschini, F., Muscas, C., Pidkova, S., Bartoli, M., Rovere, M., & Tagliaferro, A. (2021). A comprehensive review on Raman spectroscopy applications. *Chemosensors*, *9*(9), 1–28. https://doi.org/10.3390/chemosensors9090262

Ormerod, R. M. (2003). Solid oxide fuel cells. *Chemical Society Reviews*, *32*(1), 17–28. https://doi.org/10.1039/b105764m

Ozlu Torun, H., Cakar, S., Ersoy, E., & Turkoglu, O. (2015). The bulk electrical conductivity properties of δ-Bi2O3 solid electrolyte system doped with Yb2O3. *Journal of Thermal Analysis and Calorimetry*, *122*(2). https://doi.org/10.1007/s10973-015-4785-8

P.J. Hendra, & Stratton, P. M. (1968). *LASER-RAMAN SPECTROSCOPY*. *4*.

Pappas, N. (2006). Calculating Retained Austenite in Steel Post Magnetic Processing Using X-Ray Diffraction. *B.S. Undergraduate Mathematics Exchange*, *4*(1).

Park, J. Y., Yoon, H., & Wachsman, E. D. (2005). Fabrication and characterization of high-conductivity bilayer electrolytes for intermediate-temperature solid oxide fuel cells. *Journal of the American Ceramic Society*, *88*(9). https://doi.org/10.1111/j.1551-2916.2005.00475.x

Pathak, P. D., & Vasavada, N. G. (1970). Thermal expansion of NaCl, KCl and CsBr by X-ray diffraction and the law of corresponding states. *Acta Crystallographica Section A*, *26*(6). https://doi.org/10.1107/S0567739470001602

Patterson, A. L. (1939). The scherrer formula for X-ray particle size determination. *Physical Review*, *56*(10). https://doi.org/10.1103/PhysRev.56.978

Pederson, R. (2002). *Microstructure and Phase Transformation of Ti-6Al-4V*.

Perry Murray, E., Tsai, T., & Barnett, S. A. (1999). A direct-methane fuel cell with a ceria-based anode. *Nature*, *400*(6745). https://doi.org/10.1038/23220

Pierret, R. F. (1987). Advanced Semiconductor Fundamentals. *Book*, *121*(7).

Pirovano, C., Vannier, R. N., Capoen, E., Nowogrocki, G., Boivin, J. C., Mairesse, G., Anne, M., Dooryhee, E., & Strobel, P. (2003). Characterisation of the electrode-electrolyte BIMEVOX system for oxygen separation: Part I. In situ synchrotron study. *Solid State Ionics*, *159*(1–2). https://doi.org/10.1016/S0167-2738(03)00077-8

Placke, T., Kloepsch, R., Dühnen, S., & Winter, M. (2017). Lithium ion, lithium metal, and alternative rechargeable battery technologies: the odyssey for high energy density. *Journal of Solid State Electrochemistry*, *21*(7). https://doi.org/10.1007/s10008-017-3610-7

Poornima Parvathi, V., Parimaladevi, R., Sathe, V., & Mahalingam, U. (2019). Graphene boosted silver nanoparticles as surface enhanced Raman spectroscopic sensors and photocatalysts for removal of standard and industrial dye contaminants. *Sensors and Actuators, B: Chemical*, *281*. https://doi.org/10.1016/j.snb.2018.11.007

Price, R., Cassidy, M., Grolig, J. G., Longo, G., Weissen, U., Mai, A., & Irvine, J. T. S. (2021).

Upscaling of Co-Impregnated La0.20Sr0.25Ca0.45TiO3 Anodes for Solid Oxide Fuel Cells: A Progress Report on a Decade of Academic-Industrial Collaboration. *Advanced Energy Materials*, *11*(15). https://doi.org/10.1002/aenm.202003951

Przenioslo, R., Sosnowska, I., Hohlwein, D., Hauß, T., & Troyanchuk, I. O. (1999). Magnetic ordering in the manganese perovskite CaMn7O12. *Solid State Communications*, *111*(12). https://doi.org/10.1016/S0038-1098(99)00269-0

Putnam, C. D., Hammel, M., Hura, G. L., & Tainer, J. A. (2007). X-ray solution scattering (SAXS) combined with crystallography and computation: Defining accurate macromolecular structures, conformations and assemblies in solution. In *Quarterly Reviews of Biophysics* (Vol. 40, Issue 3). https://doi.org/10.1017/S0033583507004635

Raman, S. C. V. (1941). New methods in the study of light scattering - Part I. Basic ideas. *Proceedings of the Indian Academy of Sciences - Section A*, *14*(3). https://doi.org/10.1007/BF03046063

Razeghi, M. (2018). Fundamentals of solid state engineering. In *Fundamentals of Solid State Engineering*. https://doi.org/10.1007/978-3-319-75708-7

Rebuffi, L., Troian, A., Ciancio, R., Carlino, E., Amimi, A., Leonardi, A., & Scardi, P. (2016). On the reliability of powder diffraction Line Profile Analysis of plastically deformed nanocrystalline systems. *Scientific Reports*, *6*. https://doi.org/10.1038/srep20712

Rodrigues, S., Munichandraiah, N., & Shukla, A. K. (1999). AC impedance and state-of-charge analysis of a sealed lithium-ion rechargeable battery. *Journal of Solid State Electrochemistry*, *3*(7–8). https://doi.org/10.1007/s100080050173

Rohleder, D., Kocherscheidt, G., Gerber, K., Kiefer, W., Köhler, W., Möcks, J., & Petrich, W. (2005). Comparison of mid-infrared and Raman spectroscopy in the quantitative analysis of serum. *Journal of Biomedical Optics*, *10*(3). https://doi.org/10.1117/1.1911847

Rowley-Neale, S. J., Randviir, E. P., Abo Dena, A. S., & Banks, C. E. (2018). An overview of recent applications of reduced graphene oxide as a basis of electroanalytical sensing platforms. In *Applied Materials Today* (Vol. 10). https://doi.org/10.1016/j.apmt.2017.11.010

Sansom, J. E. H., Richings, D., & Slater, P. R. (2001). Powder neutron diffraction study of the oxide-ion-conducting apatite-type phases, La9.33Si6O26 and La8Sr2Si6O26. *Solid State Ionics*, *139*(3–4). https://doi.org/10.1016/S0167-2738(00)00835-3

Sansom, J. E. H., & Slater, P. R. (2004). Oxide ion conductivity in the mixed Si/Ge apatite-type phases La 9.33Si6-xGexO26. *Solid State Ionics*, *167*(1–2). https://doi.org/10.1016/j.ssi.2003.12.015

Scherer, P. O. J. (2017). *Graduate Texts in Physics Computational Physics*.

Schmidt, C., Rittmeier-Kettner, M., Becker, H., Ellert, J., Krombach, R., & Schneider, G. M. (1994). Differential thermal analysis (DTA) and differential scanning calorimetry (DSC) at high pressures. Experimental techniques and selected results. *Thermochimica Acta*, *238*(C). https://doi.org/10.1016/S0040-6031(94)85217-0

Schober, T., & Friedrich, J. (1998). The oxygen and proton conductor Ba2In2O5: Thermogravimetry of proton uptake. *Solid State Ionics*, *113–115*. https://doi.org/10.1016/s0167-2738(98)00302-6

Schober, T., Friedrich, J., & Krug, F. (1997). Phase transition in the oxygen and proton conductor Ba2In2O5 in humid atmospheres below 300°C. *Solid State Ionics*, *99*(1–2). https://doi.org/10.1016/s0167-2738(97)00203-8

Sedigh Rahimabadi, P., Khodaei, M., & Koswattage, K. R. (2020). Review on applications of synchrotron-based X-ray techniques in materials characterization. *X-Ray Spectrometry*, *49*(3), 348–373. https://doi.org/10.1002/xrs.3141

Sekar, S. K. V., Mosca, S., Farina, A., Martelli, F., Taroni, P., Valentini, G., Cubeddu, R., & Pifferi, A. (2017). Frequency offset Raman spectroscopy (FORS) for depth probing of diffusive media. *Optics Express*, *25*(5). https://doi.org/10.1364/oe.25.004585

Selçuk, A., Merere, G., & Atkinson, A. (2001). The influence of electrodes on the strength of planar zirconia solid oxide fuel cells. *Journal of Materials Science*, *36*(5). https://doi.org/10.1023/A:1004833909780

Shao, Z., Zhou, W., & Zhu, Z. (2012). Advanced synthesis of materials for intermediate-temperature solid oxide fuel cells. In *Progress in Materials Science* (Vol. 57, Issue 4).

https://doi.org/10.1016/j.pmatsci.2011.08.002

Sharma, B., Frontiera, R. R., Henry, A. I., Ringe, E., & Van Duyne, R. P. (2012). SERS: Materials, applications, and the future. In *Materials Today* (Vol. 15, Issues 1–2). https://doi.org/10.1016/S1369-7021(12)70017-2

Sharma, R., Bisen, D. P., Shukla, U., & Sharma, B. G. (2012). X-ray diffraction: a powerful method of characterizing nanomaterials. *Recent Research in Science and Technology*, *4*(8).

Shiman, O., Gerbreders, V., Sledevskis, E., & Bulanovs, A. (2012). Selective wet-etching of amorphous/crystallized Sb-Se thin films. *Latvian Journal of Physics and Technical Sciences*, *49*(2). https://doi.org/10.2478/v10047-012-0010-8

Shuk, P., Wiemhöfer, H. D., Guth, U., Göpel, W., & Greenblatt, M. (1996). Oxide ion conducting solid electrolytes based on Bi2O3. *Solid State Ionics*, *89*(3–4), 179–196. https://doi.org/10.1016/0167-2738(96)00348-7

Singh, B., Ghosh, S., Aich, S., & Roy, B. (2017). Low temperature solid oxide electrolytes (LT-SOE): A review. *Journal of Power Sources*, *339*, 103–135. https://doi.org/10.1016/j.jpowsour.2016.11.019

Singhal, S. C. (2002). Solid oxide fuel cells for stationary, mobile, and military applications. *Solid State Ionics*, *152–153*. https://doi.org/10.1016/S0167-2738(02)00349-1

Sivia, D. S. (2011). Elementary Scattering Theory for X-ray and Neutron Users. In *Neutron News* (Vol. 23, Issue 1).

Skafte, T. L., Hjelm, J., Blennow, P., & Graves, C. (2016). Quantitative review of degradation and lifetime of solid oxide cells and stacks. *EFCF 2016 Proceedings, B0501*.

Slodczyk, A., Torrell, M., Hornés, A., Morata, A., Kendall, K., & Tarancón, A. (2018). Understanding longitudinal degradation mechanisms of large-area micro-tubular solid oxide fuel cells. *Electrochimica Acta*, *265*. https://doi.org/10.1016/j.electacta.2018.01.184

Smith, E., & Dent, G. (2019). Modern raman spectroscopy: A practical approach. In *Modern Raman Spectroscopy: A Practical Approach*. https://doi.org/10.1002/0470011831

Stambouli, A. B., & Traversa, E. (2002). Solid oxide fuel cells (SOFCs): A review of an environmentally clean and efficient source of energy. In *Renewable and Sustainable Energy Reviews* (Vol. 6, Issue 5). https://doi.org/10.1016/S1364-0321(02)00014-X

Stamenkovic, V. R., Strmcnik, D., Lopes, P. P., & Markovic, N. M. (2016). Energy and fuels from electrochemical interfaces. In *Nature Materials* (Vol. 16, Issue 1). https://doi.org/10.1038/nmat4738

Stöckle, R. M., Suh, Y. D., Deckert, V., & Zenobi, R. (2000). Nanoscale chemical analysis by tip-enhanced Raman spectroscopy. *Chemical Physics Letters*, *318*(1–3). https://doi.org/10.1016/S0009-2614(99)01451-7

Subbaiah, Y. P. V., Prathap, P., & Reddy, K. T. R. (2006). Structural, electrical and optical properties of ZnS films deposited by close-spaced evaporation. *Applied Surface Science*, *253*(5). https://doi.org/10.1016/j.apsusc.2006.04.063

Subramanian, M. A., Aravamudan, G., & Subba Rao, G. V. (1983). Oxide pyrochlores - A review. In *Progress in Solid State Chemistry* (Vol. 15, Issue 2). https://doi.org/10.1016/0079-6786(83)90001-8

Sun, C., Hui, R., & Roller, J. (2010). Cathode materials for solid oxide fuel cells: A review. *Journal of Solid State Electrochemistry*, *14*(7). https://doi.org/10.1007/s10008-009-0932-0

Sun, Y., He, S., Saunders, M., Chen, K., Shao, Z., & Jiang, S. P. (2021). A comparative study of surface segregation and interface of La0·6Sr0·4Co0·2Fe0·8O3-δ electrode on GDC and YSZ electrolytes of solid oxide fuel cells. *International Journal of Hydrogen Energy*, *46*(2), 2606–2616. https://doi.org/10.1016/j.ijhydene.2020.10.113

Takahashi, T., Iwahara, H., & Arao, T. (1975). High oxide ion conduction in sintered oxides of the system Bi2O3-Y2O3. *Journal of Applied Electrochemistry*, *5*(3). https://doi.org/10.1007/BF01637268

Takata, M., Nishibori, E., Umeda, B., Sakata, M., Ohno, M., Shinohara, H., & Saito, Y. (1996). Determination of the endohedral nature of the metallofullerene Y@C 82 by MEM . *Acta Crystallographica Section A Foundations of Crystallography*, *52*(a1). https://doi.org/10.1107/s0108767396083377

Tallman, D. E., Spinks, G., Dominis, A., & Wallace, G. G. (2002). Electroactive conducting polymers for corrosion control. *Journal of Solid State Electrochemistry*, *6*(2). https://doi.org/10.1007/s100080100212

Tatsuki, T., Adachi, S., Itoh, M., Tamura, T., Wu, X. J., Jin, C. Q., Koshizuka, N., & Tanabe, K. (1995). High-pressure synthesis of superconducting (Ca, K)2 CuO2Cl2. *Physica C: Superconductivity and Its Applications*, *255*(1–2). https://doi.org/10.1016/0921-4534(95)00587-0

Taylor, M. A., Kilo, M., Borchardt, G., Weber, S., & Scherrer, H. (2005). 96Zr diffusion in polycrystalline scandia stabilized zirconia. *Journal of the European Ceramic Society*, *25*(9). https://doi.org/10.1016/j.jeurceramsoc.2004.05.020

Thompson, P., Cox, D. E., & Hastings, J. B. (1987). Rietveld refinement of Debye–Scherrer synchrotron X-ray data from Al2O3. *Journal of Applied Crystallography*, *20*(2). https://doi.org/10.1107/S0021889887087090

Tilley, R. (2004). Understanding Solids; The Science of Materials. *Materials Technology*, *19*(4). https://doi.org/10.1080/10667857.2004.11753095

Toraya, H. (2016). Introduction to X-ray analysis using the diffraction method. *Rigaku Journal*, *32*(2).

Tsuneda, T., Iwasa, T., & Taketsugu, T. (2019). Roles of silver nanoclusters in surface-enhanced Raman spectroscopy. *Journal of Chemical Physics*, *151*(9). https://doi.org/10.1063/1.5111944

Tuinstra, F., & Koenig, J. L. (1970). RAMAN SPECTRUM OF GRAPHITE. *Journal of Chemical Physics*, *53*(3). https://doi.org/10.1063/1.1674108

Ungár, T. (1998). Strain broadening caused by dislocations. *Materials Science Forum*, *278–281*(PART 1). https://doi.org/10.4028/www.scientific.net/msf.278-281.151

Ungár, T., Révész, Á., & Borbély, A. (1998). Dislocations and Grain Size in Electrodeposited Nanocrystalline Ni Determined by the Modified Williamson-Hall and Warren-Averbach Procedures. *Journal of Applied Crystallography*, *31*(4). https://doi.org/10.1107/S0021889897019559

Usher, T. M., Olds, D., Liu, J., & Page, K. (2018). A numerical method for deriving shape functions of nanoparticles for pair distribution function refinements. *Acta Crystallographica Section A: Foundations and Advances*, *74*(4). https://doi.org/10.1107/S2053273318004977

Van Overbeke, E., Devaux, J., Legras, R., Carter, J. T., McGrail, P. T., & Carlier, V. (2003). Phase separation in epoxy-copolyethersulphone blends: Morphologies and local characterisation by micro-Raman spectroscopy. *Polymer*, *44*(17). https://doi.org/10.1016/S0032-3861(03)00484-1

Verkerk, M. J., & Burggraaf, A. J. (1981). High Oxygen Ion Conduction in Sintered Oxides of the Bi2 O 3 - Dy2 O 3 System. *Journal of The Electrochemical Society*, *128*(1). https://doi.org/10.1149/1.2127391

Vivier, V., & Orazem, M. E. (2022). *Impedance Analysis of Electrochemical Systems*. https://doi.org/10.1021/acs.chemrev.1c00876

Walker, C. T. (1967). Solid State Physics over 13 Years: Introduction to Solid State Physics . Charles Kittel. Wiley, New York, ed. 3, 1966. 662 pp., illus. $12.50. . *Science*, *155*(3765). https://doi.org/10.1126/science.155.3765.991.b

Wang, F., Lyu, Y., Chu, D., Jin, Z., Zhang, G., & Wang, D. (2019). The electrolyte materials for SOFCs of low-intermediate temperature: review. In *Materials Science and Technology (United Kingdom)* (Vol. 35, Issue 13). https://doi.org/10.1080/02670836.2019.1639008

Wartak, M. S., & Fong, C.-Y. (2019). Bragg's Law. In *Field Guide to Solid State Physics*. https://doi.org/10.1117/3.2510243.ch16

Watson, W., & Orazem, M. E. (2020). EIS: Measurement Model Program. *Can Be Found under Ecsarxiv.Org/Kze9x*, *{MA}2020-0*(20).

Weertman, J. R. (1993). Hall-Petch strengthening in nanocrystalline metals. *Materials Science and Engineering A*, *166*(1–2), 161–167. https://doi.org/10.1016/0921-5093(93)90319-A

Wermelinger, T., Charpentier, C., Yüksek, M. D., & Spolenak, R. (2009). Measuring stresses in thin metal films by means of Raman microscopy using silicon as a strain gage material. *Journal of Raman Spectroscopy*, *40*(12). https://doi.org/10.1002/jrs.2332

West, A. (2014). Solid State Chemistry and its Applications, 2nd Edition, Student Edition. In *WILEY*.

West, A. R. (2014). Solid State Chemistry and its Applications. In *Solid State Chemistry*.

Whittingham, M. (1989). Basic solid state chemistry Anthony R. West, John Wiley & Sons, New York (1988), 415 pages £13.95 ($32.95). *Solid State Ionics*, *34*(3). https://doi.org/10.1016/0167-2738(89)90043-x

Williamson, G. K., & Hall, W. H. (1953). X-ray line broadening from filed aluminium and wolfram. *Acta Metallurgica*, *1*(1), 22–31. https://doi.org/10.1016/0001-6160(53)90006-6

Willmott, P. (2011). An introduction to synchrotron radiation: Techniques and applications. In *An Introduction to Synchrotron Radiation: Techniques and Applications*. https://doi.org/10.1002/9781119970958

Winter, C. (2000). *Efficiently Optimizing Manufacturing Processes Using Iterative Taguchi Analysis*. *45227*(513), 1–4.

Wood, E. A. (1964). Vocabulary of surface crystallography. *Journal of Applied Physics*, *35*(4). https://doi.org/10.1063/1.1713610

Wuensch, B. J., & Eberman, K. W. (2000). Order-disorder phenomena in A2B2O7 pyrochlore oxides. *JOM*, *52*(7). https://doi.org/10.1007/s11837-000-0155-4

Xia, C., Qiao, Z., Feng, C., Kim, J. S., Wang, B., & Zhu, B. (2017). Study on zinc oxide-based electrolytes in low-temperature solid oxide fuel cells. *Materials*, *11*(1). https://doi.org/10.3390/ma11010040

Yamamoto, O. (2000). Solid oxide fuel cells: Fundamental aspects and prospects. *Electrochimica Acta*, *45*(15–16). https://doi.org/10.1016/S0013-4686(00)00330-3

Yamamura, H., Yamazaki, K. I., Kakinuma, K., & Nomura, K. (2002). The relationship between crystal structure and electrical conductivity in the LaY1-xInxO3 (x=0.0-0.7) system. *Solid State Ionics*, *150*(3–4). https://doi.org/10.1016/S0167-2738(02)00521-0

Yang, D., & Ying, Y. (2011). Applications of raman spectroscopy in agricultural products and food analysis: A review. In *Applied Spectroscopy Reviews* (Vol. 46, Issue 7).

https://doi.org/10.1080/05704928.2011.593216

Yao, T., Uchimoto, Y., Kinuhata, M., Inagaki, T., & Yoshida, H. (2000). Crystal structure of Ga-doped Ba2In2O5 and its oxide ion conductivity. *Solid State Ionics*, *132*(3). https://doi.org/10.1016/s0167-2738(00)00658-5

Yaremchenko, A. A., Kharton, V. V., Naumovich, E. N., & Tonoyan, A. A. (2000). Stability of δ-Bi2O3-based solid electrolytes. *Materials Research Bulletin*, *35*(4). https://doi.org/10.1016/S0025-5408(00)00237-3

Yasuda, I., Matsuzaki, Y., Yamakawa, T., & Koyama, T. (2000). Electrical conductivity and mechanical properties of alumina-dispersed doped lanthanum gallates. *Solid State Ionics*, *135*(1–4). https://doi.org/10.1016/S0167-2738(00)00473-2

Yoo, W. S., Kim, J. H., & Han, S. M. (2014). Multiwavelength Raman characterization of silicon stress near through-silicon vias and its inline monitoring applications. *Journal of Micro/Nanolithography, MEMS, and MOEMS*, *13*(1). https://doi.org/10.1117/1.jmm.13.1.011205

Zakaria, Z., Awang Mat, Z., Abu Hassan, S. H., & Boon Kar, Y. (2020). A review of solid oxide fuel cell component fabrication methods toward lowering temperature. In *International Journal of Energy Research* (Vol. 44, Issue 2). https://doi.org/10.1002/er.4907

Zakaria, Z., & Kamarudin, S. K. (2021). Advanced modification of scandia-stabilized zirconia electrolytes for solid oxide fuel cells application—A review. In *International Journal of Energy Research* (Vol. 45, Issue 4). https://doi.org/10.1002/er.6206

Zarabi Golkhatmi, S., Asghar, M. I., & Lund, P. D. (2022). A review on solid oxide fuel cell durability: Latest progress, mechanisms, and study tools. *Renewable and Sustainable Energy Reviews*, *161*(January), 112339. https://doi.org/10.1016/j.rser.2022.112339

Zhang, Y., Colella, R., Kycia, S., & Goldman, A. I. (2002). Absolute structure-factor measurements of an Al-Pd-Mn quasicrystal. *Acta Crystallographica Section A: Foundations of Crystallography*, *58*(4). https://doi.org/10.1107/S0108767302007985

Zhao, F., Wang, W., Zhong, H., Yang, F., Fu, W., Ling, Y., & Zhang, Z. (2021). Robust

quantitative SERS analysis with Relative Raman scattering intensities. *Talanta*, *221*. https://doi.org/10.1016/j.talanta.2020.121465

Zhao, Q., & Wagner, H. D. (2004). Raman spectroscopy of carbon-nanotube-based composites. In *Philosophical Transactions of the Royal Society A: Mathematical, Physical and Engineering Sciences* (Vol. 362, Issue 1824). https://doi.org/10.1098/rsta.2004.1447

Zhu, B., Yun, S., & Lund, P. D. (2018). Semiconductor-ionic materials could play an important role in advanced fuel-to-electricity conversion. In *International Journal of Energy Research* (Vol. 42, Issue 11). https://doi.org/10.1002/er.4105

Zhu, H., Kee, R. J., Janardhanan, V. M., Deutschmann, O., & Goodwin, D. G. (2005). Modeling Elementary Heterogeneous Chemistry and Electrochemistry in Solid-Oxide Fuel Cells. *Journal of The Electrochemical Society*, *152*(12). https://doi.org/10.1149/1.2116607

Zhu, L., Zhang, L., Zhao, F., & Virkar, A. V. (2014). Concepts for Ultra-High Power Density Solid Oxide Fuel Cells (SOFC). *ECS Transactions*, *61*(1). https://doi.org/10.1149/06101.0177ecst

Supplementary Information

X-ray diffraction

Laboratory experimental data analysis:

5.1.7 8.5 – 10 mol % dopant concentration:

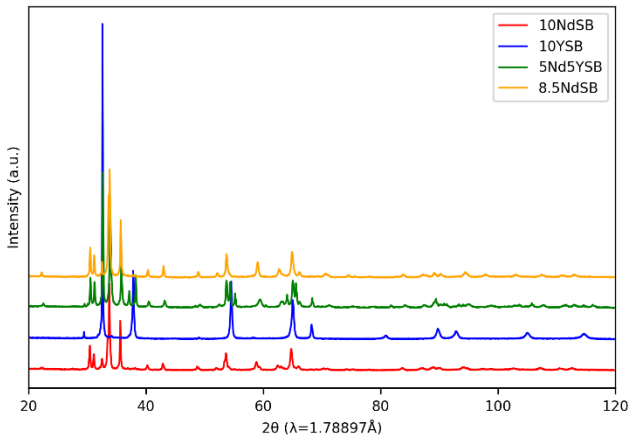


Figure 5.1.82:The XRD patterns obtained for all samples within the 8.5 – 10 mol % dopant concentration range using the D2 phaser.

The above figure, figure 5.1.86 shows the XRD patterns obtained for both single doped samples, as well as a double doped sample using the laboratory X-ray diffractometer, the D2 phaser. From the diffractogram obtained, it is observed that the two single doped samples with Nd as the dopant, namely 8.5NdSB, as well as 10NdSB both indicated a mixture of phases with the samples, contrary to what was obtained by the study conducted by Jolley et al. (Jolley et al., 2019). The 8.5NdSB sample co-existed as a majorly rhombohedral sample, with the presence of minor phases, namely the tetragonal and cubic phases. The 10NdSB sample co-existed as a majorly rhombohedral sample, with the presence of a minor phase, namely the monoclinic phase. The 10YSB sample was also studied and yielded a purely cubic sample. A double doped sample, the 5Nd5YSB sample was also studied and was found to co-existed as a majorly rhombohedral sample, with the presence of a monoclinic minor phase.

5.1.8 20 mol % dopant concentration:

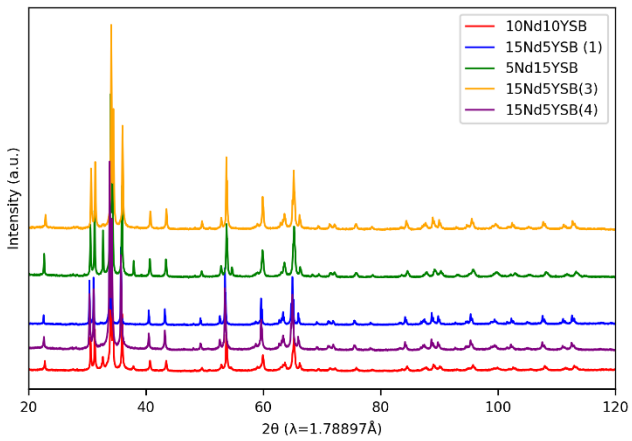


Figure 5.1.83:The XRD patterns obtained for all samples within the 20 mol % dopant concentration range using the D2 phaser.

Figure 5.1.87 shows the XRD patterns obtained for double doped sample using the laboratory X-ray diffractometer, the D2 phaser. From the diffractogram obtained, it is observed that the 10Nd10YSB sample co-existed as a majorly rhombohedral sample, with the presence of minor phases, namely the monoclinic and tetragonal phases. All 15Nd5YSB samples existed as pure rhombohedral phase samples, with the labels (1), (3) & (4) different samples synthesised with the same composition just at different times.

5.1.9 17.5 mol% dopant concentration:

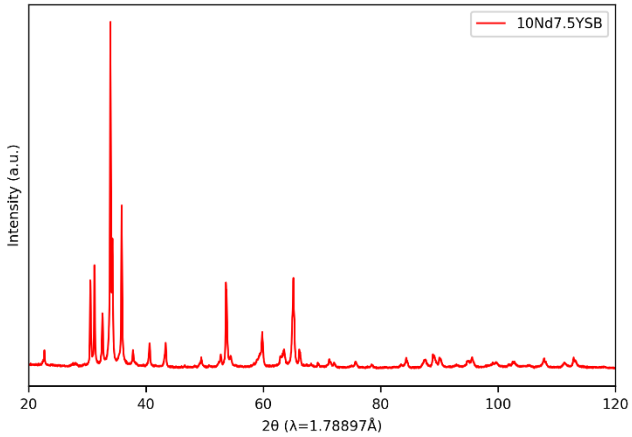


Figure 5.1.84: The XRD patterns obtained for all samples within the 17.5 mol % dopant concentration range for the double-doped samples using the D2 phaser.

Figure 5.1.88 above is representative of the XRD pattern obtained for a double doped sample using the laboratory X-ray diffractometer, the D2 phaser. The diffractogram obtained, indicates that the 10Nd7.5YSB sample existed as a pure rhombohedral phase sample.

5.1.10 22.5 mol % dopant concentration (double-doped):

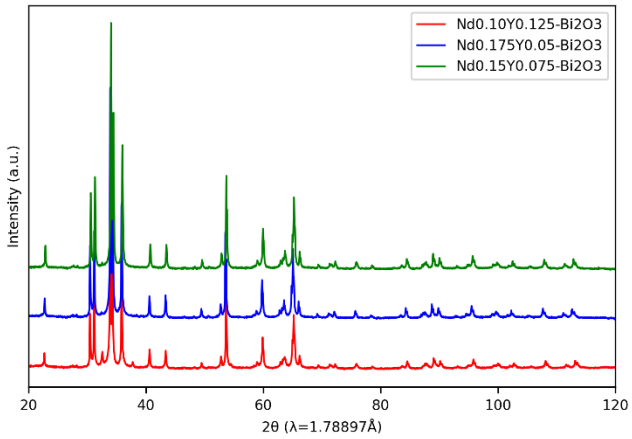


Figure 5.1.85: The XRD patterns obtained for all samples within the 22.5 mol % dopant concentration range for the double-doped samples using the D2 phaser.

Figure 5.1.89 shows the XRD patterns obtained for double doped sample using the laboratory X-ray diffractometer, the D2 phaser. From the diffractogram obtained, it is observed that the 10Nd12.5YSB sample co-existed as a majorly rhombohedral sample, with the presence of a cubic minor phase. The 17.5Nd5YSB, and 15Nd7.5YSB samples existed as a pure rhombohedral phase samples.

5.1.11 22.5 mol % dopant concentration (triple-doped):

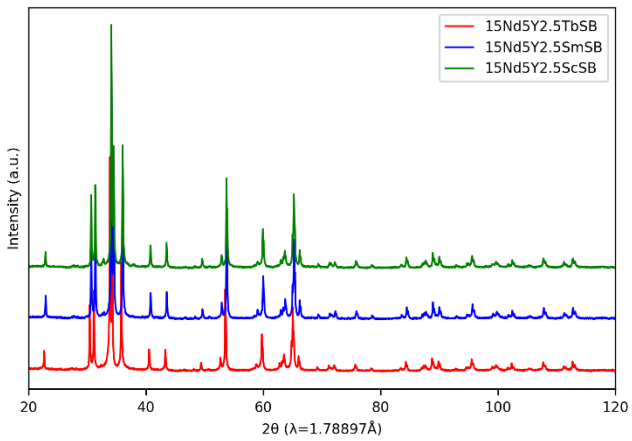


Figure 5.1.86: The XRD patterns obtained for all samples within the 22.5 mol % dopant concentration range for the triple-doped samples using the D2 phaser.

The above figure, figure 5.1.90 shows the XRD patterns obtained for the triple doped samples sample using the laboratory X-ray diffractometer, the D2 phaser. The diffractogram obtained, indicates that the two triple doped samples are phase pure, with one of the triple doped samples indicating a mixture of phases. The 15Nd5Y2.5TbSB, and 15Nd5Y2.5SmSB samples existed as a pure rhombohedral phase samples. However, the 15Nd5Y2.5ScSB sample co-existed as a majorly rhombohedral sample, with the presence of a cubic minor phase.

5.1.12 Aged samples (various dopant concentrations):

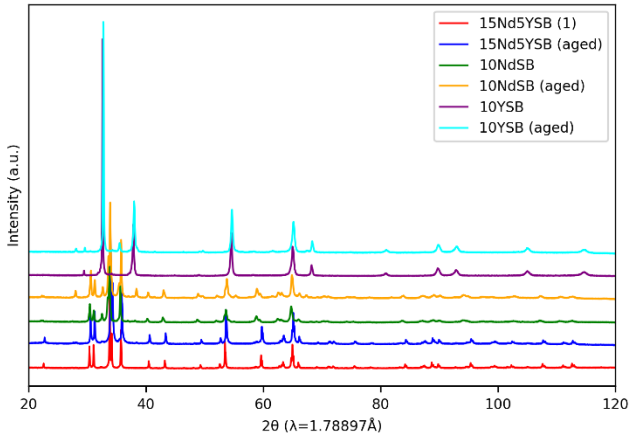


Figure 5.1.87: The XRD patterns obtained for aged samples within various dopant concentration ranges using the D2 phaser.

Figure 5.1.91 shows the XRD patterns obtained for both single doped samples, as well as a double doped sample aged over a period of 8 months using the laboratory X-ray diffractometer, the D2 phaser. From the diffractogram obtained, it is observed that for the two single doped samples, namely 10NdSB, as well as 10YSB during the aging process do not change drastically with the 10NdSB sample still co-existing as a majorly rhombohedral sample, with the presence of a minor phase, namely the monoclinic phase. The 10YSB, however, upon the aging process starts indicating the presence of a secondary phase, thus moving from initially co-existing as a phase pure cubic sample, to now having a dibismuth carbonate dioxide (Imm2) minor phase. The 15Nd5YSB sample existed as pure rhombohedral phase sample even after aging, and thus indicates phase stability.

D9 Advance diffractometer data analysis:

5.2.1 20 mol % dopant concentration:

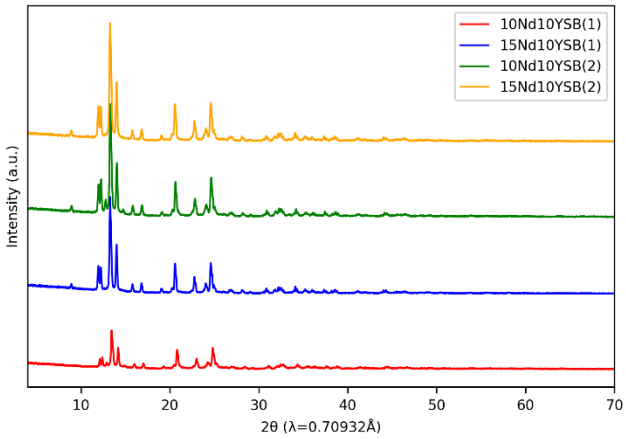


Figure 5.1.88: The XRD patterns obtained for all samples within the 20 mol % dopant concentration range using the D9 advance.

The above figure, figure 5.1.92 shows the XRD patterns obtained for a double doped samples using the laboratory X-ray diffractometer, the D9 advance, which uses a molybdenum cathode ray tube which allows for better resolution for the data obtained due to the lower wavelength of the molybdenum. From the diffractogram obtained, the 10Nd10YSB samples co-existed as a majorly rhombohedral sample, with the presence of minor phases, namely the monoclinic and tetragonal phases. The 15Nd5YSB samples existed as pure rhombohedral phase samples. The (1) and (2) labels indicate that the samples were synthesised at different times.

5.2.2 22.5 mol % dopant concentration:

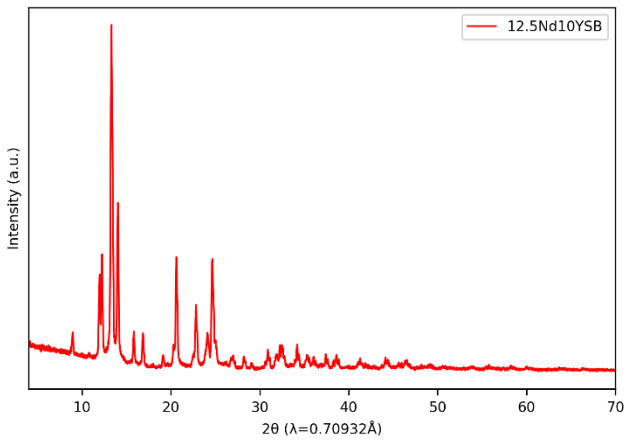


Figure 5.1.89: The XRD patterns obtained for all samples within the 22.5 mol % dopant concentration range using the D9 advance.

Figure 5.1.93 shows the XRD patterns obtained for a double doped samples using the laboratory X-ray diffractometer, the D9 advance. The diffractogram indicates that the 12.5Nd10YSB samples existed as a phase pure rhombohedral sample.